'Cluster' converters based on multi-port active-bridge : application to smartgrids

Soleiman Galeshi Mooziraji

▶ **To cite this version:**

Soleiman Galeshi Mooziraji. 'Cluster' converters based on multi-port active-bridge : application to smartgrids. Electric power. Université Grenoble Alpes [2020-..], 2021. English. NNT : 2021GRALT011 . tel-03273447

HAL Id: tel-03273447

https://theses.hal.science/tel-03273447

Submitted on 29 Jun 2021

HAL is a multi-disciplinary open access archive for the deposit and dissemination of scientific research documents, whether they are published or not. The documents may come from teaching and research institutions in France or abroad, or from public or private research centers.

L'archive ouverte pluridisciplinaire **HAL**, est destinée au dépôt et à la diffusion de documents scientifiques de niveau recherche, publiés ou non, émanant des établissements d'enseignement et de recherche français ou étrangers, des laboratoires publics ou privés.

THÈSE

Pour obtenir le grade de

DOCTEUR DE L'UNIVERSITE GRENOBLE ALPES

Spécialité : **Génie Electrique**

Arrêté ministériel : 25 mai 2016

Présentée par

Soleiman GALESHI

Thèse dirigée par **Yves LEMBEYE, PROFESSEUR, G2Elab**, et codirigée par **David FREY, Maître de conférences, G2Elab**

préparée au sein du **Laboratoire G2Elab**
dans **l'École Doctorale EEATS**

Convertisseur « cluster » à base de multi ports active-bridge: application aux smartgrids

'Cluster' converters based on multi-port active-bridge: application to smartgrids

Thèse soutenue publiquement devant le jury composé de :

Monsieur Philippe LADOUX
PROFESSEUR DES UNIVERSITES, Université de Toulouse, Rapporteur

Monsieur Philippe LE MOIGNE
PROFESSEUR DES UNIVERSITES, Université de Lille, Rapporteur

Monsieur Frédéric WURTZ
DIRECTEUR DE RECHERCHE, G2Elab, Grenoble INP, Président

Monsieur Hossein IMAN-EINI
PROFESSEUR ASSOCIE, Université de Téhéran, Examinateur

Monsieur Yves LEMBEYE
PROFESSEUR DES UNIVERSITES, Université Grenoble Alpes, Directeur de thèse

Monsieur David FREY
MAITRE DE CONFERENCE, Université Grenoble Alpes, Examinateur

Acknowledgements

First, I would like to thank my supervisors, David and Yves, who supported me all along these years. Your help and ideas were always useful and productive and you always knew how to keep the balance between innovative fancy ideas and real world solutions. I learned a lot from you not only on the technical and scientific aspect, but also on the human aspects of being a researcher. I honestly believe I could not have better supervisors for doing this PhD.

I must express my gratitude to the jury members for their useful and productive questions and discussions. I thank Mr. Frederic Wurtz for being the president of the jury. Many thanks to Mr. Philippe Ladoux and Mr. Philippe Le Moigne for all the time and effort that they put on carefully reading the thesis and writing an accurate and detailed report. Special thanks to Mr. Hossein Imaneini, with whom I have a long history since my master studies.

I would like to thank G2ELab, the administrative team and the technical team especially Benoit, for providing a pleasant and efficient environment for the researchers. Many thanks to Eco-SESA and Institut Carnot for funding this project.

During the period of working in G2ELab I got to know many great people. I would like to thanks all my friends in power electronics and other teams for the wonderful times we had, sharing and helping each other, the coffee breaks and after work plans: Adrien, Andre, Antoine, Anh-Tuan, Aureliene, Bakr, Blazej, Damien, Fadel, Gaetan, Glauber, Hugo, Lou, Luciano, Joe, Lucas, Mohsen, Morteza, Nisith, Nicolas, Nasreddin, Nelly, Pawel, Phan, Reza, Theo, Uyen, Vahid, and many others. Additionally, all the professors Yvan Avenas, Seddik Bacha, Yann Bultel, Jean-Christophe Crebier, Jean-Paul Ferrieux, Laurent Gerbaud, Pierre-Olivier Jennin, Pierre Lefranc and Jean-Luc Schanen.

Finally, many thanks to my family, Rahman, Maryam, Mahsa and Ali, for their unconditional love and support during these years. Without your support, I would not be able to go this far. Also my friends, in Iran and in France, who were always there for me and ready to have fun times together.

Abstract

This work proposes a network architecture based on a generic converter structure as its core block, multi-port active-bridge (MAB) structure, for application in microgrids with renewable sources, energy storage devices, DC grids and AC grids. It starts with an introduction to the architecture and its characteristics. The potentials of clustering in enhancing efficiency, flexibility, and reliability of the system are discussed in the first chapter. Simulations are used to show that clustering and a global optimization strategy based on converter models are able to enhance the global system efficiency. The MAB structure, as the core block of the cluster converter, is the subject of a major part of this thesis.

The second chapter starts by comparing the MAB topology to other topologies, and discussing the benefits of MAB converters in a cluster of converters. A MAB converter can simultaneously exchange energy between all sources and loads in either directions, while providing galvanic isolation between them. Its scalable and symmetric topology allows structured and modular optimization algorithms for modeling, design and control. Different models of MAB converters and power control methods are proposed. Additionally, a design procedure for MAB converters is presented.

The third chapter continues the discussions on MAB converters. It starts by studying different types of losses in these converters and proposing loss models for different applications. Risk of saturation in magnetic of the transformer are explained. The origins of the DC currents in transformer windings, that cause saturation, are studied and solutions are presented. An innovative setup is proposed for measurement of DC currents along with experimental validation. Different voltage modulations for addressing DC link voltage variations that often occur in MAB converters are introduced and compared, using the loss model.

A four-port 4×2 kW MAB converter prototype was designed and built in G2Elab. It was used for implementation and validation of the models and control schemes that were proposed in this work. Additionally, hardware-in-the-loop (HIL) validation was used as a first validation and as a quick and low-risk tool for solving potential issues in implementation of the embedded control. Different scenarios and operating points were tested on the prototype, comparing theoretical models, predictions and control methods against the experimental measurements. The results showed good conformities and certain nonconformities, all of which are discussed in detail.

The final part of this work concludes that the proposed cluster of MAB converters is a promising solution for electrical network of microgrids. Studying MAB topology showed that it can be modeled and controlled in a scalable way, allowing for implementation of modular optimization modeling, design and control schemes in large scale clusters.

Résumé

Cette thèse présente une architecture de réseau Smart-grid AC et DC dans lesquels se trouvent des sources renouvelables et des systèmes de stockage d'énergie. Les blocs permettant de les interconnecter sont des systèmes de conversion génériques basés sur une structure de type multi port active-bridge (MAB). Ce manuscrit commence par une introduction de l'architecture globale et de ses caractéristiques.

Le premier chapitre étudie les possibilités de « Clustérisassions » afin d'améliorer la flexibilité, le rendement et la fiabilité au niveau système. Des simulations sont utilisées pour montrer que cette approche, associée à une stratégie d'optimisation globale basée sur des modèles de convertisseurs, est capable d'améliorer l'efficacité globale du système. La structure MAB, en tant que bloc central du convertisseur cluster, est le sujet d'une grande partie de cette thèse.

Le deuxième chapitre débute par une comparaison de la topologie MAB avec d'autres topologies et discute des avantages des convertisseurs MAB dans un cluster de convertisseurs. Un convertisseur MAB peut échanger simultanément de l'énergie entre toutes les sources et les charges dans les deux sens, tout en assurant une isolation galvanique entre elles. Sa topologie évolutive et symétrique permet de concevoir des algorithmes d'optimisation structurés et modulaires pour la modélisation, la conception et le contrôle. Différents modèles de convertisseurs MAB et différentes méthodes de contrôle de la puissance sont proposés. En outre, une procédure de conception pour les convertisseurs MAB est présentée.

Le troisième chapitre poursuit les discussions sur les convertisseurs MAB. Il commence par étudier les différents types de pertes dans ces convertisseurs et propose des modèles de pertes pour différentes applications. Les risques de saturation dans le circuit magnétique du transformateur sont expliqués. Les origines des courants continus dans les enroulements des transformateurs, qui provoquent cette saturation, sont étudiées et des solutions sont présentées. Un dispositif innovant pour la mesure des courants continus ainsi est proposé et validé expérimentalement. Différentes modulations de tension permettant de gérer les variations de tension d'entrée continues du MAB qui peuvent se produire du fait des caractéristiques des sources/charges connectées, sont introduites et comparées, en utilisant le modèle de perte.

Un prototype de convertisseur MAB 4×2 kW à quatre ports a été conçu et construit au G2Elab. Il a été utilisé pour la mise en œuvre et la validation des modèles et des schémas de

contrôle qui ont été proposés dans le cadre de ce travail. En outre, une solution « Hardware-in-the-Loop » (HIL) a été utilisée afin de valider les lois de contrôle et leur implémentation dans le contrôleur avant de le connecter à la structure de conversion finale. Différents scénarios et points de fonctionnement ont été testés sur le prototype, en comparant les modèles théoriques, les prédictions et les méthodes de contrôle aux mesures expérimentales. Les résultats ont montré de bonnes conformités et certaines non-conformités, qui sont discutées en détail.

La dernière partie de ce travail conclut que le cluster de convertisseurs MAB proposé est une solution prometteuse pour les réseaux électriques de type Smart-grids. L'étude de la topologie du MAB a montré qu'elle peut être modélisée et contrôlée de manière évolutive, ce qui permet de mettre en œuvre des schémas de modélisation, de conception et de contrôle permettant l'optimisation modulaire dans des grappes à grande échelle.

Table of contents

Introduction

Today's world of electrical energy is experiencing substantial revolutions in its different aspects. The increase in the world generation and consumption of electricity is not a result of global increase in energy consumption alone, but the share of electricity in total energy generation and consumption that is increasing, too. This is evident in Figure 1, where the increase rate of electricity generation is more than twice that of global energy consumption [1], [2]. Access to electrical energy has increased from around 72% world population in 1990 to more than 87% in 2016 [3], empowering over half a billion people with electricity. Penetration of electricity consuming devices in today's life is as significant as penetration of renewable generation and storage devices in electrical networks.

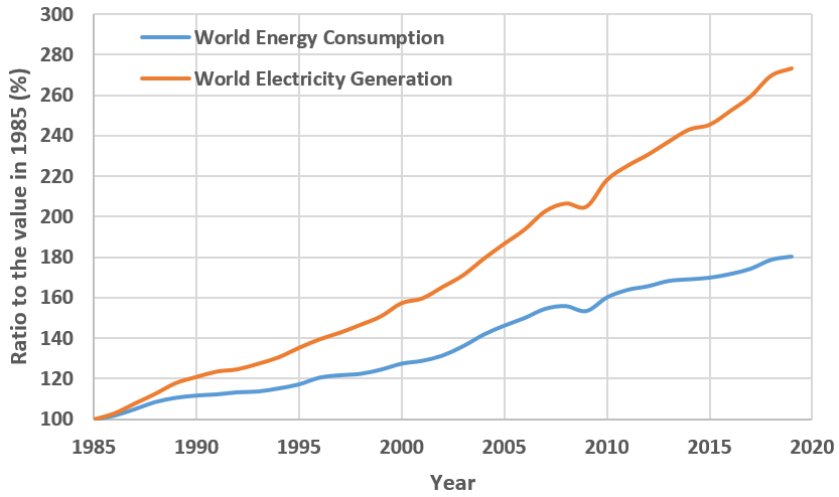

Figure 1: The increase in global energy consumption and world electricity generation since 1985 [1].

More revolutionary changes are yet to come, including:

- Wide application of electric vehicles;
- Substantial increase in consumption of data centers and wireless networks up to 20% global electricity consumption in 2030 [4];
- Renewable energy sources becoming a major source of electricity over the world [1], [5] (Figure 2);
- Wide application of small and large capacity storage devices over the network; and
- AC and DC networks, expected to reach a peaceful coexistence in buildings, after the "war of the currents" in 1880.

The aforementioned changes in the world of electrical energy and electrical networks have numerous consequence. One of these consequences that involves power electronics is the sharp increase in application of converters [6]. Power electronic converters have become an essential component on many levels, from smart phone chargers [7], to storage devices [7,8], microgrids [10], more-electric aircraft [11] and offshore wind farms [12]. The wide range of applications has accelerated the research in this field. Introduction of new topologies as well as adapting existing ones for each application [13]. Application of new materials such as gallium-nitride and diamond in semiconductors [14], [15]. More focus on subjects such as reliability [16], [17], and automated design [18], [19] can all be linked to the fact that power electronics plays a vital role in future's world of electrical networks.

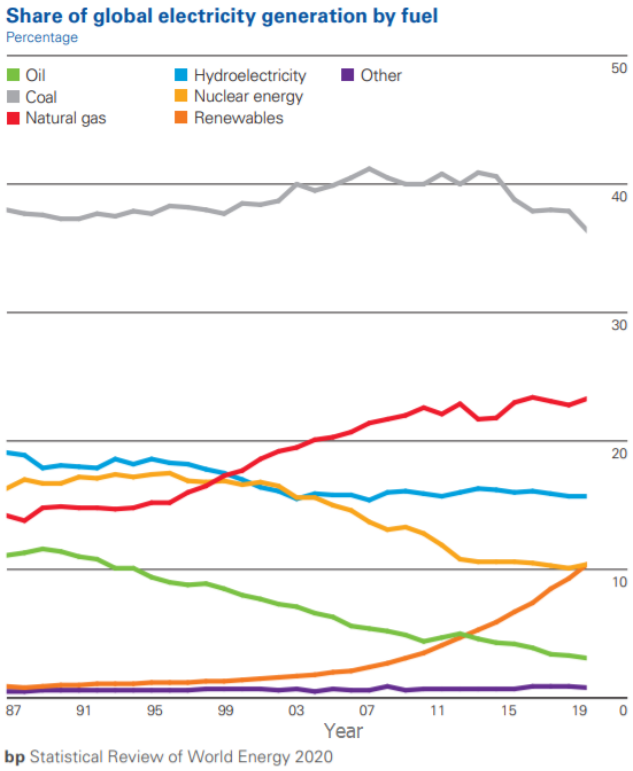

Figure 2: Increasing share of renewable energy sources in electricity generation [1].

The focus of this work is proposing a new electrical network architecture and a converter as its building block, trying to solve some of the challenges of classical electrical networks in microgrids. This work is a part of the 4th research front of "Eco-SESA cross-disciplinary project". Eco-SESA seeks to produce knowledge and tools that can help to address five key objectives in integration of on-the-spot renewable energy generation in urban areas, including:

- Understanding the effects of massive deployment of variable renewable energies;
- Assessing the impact of self-consumption;

- Comprehending and predicting the behavior of consumers and of district stakeholders;
- Governing and coordinating energy at the district/urban scale; and
- Designing adequate energy components.

The 4th research front involves new architectures for integration of renewable on-the-spot generation. The outcome expected from this thesis, and research works that will potentially start in continuation of it, is to provide a network of converters that can be used by other research fronts as a tool for implementing their network planning and energy strategy.

The classic architectures, an example of which is shown in Figure 3-a, employ several two-port AC/DC and DC/DC converters to perform energy exchange, voltage step-up/step-down, and voltage control functions. Each converter has its own design procedure, control rules, limitations and dynamics. Implementing a strategy such as energy optimization over the network requires taking into account all these aspects for each converter, which is not an easy task. Some of these converters are not isolated, making coordination of protection systems more difficult. Adding isolation, on the other hand, can add to the cost, size or complexity of the converter. Another challenge with power electronic converters is that their efficiency generally drops if the power they are processing is much lower than their nominal power. Considering the nature of renewable resources, their output power can be far from their nominal output for long periods, leading to considerable reduction in converter efficiency.

Chapter 1 is dedicated to introduction and analysis of the architecture proposed in this work. This architecture, illustrated in Figure 3-b, employs multiple small multi-port converters as a cluster. A cluster of converters has the potential to enhance flexibility and reliability of the system through its redundancy. These characteristics of a cluster of converters are discussed in more detail in the first chapter. Based on instantaneous power exchange, the control system can decide on using a certain number of these converters and disconnecting the rest, in order to reduce the conversion losses. Simulations based on data from a smart building will be used to determine to the extent of efficiency increase provided by clustering.

Chapter 2 introduces multi-port active-bridge (MAB) converter topology, displayed in Figure 4, as the building blocks of the proposed cluster of converters. This chapter discusses the reasons why this topology has been chosen, and makes brief comparison to other topologies. Each MAB converter can connect all sources and loads of the microgrid, namely renewable source, batteries, DC network and AC network, in one place and exchange energy between them in all possible directions at the same time. This converter can perform energy exchange

and voltage step-up/step-down functions. It has a symmetric and bidirectional structure, allowing development of structured and modular design, optimization and control algorithms. Chapter 2 presents and compares different ways of modeling MAB converters and controlling the flow of power between their ports. Furthermore, it proposes a design procedure for MAB converters, based on the models. To achieve this goal a model of losses in MAB converters is proposed in this chapter when discussing design procedure and power control methods.

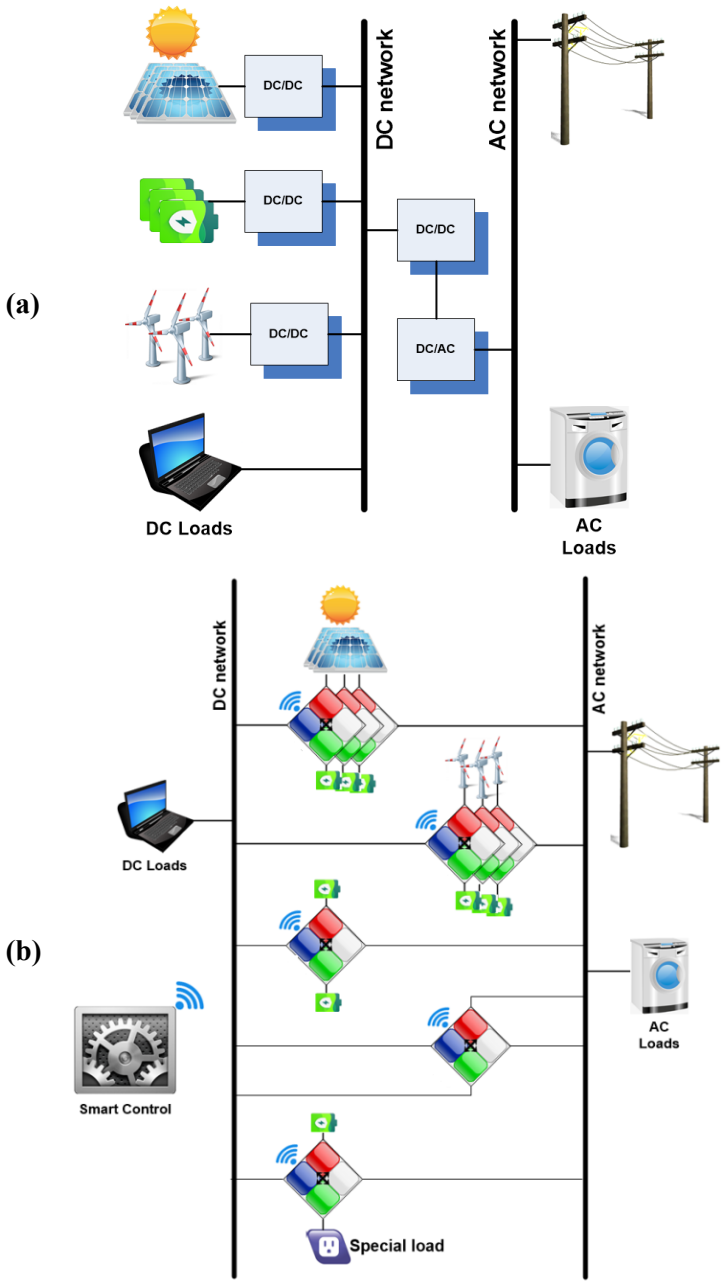

Figure 3: (a) An example of a classic microgrid structure; (b) The proposed cluster of converters.

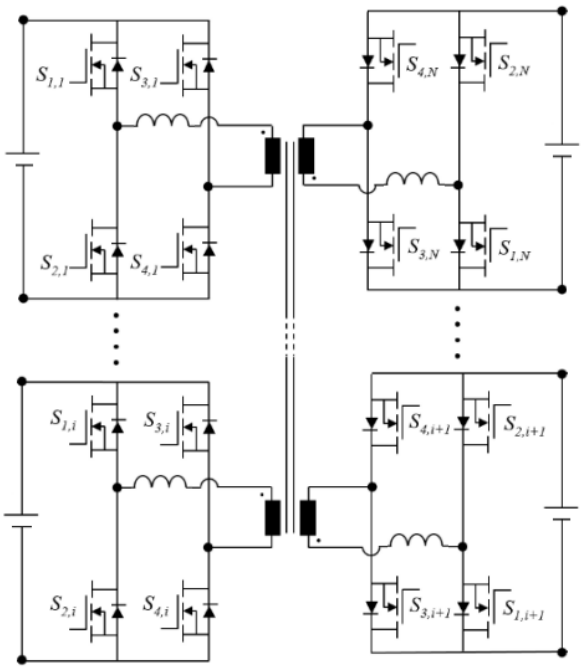

Figure 4: General topology of multi-port active-bridge converters, with one active bridge and one inductor on each port and a multi-winding transformer acting as their coupling point.

Chapter 3 expands the discussions on MAB converters, covering three major subjects. It includes close study of different sources of losses in these converters. Two models, each one suitable for certain applications, are proposed. The second subject is the saturation of magnetic of the transformer as a result of DC currents in the windings. The origins of these DC currents are studied and appropriate solutions are proposed for avoiding them. In order to address the challenge of measuring the DC currents in transformer windings, an innovative setup based on a CT and a Hall effect sensors is presented. This sensor setup is then validated through experimental results. Variations of DC link voltages is another challenge in operation of MAB converters that is discussed in this chapter. Different voltage modulations are introduced for counteracting DC link voltage variations. These modulations are compared in terms of corresponding conversion losses over a certain range of voltage and power, using the model of losses.

Chapter 4 presents the four-port 4×2 kW MAB converter prototype that was built in G2Elab for validation of models and control methods. The design procedure is explained in the beginning of this chapter. Hardware-in-the-loop (HIL) validation is then presented as the tool for early validation of proposed models and control methods. HIL was also used as a quick, low-risk and low-cost tool for debugging any problems in implementation of the embedded control. The rest of this chapter is dedicated to comparing theoretical models, predictions and control methods against the results and measurements from the prototype. The conformities and

nonconformities between the experimental results and the expectations from theories are discussed and studied closely in this chapter.

Conclusions and outlook for future works are presented at the end of this thesis. This work investigated a new network architecture, which is a cluster of multi-port converters, and its benefits on the system level. The chosen converter topology, multi-port active bridge, was studied closely. Modular loss models and power control methods were proposed for the MAB topology, proving it as a suitable candidate with characteristics that are compatible with clustering. Experimental tests on a prototype showed that the discussed theories are capable of modeling and controlling this converter, while addressing operation challenges such as magnetic core saturation, large losses and voltage variations. In short, this work proved the potential of the cluster of MAB converters for application in microgrids and provided tools for modeling and controlling the converters. Future works may improve these tools or use them for proposing cluster-level optimal design and control methods, and better investigate the benefits of clustering on system level.

1. Clustering

Micro-grids have several generation, loads and storage devices with different nature. Considering the variability of the loads and unpredictable renewable generation, an energy system that connects all these objects and exchanges energy between them will face several challenges. Some of these challenges are reliability, efficiency, and flexibility. This chapter proposes a cluster of multi-port converters for energy exchange in micro-grids and shows how it can help solve some challenges of micro-grid energy systems. The next section shortly presents classic solutions that employ one converter per function (each power exchange between two points is considered as one function). Section 3 will study how energy systems of micro-grids can benefit from sharing multiple functions among a cluster of converters rather than employing a single converter for each function. Control and optimal operating point of a cluster will be studied in section 4. The fifth section will present a test case and discuss simulation results. The last section includes a conclusion.

1.1. Classical energy system of a micro-grid

Classical solutions for energy exchange systems in micro-grids involve using multiple AC/DC and DC/DC converters. One general solution is to connect each object to the AC network through isolated DC/DC and DC/AC converters. Isolation is not mandatory, but leads to easier coordination of protection systems in the buildings and enhanced safety. One major drawback of this solution is that it involves several energy conversions between the sources and the loads. Additionally, there is only one converter per function, meaning that the converters should be designed regarding the maximum power level corresponding to the function. For instance, the converter that is connected to the batteries will be sized based on the maximum power that will be exchanged with the batteries. However, the power exchange with the batteries is usually smaller than the maximum power. In case of other objects such as PV panels or loads, maximum power flow does not occur very often either. Therefore, the converters will operate at a fraction of their nominal power for a large portion of their lifetime. Due to the nature of power electronic converters, their efficiency is low when they operate at low power levels (Figure 1.1). Therefore, this classical solution (one converter per function) is not an optimized one in terms of efficiency.

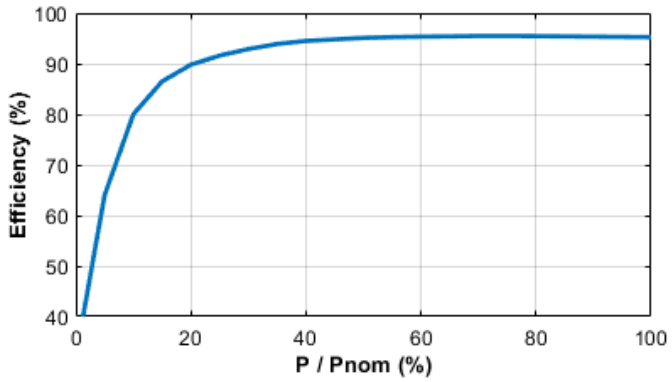

Figure 1.1: Efficiency as a function of power in a converter; P is the transferred power and Pnom is the nominal power for which the converter is designed.

Figure 1.2 shows a classic solution with a low number of converters, compared to the general solution. In this case, it is possible to store PV power in the battery with only one conversion, but at the cost of losing electrical isolation between them. However, energy exchange between AC grid and DC consumers in this solution involves three conversion steps, which means high losses. With low number of converters, this solution seems promising in terms of statistical reliability because it has low number of switches. However, in case of troubleshooting of one converter, a major system functions might be lost, i.e., reliability of the system is not optimal.

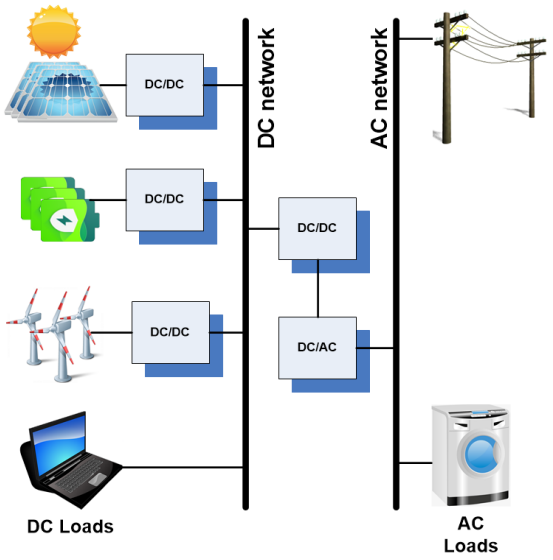

Figure 1.2: Electrical network of a future smart building based on classic DC/DC and DC/AC converters.

1.2. The proposed cluster architecture

In order to solve the challenges of the classical solution that were presented in previous section, a cluster of converters can be employed. In an energy system with a cluster of converters, each function is performed by multiple converters, contrary to the classical single-converter solution. Figure 1.3 shows the proposed cluster of converters. There are several

functions displayed in Figure 1.3, e.g., connecting wind turbines to storage and grids, or energy exchange between AC grid and DC grid. As it can be noticed, there are multiple converters in parallel for each function. The converters in Figure 1.3 are quad-active-bridge (QAB) converters, which will be presented and studied in detail in the next chapter. QAB converters in the cluster can connect an AC grid, a DC grid, a storage device, and a renewable resource altogether in one place and simultaneously exchange energy between all of them. Each QAB converter is designed based on a fraction of the overall nominal power of its corresponding function. This architecture, its potential benefits and challenges in smart buildings will be studied in the following sections.

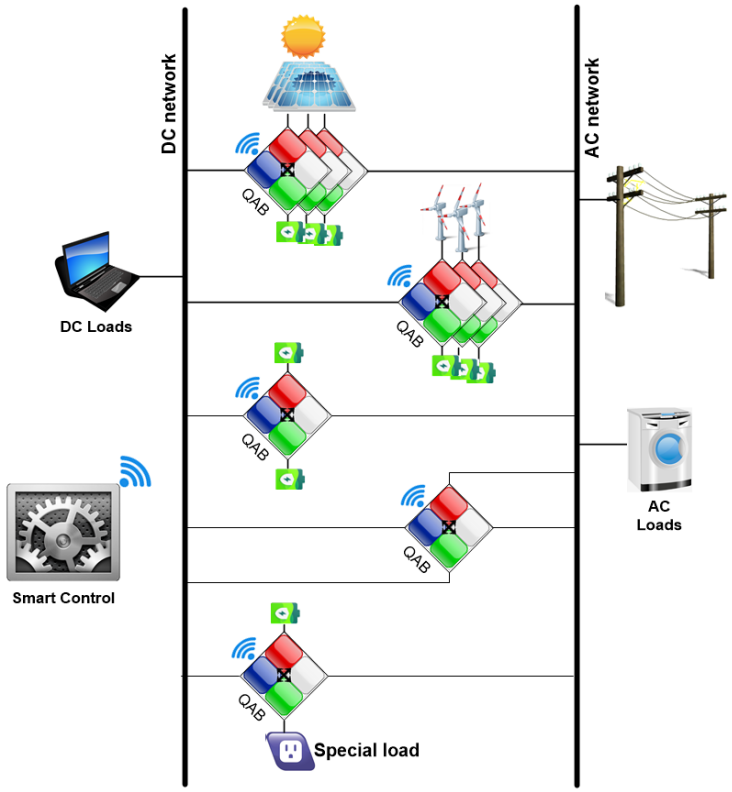

Figure 1.3: A cluster of QAB converters, managed by a central controller.

1.3. Smart grids and internet of energy

IEEE standards association defines smart grids as "systems of distributed systems whose domains span the more traditional domains of bulk generation, transmission, distribution, consumers, markets, and power electronics, with the growing penetration of relatively newer domains such as renewables, electric vehicles, and demand-response-compatible loads. Smart Grid control enables prescriptions for interconnections and interactions among these traditional and emerging domains at the right instants, at the right locations, and in the right manner. The combined expertise of control engineers and scientists will ensure that appropriate loops are

closed, optimal set points and supervisory commands are generated, and desired goals of resiliency, renewables integration, reliability, security, and empowerment of consumers are met. The underlying physics, the interconnection topologies, and the dynamic interactions among various domains will inform control algorithms and architectures" [20].

Figure 1.4 illustrates a schematic of different layers of a smart grid. The control, optimization, and estimation algorithms are part of the cyber layer. Noteworthy is the fact that the information flow among the physical, cyber, and economic components (red arrows) is bi-directional, i.e., measurements data is sent from the physical layer to the cyber layer, and in turn, control and command signals are destined to the physical layer originating from the cyber layer. Decisions are made in cyber layer based on the data gathered from physical & operation and economic & planning layers. In the end, the physical energy exchange system, as a part of the physical layer, is responsible for flowing desired amount of power in desired direction between certain points or objects of the grid.

Considering its capability of efficient, flexible and simultaneous power exchange between multiple objects of a grid, a cluster of multi-port converters can be an interesting candidate for the energy exchange system in the physical and operations layer of a smart grid. Each converter has voltage and current sensors installed on each one of its ports, hence, a cluster of converters can act as a distributed sensing network (the sensing devices in Figure 1.5). In this regard, a cluster of converters distributed all over the grid can provide the cyber layer with measurement data required for decision-making. Furthermore, it owns agents (the converters) all over the network who can execute the command received from the cyber layer and realize the decisions made (the actuators in Figure 1.5).

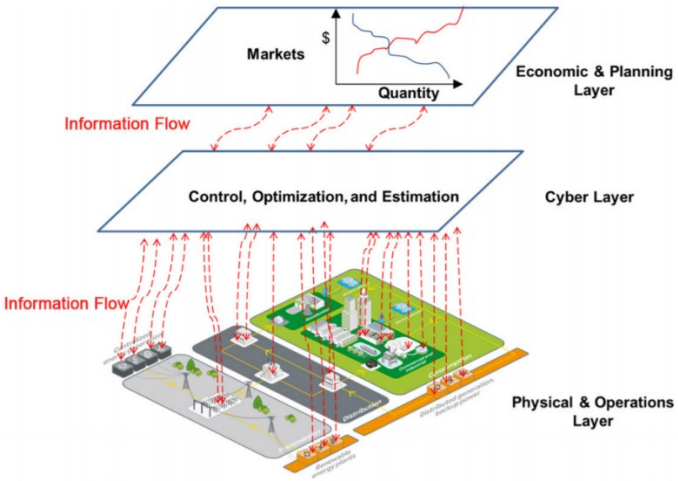

Figure 1.4: A schematic of the grid domains illustrating the physical, cyber, and economic layers [20].

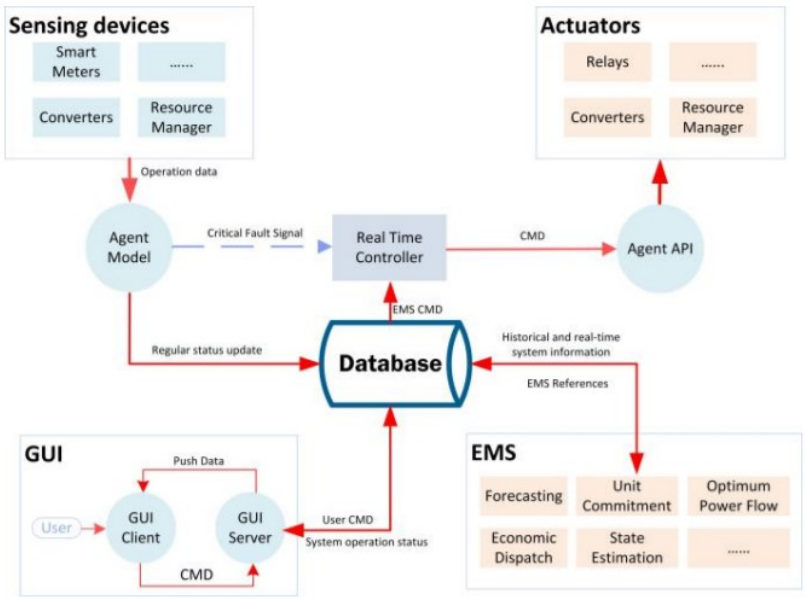

Figure 1.5: Schematic diagram of a micro-grid [21].

Today's technological advances, restructuring of electricity networks and the rapid paradigm shift in definition of producer and consumer roles and in the interactions between them, led to emergence of new concepts, such as collective auto-consumption [22], [23] and internet of energy [24], [25]. Collective auto-consumption is a smart grid based on eco-districts with prosumers (proactive producer and consumer of energy). Internet of energy is a more generalized concept compared to smart grids, and involves thermal, chemical and electrical energies coordinated in wide area exploiting open-information data networks. Energy hubs [21], [24], [26]–[30], as building blocks for smart grids and internet of energy, have been the subject of many researchers' works during the past years. Some researches study high-level control and algorithms without specific concerns for the physical realization of the interconnections and converters [24], [26], [28], while others try to propose real structures of networks and converters of different forms of energy [21], [31]. Although the first group commonly regards the converters as black boxes, as illustrated in Figure 1.6, they still need some knowledge of internal interactions and phenomena of these black boxes, usually in the form of mathematical models to be able to design optimal control. The challenge is that many of the proposed physical structures have disparate internal phenomena. In this regard, a QAB converter can be considered as an electrical energy hub, which is intrinsically symmetric and modular. These characteristics of QAB converters along with efficient power control and efficient model of losses, which will be presented in the next chapters, can help easier programming and implementation of scalable optimization strategies over the grid.

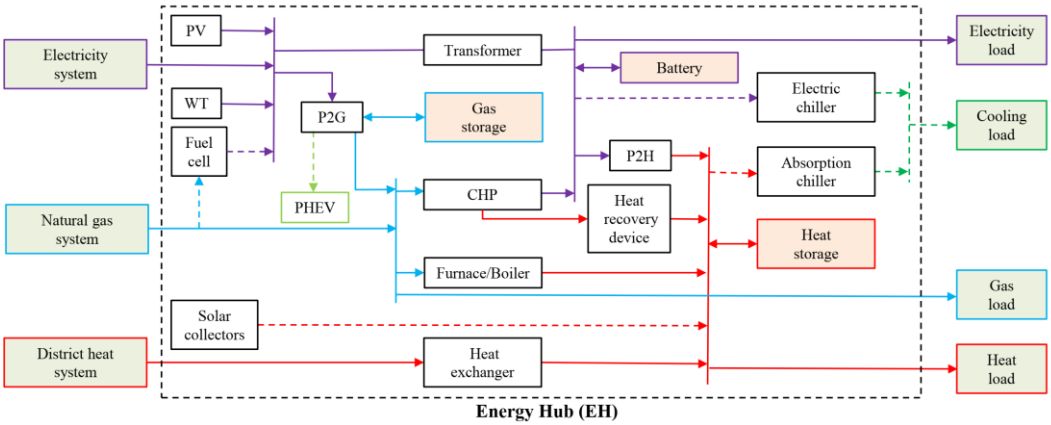

Figure 1.6: Schematic of an energy hub in a control optimization study, without clear indication of the physical components [29].

1.4. Challenges

Along with several advantages, clustering does bring its own challenges. Complexity of control is the main challenge. Due to having many converters that interact with each other, the clustering calls for advanced control methods. Redundancy, as a positive point of clustering, requires a complex control system. Finding optimal or even close-to-optimal operating point for a cluster of converters can be much more difficult, compared to a single-converter system. This section seeks to better study these challenges.

A cluster of converter has multiple levels of control: the higher level maintains coordination between the converters, and the lower level corresponds to the internal control of each converter. In other words, there is a central or distributed cluster controller, who decides the power flow of the converters in the cluster. Additionally, there is an internal controller in each converter to generate switching signals in a way that corresponds to its power flow. This control scheme requires real-time exchange of measurement data, sent from the converters to the cluster controller, and command signals, sent from the cluster controller to the converter control units. Exchange, validation and storage of all these data requires an existing operational data network. The cluster control scheme can take advantage of the data network of an existing smart grid, if any, as illustrated in Figure 1.4. In any case, data network can be an additional challenge that clustering brings about.

Power flow of a cluster of converters means how much power is fed to or derived from each port of each converter, i.e., it indicates operating point of each converter in the cluster. In a cluster of converters, there are multiple ways to flow the power between production, storage and consumption points. Each possible power flow leads to different amounts of losses in each converter and in the whole system. Therefore, it is important to find the optimal power flow in

order to minimize the energy losses. In cases where finding the optimal power flow is too difficult, finding a close-to-optimal power flow can be a good option.

Finding an optimal or close-to-optimal power flow needs good knowledge of the converters and their losses. Next chapter will present the converter that is proposed for application in a cluster of converters, and it will study its internal behavior and losses. Being able to predict the losses in each converter based on its operating point, a cluster control system can attempt to find the optimal power flow of the cluster. It should be taken into account that the model of losses should have a good balance between accuracy and simplicity. If the model is not accurate enough, the results will not be reliable. If it is not simple enough, the control system will not be able to find the optimal power flow in real-time or even close-to-real-time manner. In this regard, the next chapter will present an efficient model of losses that can be used for real-time optimization of power flow in a cluster of converters. A very simple model of losses will be used at the end of this chapter to show how loss-model-based optimization of the power flow can reduce the losses.

1.5. Costs and implementation

Implementing a cluster of smaller converters instead of a classical single-converter solution increases the capital costs and complexity of installation and maintenance. However, clustered converters increase the energy efficiency, which means less pollution and lower costs of buying energy from utility grid. A detailed economic analysis can determine to what extent does the reduction in energy costs compensate for additional capital costs.

Standardization of design and manufacturing processes is a trending subject that can lead to significant reduction in costs [32]. Assuming that standard converters, designed specifically for clustering, will be available in the market someday in the future, it would be cheaper to build a modular cluster of these small converters, compared to designing and building a single big converter. Moreover, regarding the size of cluster converters, it will be possible to install them along with a small cluster storage in existing free spaces such as electrical panels and avoid additional costs of providing a dedicated space for big converters and storage devices.

It should be noted that higher efficiency is not the only way that clustering reduces the life cycle costs of the system. Flexibility in energy distribution and improved reliability of the whole system, are the other advantages that contribute to cost reduction.

1.6. Reliability

A cluster of converters has many more switches and components compared to a classical single-converter energy system. From a statistical point of view, clustering increases probability of failure and it may be concluded that it undermine reliability of the system. Considering λ as rate of failure per hour for an active-bridge, reliability of a single QAB as a function of operating time (t) would be [33]

$$R(t) = e^{-4\lambda t} \tag{1.1}$$

which gives its mean time to failure (MTTF) as

$$MTTF_{single} = \int_0^{+\infty} R(t) = {}^{1}/_{4\lambda} \tag{1.2}$$

Design parameters of the cluster converters will be different from those of a single converter because their nominal power is n times smaller than that of a single converter (n being number of converters in the cluster). Therefore, failure rate of active-bridges in cluster converters might be a little different from λ. With some approximations, rate of failure of a cluster of n converters can be considered to be $4n\lambda$, hence

$$MTTF_{cluster} = \int_0^{+\infty} R(t) = {}^{1}/_{4n\lambda} \tag{1.3}$$

It should be noted that the converters in a cluster work discontinuously and there are times that they will turn off (or probably go into a certain stand-by mode). Turning the converters on and off repeatedly increases the power cycles and turn-on procedures they go through, which can lead to shorter MTTF [34]. Therefore, clustering multiple converters in general increase the probability of failure. On a system-level point of view, on the other hand, occurrence a failure can lead to losing one converter, but does not stop the whole cluster from functioning. The energy system can continue to provide services on a certain reduced level, despite losing a few converters of the cluster. Therefore, $R(t)$ and $MTTF$ as measures of failure probability do not have a direct and simple relation with reliability of the cluster. A more complex reliability function should be defined in this case, which is out of scope of this work.

There are yet other aspects that clustering can further improve system-level reliability. One approach to provide full services to the load despite losing one converter is overloading the rest of the converters that still work. In many smart building applications, the maximum demand only occurs for a limited period. The overload after losing one converter in a cluster of n would

be $\frac{100}{n-1}$ %, hence the bigger the number of converters in the cluster, the smaller the overload. In cases where maximum demand occurs quite often or overloading is not an option, e.g., to prevent further increase in rate of failure, overdesigning the converters can be a solution. This is equivalent to installing a few more converters than the required number of converter. Considering $\frac{n}{n-1}$ % overdesign during design stage, can help the cluster work without any overload after losing one converter. For instance, 5.2 % overdesign in a cluster of 20 converters is enough to be able to provide the full demand after the first failure. In case of classical solution, the single converter will not be able to operate after the first failure and neither overloading nor overdesign help preventing total load loss.

During the repairing procedure of a classical single-converter system, the services have to stop. In case of a clustered system, the system can continue providing the load (with the limitations stated above). It is also predictable that repairing or replacing a small cluster converter is easier than the bulky converter of the classical solution.

It was shown that clustering undermines reliability in classical statistical definition, which is not a proper measure in the current case. Without exact quantitative assessment of reliability, it is still possible to conclude that a cluster of converters improves reliability on system-level and decreases probability of load loss. Table 1-1 summarizes the main points of this section.

Table 1-1: Impact of clustering on reliability and probability of load loss

Architecture	QABs	MTTF	After 1st failure	Overdesign or Overload	Repairing
Single	1	$\frac{1}{4\lambda}$	Total load loss	Does not help	System should stop
Cluster	n	$\frac{1}{4n\lambda}$	Unable to provide loads beyond $(\frac{n-1}{n})$ p.u	No load loss after the 1st failure	The failed converter gets fixed while the rest work seamlessly

1.7. Efficiency

Improving energy efficiency is a key element in every plan to reduce CO2 emissions and avoid adverse consequences of climate change. According to different reports [35], [36] (Figure 1.7), buildings are responsible for approximately 40% of energy consumption and 36% of CO2 emissions in the European Union (EU), making them the single largest energy consumer in Europe. In 2007, the EU has set the target of 20% improvement in its energy efficiency by 2020, known as 20-20-20 climate & energy package [37]. It has reported in March 2019 that the EU countries are on track of achieving the target. The EU has again in 2018 set binding targets of at least 32.5% energy efficiency by 2030, relative to a 'business as usual' scenario [36]. Therefore, improving energy efficiency in buildings is an important issue for reduction of

CO2 emissions. According to UN Environment Finance Initiative, EU needed to invest $1.3 trillion to help keep global temperature rise below 2 degrees [36].

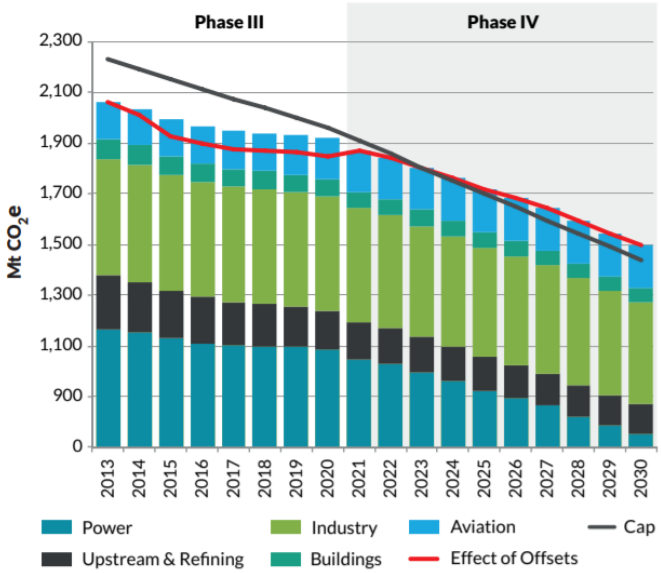

Figure 1.7: Projection of achieving the EU planned target in reduction of CO2 emissions [36].

An IEA analysis in 2012 [38] showed that a big part of the potential efficiency improvement remains untapped without setting proper policies and investing on innovations (Figure 1.8). Currently, major part of improving energy efficiency in buildings involves improving thermal isolation. However, statistics show that share of electricity in energy consumption of buildings is increasing (Figure 1.9). Electricity consumption of buildings will see around 50% increase by 2035, compared to 2018 consumption. It means that electrical energy systems will play an important role in achieving the emission reduction targets. In the following, efficiency improvement due to clustering will be explained. A test case will be studied in the section 4 of this chapter to assess the extent of improvement in real smart grid applications.

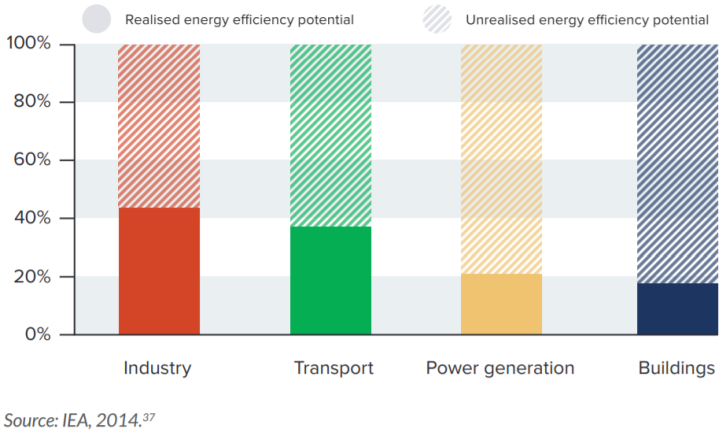

Figure 1.8: Impact of policies on efficiency increase, comparing potential and projected realized improvement by 2035 [38].

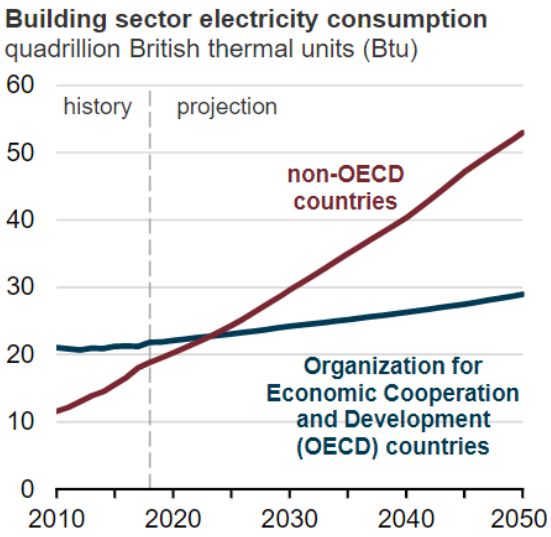

Figure 1.9: Increase in electricity consumption of buildings

As discussed previously, classical solutions do not provide high efficiency over their whole power range. This fact is better illustrated in Figure 1.10. Figure 1.10 presents a classic efficiency curve of a power electronic converter, on the left side. The curves on the right show how the efficiency of low power regions improves if the converter is replaced by multiple smaller ones. The power range is 0 kW to 10 kW and for each case, and the converters are designed based on maximum power of 10 kW divided by number of converters in the cluster. In this regard, the converter corresponding to the left-most curve is a single converter of 10 kW, while the right-most curve corresponds to eight converters of 1.25 kW nominal power. The efficiency curve of each single converter is assumed to be the same in all cases, for the range of 0 to 100% its nominal power. This is an approximation because generally the efficiency curve of power electronic converters improves slightly when the rated power increases. Figure 1.10 shows that a cluster with eight converters provides high efficiency in almost its whole power range.

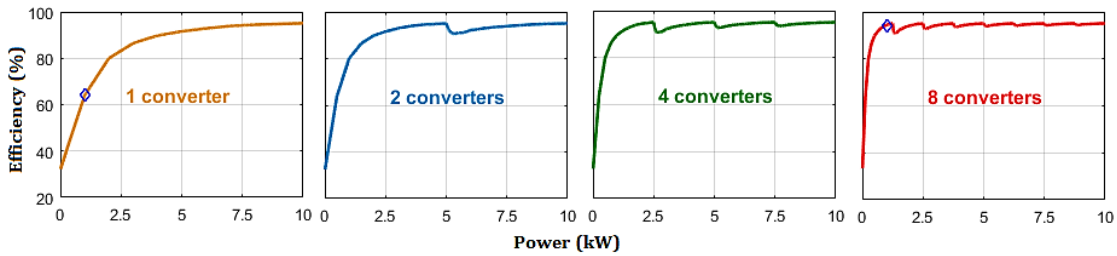

Figure 1.10: Efficiency of a cluster of converters with different number of converters, for zero to 10kW power transfer.

Based on Figure 1.10, if a single converter with nominal power of 10 kW, were employed to transfer 1 kW of power, which is 10% of its nominal power (the blue diamond in left-most

curve of Figure 1.10), its efficiency would be around 64%. It means the conversion involves 360 W of conversion losses. Meanwhile, the 10 kW converter can be replaced by a cluster of eight converters of 1.25 kW nominal power. In this case, it would be possible to turn off seven converters, and use only one for transferring 1 kW. The converter will operate at 80% of its nominal power, i.e., its efficiency will be around 94% (the blue marker in Figure 1.10, with 8 converters). In this case, total losses would be 60 W, compared to 360 W losses in case of a single 10 kW converter. In case of higher power transfers, certain number of converters can be employed to perform the energy exchange, while the rest will be turned off (or remain in stand-by mode, depending on the strategy). Choosing how many converters to involve in energy exchange, and how to share the task among them are optimization problems, which will be discussed further in section 1.9.

There are other ways that the proposed cluster of converter can contribute to efficiency improvement. Clustering of PV panels, can lead to better maximum power point tracking because clusters of PV panels might have different radiation, cleaning level and clouding conditions. Due to the isolation between the ports, it is also possible to connect resources that cannot be clustered, using multiple converters. As an example, a 10kW CHP unit can be interfaced to the grid using five parallel converters of 2kW. Based on the power output of the CHP unit at each moment, some converters will be disconnected, while the others will operate close to their nominal power with high efficiency.

1.8. Software simulations

This section seeks to assess the potential of efficiency improvement with clustering. In many improvements on energy systems of micro-grids, the final gain depends on several factors that are specific to the application or the user. Some of these factors are solar radiation profile, wind speed profile, electricity tariffs, storage capacity, and consumption profile. The impact of peak shaving optimization schemes, as an example, on cost reduction highly depends of the electricity tariffs. Peak shaving can lead to a considerable cost reduction for the customer only if the difference between electricity price during peak hours and off-peak hours is large enough. As another example, optimal sizing of energy storage does not have a significant impact if the renewable generation output is not comparable to the consumption. In this regard, the simulations of a smart grid in this section are based on a real test case to be able to better compare energy efficiency of a cluster of converters with a single-converter system. The GreEn-Er building, housing G2ELab, Grenoble INP ENSE3, PREDIS and MEE Lab, is studied as the

test case of this work. Figure 1.11(a) shows the consumption profile of the building. It consists of five main categories: lighting, heating, cooling, ventilation, and wall plugs.

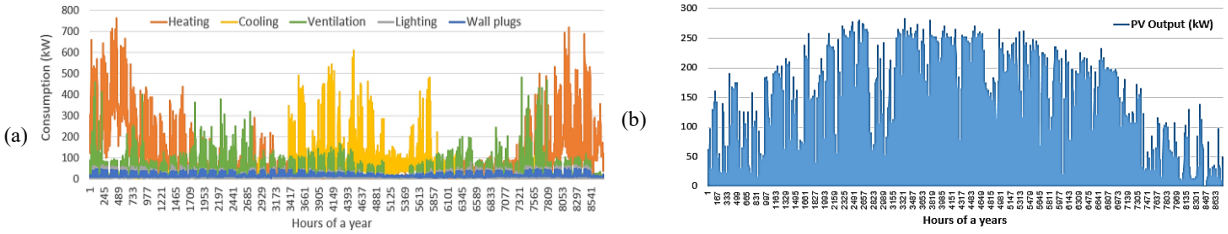

Figure 1.11: (a) Load, and (b) PV generation profiles of GreEn-ER building during a year, with resolution of one hour.

Overall consumption of the building is more than 1.7 GWh per year. Currently, there is one array of 90 PV panels installed on roof of a bicycle parking. PV output energy is 24 MWh per year, which is too small compared to the consumption. A few assumptions are made, in order to match the generation and the demand. First, it is assumed that 14 arrays of 90 PV panels will be installed on the building roof as forecast, which takes less than 50% of the available area on the roof. Therefore, the yearly renewable generation would be 360 MWh from 1350 PV panels. PV power generation profile is illustrated in Figure 1.11(b). Second, it is assumed that a DC network exists in the building, to which the LED lighting and wall plugs are connected. Majority of the loads on wall plugs are PCs, which have DC nature. Hence, it is not far from reality to assume that they will be connected to the DC network in the coming future. Lightings and wall plugs consume around 310 MWh per year. The rest of the loads are connected to the AC network and directly provided by utility grid. The renewable resources and storage devices provide the loads on DC network through multi-port converters. Multi-port converters provide the possibility of exchanging energy with AC network simultaneously. Therefore, in case of shortage or excess of energy balance between DC loads, PV generation and storage devices, the AC network can be treated as an infinite energy source/sink. The overall structure of the system would be as the one displayed in Figure 1.3, while the laptop and the washing machine in Figure 1.3 represent DC loads and AC loads, respectively.

As discussed before, the improvement of clustering is using several small multi-port converters instead of a single bulky one. A cluster controller is needed to take into account several factors, such as solar irradiation on each cluster of PV panels, state of charge of each battery cluster, demand on AC and DC grids, and electricity tariffs, in order to determine optimum operating point of the cluster for each time slot. In other words, it determines optimal energy distribution between all the converters, resources and grids in the energy system. Each converter has its own internal control scheme that receives its planned power flow from the

cluster controller and then decides on its internal optimum operating point. There are several different strategies to find an optimum or close-to-optimum operating point for a cluster. In this section, a straightforward cluster control strategy is used in the simulations. Figure 1.12 illustrates the flowchart of the control strategy. The first priority in this strategy is to provide the loads using renewable generation. If the renewable generation alone was not enough to provide the load, the energy stored in storage devices will be used, and if the loads were not still met, AC grid would provide the rest.

The strategy that is used in the simulations include a balancing scheme to balance utilization of resources. Balancing is especially important in case of storage devices, such as batteries, because it directly affects their life cycle and capacity. Without balancing, some batteries may be charged and discharged more than the rest. This problem can occur as a consequence of using a control algorithm that always starts its control loops from converter #1 and does not have a rotation scheme. As an example, a cluster of four converters can be assumed, where 100% of PV generation of converters #1 and #2, and 50% of PV generation of converter #3 supply the load, while 50% of PV generation of converter #3 and 100% of PV generation of converter #4 are stored in their corresponding batteries. If batteries are full, the corresponding energy will be injected to the AC grid. In this strategy, battery #4 always has the highest chance of getting charged. Therefore, when the energy stored in batteries is needed to feed the DC grid, battery #4 will probably be used more often compared to battery #1. It means that battery #4 will be charged and discharged more often and age faster. A rotating algorithm, which rotates the beginning point of control loops amongst the batteries, balances the battery utilization.

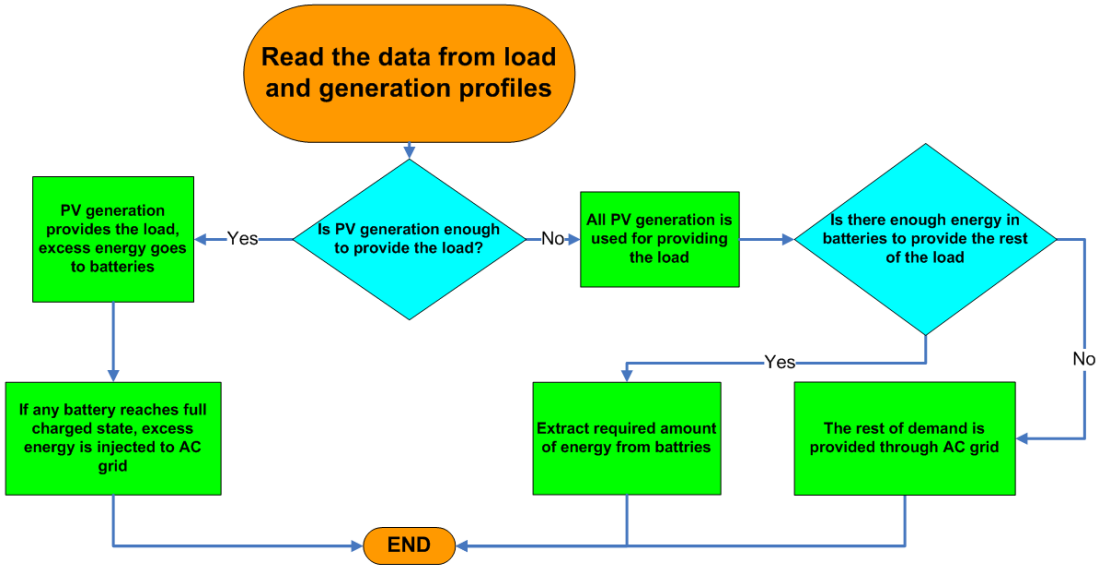

Figure 1.12: Flowchart of a straightforward control strategy for a cluster of converters; it runs for each time slot to determine power transfer of each port of each converter in the cluster.

The control strategy depicted in Figure 1.12 determines operating point of the cluster for each time slot, and then, conversion losses can be calculated hour by hour for a full year. It should be noted that, the losses of a multi-port converter, and hence its efficiency, depend on the overall power flow of all of its ports. Although, approximately speaking, some types of losses such as switching losses can be independently calculated for each port, certain types of losses, such as transformer losses, depend on the overall power flow. Generally, a mathematical model of losses can determine the losses in a four-port converter as a function of the four powers. A model that determines all the losses will be too complicated. Although this model can be used for design and simulations, it would not be applicable in case of a real control system that seeks to minimize the losses in a real-time or close-to-real-time manner. In this regard, two models of losses will be presented in chapter 2: a detailed model that can be used for offline applications such as design and simulations; and an approximate model that can run efficiently on a controller chip with limited resources. The model includes iron losses in transformer and inductor cores, conduction losses in transformer and inductor windings, and conduction losses in the switches. An efficiency curve is used in the simulations of this section. It is based on the model that will be presented in chapter 2. Based on this efficiency curve, illustrated in Figure 1.1, efficiency of the converter can be determined as a function of the mean power transfer (absolute values) of all ports of the converter. Although it is not an accurate way to calculate conversion losses, it is good enough to show how clustering can improve the efficiency of the energy system. More accurate comparisons will be performed after presenting the loss models in chapter 2.

Specifications of the simulation and the study case are listed in Table 1-2. Figure 1.13 shows overall efficiency of a cluster with different number of converters, employed in the presented study case. The overall efficiency is considered as the sum of the energy delivered to the consumers, which are on the DC grid, divided by the sum of the energy produced by PV panels and the net energy imported from utility grid. The efficiency is calculated for a period of one year. It shows that for a single-converter system, the overall efficiency is around 69%. The efficiency quickly increases up to 80% with a cluster of four converters, while it goes up to 82% with 12 converters. A cluster of four converters, as an example, would lead to 62 MWh energy saving per year. Considering the savings in yearly costs of energy, against costs of adding each converter to the cluster, a detailed costs analysis could find the optimum number of converters for each study case.

Table 1-2: Simulation parameters

Number of converters	n = 1 up to 20	**Yearly Generation**	360 MWh
Peak demand	115 kW	**Nominal power (each converter)**	280/n kW
Peak generation	282 kW	**Battery capacity (each battery)**	560/n kWh
Yearly consumption	310 MWh	**PV panels**	1350 panels

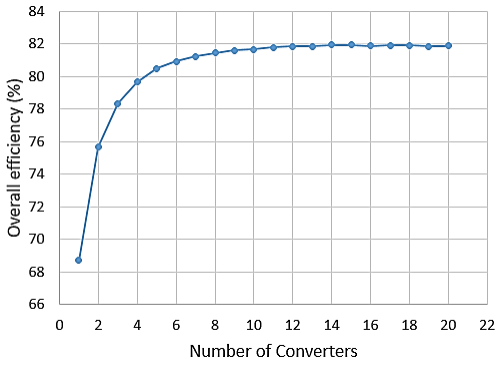

Figure 1.13: Overall efficiency of the energy system based on different number of converters.

Figure 1.14 displays operating point and efficiency of different numbers of converters during 48 hours. It clearly explains how clustering can increase efficiency. Considering the operating point of the system, illustrated in the bottom curve of Figure 1.14, the power transfer is below 20% maximum power almost half the time. A cluster of eight converters would operate at minimum efficiency of 90% for almost the whole time, while in case of a single converter the efficiency could drop below 70% for a considerable amount of time.

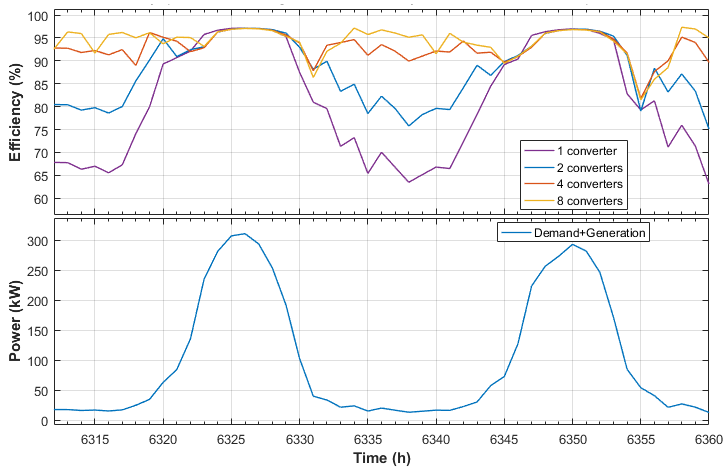

Figure 1.14: Power transfer and efficiency of different clusters of converters, for two consecutive days (The horizontal axis is the hour of a year. This figure shows 21-22 September)

1.9. Optimal power flow using loss models

As stated before, there can be many different ways to employ the cluster converters to provide the demand, based on the demand on DC grid, the generation of renewable resources, and the energy stored in the batteries at each moment. In order to take advantage of redundancy and flexibility, an energy management strategy is required to find the optimal flow of power among the converters. The optimization goal is to minimize conversion losses. The energy management strategy that was used in the simulations of previous section was a straightforward strategy. The strategy was to employ as few converters as possible to perform the task of power transfer. This section seeks to propose different strategies and to assess the level of their impact on global loss reduction in the cluster, based on the test case from the previous section.

1.9.1. The domain of optimization

The goal is to find optimal power distribution in a cluster of parallel converters, or to be more specific, to find optimal the number of converters to participate in power transfer. It should be noted that usually all photovoltaic panels generate power during the day, therefore, all converters that connect to photovoltaic panels should be turned on and operate during the day. Therefore choosing optimal number of converters is not a case in this situation. During the nights, however, the power is totally provided by the AC grid (it is assumed that the storage devices are quickly discharged in the beginning of the evening). In this case, it is possible to choose the number of converters that participate in power transfer. An example situation is a cluster of 20 converters, each designed for 1 kW nominal power, when the demand on DC grid is 15 kW. It is possible to employ 15 converters, each transferring 1 kW, employ 20 converters, each transferring 0.75 kW, or any number of converters between 15 and 20.

1.9.2. Model-based optimization

The main losses of MAB converters are: 1) conduction losses in the windings of transformers, inductors and switches; and 2) magnetic core losses in transformers and inductors. Employing more converters in power conversion leads to reduction of sum of current squares, hence, lower conduction losses. On the other hand, in order to minimize core losses, it is better to employ as few converters as possible. The tradeoff between these two losses can give the optimal power flow. An approximate model of losses will be used in this section to find the optimal power flow.

The conduction losses in a single QAB converter can be determined as $\sum_{ports} RI^2$, where R and I are overall equivalent resistance of windings and switches, and effective current, respectively. Current can be approximated as power (P) divided by voltage (V), therefore

$$Loss_{cond} = \sum_{ports} RI^2 = \sum R(\frac{P}{V})^2 \tag{1.4}$$

Core losses can be predicted using different methods. The iGSE method [39] is commonly used for predicting core losses when the voltage across the windings are non-sinusoidal, as in case of QAB converters. The core losses in iGSE method depend on core geometry and material, and the voltage waveform. Although the voltage waveform changes with the power, it can be approximated as a constant value in order to simplify the calculations. The core losses are assumed to be a constant value, P_{core}, in each QAB converter. Therefore, total losses of a cluster that employs n converters to transfer P kilowatts from AC grid to DC grid would be

$$Loss_{tot} = nLoss_{cond} + nP_{core} = n\sum R(\frac{P}{nV})^2 + nP_{core} \tag{1.5}$$

It is assumed that the power is equally divided between the converters, therefor the current in each converter would be $\frac{P}{nV}$. In order to find the minimum losses, $\frac{dLoss_{tot}}{dn} = 0$ should be solved, which gives

$$n = \sqrt{\frac{R\sum\left(\frac{P}{V}\right)^2}{Loss_{core}}} \tag{1.6}$$

1.9.3. Efficiency-curve-based optimization

As explained in the previous section, the optimization studied in this section is only possible when there is no power exchange with renewable resources and storage devices. Under this condition, only two ports of each converter (the ports connected to AC and DC grids) will be transferring power, hence, the QAB can be regarded as a DAB. An efficiency curve for a DAB can be determined theoretically, through an accurate model of losses, or experimentally, through measurements.

A simple method of finding optimal number of converters is to try to operate the converters at their maximum efficiency point. In case of a converter with a non-flat efficiency curve, the number of converters can be determined based on

$$n = \frac{P}{P_{max-eff}} \tag{1.7}$$

where $P_{max-eff}$ is the power at which maximum efficiency occurs.

1.9.4. Simulations and results

Two methods were introduced in previous sections for finding optimal number of converters for performing power conversion task. Simulation results can help comparing global efficiency of these methods and the method that was used in section 1.8. The extent of efficiency increase is expected to be dependent on load profile and converter design. In order to better assess performance of the proposed methods, two different converter designs (called A and B) will be studied. Figure 1.15 shows efficiency curves of these converters. Peak efficiencies of converter designs A and B are 94.8% and 91.6%, which occur at 100% and 50% nominal power, respectively.

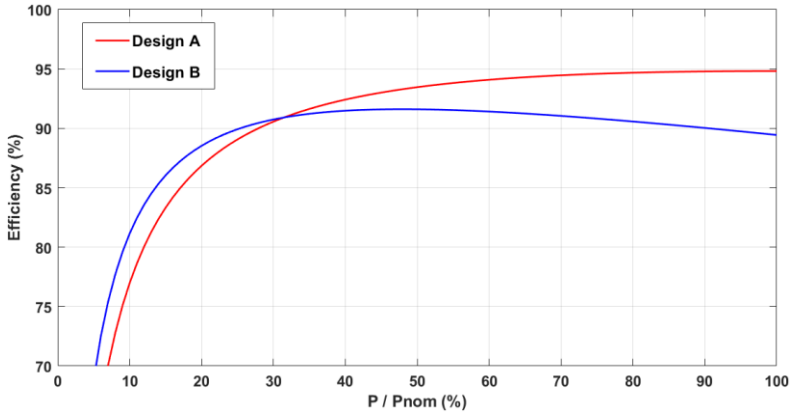

Figure 1.15: Efficiency curves of the two converters used for simulations

1.9.5. Efficiency over the whole range of power

In the first step, the efficiency was compared while the power increased linearly from zero to 100% nominal power. Figure 1.16 shows the simulation results of a cluster of 20 parallel converters. The horizontal axis represents the power flowing from AC grid to DC grid, normalized based on nominal power of the cluster.

As already discussed, the optimal point is the balance between conduction losses and core losses. The converter design A has small resistances, therefore, conduction losses are small and core losses are the dominant losses. In this case, the optimal solution is to use as few converters as possible, which was the strategy used in section 1.8. This fact is verified in the simulation results of Figure 1.16-a, where performance of the method in section 1.8 is similar to the optimized solutions.

(a)

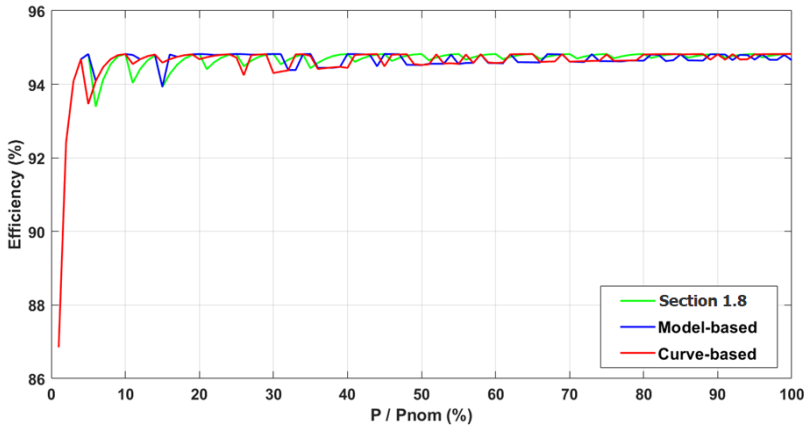

(b)

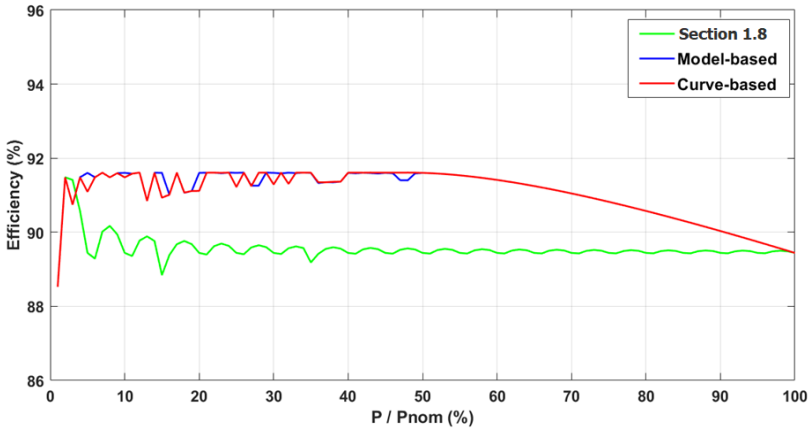

Figure 1.16: Comparing efficiency of different methods over full power range for: (a) design A, and (b) design B.

In case of converter design B, however, resistances are higher and conduction losses are the dominant losses. As explained before, it is better to employ as many converters as possible in this case. This is the reason why performance of the method used in section 1.8 is relatively lower than the other optimized methods, since it employs as few converters as possible. The results illustrated in Figure 1.16 show that the two proposed methods are equivalent in almost all the operating points.

1.9.6. Simulation results of the test case

Simulation of the test case in section 1.8 was repeated using the two proposed optimization strategies. Figure 1.17 shows efficiency of the system for three consecutive days (15^{th}-17^{th} November). It clearly shows that optimized strategies improve the efficiency during the nights.

Similar to what was illustrated in previous section, in case of converter design A, different strategies have almost the same performance. In case of the converter design B, however, the proposed strategies lead to 1-2% higher efficiency during the nights. The strategy used in section 1.8 employs the converters at 100% nominal power, while maximum efficiency of converter design B is at 50% nominal power. The optimized strategies, on the other hand, are

able to employ the converters as close as possible to their maximum efficiency point. In case of design A, total yearly losses of the system is almost equal for all strategies, while the optimized strategies were able to reduce the total losses by around 5% in case of design B. It is worth mentioning that clustering itself had already reduced the losses around 40%, when compared to the classical single-converter solution in section 1.8.

Table 1-3: Comparing yearly losses of different strategies on the test case for converter design B

Strategy	**Total yearly losses (MWh)**
Section 1.8	37.9
Model-based	36 (5% reduction)
Curve-based	36.3 (4.3% reduction)

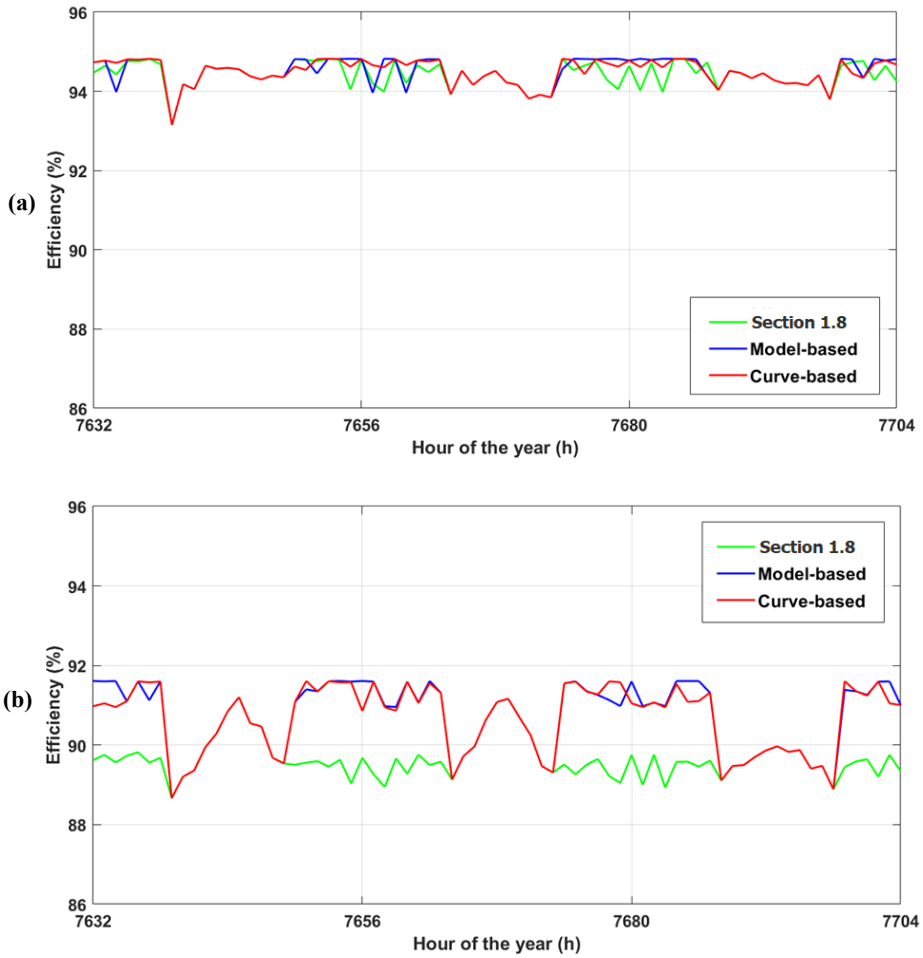

Figure 1.17: Efficiency over three consecutive days for (a) converter design A; and (b) converter design B.

1.10. Conclusion

This chapter proposed a solution for electrical energy system of micro-grids equipped with renewable resources and storage devices. The solution seeks to solve challenges and shortcomings of current classical solutions. The classical solutions use one converter per function, designed for being able to provide maximum demand. Therefore, the converters work far from their nominal power with poor efficiency for a considerable portion of their lifetime. Additionally, losing one converter could lead to loss of the whole system or a big part of it. In order to address these challenges, this chapter proposed using a cluster of multi-port converters. Each converter is designed for a fraction of the nominal power. In this case, if a fault occurs in one converter, only a small part of the whole system is lost. Flexibility and additional functionalities are the other advantages of using a cluster of converters. It is possible to reduce the overall cost of the system through standardization of the converters as building blocks of the cluster. A high-level controller monitors different parameters of the micro-grid and decides on how to distribute the power flow among converters of the cluster. When the power transfer is low, some converters will be disconnected and the rest would operate closer to their nominal power with higher efficiency. Results of simulation on a study case showed that the efficiency could increase from 69% with one converter, up to 82% with a cluster of multiple ones (published in [40]). It was shown that further efficiency improvement is possible through applying optimization strategies over the cluster. Two simple strategies were tested and results showed that they are able to reduce the losses by 5% compared to a cluster control without optimization strategy (accepted in [41]).

2. Multi-port active-bridge converters: introduction, design, and control

Micro-grids can include several types of generation and storage devices (called objects) whose typical characteristics are listed in Table 2-1. Some of these objects are bidirectional in terms of power (such as storage devices and utility grid) and others are unidirectional (such as PV panels and wind turbines). While storage devices are limited controllable sources and sinks of energy, utility grid can be regarded as a controllable infinite source and sink. Renewable resources, on the other hand, are uncontrollable (in terms of available power) and source-only objects. Each object has a voltage and current characteristics that is different from the others, including their dc and ac nature. Considering all the variability and differences, proposing a real-time efficient system that can exchange energy between these objects is challenging task. A cluster of multi-port converters was proposed in the previous chapter as a potential solution for this application. This chapter will study the multi-port converter itself as the building block of the cluster.

Table 2-1 Variability of different sources and loads in a smart building

Object	Voltage nature	Voltage level	Power direction	Controllable Output
PV panels	DC	12 to 600	Unidirectional	No
Wind turbines	AC	690	Unidirectional	No
AC grid	AC	400	Bidirectional	Yes
DC grid	DC	40-400	Bidirectional	Yes
Batteries	DC	12 to 96	Bidirectional	Limited by SoC and capacity

There are several two-port AC/DC and DC/DC converters in a classic energy system of a micro-grid, each converter performing energy exchange between a pair of sources, loads, and/or storage devices (Figure 1.2). The previous chapter showed how employing a cluster of converters instead of the common one-converter-per-function architecture in micro-grids has the potential to improve efficiency, reliability, and flexibility of energy systems. The converter

topology chosen as the building blocks of the cluster has a significant impact on the extent of potential benefits of clustering that are achievable. This work proposes using multi-port active-bridge (MAB) converters as the building blocks, in order to tap the full potential of clustering. The whole system would look like Figure 1.3, where the same MAB converter is used for different functions as the building blocks of the cluster. In addition to improvements in efficiency, reliability, and flexibility, some advantages are specific to this topology, including:

1. Bidirectional power exchange between multiple ports at the same time, reducing conversion stages and hence the losses;
2. Voltage level compatibility, or the ability to connect objects with different voltage levels through adjusting transformer turns ratio;
3. Symmetric topology, which allows for easier design, control, and optimization;
4. Cost reduction through standardization of the building blocks and avoiding design costs;
5. Providing a hardware-level infrastructure for realization of smart grids and the internet of energy.

This chapter is dedicated to presenting the MAB topology, its modeling, design, and control. The goal is to better understand its internal phenomena, how it works, and the ways to model and control it.

2.1. Multi-port active-bridge DC/DC topology

DC/DC converters with a high-frequency transformer are among the best candidates for applications where safety and isolation between the ports is an important factor. Active-bridge converter topology is one of them. It has a number of active-bridges that are connected to a high-frequency transformer through inductors, as displayed in Figure 2.1. Dual active-bridge converters (DAB), as the simplest converters of this kind, have been employed in various applications since the 90's. Many works in the literature studied DAB, its design, control, and optimization [42]–[44]. Application of active-bridge converters with more ports, mostly triple active-bridge converters (TAB), has become interesting over the past decade [45], [46], [46]–[53].

There are several reasons why MAB topology is gaining more and more attention today. The first reason is that it can exchange energy between several sources and loads at the same time. The magnetic core of the multi-winding transformer acts as an energy hub that can transfer

energy between several ports. The topology is modular and scalable, i.e., adding a port is as simple as adding another winding on the transformer and connecting it to an active-bridge with an inductor. This would also allow for modular and scalable design, control, and optimization schemes. Another key advantage is the galvanic isolation between the ports that comes as an intrinsic property of the transformer, without any additional costs. Some topologies require additional components, hence increased cost and size for having galvanic isolation. Another advantage that the transformer brings about is voltage compatibility, providing the possibility to connect objects with different voltage levels by adjusting the turn ratios.

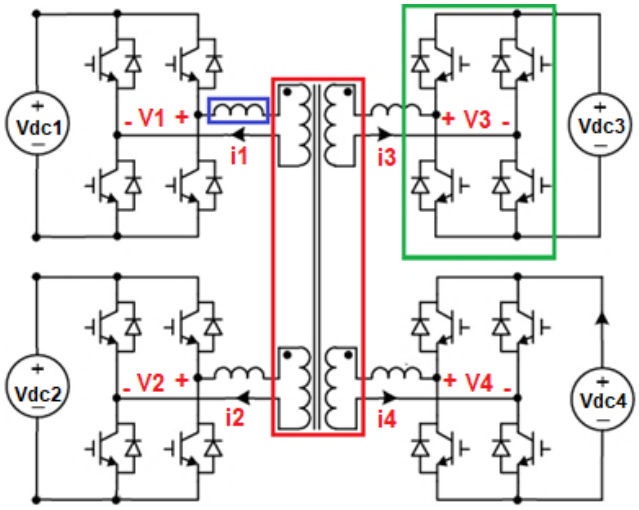

Figure 2.1: A QAB converter: the green box shows an active bridge; the red box is a multi-winding transformer; the blue box is an inductor, which can be either an external one or the leakage inductance of the transformer.

The MOSFETs in the active-bridges usually switch under soft-switching conditions (detailed analysis will be presented in the next chapter). Therefore, the switching losses are negligible and there is the possibility to increase switching frequency. Higher switching frequency means the magnetic cores of the transformer and inductors can be very small, hence reduction in size and weight of the converter. Depending on the application, the switching frequency can be in a range where low cost magnetic materials can be employed without large magnetic losses, e.g., ferrites are good candidates where switching frequency is below 100 kHz. The inductors act as high frequency energy storage, therefore are small. In addition, they are a means of controlling the current flow. The inductance value is inversely related to the nominal power of the converter. Therefore, the inductor cores can be very small even in high power converters. It is worth noting that several works in the literature used the leakage inductance of the transformer because it was large enough and avoided using any external inductances.

All the above-mentioned advantages of MAB converters led to choosing them as the candidate for building blocks of the cluster. A comparison between this topology and some of the other possible topologies with similar structures will be presented in the following.

2.1.1. Applications of MAB in the literature

MAB converters are becoming a common solution in different applications and the reason is the advantages mentioned in the previous section. This section will have a short review on different types of applications of MAB converters.

Electrical networks in aircrafts:

Reference [54] studies application of MABs in more-electric aircraft. In this application, a QAB converter is used for exchanging energy between the AC generator, HVDC network & LVDC network. The study presents complete integration of MAB converters in electrical distribution network of an aircraft with a ring architecture and fault tolerance. The proposed design has only HVDC buses, which are fed by the generators through AC/DC converters. With two of its ports, the QAB is able to make the connection between LVDC loads and two HVDC buses. In case of a fault on one of the HVDC buses, the QAB can provide the loads from the other HVDC bus. The same design is studied in [55], with more focus on the QAB. Application of a QAB for energy exchange between DC network of an aircraft and a hybrid of different storage technologies is studied in [56]. It shows how decoupling of the power transfer between different ports can help achieving a simpler control and optimization, in order to increase the efficiency. The decoupling uses linearization of the power flow equations. A hybrid storage system including batteries, a fuel cell, and a supercapacitor is proposed in [56]. Employing the decoupled control with additional current feed forward loops, they designed a control system that responds to power steps depending on the characteristic of each storage technology. The supercapacitor has the quickest control because it can respond to quick changes in the demand. The fuel cell however is controlled in a way that its power output remains as constant as possible. The battery is responsible for the slow dynamics of the demand. Feeding a DC load with hybrid storage is studied in [57], too.

Electric vehicles:

A QAB converter is proposed in [58] for a fast charging station of electric vehicles (EVs). It is used to interface energy production and storage with electric vehicles and the MAB topology is a good candidate because it reduces energy conversion stages, it does not need for an intermediate DC bus and connects different DC voltage levels. Reference [49] proposes a

TAB for charging of electric vehicles, interfacing a DC grid, photovoltaic panels and the EV battery. It studies the effect of variation on DC voltage of EV battery on design parameters of the TAB converter.

Microgrids and smart buildings:

A DC distribution system is proposed in [59] for smart buildings of future. The proposed structure includes three DC voltage levels of 5 V, 48 V and 120 V. A smart socket is proposed that provides possibility to connect plugs to each of the DC voltages, in addition to the conventional 240 V AC network. The smart socket is fed by a main 120 V DC network. The main DC network itself can be connected to renewable resources, storage devices, the AC network and probably to a DC utility network. Several DC/DC choppers located inside the smart socket, provide 5 V and 48 V. Considering its modularity and capability to connect several ports in one place, MAB topology can be a candidate in this architecture or similar topologies for smart buildings. Application of MAB in DC microgrids and smart buildings is studied is several works [60], [61].

Battery management systems:

Another interesting application of MAB converters is in battery management systems (BMS). Using lithium-ion batteries as storage systems is increasing in different application, such as electric vehicles and smart grids. These battery packs have several cells in parallel and series to increase the voltage and current level. Characteristics of these cells are slightly different, due to imperfect manufacturing process and different aging and thermal processes they have gone through. This can lead to imbalance in utilization of the cells and over-charge/over-discharge in the cells [62], [63]. A MAB converter can be used as a DC/DC multi-port converter that can exchange energy between different cells, trying to balance their voltages and charges. Figure 2.2 shows the proposed application of a MAB in a BMS system [62]. Classical passive balancing methods based on dissipation of extra charge in a switched parallel resistor are widely used because of cost effective implementation, however, they have issues such as low efficiency, uni-directionality, and heat dissipation especially when balancing high capacity cells [62]. A MAB can exchange the energy between the cells in any direction, increasing the efficiency and solving the thermal issues. A highly integrated balancing system was proposed and built in [63]. The converter is the size of a small coin (Figure 2.3) and can transfer 8.5 W power at 5 V with 86% efficiency. The power density of the converter is 9.9

kW/L, which shows high potential of MAB converters as a cell balancing solution for BMS systems.

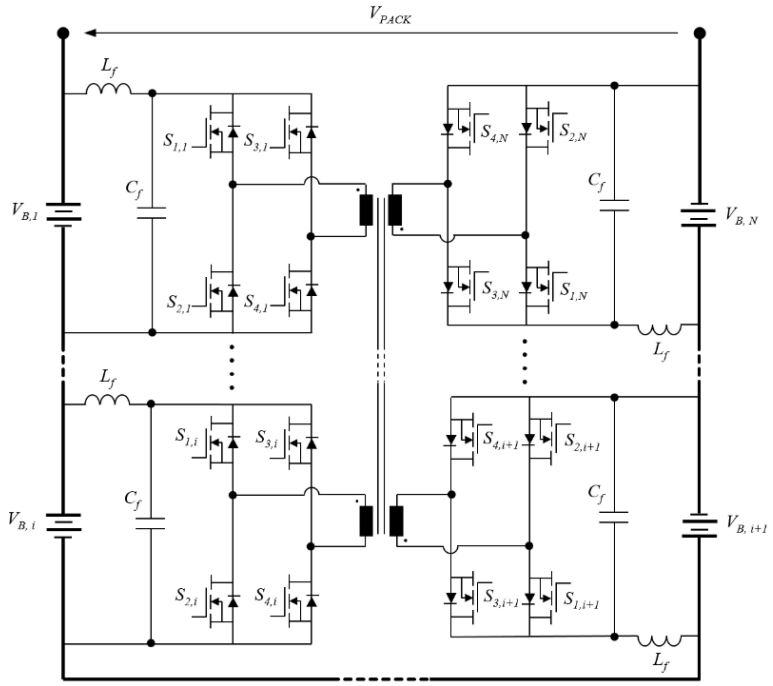

Figure 2.2: Application of a MAB converter in BMS; it is used to exchange energy between different cells for charge and voltage balancing among the cells [62].

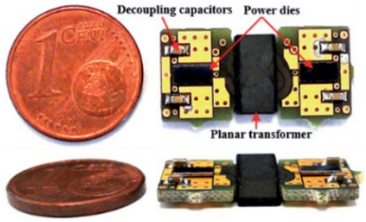

Figure 2.3: The DAB converter built based on 0.35 µm 5 V CMOS technology with a planar transformer, which can be used in a BMS system [63].

2.1.2. Comparison with other topologies

Different multi-port topologies can be chosen as the building blocks of the cluster of converters. Each topology itself may employ different types of switching cells. This section studies some of these topologies and switching cells.

Resonant MAB topology:

As explained in the beginning of this section, the transformer has an important role in many of the advantages, including galvanic isolation, simultaneous and one-step power transfer between several ports, and voltage compatibility. Therefore, topologies with a multi-winding

transformer are suitable for the purpose of this work. Figure 2.4 shows a series LC resonant DAB as a well-known structure, which can be generalized to a multi-port converter.

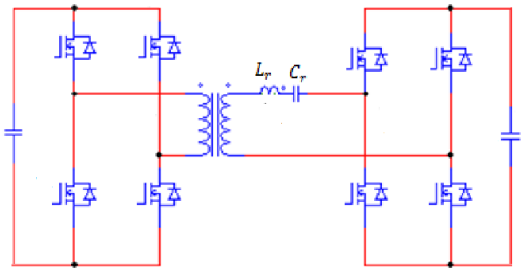

Figure 2.4: A resonant DAB converter with Lr and Cr as its resonance tank.

Compared to MAB, series resonant converters allow more freedom in choosing design parameters such as switching frequency and size of inductances. In this topology, the resonance frequency of the tank is close to the switching frequency, so the first harmonic of the current is almost the only current harmonic that transfers the power. MAB, on the other hand, employs all harmonics for power transfer, leading to higher power density. A more detailed analysis will be presented later in this chapter. The resonant tank guarantees that no DC currents will flow in the transformer windings, but it will also increase the footprint of the converter. Avoiding DC currents in a MAB converter requires additional control considerations and sometimes even additional hardware. The high-voltage film capacitors that are commonly used in resonant tanks of these converters, can be large and undermine system reliability with hazardous failure consequences [64], shown in Figure 2.5. On the control point of view, one control parameter has to be dedicated to keeping the resonance, i.e. less degree of freedom for other control purposes. On electromagnetic compatibility point of view, a variable frequency resonant converter, connected to the network has the potential to cause some issues. Parallel LC and series-parallel (LLC and LCC) resonant DAB converters are the other topologies of this class that can be used. A challenge that is common in the resonant converters is the no-load and light-load conditions where infinite switching frequency or large currents are required to maintain control of the converter [65].

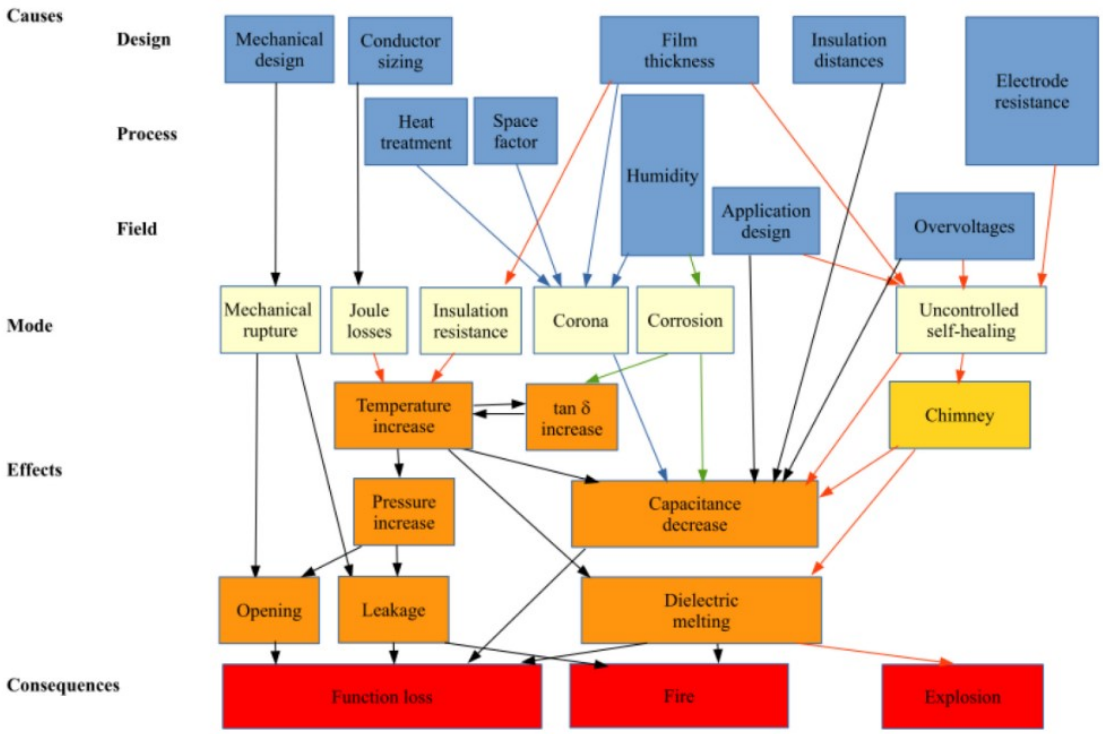

Figure 2.5: Failure modes of metalized film capacitors with their causes and consequences [64].

Different switching cells:

Reference [66] studied application of different basic cells as DC/AC stage of a MAB converter in a smart transformer. Application of H-Bridge (HB), T-Type (TT), Neutral Point Clamped (NPC), and Flying-Capacitor (FC) cells, shown in Figure 2.6, were compared. With the aim of doing a fair comparison, a design method was proposed and a list of semiconductors was used to choose a proper device for each type of cell. The results of the comparative evaluation in two different scenarios showed that HB, NPC, and FC had relatively similar performance, with higher than 99% efficiency. HB cells required switches with higher breakdown voltage and consequently higher forward voltage drop, while NPC and FC were using switches with lower break down voltages but led to higher effective currents due to their topology. TT cells showed the lowest efficiency. The reason is that IGBTs in TT cells were high-voltage switches with higher forward voltage drop, and at the same time, the topology leads to higher effective currents, i.e., it has both negative points.

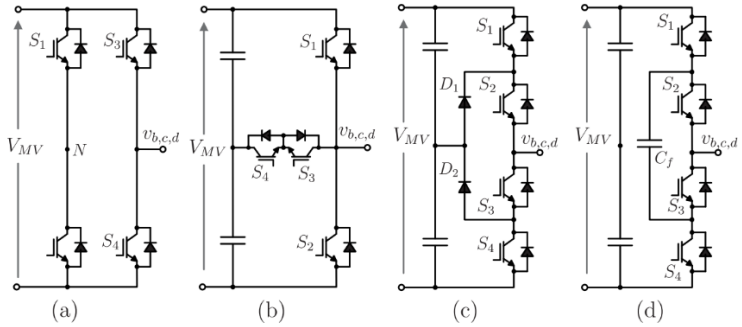

Figure 2.6: The basic cells used in the medium-voltage side of a QAB converter [66]: (a) H-Bridge (HB), (b) T-Type (TT), (c) Neutral-Point Clamped (NPC), (d) Flying-Capacitor (FC).

After all, each topology and cell type has its specific positive and negative points and a detailed comparison including losses, costs, size, and probably other factors that are important to the user is required to be able to choose one. Even with a detailed and accurate comparison, the results will probably vary for different mission profiles. In the current work, as a starting point to study application of a cluster of multi-port converters in smart buildings, the MAB structure was chosen as the building blocks of the cluster. Future works may study different types of converters to get a deeper understanding of the pros and cons of each topology.

2.1.3. Interfacing to different sources and networks

A close comparison of the QAB that is illustrated in Figure 2.1 with the building blocks of Figure 1.3 shows that the AC network and photovoltaic panels are directly connected to their corresponding active bridges, but this is not the case in the current work. The focus of this research work is on MAB as a DC/DC converter and the clustering. Hence, it is assumed that the connection of the MAB to the AC network and photovoltaic panels is done through some interface converters (Figure 2.7). The interface converters, e.g. a DC/DC converter as MPPT for interfacing the photovoltaic panels or an AC/DC converter for the AC network, are not the subject of this research.

It should be mentioned that direct connection between the active-bridge topology and single-phase or three-phase AC networks has already been studied in several researches. A single-stage three-phase AC/DC DAB-based converter is proposed in [67], using a matrix converter with four quadrant switches. The converter is used for energy exchange in an electric vehicle. Reference [68] presents a novel topology of QAB that directly connects a three-phase network into active bridges. A neutral voltage lift method is proposed in [68] allowing for direct connection between the active bridges and the mains. The proposed topology needs no intermediate high voltage bus or bipolar voltage switches, and the average voltage stress is half the voltage stress of a six-switch inverter. Another proposed topology of single-stage three-

phase AC/DC converter based on DAB is proposed in [42]. The topology, called I3DAB, is similar to a QAB converter on functional point of view, which is interfacing a three-phase AC network with three DC ports. The difference between QAB and I3DAB is that I3DAB has three separate transformers, hence probably higher magnetic losses and a larger footprint. The proposed control, with modifications, might be appropriate for direct connection of a single-phase network with an active bridge converter.

Reference [69] presents a DAB with direct connection to PV panels and a single-phase AC network. The active bridge on the PV side is able to handle maximum power point tracking (MMPT) function. The AC network side is a four-quadrant full-bridge with a series resonant tank. Another work that studies integration of the MPPT function in the active-bridge control is [70].

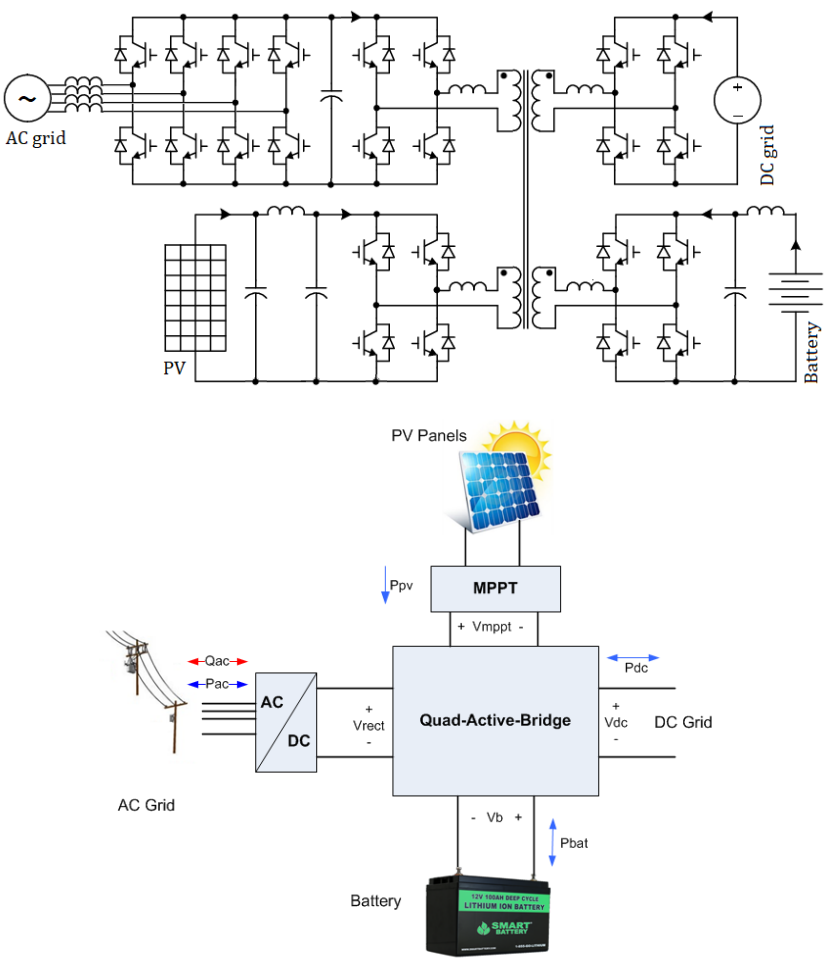

Figure 2.7: A QAB that is connected to a three-phase network and PC panels using interface converters.

Although direct interfacing is a possible option to implement, as in the works introduced in the previous paragraphs, it is not possible to determine if it is a positive point without a detailed

comparison between advantages and disadvantages in terms of key factors such as efficiency, complexity of control, cost and reliability.

2.2. Modeling and analysis

Active-bridges of a MAB converter can generate two-level and three-level square-wave voltages. Since it is a voltage source converter, characteristics of the synthesized voltage waveforms of the active-bridges are the main parameters that determine the flow of power between the ports. Figure 2.8 shows an example of voltages in the QAB that was displayed in Figure 2.1, with different DC link voltages and active-bridge voltage modulations. The curves in the bottom part of Figure 2.8 are the corresponding currents. The following parts of this section will present different approaches to model a MAB converter, each one being suitable for certain types of applications. In some approaches, the analysis will start by the simplest of MAB converters, DAB, and then increase the number of the ports to find a generalized approach for a MAB with any number of ports.

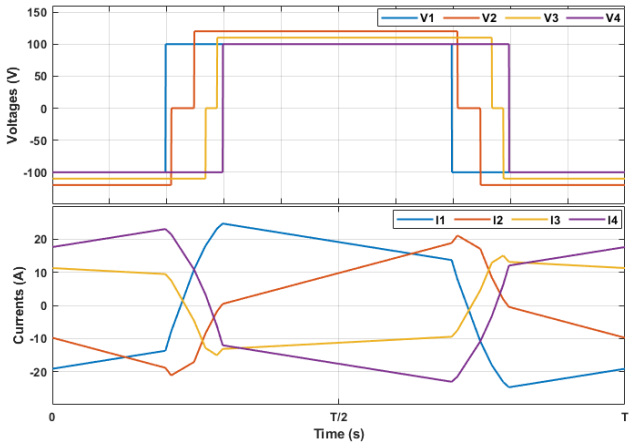

Figure 2.8: An example of voltages and currents in a QAB during a switching cycle of T.

Phase shifts are the main control parameters in a MAB. Two types of phase shifts can be defined: internal phase shifts and external phase shifts, as displayed in Figure 2.9 for a DAB. Internal phase shift is the phase shift (or time delay) between switching of two legs of a single active-bridge. Internal phase shift controls the duty cycle of the output voltage of the active-bridge and lead to periods where the output voltage is zero. Therefore, it will be referred to as "duty cycle" from now on, for the sake of simplification. External phase shift is the phase shift between first harmonics of output voltages of two active-bridges. External phase shift will be called "phase shift" from now on. A model can determine shapes of the currents, their peak and effective values, the corresponding losses and the power exchange between the ports.

Additionally, a model can be used to determine what duty cycles and phase shifts to apply to each port, in order to have a desired flow of power between the ports.

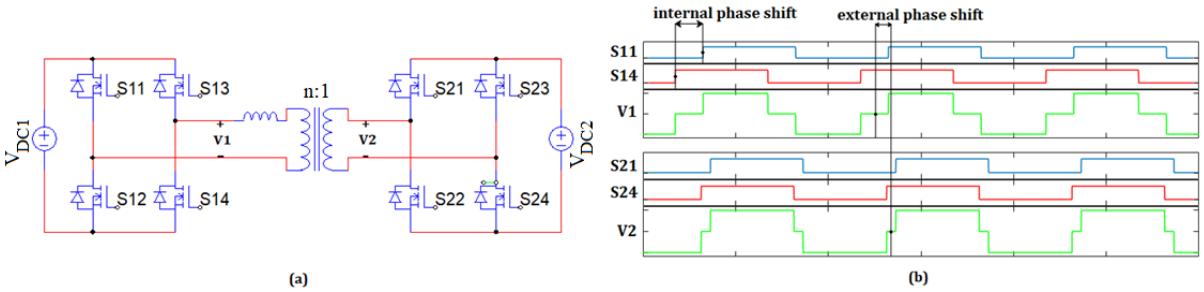

Figure 2.9: internal and external phase shifts in switching of a DAB. Switches on the same arm are switched complementarily.

2.2.1. Analysis of square-wave voltages

For the DAB displayed in Figure 2.9-a, if both active-bridges synthesize 2-level voltages (full conduction or 50% duty cycles) as in Figure 2.10, the peak inductor current can be determined as

$$I_{L-max} = \frac{1}{2L}\int_{\varphi_1}^{\varphi_3}(V_{DC1} + nV_{DC2})\frac{d\varphi}{2\pi f} = \frac{V_{DC1}}{L}\frac{\varphi}{2\pi f} \tag{2.1}$$

where V_{DC1} and V_{DC2} are the primary and secondary side DC link voltage, respectively, L is the total inductance between the active-bridges, φ is the phase shift (in radians) and f is the switching frequency. It is assumed that phase shift is in the range of ± 180 degrees, transformer turn ratio is n: 1 and the DC link voltages are equal to their nominal values ($V_{DC1} = nV_{DC2}$). All the parameters are transferred to the primary side of the transformer. The active power of the first port can be determined as f times the energy that is exchanged in one cycle as

$$P_1 = f\int_0^{1/f} V_{DC1} i_L(t)dt = 2fV_{DC1}I_{L-max}\frac{\pi - \varphi}{2\pi f} = \frac{\varphi(\pi - \varphi)V_{DC1}^2}{2\pi^2 fL} \tag{2.2}$$

where $i_L(t)$ is the instantaneous inductor current. Figure 2.11 shows how active and reactive power transfer changes as a function of phase shift between voltages of the two sides. The maximum active power transfer occurs when the phase shift is 90 degrees and is equal to

$$P_{\max} = \frac{V_{DC1}^2}{8fL}. \tag{2.3}$$

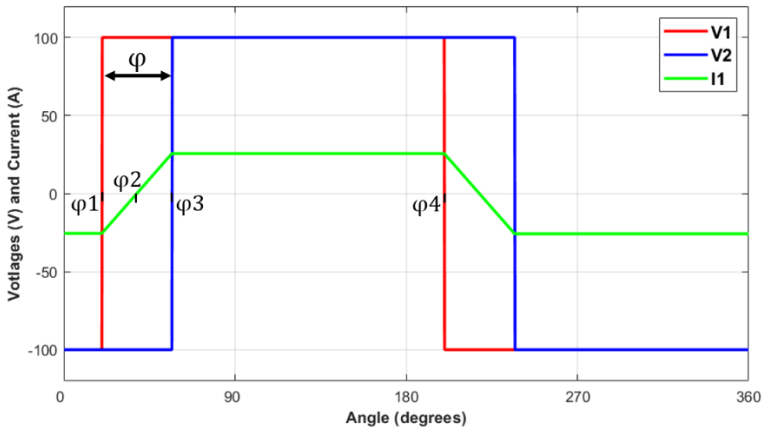

Figure 2.10: Voltages and current in a DAB with equal DC link voltages and 100% duty cycle on both sides. The horizontal axis is the angle of a full switching cycle of 360 degrees.

Reactive power is the power that travels back and forth between the two sides and does not contribute to power transfer between the ports. It is the power transfer between φ_1 and φ_3 in Figure 2.10 and can be expressed as

$$Q_1 = 2f \int_{\varphi_2}^{\varphi_3} V_{DC1} i_L(t) dt = 2f \frac{V_{DC1} I_{L-max}}{2} \frac{\frac{\varphi}{2}}{2\pi f} = \frac{\varphi^2 V_{DC1}^2}{8\pi^2 f L} \tag{2.4}$$

Figure 2.11 shows that reactive power increases with the phase shift, therefore it is better to limit the phase shift in a certain range. Using equation (2.2), it is possible to choose the inductance and the switching frequency in a way that the phase shift for transferring nominal power falls in a limited range. It will be discussed as a design consideration later in this chapter.

The case illustrated in Figure 2.10 was a simple operating point where DC link voltages were at their nominal values and both sides generated two-level voltages. In case of variations from nominal value on the DC link voltages and one or two active-bridges generate three-level voltage, the calculations will be more complex and depend on the operating point. It is shown in [65] that 12 different voltage sequences can take place in a DAB. Detailed analysis of all the 12 sequences and the borders between them is presented in [65]. It should be noted that all these variety and complexity is for a DAB. In case of a MAB converter with three or more ports, this kind of analysis will be even more complex. It is worth mentioning that despite all the complexities, the calculations based on square waves can be the most suitable option for certain purposes, such as a computational-cost efficient model of losses, which will be presented in the next chapter.

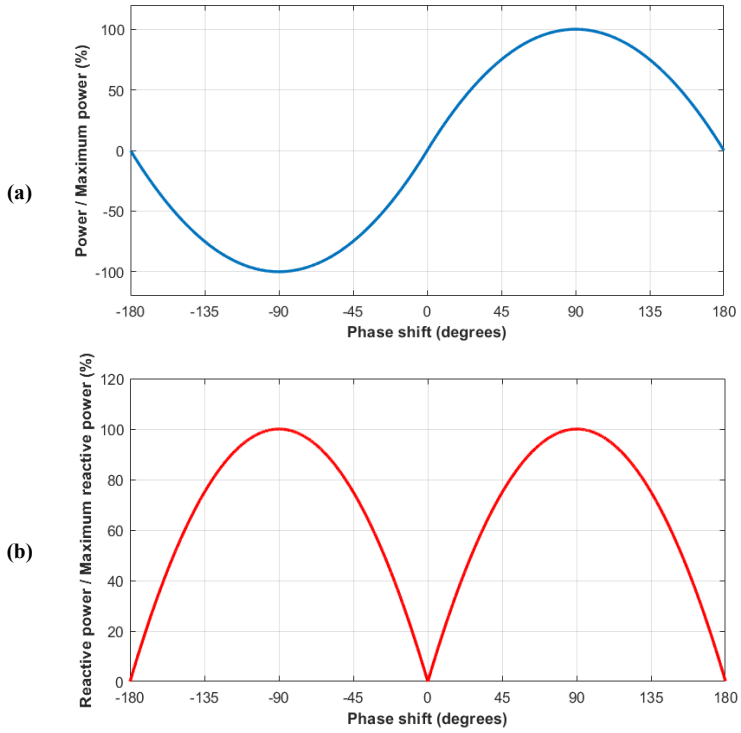

Figure 2.11: (a) Active and (b) reactive power transfer in a DAB as a function of phase shift.

2.2.2. First harmonic analysis

In order to avoid all the complexities of square-wave analysis, first harmonic approximation will be used in this work for most of the analyses of MAB converters. The first harmonic analyses is significantly easier than the calculations based on square waves because the same equations are valid for all possible values of phase shifts and duty cycles. It allows for phasor space calculations, too. The voltage duty cycles cannot be represented directly in this analysis, but they determine the magnitudes of voltage phasors. In this regard, the "phase shifts" and "duty cycles" in the square-wave analysis are equivalent to "phase angles" and "magnitudes" of voltage phasors in phasor space. Therefore, considering variations in DC link voltages and three-level voltage modulation will not be complex. The potential problem of the first harmonic approximation and phasor space analysis is that the results are not as accurate as the calculations based on square waves. This is because real voltages are square waves, but first harmonic analysis approximates them as sinusoidal waveforms.

In the first harmonic analysis, the output voltages of the active bridges illustrated in Figure 2.9 can be defined as

$$v_1(\mathrm{t}) = \frac{4}{\pi} V_{DC1} \sin(\omega t) \tag{2.5}$$

$$v_2(\mathrm{t}) = \frac{4}{\pi} n V_{DC2} \sin(\omega t - \varphi) \tag{2.6}$$

where ω is the angular frequency, equal to $2\pi f$, and $\frac{4}{\pi}$ is the ratio between amplitude of a square wave and amplitude of its first harmonic (Fourier series coefficient). The primary current can be determined as

$$i_1(\mathrm{t}) = \int \frac{v_1(t) - v_2(t)}{L} dt = \frac{4}{\pi\omega L} \left(-V_{DC1} \cos(\omega t) + n V_{DC2} \cos(\omega t - \varphi)\right) \tag{2.7}$$

and the instantaneous power will be

$$S_1(\mathrm{t}) = v_1(\mathrm{t}) i_1(\mathrm{t}) =$$
$$\frac{16 V_{DC1}}{\pi^2 \omega L} \left(-V_{DC1} \sin(\omega t)\cos(\omega t) + n V_{DC2} \sin(\omega t)\cos(\omega t - \varphi)\right) =$$
$$\frac{8 V_{DC1}}{\pi^2 \omega L} \left(-V_{DC1} \sin(2\omega t) + n V_{DC2} \sin(2\omega t - \varphi) + n V_{DC2} \sin(\varphi)\right). \tag{2.8}$$

Active power is f time the integration of $S_1(\mathrm{t})$ for one cycle, which is

$$P_1 = f \int_0^{\frac{1}{f}} S_1(\mathrm{t}) dt$$
$$= f \int_0^{\frac{1}{f}} \frac{8 V_{DC1}}{\pi^2 \omega L} \left(\frac{V_{DC1}}{2\omega} \cos(2\omega t) - \frac{n V_{DC2}}{2\omega} \cos(2\omega t - \varphi) + n V_{DC2} \sin(\varphi) t\right) dt$$
$$= \frac{8 V_{DC1} n V_{DC2}}{\pi^2 \omega L} \sin(\varphi). \tag{2.9}$$

and reactive power is

$$Q_1 = \frac{8 V_{DC1} (V_{DC1} - n V_{DC2} \cos(\varphi))}{\pi^2 \omega L} \tag{2.10}$$

Equation (2.9) is the equivalent of equation (2.2) with first harmonic approximation. The difference between these two equations is displayed in Figure 2.12. This difference is not significant showing that the first harmonic approximation is accurate enough for the purpose of this work. A more detailed comparison is presented in Figure 2.13. As shown in Figure 2.13-c, the power transferred by square-wave voltages is more than the power transferred by the first harmonic for small phase shifts, but then it decreases as the phase shift becomes larger. For phase shifts larger than 58 degrees, the power transferred by the first harmonic is larger than the power transferred by square-wave voltages. This fact is due to the power transferred by

higher harmonics, mostly 3rd and 5th harmonics. As an example, when phase shift is 20 degrees, the 3rd and the 5th harmonics transfer around 9.4 % and 2.3 % the power transferred by the 1st harmonic, respectively. If the phase shift increases up to 75 degrees, then the power transferred by the 3rd and the 5th harmonics would be -2.7 % and -0.2 % the power transferred by the 1st harmonic. The negative sign means that the 3rd and the 5th harmonics transfer active power in the opposite direction with regard to the 1st harmonic.

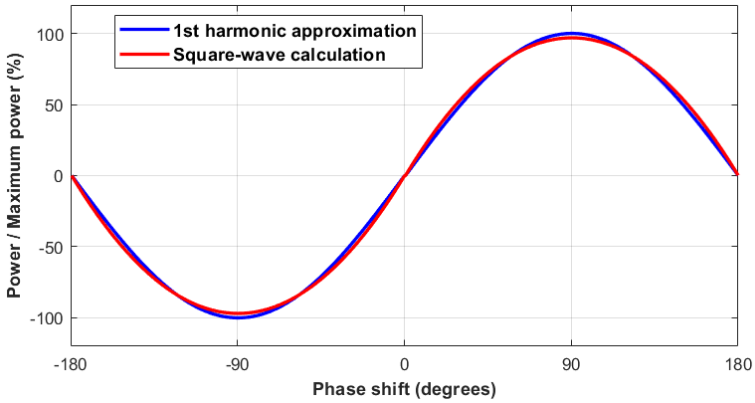

Figure 2.12: Comparing the power transfer calculated by the two methods: first harmonic approximation and square-wave calculations.

The comparisons in Figure 2.12 and Figure 2.13 can be used for the analysis in section 2.1.3 for comparing the MAB and the resonant converters, as the resonant converter only uses the first harmonic of the current. They show that MAB converter is capable of transferring the same amount of power with smaller peak current, which can be a key factor in sizing the converter.

All the calculations so far were for a DAB converter. It is possible to generalize the 1st harmonic analysis for a MAB. Figure 2.14-a shows the first harmonic approximate model of a QAB converter. The transformer was assumed an ideal transformer, with infinite magnetizing inductance and therefore it is not shown in the model. All voltage and current phasors displayed in Figure 2.14 are transferred to primary side of the converter. The model can be easily generalized for *n* number of ports. For an *n*-port converter, there will be *n*-1 independent equations for n-1 voltage loops and one equation for the point where all inductances connect together (which is the transformer). Putting all voltage and current equations in a matrix gives

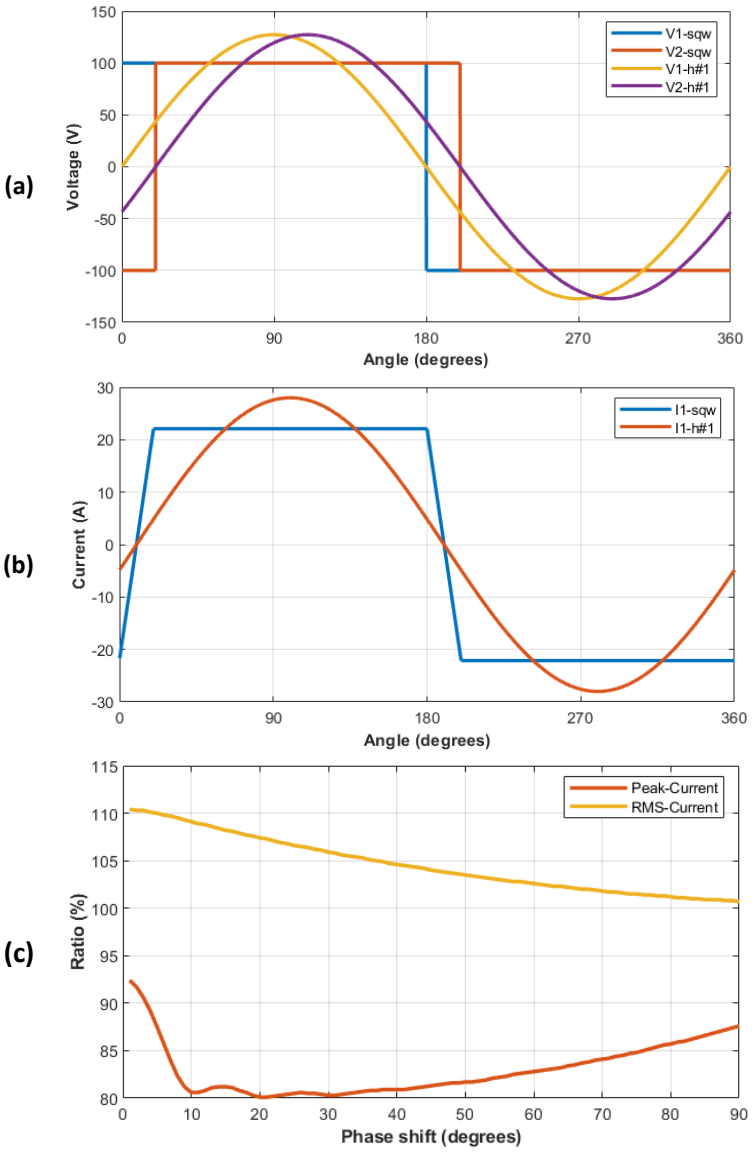

Figure 2.13: Comparison between results of first harmonic approximation and square-wave analysis: (a)Voltages and (b) Currents for phase shift of 20 degrees; (c) Variation of the ratio of square-wave to 1st harmonic parameters including power, peak current and effective current for phase shift of zero to 90 degrees.

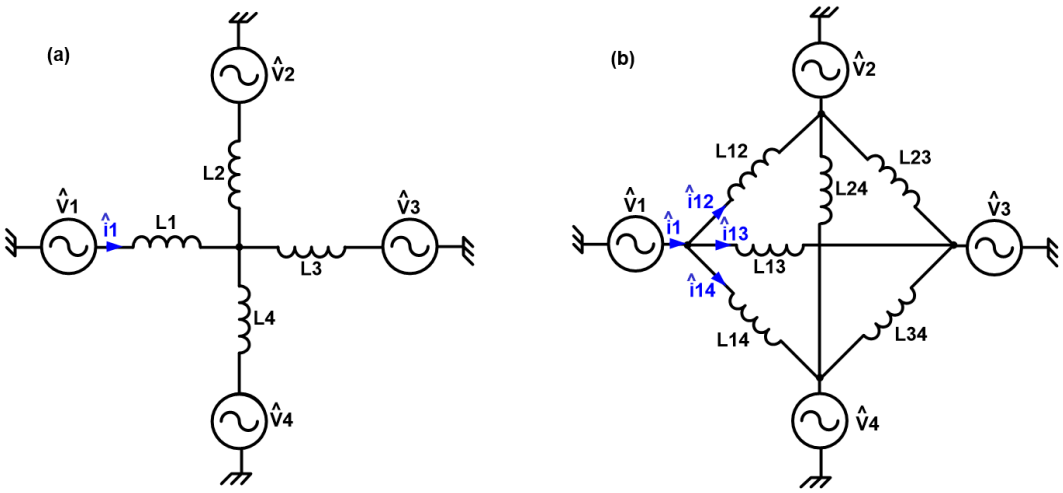

Figure 2.14: (a) First harmonic model of a QAB converter; (b) The first harmonic model of a QAB after applying star-to-delta transform on the network of inductances.

$$\begin{bmatrix} 0 \\ \hat{v}_1 - \hat{v}_2 \\ \cdots \\ \hat{v}_{n-1} - \hat{v}_n \end{bmatrix} = \begin{bmatrix} 1 & 1 & \cdots & 1 & 1 \\ -\mathrm{j}X_1 & jX_2 & \cdots & 0 & 0 \\ \cdots & \cdots & \cdots & \cdots & \cdots \\ 0 & 0 & \cdots & -\mathrm{j}X_{n-1} & \mathrm{j}X_n \end{bmatrix} \times \begin{bmatrix} \hat{\imath}_1 \\ \hat{\imath}_2 \\ \cdots \\ \hat{\imath}_n \end{bmatrix} \tag{2.11}$$

where X_k is ωL_k. The three matrices in (2.11) will be referred to as V_Δ, X and I, respectively from left to right. The currents can be calculated from

$$I = X^{-1} \times V_\Delta \tag{2.12}$$

and active powers can be determined as

$$P = \begin{bmatrix} P_1 \\ P_2 \\ \cdots \\ P_n \end{bmatrix} = \text{real part of } V \times I^* \tag{2.13}$$

where

$$V = \begin{bmatrix} \hat{v}_1 & 0 & \cdots & 0 \\ 0 & \hat{v} & \cdots & 0 \\ \cdots & \cdots & \cdots & \cdots \\ 0 & 0 & \cdots & \hat{v}_n \end{bmatrix}. \tag{2.14}$$

Although determining currents and powers is possible through mathematical software tools using (2.12) and (2.13), the calculation will still be too complex. For example, the active power of the first port of the QAB is

$$P_1 = \frac{a_1}{2(L_1L_2L_3 + L_1L_2L_4 + L_1L_3L_4 + L_2L_3L_4)\omega} * (\cos\varphi_1 [a_1 \sin\varphi_1 * (L_2L_3 + L_2L_4 + L_3L_4) - L_3L_4a_2\sin\varphi_2 - L_2L_4a_3\sin\varphi_3 - L_2L_3a_4\sin\varphi_4)] - \sin\varphi_1 [a_1\cos\varphi_1 * (L_2L_3 + L_2L_4 + L_3L_4) - L_3L_4a_2\cos\varphi_2 - L_2L_4a_3\cos\varphi_3 - L_2L_3a_4\cos\varphi_4)]) \quad (2.15)$$

where a_k is magnitude of the voltage phasor of port k. Equation (2.15) shows the coupling of power between the ports, as any changes in any of the phase shifts will affect the power transfer of every port. In order to make the calculation of currents and powers easier, a star-to-delta transform can be applied to the inductances that are connected together in Figure 2.14-a. The outcome is illustrated in Figure 2.14-b. The inductances in Figure 2.14-b can be determined from

$$L_{i,j} = L_iL_j \sum_{k=1}^{n} \left(\frac{1}{L_k}\right). \quad (2.16)$$

The converter model illustrated in Figure 2.14 can be considered as six separate DABs. Therefore, equations (2.7) and (2.9) can be used to determine the currents and power transfers between each pair of ports.

$$\hat{\imath}_k = \sum_{l=1}^{n} \frac{\hat{v}_\mathrm{k} - \hat{v}_\mathrm{l}}{jX_{kl}} \quad (l \neq k) \quad (2.17)$$

$$P_k = \sum_{l=1}^{n} P_{kl} = \sum_{l=1}^{n} \frac{8|\hat{v}_\mathrm{k}|.|\hat{v}_\mathrm{l}|}{\pi^2 X_{kl}} \sin(\varphi) \quad (l \neq k) \quad (2.18)$$

This is a very common modeling method for MAB converters. It is used in many works in the literature for analysis, design and control purposes.

2.3. Design rules and considerations

MAB converters include several types of components, including semiconductor devices, inductances and a multi-winding transformer. This section will study design and sizing of these components as well as the topology itself, along with some additional considerations (published in [71]).

2.3.1. Defining nominal power

The power transfer in a MAB converter is determined by the phase shift, DC link voltages, size of the inductors and switching frequency. Therefore, defining nominal power must be the

first step in design of a MAB converter due to its impact on several other parameters. Figure 2.15 illustrates how the current changes in a DAB, as the power transfer increases and gets close to the maximum possible power transfer (or the phase shift gets close to 90 degrees). The non-linear increase in the current is due to the increase in reactive power exchange. Limiting the power transfer to a certain portion of maximum power is a way of avoiding large nonlinear increase in the currents. However, this solution leads to oversizing the converter, so the limit must be chosen regarding this tradeoff. 60% maximum power can be considered as a good limit for power transfer, as the nonlinear increase in the current becomes larger than 10% around this point. Therefore, it is better if the nominal power of the converter, P_{nom}, is equal to 60% maximum possible power transfer, P_{max}. The P_{nom}/P_{max} ratio of 60% also sets maximum phase shift between the two ports, φ_{max}, to 37 degrees.

In case of an n-port MAB converter, there are $n-1$ phase shifts and $n-1$ power transfers for each port. As shown in Figure 2.15, the current between two active bridges will be close to linear versus the power transfer if the phase shift between them is within the range of ±37 degrees. Considering the delta model illustrated in Figure 2.14-b and superposition of currents in Equation (2.17), the current of each port of a MAB will be close to linear if the phase shift between that port and all other ports is within the range of ±37 degrees. In this case, the converter must be able to transfer the nominal power on each port while no phase shift between the ports exceeds ±37 degrees.

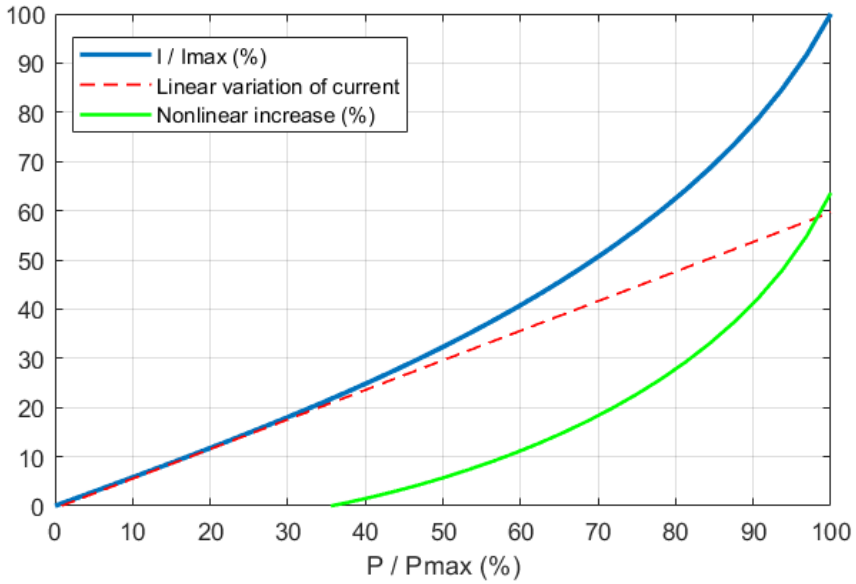

Figure 2.15: Nonlinear increase in current of an active-bridge in a QAB, as the power transfer of the corresponding port gets close to its maximum value. The dotted line displays an imaginary linear increase, to indicate the extent of the nonlinear increase in current.

Defining nominal power in a multi-port converter is a complex task. As expressed before, the nominal power has a direct impact on design of the converter and hence on its performance. Therefore, it has to be studied more closely. In a first attempt, nominal power can be defined as "the maximum power that can be exchanged between each pair of ports" while the phase shift between them is ±37 degrees. This definition only considers the power transfer and phase shift between two ports, regardless of the rest of the ports. Another definition can be the "maximum power that each port can provide or absorb" while all phase shifts are ±37 degrees. Figure 2.16 shows how these two definitions lead to different values in a QAB. The QAB has a symmetrical design with 100 V as DC link voltage and 10 µH inductors on every port. The switching frequency is 20 kHz. The transformer is ideal with equal turns on every port. The four vectors in Figure 2.16 are voltage phasors of the four ports, and P1 to P4 are the power transfer of each port. The positive value for power means providing power and negative value means absorbing power.

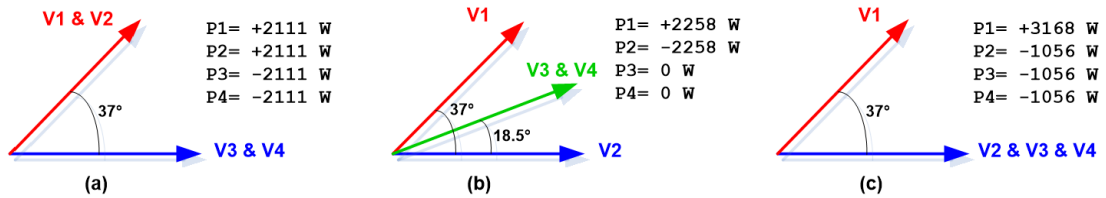

Figure 2.16: The power flow for different phase shifts between voltage phasors of a QAB converter. All DC link voltages are 100 V, all the inductances are 10 µH, the switching frequency is 20 kHz and all transformer turns are equal.

Analyzing Figure 2.16 shows that for the same converter, the "maximum power transfer between two ports" (first definition) is 2258 W as in "case b" (Figure 2.16-b), while the "maximum power each port can provide or absorb" (the second definition) is 3168 W as in "case c" (Figure 2.16-c). It should be noted that the power transfer between the first and the second port decreases from 2258 W in "case b" to 1056 W in "case c", while the phase shift between the ports does not change. It is clear that if the nominal power is defined to be 2258 W or 3168 W based on "case b" or "case c", respectively, the converter will not be able to provide the nominal power in a situations such as "case a" without exceeding 37 degrees for phase shifts. In other words, "case a" is the worst case and should be considered as the nominal power with 37 degrees phase shift for all ports. Considering this definition, the nominal power would be 2111 W and the converter can always provide this amount of power in situations similar to "case b" or "case c" with phase shifts of less than 37 degrees. Therefore, nominal power is defined as the power transfer in Figure 2.16-a.

2.3.2. Inductors

The second design parameter to address is sizing the inductors. The inductor size is important because it determines the maximum possible power transfer on each port, as in Equation (2.3) and the peak current, as in Equation (2.1). As explained in the previous section, the nominal power is considered as the power transfer in Figure 2.16-a and equal to 60% of maximum possible power transfer. Therefore, the inductance can be sized using Equation (2.3) considering $P_{max} = \frac{P_{nom}}{0.6}$.

Choosing a magnetic core and designing the winding would be the next step in design of the inductors. The magnetic core can be chosen based on common rules, which determine a parameter called area product (A_P) from the specifications of the converter. The area product is the product of core cross section area and the available window for placing the winding. A magnetic core that has a product area bigger than the specified A_P can be chosen. The A_P of the inductor for port k can be determined as

$$A_{p-k} = \frac{L_k I_{max-k} I_{RMS-k}}{k_b J B_{max}} \tag{2.19}$$

where k_b indicates how well the winding is accommodated in the window of the core and is usually considered between 0.3 and 0.5; I_{max} is the maximum current in the winding at nominal power, which can be determined from Equation (2.1); I_{RMS} is the effective current at nominal power; J is the current density in the wires and usually considered between 3 and 5 Amperes per square millimeters; and B_{max} is the magnetic flux density in the core. The coefficient k_b specifies what portion of the area occupied by the winding is actually copper as the inductor. Since round wires are commonly used, there are always empty spaces between the turns. If Litz wire is used, then each wire is composed of a certain number of smaller round wires with empty spaces between them, too. The insulator takes some space, too, especially if Litz wire is used or if additional insulations are added between different layers of the winding. Current density, J, directly affects the conduction losses in the winding and should be chosen carefully. If the topology of the core allows free flow of air as the natural cooling medium and the winding is not multi-layer, J can be considered up to 5 $\frac{A}{mm^2}$. However, it is better to carefully consider the core losses, too. The losses in magnetic core of the inductors are small in low powers because the effective voltage across the windings is small. Still, similar to the conduction losses, these losses increase with the power and it is important to make sure conduction and core losses do not add up to form an unstable positive feedback and thermal runaway. Therefore, the same

considerations apply to B_{max} because it has a direct impact on core losses. After choosing a core, the number of turns can be determined from

$$N_k = \frac{L_k I_{max-k}}{A_{c-k} B_{max}} \tag{2.20}$$

where A_c is the cross section area of the core. The area that the winding will occupy can now be calculated as

$$A_{winding} = \frac{N I_{RMS}}{k_b J}. \tag{2.21}$$

The window area of the chosen core should be verified again to make sure it could accommodate the winding. Since a coil former will be installed between the core and the winding and take some space, the window area should be well above $A_{winding}$ to be able to easily accommodate the winding and leave some free space to enhance the cooling. If the chosen core is a toroid core, the cooling will be less of an issue.

2.3.3. Transformer

The transformer is the connection point between the ports and acts as a hub where all the energy is exchanged between them. As the application of MAB converters increases, the interest in studying multi-winding transformers increases, too. A modular design of multi-winding transformers that allows addition of windings is studied in [Honorio1]. The modular designs proposed in literature may have some disadvantages such as lower efficiency, higher leakage inductance, or mechanical strain, but the increasing need for MAB and other isolated DC/DC converter topologies can lead to more research on this type of design and introduction of enhanced manufacturing techniques [72].

Design of multi-winding transformers for MAB converters is studied in [73]. It compares application of different materials, including silicon steel, ferrite, amorphous and nano-crystalline for the magnetic core. Ferrite is suggested as the most suitable material, despite its low saturation flux density (around 400 mT), because it has relatively low losses at high frequencies and comes in many different shapes and sizes at a low price. Silicon steel and amorphous materials have higher saturation flux density but their losses at high-power high-frequency applications are large. Nano-crystalline has high saturation flux density (around 1.2 T) and relatively low losses at medium frequencies. However, its losses increase at frequencies higher than 15 kHz. Nano-crystalline is expensive and its commercial availability is not as high as ferrite cores [73], [74]. Considering all the parameters, ferrite cores seem to be the most

practical candidate for application in transformers of MAB converters. Figure 2.17 displays a summarized comparison of characteristics of the materials [73].

Winding placement in a four-winding transformer is also studied in [73] for a specific application of QAB converter. The QAB feeds DC network of a smart building, using energy from utility AC grid, PV panels and batteries. Since the final goal is defined as providing the DC network, most of the intended power flows involve the port that connects to this network, except charging the battery from AC grid or PV panels. In this regard, they seek to maximize coupling of the winding that corresponds to the DC network with the other windings. The four different winding placements on a CI ferrite core, shown in Figure 2.18, were studied with finite elements analysis in ANSYS. Case B in Figure 2.18 showed maximum coupling between the windings, however, since the goal was to maximize coupling of the DC network (port 4 in Figure 2.18), case C was chosen because it reduces winding length of the other ports. This asymmetric design can be an option for specific applications. Insulation and core shape are the other parameters that must be considered, too. In high voltage applications, case A can be a better solution because it facilitates the insulation between the windings. On the contrary, case B imposes the highest insulation constraints. The core shape can be another limiting factor in designing the windings of the multi-winding transformer, e.g., if a EI core is chosen, the windings will be most likely similar to case B. The target application of this research work, however, intends to facilitate power transfer in every possible direction to increase the flexibility of the converter as an energy exchange tool in smart grids. Therefore, a symmetric design is more favorable.

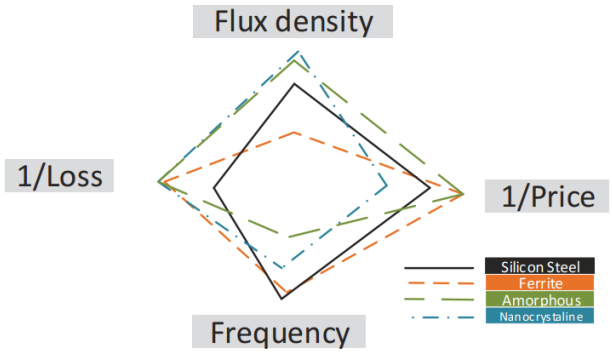

Figure 2.17: Comparing characteristics of different materials for magnetic cores [73].

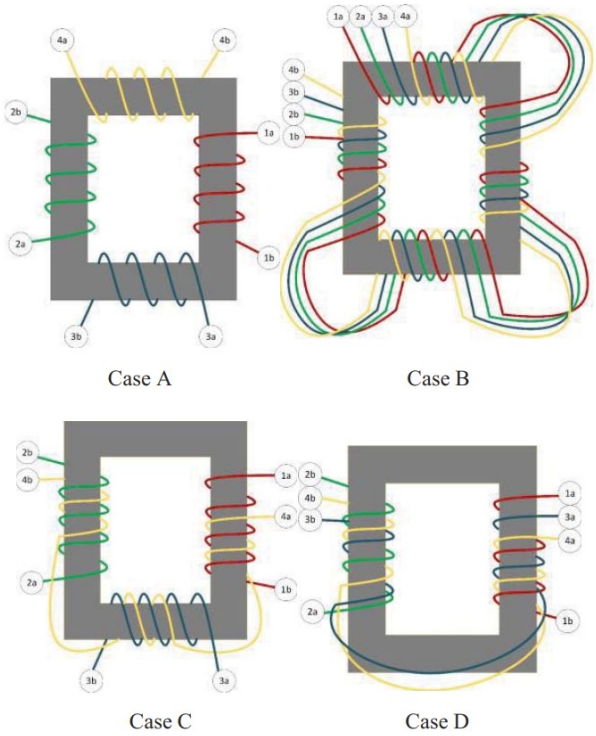

Figure 2.18: Different winding placement in a four-winding transformer, studied in [73].

The common rules for design of a multi-winding transformer is similar to the rules for a two-winding transformer in general. The area product of the transformer is determined from

$$A_p = \frac{2pP_{nom}}{\pi^2 k_b f J B_{max}} \tag{2.22}$$

where p is the number of ports. The number of turns for port k can be calculated after choosing the core, as

$$N_k = \frac{2V_{DC-k}I_{rms-k}}{\pi^2 f A_c B_{max}}. \tag{2.23}$$

Unlike inductors, the voltages across transformer windings are large, but they decrease as the powers increase. Therefore, the interplay between temperature rise of the windings and the magnetic core of the transformer, and the resulting thermal runaway are not likely to happen. Nonetheless, it should be taken into consideration that there are multiple windings on the core, hence, the total conduction losses can be large. The windings are most likely multilayer, allowing little cooling for the inner layers. Saturation of the transformer core is another possible issue that can happen as a result of DC currents in the windings. This issue and its solutions will be studied with more details in the next chapter. Considering all these points, cooling of the transformer and enough safety margin must be taken into consideration in the design procedure.

2.3.4. Semiconductors

Choosing semiconductors is an important part of the design procedure, because generally they have the second shortest MTTF, after capacitors. The power semiconductors are usually chosen based on the maximum blocking voltage and effective current that will occur during operation of the converter. Power metal-oxide semiconductor field-effect transistor (Power MOSFET) and insulated-gate bipolar transistor (IGBT) devices are the candidates for this application. They both work with simple gate drives, but power MOSFETs have higher commutation speeds and lower losses at low voltage applications. Characteristics of power MOSFETs allow low turn-off losses and fast switching. In high current applications, IGBTs show lower on-state losses, but higher turn-off losses. For the purpose of the current work, which is cluster converters in buildings, the voltage level would be below 1 kV and the power of each converter would be a couple of kilo Watts. Considering these parameters, power MOSFETs are a better choice.

The two mature technologies of power MOSFETs are silicon and silicon carbide. Gallium nitride MOSFETs have been recently introduced to the market. It seems to be a promising technology in power electronics and microelectronics, and there are several commercial products available. However, application of gallium nitride MOSFETs requires certain considerations and is still under study. Diamond MOSFETs are another new type of MOSFETs, but still in research and development stage. On application point-of-view, this work focuses on stationary application where the main criteria are cost and reliability. Therefore, employing low-cost widely-used well-known switches is an advantage and there is no necessity in using gallium nitride MOSFETs which are more costly and lack a long-tome history of application. Therefore, this work will only consider silicon and silicon carbide MOSFETs as the candidates for semiconductors. Silicon MOSFETs are the choice for voltages below 600 V because silicon carbide MOSFETs start from voltages above 600 V. The limit with silicon power MOSFETs is their blocking voltage and large on-state resistance as the voltage increases. Silicon-carbide power MOSFETs solve this issue and show better performance compared to silicon MOSFETs at voltages above 600 V. Several manufacturers have a range of silicon carbide MOSFET that are able to block 1.2 kV and conduct around 100 A.

Several parameters that have to be taken into consideration when choosing MOSFET switches, in addition to voltage and current specifications. The channel on-state resistance is an important factor because it is directly related to conduction losses. Switching characteristics are important, too. The output capacitance of the MOSFET determines the limit between soft

switching and hard switching. The smaller the output capacitance, the wider the hard switching region. The output capacitance and reverse recovery losses of the body diode determine the amount hard switching losses. Application of high voltage silicon carbide Schottky diodes in parallel with the MOSFETs helps reduce hard switching losses because these diodes have no reverse recovery losses. The junction-case thermal resistance is another factor that has an impact on reliability and can affect conduction losses, too.

As explained in this section, several factors must be considered when choosing semiconductor devices for a MAB converter. Choosing the best device requires good knowledge of the losses in the converter, its mission profile, and control strategy. If mission profile of a converter includes long duration of working at low powers, choosing a MOSFET that has a wide range of soft switching and low hard switching losses becomes important. If the mission profile mainly includes operating points close to nominal power or a control scheme is employed that can guarantee wide soft switching range, the priority in choosing the MOSFETs would be to have minimal on-state channel resistance. In order to do a control-aware design of a converter optimized for a specific mission profile, a mathematical model is required. This model must be able to predict the losses for different operating points. Using this model, along with enough knowledge of the control scheme and information about future mission profile of the converter, makes it possible to test a range of available devices in the market and choose one. This can help in design of the transformer and inductors, too. In this regard, a model of losses will be presented in the next chapter.

2.3.5. Specific design considerations

General considerations and design rules of semiconductors, inductors and transformers as the main components of MAB converters, have been studied in the previous sections so far. This section will discuss some points that are specific to MAB converter topology.

External inductances:

Many works in the literature do not add any external inductances and employ the leakage inductance of the transformer. It should be noted that the limit for inductance size in Equation (2.3) is for its maximum size, and there are no lower limits for the inductance in theory. In other words, the inductance can be much smaller than the value determined from Equation (2.3). In this case, P_{nom} would be much smaller than P_{max}, which not only is not a problem, but also helps minimize reactive powers and conduction losses. Therefore, it is better to consider a lower limit for the inductances in practice. Variation of DC link voltages may happen very often on

some ports, such as the one connected to the batteries. In this case, the maximum current value will significantly increase if the inductance is too small. If a variation of ΔV occurs in the primary DC link voltage of the DAB illustrated in Figure 2.8, the maximum inductor current would be as expressed in Equation (2.24). The second term is the result of the voltage variation and can be large if the inductance is too small.

$$I_{max} = \frac{V_{DC1}\,\varphi_{max}}{2\pi f L} + \frac{\pi \Delta V}{4\pi f L} \tag{2.24}$$

Another consequence of having a very small inductance is that the phase shift will be limited to a very small range, compared to the range of ±37 degrees that was chosen earlier. Therefore, very small changes in phase shift can lead to large changes in power transfer. If the switching frequency is high, considering the time step of industrial controller chips of a real converters and discretization of switching signals, the controller might not be able to apply desired phase shifts with enough accuracy. For example, if a PWM hardware with the smallest time step of 20 ns was used to generate switching signals at 50 kHz, the smallest phase shift change it would be able to apply would be around 0.2 degrees. If the inductance are for example very small, limiting phase shift in the range of ±5 degrees, the smallest possible step change in power would be around 4% the nominal power, which is a large step in some applications. However, in cases where the switching frequency is too high and/or the nominal power is too low, even Equation (2.3) will give a very small value for the inductance, making it impossible to use larger inductances.

Symmetric design:

As explained in section 2.3.2, the inductors define the limit of power transfer. It was shown that the currents and hence the conduction losses will increase rapidly if the power gets close to this limit. The nominal power of the converter was defined far enough from the limit, to ensure low losses and high efficiency of the converter. Since the converter was assumed to be symmetric, the nominal power of all ports would be the same, hence the ratio between the inductances would be equal to squares of transformer turn ratios, or

$$\frac{L_j}{L_k} = \left(\frac{N_j}{N_k}\right)^2 = \left(\frac{V_j}{V_k}\right)^2 = \left(\frac{I_k}{I_j}\right)^2 \tag{2.25}$$

which means the area product in Equation (2.19) will be the same for every port. In addition to simplifying the design procedures, symmetric design of the converter brings about other advantages including scalable and symmetric modeling of all of its aspects. This leads to easier

control and optimization. If there are inductances on every port and they are sized as in Equation (2.25), the voltage across transformer windings will be minimized, leading to lower losses in its magnetic core.

Despite the advantages of symmetric design, there are reasons that can lead to choosing asymmetry. One such case [73] was explained in section 2.3.3. Another case is due to the fact that having an inductance on every port leads to power coupling. Reference [75] proposes a MAB converter, introducing one port as the master port. The master port is directly connected to the transformer without an inductance, as displayed in Figure 2.19. The leakage inductance of the transformer is considered negligible, so the voltage across transformer windings is directly controlled by the master port. This design decouples the powers and makes the control as easy as controlling independent DABs. Removing one inductance will also lead to reduction of the cost and footprint of the converter. The potential problem is that the converter will not be able to continue working with the same control scheme if the master port is lost due to a fault, either in the converter or on the grid or a stop of the connected source production. If the converter is used to feed three DC loads from an AC grid (which is connected the master port), there is no point in trying to maintain the converter after a fault occurs in the master port since the sole energy source is not present anymore. In applications such as smart buildings or micro-grids, on the other hand, there are multiple energy sources or storage devices connected to the converter. These sources and storage devices can still provide the loads and it is better to have a scalable control scheme that can maintain operation of the converter despite a fault on one port. Therefore, the symmetric solution is a better and more generic solution for the purpose of this work. Experimental tests on a converter prototype showed that the symmetric design allows easier implementation of additional control considerations, too, as will be explained in section 4.5.1.

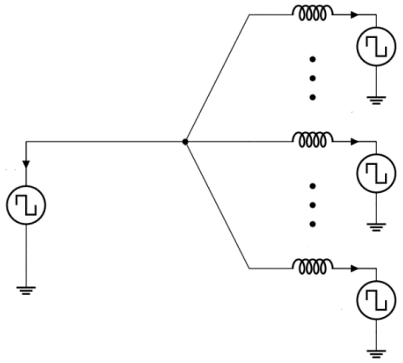

Figure 2.19: First harmonic equivalent circuit of the MAB converter proposed in [75] with one port as the master port.

2.4. Control of power flow

A MAB converter, whatever its application is, connects several generators and consumers of energy in one place. The role of the converter is to flow power between its different ports, i.e., the generators and the consumers, with a certain direction and amount. Many works propose control systems that are based on keeping load side voltage at its nominal value. This control scheme works well in applications where a DC load is fed through the converter, but it is not the case in all applications. Energy systems of smart buildings, as a common application of MAB converters, includes several sources such as photovoltaic panels, wind turbines, storage devices, and several consumers on ac and dc networks. A high-level controller takes into account several inputs of these systems (such as solar irradiance, wind speed, state of charge of the batteries, instantaneous demand, and electricity tariffs), and based on predefined strategies, determines how the power must flow. The power flow indicates how much power should be fed to or drawn from each port of the converters and the converter control is responsible for its realization. In case of the AC and DC grids, it is assumed that there are other production devices which will act as grid-forming components, keeping the voltage and/or frequency in the nominal range and the cluster of MAB converters is not responsible for voltage control, but rather for providing the necessary active and reactive (in a case of an AC grid) power. The QAB, however, will have only to manage active power flow.

This section seeks to find models and methods that can control the flow of power in MAB converters in any desired amount and direction. As explained before, the MAB is controlled using duty cycles and phase shifts. In this regard, the goal is to propose a control method that gets a desired power flow on the input, and then gives a set of duty cycles and phase shifts that will lead to that power flow if applied to the switching of the converter.

2.4.1. Power control in a DAB

It is better to start analyzing the power flow in a DAB and then move forward towards generalized solutions for any number of ports. Figure 2.20 shows an example of voltages in an ideal DAB converter along with phasor diagram of the voltages and the currents and a first harmonic approximation. The powers can be determined from the following set of phasor equations. It must be mentioned that all parameters are considered on primary side of the transformer.

$$\widehat{i_1} = \frac{\widehat{v_1} - \widehat{v_2}}{j\omega L} \tag{2.26}$$

$$S_1 = \widehat{v_1}.\widehat{i_1} = \frac{\widehat{v_1}(\widehat{v_1} - \widehat{v_2})}{j\omega L} \tag{2.27}$$

$$P_1 = -P_2 = real(S_1) = \frac{|\widehat{v_1}||\widehat{v_2}|\sin(\varphi)}{\omega L} \tag{2.28}$$

$$Q_1 = imag(S_1) = \frac{|\widehat{v_1}|(|\widehat{v_1}| - |\widehat{v_2}|\cos(\varphi))}{\omega L} \tag{2.29}$$

$$Q_2 = \frac{|\widehat{v_2}|(|\widehat{v_2}| - |\widehat{v_1}|\cos(\varphi))}{\omega L} \tag{2.30}$$

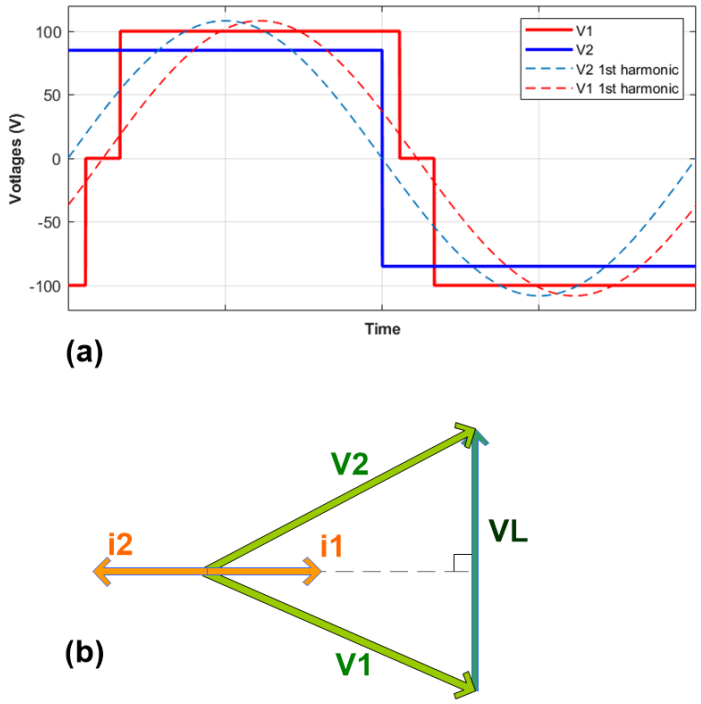

Figure 2.20: (a) output voltage of a DAB and the first harmonics; (b) phasor representation. VL is the voltage across the inductor.

The inductors are the main absorbents of reactive power, therefore

$$Q_1 + Q_2 = \frac{1}{2}L\omega|\hat{\imath}|^2 \tag{2.31}$$

If the voltage phasors have equal magnitudes, they will equally provide the reactive power of the inductor because Equations (2.29) and (2.30) would give the same value. If the magnitudes are not equal, the source with the smaller magnitude will provide less or even absorb reactive power. In this case, the source with the larger voltage phasor provides more reactive power, compared to the situation where the voltages were equal. While Equation (2.31) is still valid, the reactive power exchanged between the two sources would be

$$Q_1 - Q_2 = \frac{(|\widehat{v_1}| - |\widehat{v_2}|)\cos(\varphi)}{\omega L}. \quad (2.32)$$

The power flow problem includes two independent equations (Equation (2.28) for the desired active power and Equation (2.31) for conservation of reactive power), and three unknown parameters namely magnitudes of voltage phasors and the phase shift. Since the number of parameters is more than the number of equations, the problem is an underdetermined system and cannot have a unique solution. In practice, there are certain limits for the unknowns, such as minimum and maximum magnitudes of voltage phasors, or maximum allowed phase shift (37 degrees). The problem will still have many solutions even after applying these limitations. Underdetermined systems of equations appear in different design and control problems, and the multiplicity of the solutions provides the degree of freedom that is usually used for optimization of design and control. Solving these equations and finding the optimum is done in certain software environments such as MATLAB or CADES [22], for instance to find designs or control schemes that minimize size of magnetic cores or effective currents. Although using these software environments is a good solution for design procedure, it is not practical for real-time control of a converter. The next sections will study different approaches to find a solution for the power flow problem that can be deployed on real-time control systems. The goal is to avoid using large amounts of processing power, memory to solve the optimization problem, while being able to solve it quickly and with good accuracy.

2.4.2. Voltage modulations and phasor magnitudes

As explained in the previous section, the general power flow problem in a DAB, and in any MAB converter, has more than one solution. The difference between the possible solutions of power flow problem cannot be observed from outside of the converter, because they all transfer the same amount of active power between the DC sources. However, inside the converter, and more specifically on the AC link, the reactive power will not be same among different solutions. To be able to find a solution for the power flow problem, one additional criterion must be defined. This criterion can be on reactive power or magnitudes of voltage phasors.

Since reducing the losses is always a favorable goal, minimization of reactive power can be a suitable solution because it will minimize the reactive component of the current (active and reactive component of each current phasor is determined with regard to the voltage phasor of its corresponding port). The reactive power absorbed by the inductances is not avoidable, however, the reactive power exchange between the sources can be reduced to zero, i.e. $Q_1 - Q_2 = 0$. It requires voltage phasor magnitudes to be equal (Equation (2.32)). Although this will

reduce reactive components of the currents, it can lead to an increase in active current components when the DC link voltages are unequal. Minimizing active components of the currents requires voltage phasor magnitudes to be at their maximum possible value, because

$$P_k = \frac{|\hat{v}_k| i_{ak}}{2} \tag{2.33}$$

where i_{ak} is magnitude of the active component of the current phasor of port k. For the same amount of P_k, minimizing the active current is equivalent to maximizing voltage phasor magnitude. If DC link voltages are equal and at their nominal values, generating two-level square-wave voltage at both ports will minimize both active and reactive currents. Moreover, soft switching conditions will hold true over a wide range of power transfer. However, if one of the DC link voltages changes from its nominal value ($V_{\mathrm{DC1}} \neq V_{\mathrm{DC2}}$), active and reactive currents may change in opposite directions. In this situation, equalizing phasor magnitudes to minimize reactive currents means magnitude of the voltage phasor with the larger DC link voltage has to be reduced by reducing its corresponding duty cycle. This will lead to an increase in the corresponding active current for transferring the same amount of active power. On the other hand, keeping voltage phasors at their maximum value (100% duty cycle on both sides) to minimize the active components of the currents, means increasing the reactive currents.

The reactive current in a DAB can be determined from Equations (2.29) and (2.30) as

$$i_{rk} = \frac{2Q_k}{|\hat{v}_k|} = 2\frac{|\widehat{v_{\mathrm{k}}}| - |\hat{v}_1| \cos(\varphi)}{\omega L} \tag{2.34}$$

Sum of squares of the effective currents is directly related to conduction losses, therefore it can be considered as the parameter for comparison between different voltage modulations. Sum of current squares can be calculated from

$$\sum i_{ak}^2 + i_{rk}^2 = 4\left(\frac{P_k}{|\hat{v}_k|}\right)^2 + 4\left(\frac{|\widehat{v_{\mathrm{k}}}| - |\hat{v}_1| \cos(\varphi)}{\omega L}\right)^2 \tag{2.35}$$

Several works in the literature have addressed the power flow problem in DAB [65, 80]. They propose different types of voltage modulations, illustrated in Figure 2.21. The three-level voltage modulation is used in low powers, leading to triangular current waveform, as in Figure 2.21-c. At medium power, only one side synthesizes three-level voltage, as in Figure 2.21-b. At high power, both sides operate in two-level modulation mode and the power is controlled only by adjusting the phase shift, as in Figure 2.21-a. This mode is called phase

shift modulation. The border between these three modulations depends on DC link voltages. The proposed control scheme guarantees soft switching for all operating points.

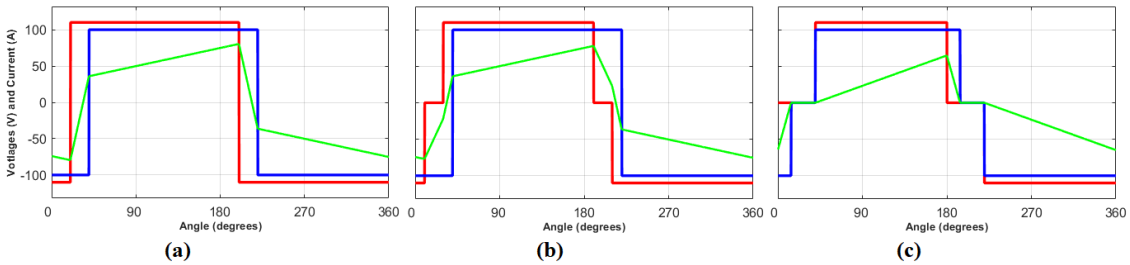

Figure 2.21: Examples of different voltage modulations proposed in [80]: (a) phase shift control for high powers; (b) intermediate modulation for medium powers; and (c) triangular modulation for low powers.

The three voltage modulations shown in Figure 2.21 are defined based on square-wave calculations. Using first harmonic analysis, three other methods can be defined which are different from those modulations but use the same concept. The first method is to have maximum possible voltage phasor on each port, which is equivalent to two-level voltage modulation (Figure 2.21-a). The second method is trying to equalize voltage phasors, which requires duty cycle control on the sides with higher DC link voltages and is equivalent to Figure 2.21-b. The third method involves equalizing average voltages of the two ports (or equalizing volt-seconds, the area below voltage waveform), which is equivalent to Figure 2.21-b but with an additional constraint concerning the current shape.

A first-harmonic ideal model of a DAB is used for this comparison. Based on the design procedures that were proposed earlier in this chapter, a 2 kW DAB with 100 V DC link voltages and 40 kHz switching frequency needs a 9.5 µH inductance to keep the phase shift in the range of ±37 degrees. Figure 2.22 shows the results of the comparison between the three voltage modulations. It shows that the reactive currents have a more significant impact when the power is low (Figure 2.22-a); therefore, the "equal phasors" and "equal Volt-seconds" modulations lead to lower conduction losses because they try to reduce reactive currents by adjusting the voltage phasor magnitudes. As the power transfer increases up to 50% nominal power (Figure 2.22-b), the active current becomes comparable to the reactive current, especially when the ratio of DC link voltages is not far from one. Therefore, "full conduction" modulation shows slightly lower losses around the diagonal region where the two DC link voltages are equal. The other two modulations still perform better in the region where DC link voltage ratio is far from one (the right and left sides of Figure 2.22-b). If the power transfer is increased further, as in Figure 2.22-c, the active current becomes the dominant factor in determining the current

magnitudes. The two-level (full conduction) modulation shows better performance at higher power levels because it minimizes active currents through maximizing magnitudes of all voltage phasors. Evolution of active and reactive currents are better illustrated in Figure 2.23.

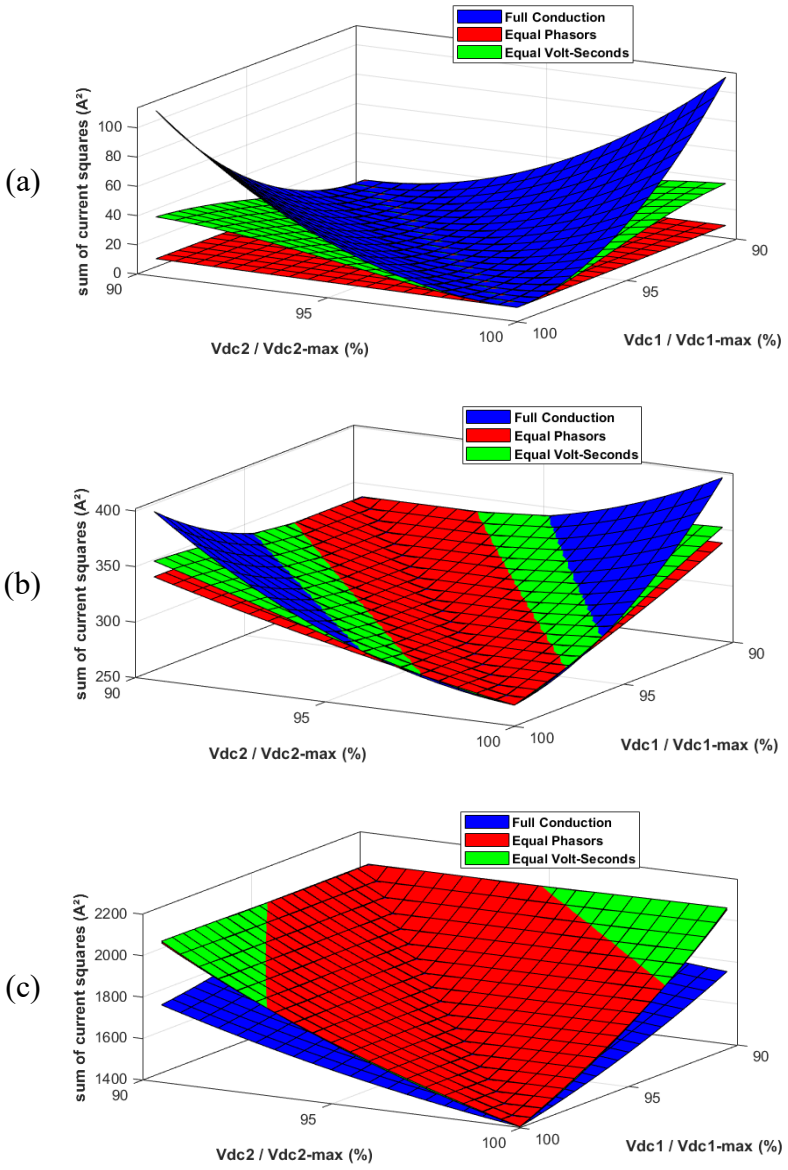

Figure 2.22: Comparing sum of current squares in different voltage modulations as DC link voltages of a DAB vary from their nominal value, when transferring (a) 20%, (b) 50% and (c) 100% nominal power. Sum of current squares is chosen as a parameter that is directly related to conduction losses in the converter.

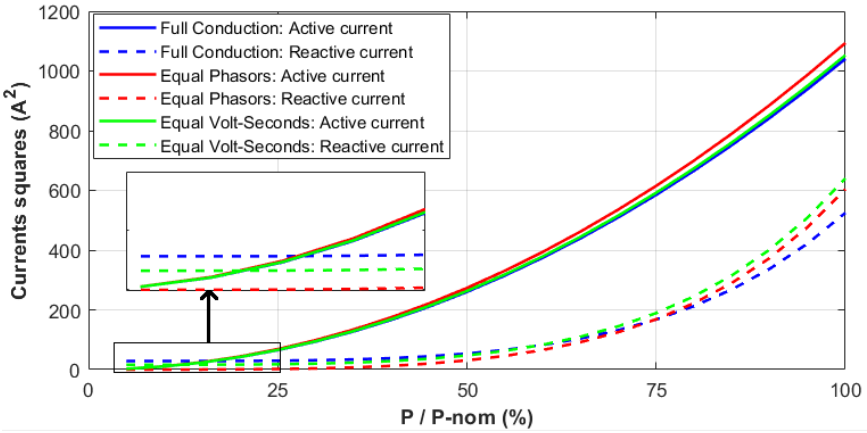

Figure 2.23: Comparing active and reactive currents of a DAB in different voltage modulations. DC link voltages of the primary and secondary are equal to 95% and 100% nominal voltage, respectively.

Figure 2.23 displays how active and reactive current squares change as the power increases. DC link voltages of the first and the second port are kept constant at 95% and 100% nominal voltage, respectively. A closer look shows how reactive current is the dominating current in "full conduction" modulation at low power region, until 15%. If the primary DC link voltages were 90% nominal voltage, the reactive current would be the dominant current up to 30% nominal power. Figure 2.23 shows how "equal phasors" and "equal Volt-seconds" lead to larger active current because they reduce the effective voltage. Furthermore, the decrease in effective voltage means that a higher phase shift must be applied to transfer the same amount of active power. Increasing the phase shift increases the reactive current determined in (2.34). As a consequent, the reactive current in "equal phasors" and "equal Volt-seconds" surpasses the reactive current in "full conduction" for the region above 60-75% nominal power, although the two methods aimed for minimization of reactive current.

It should be noted that although conduction losses are considered the major losses, other types of losses play an important role in the tradeoff that was explained in this section. The optimal choice in tradeoff depends on characteristics of the converter, such as winding resistances, output capacitance of the MOSFETs, and magnetic core properties, as well as operating parameters such as power transfer and DC link voltages. Although the method proposed in [80] seems to be a good solution for optimal control of power, using it for a MAB converter is not obvious. The reason is the coupling between the currents, which makes it difficult to control the shape of the current as easily as in DAB. As displayed in Figure 2.8, the currents in a MAB have complicated shapes, compared to a DAB. Different types of voltage modulations can still be defined in MABs, including equalizing voltage phasors and equalizing volt-seconds. Since analytical methods cannot compare these modulations in terms of total

losses in a MAB converter, a model of losses is required to do this. This model will be discussed in the next chapter.

Several methods can be used to determine the optimal modulation for different power flows and DC link voltage variations, such as pre-calculating regions using a detailed model of losses, or real-time optimization using a reduced order model (ROM). Regardless of the method, when a certain type of voltage modulation is chosen, magnitudes of voltage phasors can be determined on each port based on the corresponding DC link voltage and the duty cycle. Therefore, magnitudes of the voltage phasors are known and the power flow problem in a MAB converter is to find a set of phase shifts that leads to the desired power flow.

2.4.3. An approximate and iterative solution

As explained before, voltage magnitudes are going to be evaluated after choosing voltage modulation and then, the power flow problem will be reduced to finding a set of phase shifts that correspond to the desired power flow. This problem is still a complex problem and finding a closed-form analytical solution is not possible because of the coupling between the ports, as in (2.15). In this regard, methods that are based on approximation can be useful. The solution found by the approximations may be far from the correct solution, i.e. the phase shift that result from the approximate solution leads to a power flow, which is close, but not equal to the desired power flow. In order to improve the solutions, some iterations will be defined.

The first method (published in [76]) is based on first harmonic model of the MAB, displayed in Figure 2.24. $\widehat{v_t}$ is the phasor of the voltage across primary side of the transformer, and it is the phase reference ($\widehat{v_t} = |\widehat{v_t}| = v_t$). The MAB converter can be considered as n DAB converters, and the power transfer in Equation (2.28) will be between each active bridge and the transformer winding. The approximation is that for each port k, magnitude of the transformer and the active-bridge voltage phasors are considered equal ($|v_t| = |v_k|$), as if the currents were zero. This is not a correct assumption, but it can be used as an assumption for the initial calculation. It is assumed that $|v_t| = |v_k|$, but there is a phase shift of φ_k between them. Therefore, the power transfer in Equation (2.28) can be solved for each port separately, and phase shifts can be determined as

$$\varphi_k = \sin^{-1} \frac{\omega P_k L_k}{|\widehat{v_k}|.|\widehat{v_t}|} \tag{2.36}$$

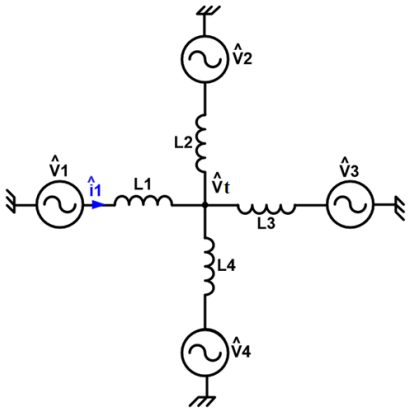

Figure 2.24: First harmonic model of a QAB.

Now that $\widehat{v_k}$ and v_t are two vectors of the same magnitude with a known phase difference of φ_k in-between, it is possible to determine the first approximation of currents as

$$\widehat{i_k} = \frac{\widehat{v_k} - v_t}{j\omega L_k} \tag{2.37}$$

Knowing the currents for every port, *n* new values for v_t can be determined through solving Equation (2.37) for every port, as

$$\widehat{v_t} = \widehat{v_k} - j\omega L_k \widehat{i_k} \tag{2.38}$$

The $\widehat{v_t}$ is considered the reference for phase shifts, therefore it is a real vector and does not have an imaginary component, while the other voltage phasors are complex vectors, defined as $\widehat{v_k} = |\widehat{v_k}|\sin(\varphi_k) + j|\widehat{v_k}|\cos(\varphi_k)$. It should be noted that the $\widehat{v_t}$ determined from Equation (2.38) is going to be a complex vector. In order to make it the reference for phase shift and a real vector again, its magnitude must be set equal to what is determined from Equation (2.38) and its phase set back to zero. For the next iteration, Equations (2.36) to (2.38) are solved again and the values are updated. In order to enhance the speed of convergence, average of all of the *n* values from Equation (2.38) must be considered as the new v_t magnitude. A stop condition must be defined based on an error limit and/or maximum iterations. The following sections will present other methods of solving the power flow problem. A comparison of all the proposed methods will be presented afterwards.

2.4.4. Iterative solution with improved approximation

The iterative approximate method proposed in the previous section is a scalable general method that works for MAB converters with any number of ports. However, the approximation can be far from reality because it considers the currents to be zero for its first guess. The error will increase especially when the power is high, which means large voltage drops on the

inductors and smaller transformer voltage. Another method will be proposed in this section, which considers the power transfers in its first guess and gives a better approximation of the transformer voltage.

The method is based on finding an equation for $\widehat{v_t}$ in complex phasor domain, and then solving it with approximations. Similar to the previous method, the $\widehat{v_t}$ vector is the phase reference, so its imaginary component is zero. Every other voltage and current phasor can be illustrated as a sum for of real (d), and imaginary (q) components as $\widehat{v_k} = v_{kd} + jv_{kq}$. Magnitude of voltage phasors, $|v_k|$, are known, based on voltage modulation. So their real and imaginary components are dependent, as $v_{kd} = \sqrt{|v_k|^2 - {v_{kq}}^2}$. It can be conclude that for an n-port MAB converter, there are $n+1$ unknown parameters including v_{1q}, v_{2q}, …, v_{nq} and $\widehat{v_t}$. The currents can be determined as

$$\widehat{i_k} = \frac{(v_{kd} + jv_{kq} - v_t)}{jX_k} \quad \rightarrow \quad i_{kd} = \frac{\widehat{v_{kq}}}{X_k} \ , \ \ i_{kq} = \frac{v_t - \widehat{v_{kd}}}{X_1} \tag{2.39}$$

The Kirchhoff's current law as $\sum_{k=1}^{n} \widehat{i_k} = 0$ must be divided into two equations of real and imaginary components and be expressed based on Equation (2.39) as

$$\frac{v_{1q}}{X_1} + \frac{v_{2q}}{X_2} + \cdots + \frac{v_{nq}}{X_n} = 0 \tag{2.40}$$

$$\frac{\sqrt{|\widehat{v_1}|^2 - {v_{1q}}^2}}{X_1} + \frac{\sqrt{|\widehat{v_2}|^2 - {v_{2q}}^2}}{X_2} + \cdots + \frac{\sqrt{|\widehat{v_n}|^2 - v_{nq}^2}}{X_n} = v_t \sum_{i=1}^{n} \frac{1}{X_i}. \tag{2.41}$$

In addition to the two equations of Kirchhoff's current law (Equations (2.40) and (2.41)), there are $n-1$ independent equations for powers. Therefore, there are total $n+1$ equations. Number of unknown parameters and equations are equal, so this is a determinate system and can have unique solutions. The real power transfer of each port can be determined as real current multiplied by transformer voltage

$$P_k = \frac{v_{kq} v_t}{X_k}. \tag{2.42}$$

Replacing v_{kq} from Equation (2.42) into Equation (2.41) gives

$$\frac{\sqrt{|\widehat{v_1}|^2 - \left(\frac{P_1 X_1}{v_t}\right)^2}}{X_1} + \frac{\sqrt{|\widehat{v_2}|^2 - \left(\frac{P_2 X_2}{v_t}\right)^2}}{X_2} + \cdots + \frac{\sqrt{|\widehat{v_n}|^2 - \left(\frac{P_n X_n}{v_t}\right)^2}}{X_n} = v_t \sum_{i=1}^{n} \frac{1}{X_i} \tag{2.43}$$

Equation (2.43) is the principal equation for v_t, which can be solved with the help of approximation. To do that, $|v|$ is defined as average of voltage phasor magnitudes, and PX as average of $P_k X_k$. If these two values replace every $|v_k|$ and $P_k X_k$ in Equation (2.43), respectively, it will turn into a simpler equation as

$$\sqrt{v_t^2 |v|^2 - (PX)^2} = {v_t}^2 \tag{2.44}$$

which gives v_t as

$$v_t = \sqrt{\frac{|v|^2 \pm \sqrt{|v|^4 - 4(PX)^2}}{2}} \tag{2.45}$$

The ± sign in the solution means that there are two possible solutions for the problem, as illustrated in Figure 2.25. Since larger magnitude of v_t leads to smaller currents (Equation (2.42)), the plus sign is the chosen solution. After finding an approximate value for v_t, real and imaginary components of all voltage phasors can be determined from Equation (2.42) and $v_{kd} = \sqrt{|v_k|^2 - {v_{kq}}^2}$.

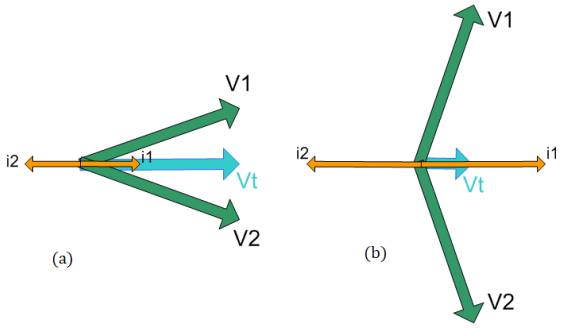

Figure 2.25: The two possible solutions for a certain real power transfer in a DAB with the same voltage magnitudes, but different transformer voltages and phase shifts: (a) with the plus sign in Equation (2.45); and (b) with the negative sign in Equation (2.45).

2.4.5. Computational cost efficient power control

The two methods that were presented for solving the power flow problem so far, can find the phase shifts that correspond to the desired power flow. Running these calculations on an industrial control chip with limited processing power and memory can occupy a large portion of the available resources and take a relatively long time to reach the final answer, especially when iterations are required. Finding a power control method that can solve the problem in a very short time will improve dynamic behavior of the system, help reduce energy storage requirement. A swift control system reduces the need for high sampling frequency of input

parameters, too. On a higher-level point of view, running a cluster control scheme with multiple iterations for several converters, especially if an optimization method based on trial and error of multiple operating points of the cluster is implemented on the controller, will take a large portion of available resources of the microcontroller. A method that can solve the power flow problem with less computational costs can help overcome this challenge. This section presents a computational cost efficient method based on a method, which is scalable and can be generalized for any number of ports (published in [77]). A similar method was already proposed in [78] for a different topology of MAB converters.

The efficient power control method is based on the star-to-delta transform of MAB, as previously presented in 2.2.2 and Figure 2.14. The power transfer of each port is the sum of its power transfer to each one of the other ports, as

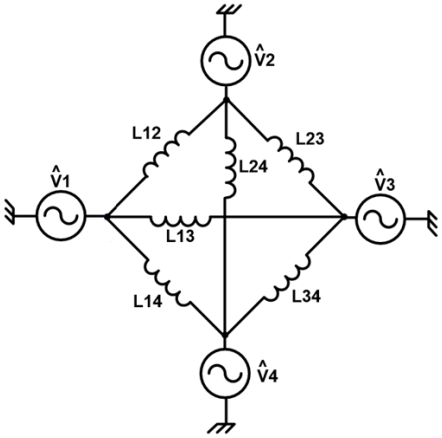

Figure 2.26: The first harmonic representation of a QAB after applying star-to-delta transform.

$$P_k = \frac{V_1.V_k}{L_{1,k}.\omega}.\sin(\varphi_1 - \varphi_k) + \frac{V_2.V_k}{L_{2,k}.\omega}.\sin(\varphi_2 - \varphi_k) + \cdots + \frac{V_n.V_k}{L_{n,k}.\omega}.\sin(\varphi_n - \varphi_k) \tag{2.46}$$

where $V_k = |\widehat{v_k}|$. As explained in section 2.3.2 on sizing the inductors, the phase shifts are limited to the range of ±37 degrees. The approximation of $sin(\varphi) = \varphi$ will have maximum 7.3% error in this range. Using this approximation, the power flow equation can be simplified as

$$P_k = \frac{V_1.V_k}{L_{1,k}.\omega}(\varphi_1 - \varphi_k) + \frac{V_2.V_k}{L_{2,k}.\omega}(\varphi_2 - \varphi_k) + \cdots + \frac{V_n.V_k}{L_{n,k}.\omega}(\varphi_n - \varphi_k) \tag{2.47}$$

and rearranged as

$$P_k = \frac{V_1.V_k}{L_{1,k}.\omega}.(\varphi_1) + \frac{V_2.V_k}{L_{2,k}.\omega}.(\varphi_2) + \cdots + \frac{V_k.V_k}{L_{k,k}.\omega}.(\varphi_k) \ldots + \frac{V_n.V_k}{L_{n,k}.\omega}.(\varphi_n) - \frac{V_k\varphi_k}{\omega}\sum_{i=1}^{n}\frac{V_i}{L_{n,i}} \tag{2.48}$$

where, $L_{k,k}$ does not have a real representation and is only added for keeping symmetry in the equations. This term will be omitted from calculations in each line of the final matrix. All the power equations can be put into one matrix equation as

$$\omega\begin{bmatrix}P_1\\P_2\\\cdots\\P_n\end{bmatrix}=\begin{bmatrix}\frac{V_1.V_1}{L_{1,1}}-V_1\sum_{i=1}^{n}\frac{V_i}{L_{1,i}} & \frac{V_1.V_2}{L_{1,2}} & \cdots & \frac{V_1.V_n}{L_{1,n}}\\ \frac{V_2.V_1}{L_{2,1}} & \frac{V_2.V_2}{L_{2,2}}-V_2\sum_{i=1}^{n}\frac{V_i}{L_{2,i}} & \cdots & \frac{V_2.V_n}{L_{2,n}}\\ \vdots & \vdots & \cdots & \vdots\\ \frac{V_n.V_1}{L_{n,1}} & \frac{V_n.V_2}{L_{n,2}} & \cdots & \frac{V_n.V_n}{L_{n,n}}-V_n\sum_{i=1}^{n}\frac{V_i}{L_{n,i}}\end{bmatrix}\times\begin{bmatrix}\varphi_1\\\varphi_2\\\cdots\\\varphi_n\end{bmatrix} \tag{2.49}$$

Determining the reverse of the matrix of coefficients in Equation (2.49) can solve the power flow problem, but this matrix may not be reversible under some conditions; for instance, when all inductances and voltage magnitudes are equal. In order to modify this matrix and make it reversible, the conservation of power can help. As P_n can be determined as $P_n=-\sum_{i=1}^{n-1}P_i$, the last row of the matrices can be omitted because it is not an independent equation and can be determined from sum of the other rows. For the same reason, V_1 can be considered as the reference for phase and φ_1 will be zero. The first column of the matrix of coefficients can be omitted without changing the outcome, because all of its elements will be multiplied by φ_1, which is zero. The final equation would be

$$\omega\begin{bmatrix}P_1\\P_2\\\cdots\\P_{n-1}\end{bmatrix}=\begin{bmatrix}\frac{V_1.V_2}{L_{1,2}} & \frac{V_1.V_3}{L_{1,3}} & \cdots & \frac{V_1.V_n}{L_{1,n}}\\ \frac{V_2.V_2}{L_{2,2}}-V_2\sum_{i=1}^{n}\frac{V_i}{L_{2,i}} & \frac{V_2.V_3}{L_{2,3}} & \cdots & \frac{V_2.V_n}{L_{2,n}}\\ \vdots & \vdots & \cdots & \vdots\\ \frac{V_{n-1}.V_2}{L_{n-1,2}} & \frac{V_{n-1}.V_3}{L_{n-1,3}} & \cdots & \frac{V_{n-1}.V_n}{L_{n-1,n}}\end{bmatrix}\begin{bmatrix}\varphi_2\\\varphi_3\\\cdots\\\varphi_n\end{bmatrix} \tag{2.50}$$

It is now possible to determine phase shifts as

$$\begin{bmatrix}\varphi_2\\\varphi_3\\\cdots\\\varphi_n\end{bmatrix}=\omega[A]^{-1}\begin{bmatrix}P_1\\P_2\\\cdots\\P_{n-1}\end{bmatrix} \tag{2.51}$$

where, $[A]$ is the matrix of coefficients in Equation (2.50).

2.4.6. Comparison of the proposed methods

Two iterative methods of solving the power flow problem were presented in previous sections. They begin with finding a first approximate solution. The solution may be far from the correct solution, but through performing some iterative calculations and updating

magnitudes of the current, they manage to get very close to the desired power flow. Those iterative methods and the efficient method presented in previous section do the same task: given the desired power flow and voltage magnitudes as inputs, these methods determine a set of phase shifts that, if applied as external phase shifts between switching of the active bridges, will correspond to the desired power flow. The major difference between these methods is the approximations they use for solving the problem. These methods will be compared in terms of accuracy of their final solution and amount of calculations they require on a controller chip.

Accuracy:

Since the reference control signal is the power transfer of each port, a good parameter for comparison of accuracy is the average difference between the desired power transfer and the one measured after applying the phase shifts. Figure 2.27 shows the defined error of consecutive iterations of the methods proposed in section 2.4.3 (labeled as "Zero Currents"), section 2.4.4 (labeled as "Complex Phasors"), and section 2.4.5 (labeled as "Modular Matrices").

Figure 2.27-a shows the ideal condition where DC link voltages are equal to nominal values, the model parameters (inductors) match the real converter, and power transfer is at nominal power on every port.

- The "Zero Currents" method starts with around 5% error in its first guess, but quickly reduces the error to around zero after two additional iterations.
- The "Modular Matrices" method leads to around 6% error. This is due to the $sin(\varphi) = \varphi$ approximation that is used in this method. The phase shifts increase as the powers increase and the difference between $sin(\varphi)$ and φ becomes larger. This difference reaches up to around 7% at the nominal power, where φ is around 37 degrees.
- It is noticeable that the "Complex Phasors" method has a very small error even in its first guess. The reason is that the averaging approximation used in this method between Equations (2.43) and (2.44), gives accurate values and has no error if voltages and inductors are equal on every port.

The second test, displayed in Figure 2.27-b, shows another operating point where there is ±5% variation in DC link voltages and ±5% mismatch between the model and the converter. The power flow is 1.5, -0.5, 0.2, and -1.2 kW on the four ports.

- The "Zero Currents" has almost the same error, but this time cannot reduce to zero after two additional iterations. If the iterations continue, the error will oscillate between 0.6%

and 0.7% and converge to a value in the range. Considering a limit for error and maximum number of iterations as a stop condition is vital in this situation.

- The error of the "Modular Matrices" method is around four times smaller this time, despite the mismatch. The reason is that the powers are smaller than the previous case. Therefore the approximation of $sin(\varphi)$ is more accurate.
- The "Complex Phasors" method again shows negligible error. A small oscillation centered at around 0.28% error is observed, similar to the "Zero Currents" method, which indicates the need for a stop condition.

The results illustrated in Figure 2.27 showed that the "Complex Phasors" method does not need any additional iterations because its first guess is accurate enough. The "Zero Currents" needs two iterations to make sure the error is small. The "Modular Matrices" cannot reduce its error and the error increases as the powers increase. Therefore, the "Complex Phasors" can be a good solution whenever computational cost is not an issue. In cases where a computational cost efficient model is needed, the "Modular Matrices" can be the solution, since it has only multiplications and additions, and can use a pre-calculated matrix, compared to power, square root, trigonometric and their inverse functions that are used in the other two methods.

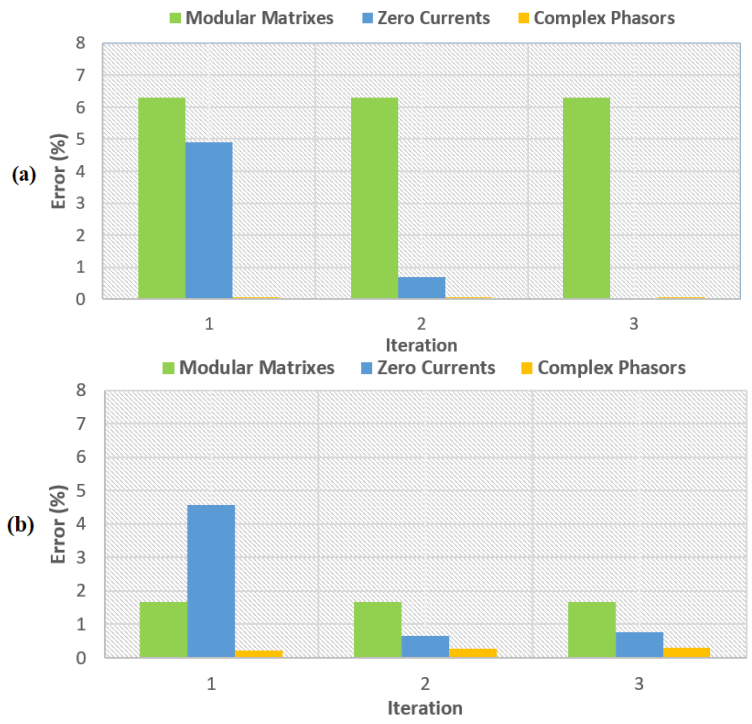

Figure 2.27: Comparing convergence of different power control methods in a modeled 2 kW QAB: (a) ideal converter with all powers and voltage at their nominal values; (b) non-ideal converter with ±5% voltage variation and ±5% mismatch between model and the converter; powers are [1.5 -0.5 0.2 -1.2] kW.

It should be noted that a feedback loop including a PI controller is usually present in the control systems that depend on models, as the three presented methods. The main goal of using a PI feedback is to eliminate the steady state errors that occur due to the mismatch between the values in the model and the real system. This feedback loop can be counted upon for eliminating the steady state error caused by the approximation of the proposed methods, too. In this regard, the steady state errors of the proposed methods, even relatively large error of the efficient model, is not going to be a major issue.

Speed:

The second comparison is the amount of calculations involved with each method. The final goal of designing a MAB is to build and use it in a real energy system. The control system for this converter should be able to work with limited resources of low-end controller chips used in industrial products. Therefore, it is important to assess performance of the presented methods on a controller and validate that they run correctly. NI myRIO 1900 system which is based on a Xilinx Z-7010 chip composed of a 667MHz ARM processor and an FPGA, was used as the controller. All methods were implemented on the target chip and run on its processor. Figure 2.28 illustrates the results. The time required to do the calculations of the "Modular Matrices" method is 4 µs, compared to 127 µs for two iterations of the "Zero Currents" method and 142 µs for the first guess of the "Complex Phasors" method. Considering the overhead processing time of 18 µs, the total runtime would be 22 µs for the "Modular Matrices" method, compared to 145 µs for two iterations of the "Zero Currents" method and 160 µs for the first guess of the "Complex Phasors" method. The comparison shows that the proposed method is computational cost efficient and a good candidate for real-time control and optimization purposes.

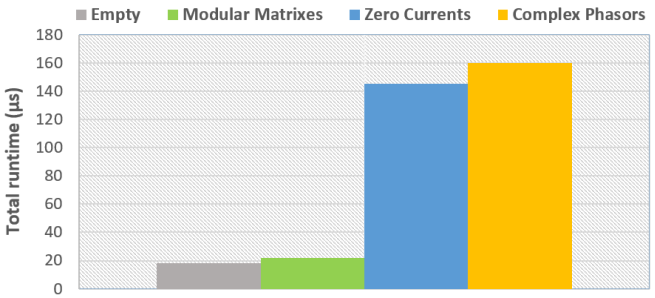

Figure 2.28: Comparing runtime of the proposed methods. The first column on the left corresponds to an empty program and indicates the overhead processing time, which is 18 µs. The second column corresponds to the "modular matrices" method, which requires 4 µs plus the additional 18 µs overhead processing time. The third and the fourth sections correspond to the "zero currents" and "complex phasors" methods, respectively.

Considering the outcome of the comparison between the proposed methods in terms of speed and accuracy, and the fact that a PI feedback loop will be present in the control system, the "Modular Matrices" is a suitable power control method for the purpose of this work. In other applications however, the choice depends on the requirements and available resources.

2.5. Conclusion

MAB converters, as the proposed candidate for application in cluster of converters, were studied in this chapter. Their advantages were presented in the beginning. Several ways of modeling these converters were proposed. Design rules and considerations were discussed for major components of the converter. The proposed models were used to find a way to control the flow of power in MAB converters. As no analytical closed-form solution were found for the power flow problem, approximate and iterative methods were proposed. The proposed methods were compared in terms of accuracy, speed of convergence and the required amount of computations. Close study of the trade-offs in design and control optimizations showed that a model of losses is needed to. The next chapter will be dedicated to proposing models of losses in MAB converters and the challenges of operating them.

3. Multi-port active-bridge converters: Operation and Losses

The previous chapter introduced MAB converters, studied its design and proposed methods for its modeling and control. The converter that was studied in the previous chapter was an ideal converter, usually working under ideal or close-to-ideal conditions. The ideal model can be used for different purposes; however, it is not able to predict the phenomena inside converter accurately. The differences between a real converter and an ideal one can lead to significant inconsistency between the performance that is expected from the converter and the performance that will be observed in real world. Moreover, the non-ideal characteristics may cause conditions that lead to failure. In this regard, it is important to study a converter with non-ideal characteristics, get a more accurate understanding of the converter and be able to address challenges of employing a real converter.

A major part of the difference between an ideal and a real converter are the inductances and resistances in the windings, MOSFET channels, PCB traces, and in the measurement devices. The mismatches between the predicted and the real value of certain parameters, such as the inductances or the thermal resistance between the MOSFET cases and the heat sinks are another type of non-ideal characteristics. Moreover, variations in DC link voltages on some ports and unequal delays in the gate-drive circuits are the conditions that may occur frequently during operation of a MAB converter.

This chapter studies a non-ideal converter working in non-ideal operating conditions to find out potential issues that will arise under these circumstances. In the beginning, a model will be presented that can predict the losses inside the converter. Non-ideal operating conditions will be presented afterward. The model will be then used for finding the best way to react to different operation conditions, i.e. optimal control, as well as for designing the best converter for a given mission profiles, i.e. optimal design.

3.1. A model of MAB with the losses

Importance of having a model of losses in MAB converters has been discussed before. This section introduces major losses that occur in a MAB converter and studies the methods to determine them. Several works in the literature have already discussed the losses of a DAB converter in detail [65], [79]. The main goal in many works is to find the best voltage

modulation that can minimize the losses. Some works [42], [80] propose switching modes that can guarantee soft switching for a wide range of power and voltage variation, while trying to minimize conductions losses, i.e., their model only includes conduction losses and the goal function is minimization of the RMS current. They use a subset of the 12 different voltage modulations and extract the calculations for each of them. Since this approach would be too complicated in case of a MAB, analytical and approximate solutions will be presented in this chapter.

There are three major types of losses in MAB converters, namely conduction losses, magnetic core losses and switching losses. Determining these losses requires analysis of the voltages and currents and certain information of the design parameters and datasheet values. A model of losses is a mathematic model, i.e. a series of calculations that gets parameters such as phase shifts, DC link voltages, and converter design on its input and gives a prediction of the losses that will occur on its output.

3.1.1. Conduction losses

Conduction losses are usually considered the most important type of losses in MAB converters as they rapidly increase with the increase in power transfer. Conduction losses occur in windings of the inductances and the transformer, as well as in the MOSFET channels. Determining conduction losses requires knowing values of the RMS currents and the resistances. There are different ways to determine these values. During design stage, the resistances must be calculated analytically using design parameters. After building a real converter, these parameters can be measured accurately using impedance analyzers.

As explained in the previous chapter, inductances are sized based on nominal voltages and power of the converter. These specifications give some criteria for the magnetic core. Checking a list of different core shapes, sizes and materials, the ones that satisfy the minimum criteria will be chosen as potential candidates.

Analytical calculation of winding resistances include the following steps

1. Determine the rating of the inductances based on nominal voltage and power of the converter, as explained in the previous chapter, ExEquation (2.3).
2. Calculate minimum area product of the magnetic core, using ExEquation (2.19).
3. Choose from a list of magnetic cores with different shapes, sizes and materials, the ones that satisfy the minimum core product criteria.

4. Calculate the length of the windings based on the geometry of the core and number of turns.

The resistance can be determined from the length of the windings and the cross section area of the wire. The cross section area is already chosen based on the desired maximum current density and the maximum effective current, as explained in previous chapter. When calculating the length of the windings, mean diameter of the winding must be considered if the winding is multi-layer. Maximum number of turns on each layer can be determined from size of the wires and the free space on the core or the coil former. The same procedure gives the resistances of transformer windings. Skin and proximity effects lead to an increase the calculated resistance when an AC current passes through the windings. The magnetic core of the inductances are usually gapped cores and the fringing effect of magnetic fields around the air gap lead to additional losses in the windings. Determining the impact of proximity effect is complex, and the additional losses due to fringing effect can be avoided through putting the windings as far as possible from the air gap. The skin effect can be modeled as reducing the effective cross section area of the wires. Depth of skin effect in a round wire is approximately equal to

$$\delta = \sqrt{\frac{\rho}{\pi f \mu}} \tag{3.1}$$

where ρ and μ are resistivity and absolute magnetic permeability of the conductor, respectively. It should be noted that Litz wire is commonly used for transformer and inductor windings to reduce the impact of skin effect, but it does not fully eliminate its impact. Therefore, the impact of skin effect can be added to calculation even if Litz wire is used, to increase accuracy of the model. Resistance of the windings will change when large currents pass through them and their temperature increases, but considering this change needs information about thermal characteristics of the windings and depends on several other parameters. In order to simplify the model, the resistance is considered constant. The conduction losses in the windings is calculated from

$$P_{cond-k} = \sum_{k=1}^{n} (R_{Lk} + R_{Tk}) I_k^2 \tag{3.2}$$

where R_{Lk} and R_{Tk} are resistances of inductor and transformer windings of port k, respectively. I_k is the effective current of port k.

Similar to design procedure of the transformer and the inductors, several MOSFETs may satisfy the minimum voltage and current requirements. In order to choose one, performance of the converter will be with all of them and the best one can be chosen. On-state resistance of the MOSFET is specified in their datasheet for different gate to source voltages, junction temperatures and drain to source currents. A simple option is to consider the on-state resistance for nominal current and at a high but safe temperature. In order to increase accuracy, changes due to temperature can be linearized using the curves given in datasheets. Changes due to power current may be linearized, too, or simply ignored. The junction temperature can be approximated based on a first approximation of conduction losses in the channel and thermal junction-to-ambient resistance.

It should be noted that body diodes of the MOSFETs might conduct, in addition to the channel, during reverse conduction periods. This would change the conduction losses in the switches. Figure 3.1 shows this situation, where the channel is modeled as a resistor and the body diode is modeled as a resistor in series with a voltage source. The turn-on condition of the diode in this model would be

$$R_{DS}I > V_f \tag{3.3}$$

where, I is the instantaneous current in the switch, R_{DS} is the on-resistance of the drain-source channel, and R_d and V_f are the dynamic resistance and forward voltage drop of the body diode, respectively (characteristics of the body diode is usually given in a curve in the datasheet). If the condition is true, then

$$I_d = \frac{(I - I_d)R_{DS} - V_f}{R_d} \tag{3.4}$$

and the total conduction losses in the switch would be

$$V_f I_{d-mean} + R_d I_{d-RMS}^2 + R_{DS}(I - I_d)_{RMS}^2 \tag{3.5}$$

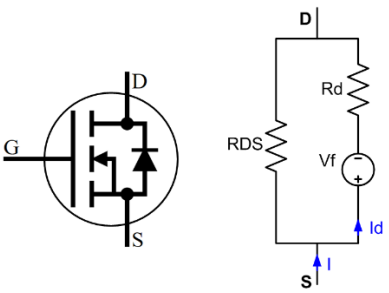

Figure 3.1: Current sharing between channel and body diode of a mosfet during reverse conduction

The last parameter to be determined is the effective value of the currents. The currents can be approximated using first harmonic analysis in ExEquation (2.17) from previous chapter. A more accurate prediction of the currents can be achieved through square-wave analysis, however, it will be too complex in case of a MAB converter. One solution, in software environments such as MATLAB, is to use an array to store active bridge output voltage for one period. Using the star-to-delta transform on the MAB converter, it is possible to determine currents of each port as vectors.

3.1.2. Magnetic core losses

The iron losses in ferrite cores include hysteresis and eddy losses. These losses are usually predicted using formulas based on experimental measurements and curve fitting. iGSE is a method that is commonly used for prediction of losses when the voltages across the windings are not sinusoidal, as in MAB converters. Core losses in iGSE are determined via

$$P_{core} = k{B_{max}}^{b-a} f \int_0^{\frac{1}{f}} \left| {dB}/{dt} \right|^a dt \tag{3.6}$$

as a function of magnetic flux density, B, which itself can be determined from the voltage across the winding. k, a and b are derived from Steinmetz coefficients for the corresponding core material. Magnetic flux density is calculated from

$$B = \frac{\int V(t)dt}{NS} \tag{3.7}$$

where $V(t)$ is the voltage across the windings on the core, N is number of turns and S is cross section area of the core. B_{max} in Equation (3.6) is equal to

$$B_{max} = \frac{1}{2NS} \int_0^{\frac{1}{2f}} V(t)dt \tag{3.8}$$

and Equation (3.7) gives

$$\left| {dB}/{dt} \right| = \left| \frac{V(t)}{NS} \right| \tag{3.9}$$

Equations (3.6), (3.8) and (3.9) can give an approximation of the losses in transformer and inductor windings. Integration of voltages across the windings is needed to be able to evaluate the losses expressed in Equation (3.6). Similar to the case of effective currents, first harmonic analysis can give an approximation of these voltages. Accuracy of predictions based on first harmonic analysis can be very bad, because the shape of the voltages are different from first

harmonic sinusoidal curves, especially in case of the inductors. Hence, it is better to use square-wave analysis, and the array calculation as explained in case of effective currents.

3.1.3. Switching losses

Switching losses in MAB converters are usually negligible, due to soft switching operation of the converter. However, if DC link voltage variations on some ports are too large or the power transfer is too small, hard switching might occur. Hard switching losses can be considerable depending on operating condition of the MAB and characteristics of the switches. This section will study the switching losses of MABs in detail. Soft switching in MABs generally involves zero voltage switching (ZVS). Soft switching happens when drain-source voltage of a switch decreases to a value close to zero before the switch turns on. It decreases turn-off losses, or more specifically body diode reverse recovery losses, too.

Soft switching:

Figure 3.2 illustrates switching instance of an active bridge in a MAB in details. The model shown in this figure is used for studying switching losses during the short switching period. The transformer voltage can be modeled as a constant DC voltage source in series with the inductance, but it is not shown in the model because it does not have an impact on the following analysis of switching process. Each switch is modeled as a parallel connection of an ideal switch (the conducting channel), its output capacitance, and the body diode. Figure 3.3 shows how voltages and currents of the channels, capacitors and diodes evolve during soft switching. The switching sequence is very short compared to the switching period. Therefore, the inductor is regarded as a constant current source. After the turn-off command for S2 and S3 has arrived (the turn-off delays are ignored), the current flows into capacitors, charging C2 and C3, while discharging C1 and C4 (Figure 3.2-b). This will continue until the voltages across C1 and C4 drop, and D1 and D4 start conducting (Figure 3.2-c). The diodes will conduct the whole current until the turn-on command for S1 and S4 arrives at the end of the dead time. When the turn-on command arrives, channels of S1 and S4 start conducting. Since the voltage across the channel is very small at that moment, the turn-on losses will be very small. Depending on the condition expressed in Equation (3.3), diodes might stop conducting or might still conduct a portion of the current. The only losses involved in the switching are the reverse recovery losses of the diodes, which will occur if the diodes stop conducting. However, the blocked voltage across the diodes would be too small and the reverse recovery losses are negligible.

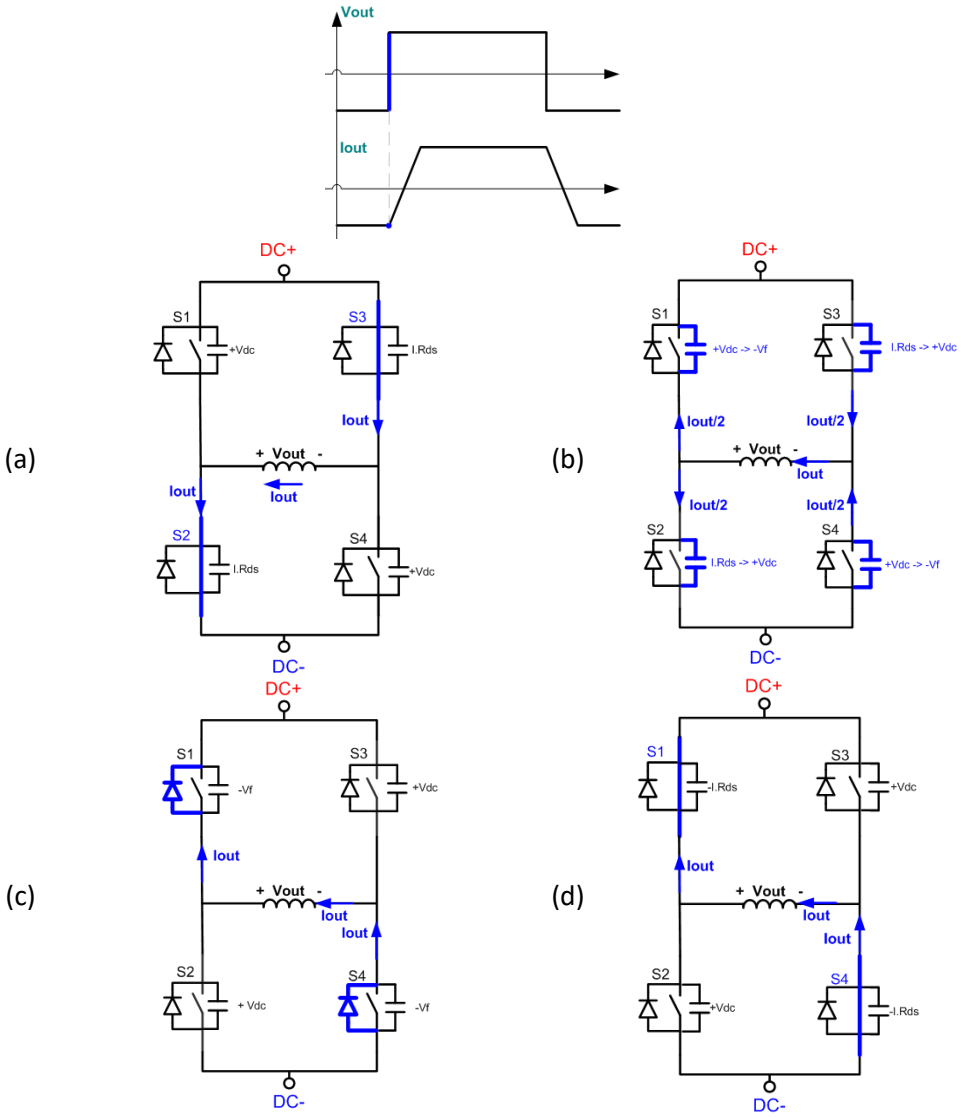

Figure 3.2: Soft switching in an active bridge; the switching process is divided into four steps of a, b, c and d.

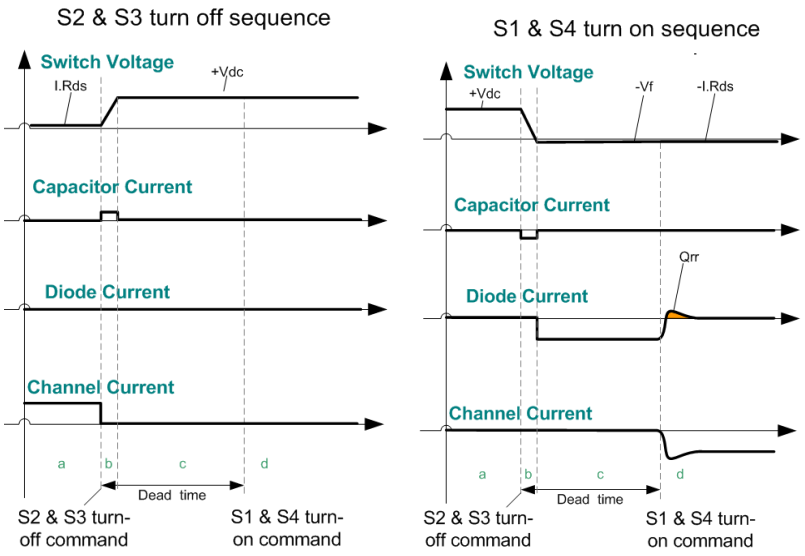

Figure 3.3: Voltages and currents during soft switching; the four steps of a, b, c and d in Figure 3.2 are illustrated here.

Hard switching:

Certain operating conditions, such as large DC link voltage variation, can lead to hard switching. Figure 3.4 shows the hard switching sequence in an active bridge. Details of voltages and currents are illustrated in Figure 3.5. It should be noted that reverse recovery current of D2 and D3, and charging current of C2 and C3 (shown as I_c in Figure 3.4-c) pass through channels of S1 and S4. However, I_c is not displayed in Figure 3.5 for the sake of simplicity.

As illustrated in Figure 3.4 and Figure 3.5, the switching losses can be divided into two parts: turn-off losses, that mainly include reverse recovery losses of two body diodes; and turn-on losses, that is mainly the energy stored in two output capacitors dissipated in the channels (Figure 3.4-c). Therefore, the hard switching losses are

$$P_{swiching} = 4f\left(V_{dc}Q_{rr}\frac{I_{out}}{I_{spec}} + \frac{1}{2}C_{oss}V_{dc}^2\right) \tag{3.10}$$

where, C_{oss} is the output capacitance of the switch, and I_{spec} is the diode current at which, the Q_{rr} value is given in the datasheet. One switching cycle has two voltage transitions, each involving losses in two switches, hence, the $4f$ coefficient.

Based on what has been discussed on soft switching so far, two situations can be determined as when soft switching does not occur:

1) If output current of the active bridge is not negative during negative-to-positive output voltage transient (Figure 3.4). This involves the hard switching losses of Equation (3.10).
2) If the dead time is too short and turn-on command arrives before the capacitors are fully discharged; i.e., the step "d" in Figure 3.2 starts in the middle of step "b". In this case, a portion of the capacitor energy will be dissipated in the channels as the turn-on loss. Turn-off losses will be negligible. The losses can be determined using linear approximation for voltages, currents and delays, with coefficient of $t_{deadtime}/t_{discharge}$, where, $t_{deadtime}$ is the dead time applied to switching signals and $t_{discharge}$ is the time needed to fully discharge the capacitors with the current at the time of switching, as

$$t_{discharge} = \frac{2C_{oss}V_{dc}}{I_{out}} \tag{3.11}$$

The losses in this condition will be

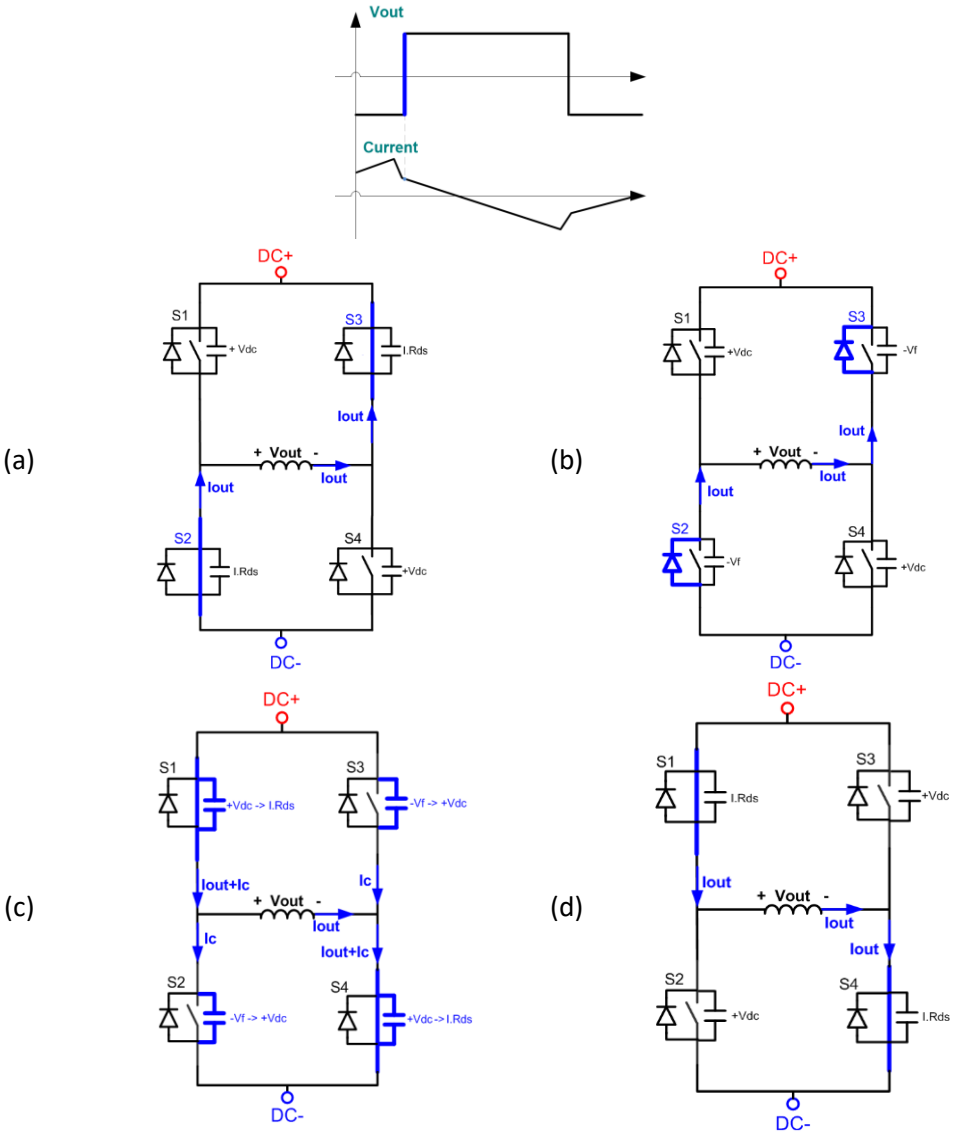

Figure 3.4: Hard switching in an active bridge; the switching process is divided into four steps of a, b, c and d.

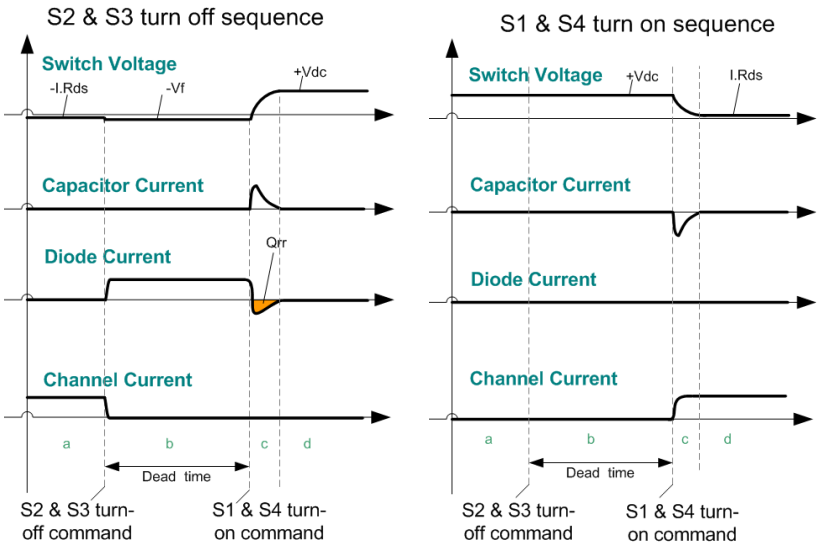

Figure 3.5: Voltages and currents during hard switching; the four steps of a, b, c and d in Figure 3.4 are illustrated here.

$$4f\left(\frac{1}{2}C_{oss}V_{sw}^2\right) \tag{3.12}$$

where

$$V_{sw} = V_{dc}\left(1 - \frac{t_{deadtime}}{t_{discharge}}\right). \tag{3.13}$$

Soft switching condition:

Based on Figure 3.2, the condition for soft switching can be expressed as "instantaneous current of the active bridge must be negative during negative to positive transient of its output voltage" which is true when the current is lagging or inductive. The inductances, as absorbents of reactive power, are the reason for inductive current on all active bridges and help in keeping this soft switching conditions. As discussed before, unequal DC link voltages can lead to reactive power exchange between the active bridges. If the difference between the DC link voltages is too large, the exchanged reactive power will increase so much that the current of the active bridge with smaller DC link voltage turns capacitive. This active bridge will lose soft switching condition in this situation and have hard switching, while the active bridges with higher DC link voltage will still have soft switching conditions, regardless of active power-flow direction, as shown in Figure 3.6 for a DAB. Despite unequal voltages, soft switching condition might hold true if the power transfer is large enough. Certain voltage modulations (section 2.4.2) can prevent hard switching, even at low powers. In any situation, the model of losses needs to know instantaneous currents and voltages to be able to evaluate soft switching conditions and switching losses. Similar to conduction and core losses, an array of instantaneous voltage and current values is a good way to determine the switching conditions and losses.

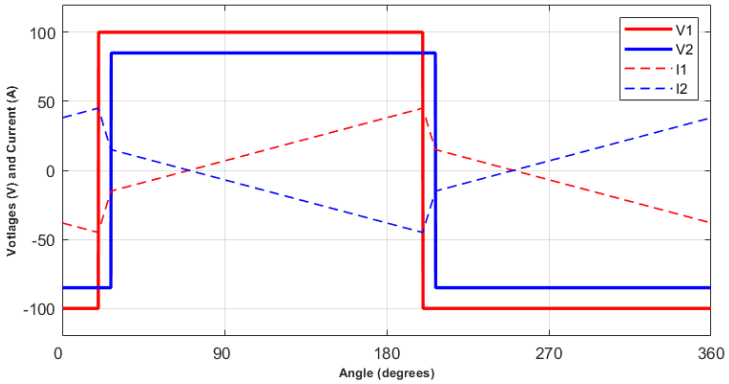

Figure 3.6: Hard switching in the active bridge due to different DC link voltages.

Energy-related and time-related output capacitance:

An important parameter in determining switching conditions and losses is the output capacitance of the MOSFETs. This value is indicated in datasheets for a specific drain-to-source voltage because it changes with the voltage. The reason is that physical characteristics of the channel change with drain-to-source voltage. Since this capacitance is not constant when charging and discharging, using a constant value specified in the datasheet or determined from $C_{oss}(V_{DS})$ curve will not give the correct charge/discharge time and its stored energy. The total stored energy that is dissipated during hard switching, previously determined in Equations (3.10) and (3.12), is in fact equal to the following integration

$$\frac{1}{2}C_{oss-E}(V) \times V^2 = \int_V^0 C_{oss}(v)\, v dv \tag{3.14}$$

where $C_{oss}(V)$ is the capacitance from $C_{oss}(V_{DS})$ curve. The $C_{oss-E}(V)$ capacitance is not a real capacitor, but a constant equivalent capacitance that gives the dissipated energy if the output capacitance is discharged from V to zero. For the same reason, the capacitance that corresponds to charge/discharge time, and was used in Equation (3.11) needs to be determined accurately in a similar way. The time needed for discharge can be determined from

$$t_{discharge} = \frac{C_{oss-t}V_{DC}}{I_{out}} = \int_{V_{DC}}^0 \frac{C_{oss}(V_{DS})}{I_{out}} dV_{DS} \tag{3.15}$$

where C_{oss-t} is not a real capacitor, but a constant equivalent capacitance whose discharge time is equal to the time needed to discharge the output capacitance from V_{DC} to zero. Similarly, the linearization used to reach Equation (3.13) can be calculated more accurately using this integration. These values can be determined by calculating the integrations in Equations (3.14) and (3.15) from the $C_{oss} - V_{DS}$ curve, or a piecewise function. Some datasheets specify C_{oss-E} and C_{oss-t}, but they are calculated for a specific voltage and current.

Enhanced calculation switching:

In the beginning of analyzing the switching processes, the inductor was modeled as a constant current source. This assumption could be far from reality, depending on several parameters, such as size of the inductances, switching frequency and length of the dead time. It should be noted that if the switching frequency was 40 kHz, a 200 ns dead time would be equivalent to 2.88 degrees of a switching cycle, which can be a considerable value compared to the phase shift in cases of low power transfer. Therefore, the changes of current during the

dead time can be comparable to its overall change and its amplitude. It means that the soft switching condition that was stated previously might not always be accurate enough. It was observed in experiments that sometimes the current at the negative to positive voltage switching moment is negative, but the measured losses are significantly higher than expected. A closer study showed that this difference can be linked to switching losses as a results of variation of the current during the dead time. In those cases, the current is negative when turn-off command of S2 and S3 arrives, but turns positive at the end of the dead time when S1 and S4 turn on. In order to enhance the ability of the model to predict switching mode and its corresponding losses, two parameters were defined. The first parameter is the charge required for total discharge of the output capacitances from DC link voltage, as

$$Q_1 = \int_{V_{DC}}^{0} C_{oss}(v)\, dv \tag{3.16}$$

and the second parameter is the net amount of charge that goes to the output capacitances as a result of the current flowing during the dead time, as

$$Q_2 = \frac{I_{start} + I_{end}}{2} t_{dead} \tag{3.17}$$

where I_{start} and I_{end} are the current in the beginning and end of the dead time. It must be mentioned that Q_1 is a negative value, while Q_2 can be negative or positive. Different switching modes can be defined based on the comparison between these two parameters:

1. $Q_2 < Q_1 < 0$: The net charge is enough to fully discharge the output capacitors, soft switching conditions apply and switching losses are negligible (Figure 3.2).
2. $Q_1 < Q_2 < 0$: The current cannot totally discharge the capacitors, but it will reduce their voltages. In this case, voltages of the middle points of the capacitors (or the ends of the inductor) vary between zero and DC link voltage. Therefore, the diodes will remain in blocking mode. The switching losses are equivalent to the energy stored in C1 and C4 that will dissipate in their corresponding MOSFET channels on turn-on.
3. $0 < Q_2$: The voltage across C1 and C4 will remain at V_{DC} level and the current is positive, therefore the D2 and D3 diodes conduct the current (as in Figure 3.3-b). The turn-on losses, including the equivalent energy stored in the output capacitors plus reverse recovery losses of D2 and D3, can be determined from Equation (3.10).

Although more accurate than the initial model, this model still misses some details, e.g., when current sign changes from positive to negative, Q2 will be different from Equation (3.17). Determining evolution of the current during the dead time and reverse recovery losses in diodes are the other complex parts of the switching process that were simplified in this model.

Predictions of the two models proposed in this section will be compared against measured losses in the next chapter. It should be noted that this work focuses on application of MAB converters in a cluster, which means they will operate at high powers where soft switching is assured. In this regard, further analysis of the switching process and its corresponding losses is out of scope of this work.

3.2. Computational-cost efficient model of losses

Optimization in power electronic converters corresponds to various aspects, such as sizing magnetic components and semiconductors, thermal analysis, cooling system design, and switching modulations. These optimizations are performed through different approaches. The first approach is to determine the optimization goal as a function of input parameters and find the optimum using mathematical analysis. As systems are getting more and more complex, this approach is not always possible, i.e., it is not possible to determine a closed form solutions that gives the optimum point in big and complex systems. Numerical approaches, such as finite element analysis in thermal design, are able to find the optimum point whenever the analytical approach fails. The main drawback of numerical approaches is that they require large memory and processing resources and take a long time to find the optimum point. It means that numerical approaches are not the proper solution in real-time optimization and online control.

In cases where analytical and numerical approaches are not an appropriate choice for optimization, reduced order models (ROM) can be helpful. With the current trend of emerging more and more complex architectures in power electronics, ROM is becoming more relevant and useful in both academic and industrial applications [81]–[83]. Reference [81]presents a ROM of and induction generator for fixed speed wind turbines. This model can be used in design and control of the generators. A ROM of modular multilevel converters (MMC) is presented in [82]. MMC is a clear example of large power electronic systems where ROM can be a handy tool. Reference [83] studies a ROM for a network of arbitrary number of parallel single-phase converters. Considering the internal phenomenon of each converter and the possible dynamic interactions between the converters, the state and solution spaces are large. Therefore, analytical and numerical approaches will not be appropriate for optimization. The

ROM in [83] can be useful in dynamic analysis and control of parallel converters. The goal of this section is to propose a ROM for MAB converters that can be used for control and optimization purposes, including optimal power flow in a cluster of MAB converters and internal control of a single converter (published in [84]). It should be mentioned that this model ignores switching losses and assumes that the control system is able to maintain soft switching conditions on every operating point. Moreover, all the DC link voltages are considered equal (all transferred into primary side of the transformer) and constant at their nominal values.

Similar to the detailed model of losses that was presented in the first part of this chapter, the ROM in this section is a series of mathematical calculations. It gives an estimation of the losses in a MAB converter based on its design parameters, such as winding resistances, size of magnetic cores and dc link voltages, as well as operating point, i.e., phase shift between switchings of active bridges.

3.2.1. Conduction losses

Conduction losses have a direct relationship with resistance of the transformer and inductor windings. As explained before, these resistances can be analytically calculated based on the length and cross section area of the wires, and geometric parameters such as core size and winding fitting coefficients. Additional losses due to skin effect and eddy losses (because of proximity effect) must be included, but doing so will add to complexity and computational cost of the ROM. In this regard, it is assumed that resistances of the windings are measured using an impedance analyzer at the switching frequency. On-state resistance of mosfet channels vary with operating conditions, too, but these variations are usually negligible compared to winding resistances. Hence, datasheet value of on-state resistance of the channels at designed gate-source voltage, nominal current and 100 °C junction temperature is used in the model. Considering these assumptions, determining effective current magnitudes will be enough for prediction of conduction losses.

Voltage and currents of a sample switching of active bridges in a QAB is shown in Figure 3.7. It can be considered as a general set of voltage/current waveforms of a QAB converter. The phase shifts, from the smallest to the largest, are φ_1, φ_2, φ_3 and φ_4, respectively. Based on Figure 3.7, currents can be approximated as trapezoidal waveforms. The two currents that correspond to the smallest and the largest phase shifts have the same general shape (i1 and i4 in Figure 3.7, respectively) and their trapezoidal approximation is shown in Figure 3.8. In order to determine effective values of i_1 and i_4, their maximum value is needed. This value can be determined from

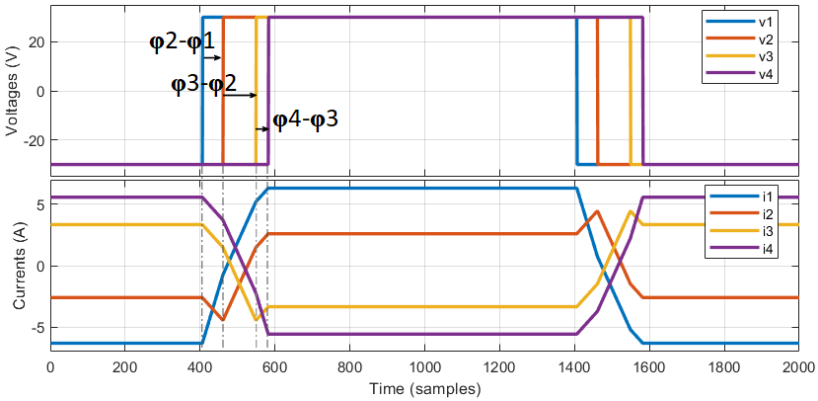

Figure 3.7: General voltage and current waveforms of a quad active-bridge converter. Each switching cycle has 2000 sampling points (horizontal axis).

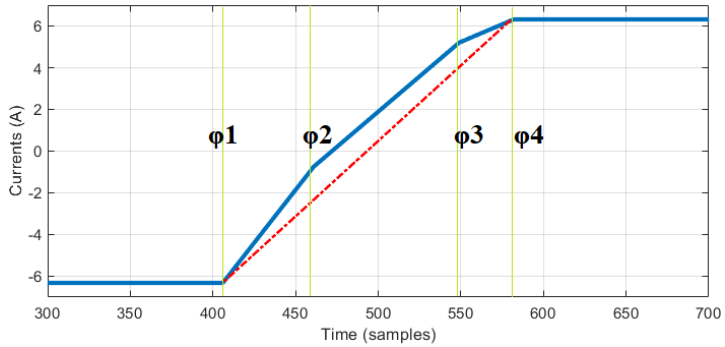

Figure 3.8: Approximated waveform (red) of the current i_1 (blue) in Figure 3.7. Similar approximation applies to current i_4. Vertical light green lines indicate phase shifts.

$$i_{Lk} = \frac{1}{L}\int v_{Lk}\,dt \tag{3.18}$$

where, v_{Lk} is the voltage across the inductor connected to the port k. Approximation of inductor voltage integration will be presented later. Knowing the maximum value of a trapezoidal waveform similar to the red waveform in Figure 3.8, its effective value can be determined from

$$I_M\sqrt{\frac{1}{\pi}\left(\pi - \frac{4}{3}\varphi\right)} \tag{3.19}$$

where, I_M is the maximum value of the current, and φ is the length of the period where the current rises or falls, in radians. In case of Figure 3.8, $\varphi = \varphi_4 - \varphi_1$.

The shape of the currents that correspond to the second and the third phase shifts, i_2 and i_3, is different from i_1 and i_4. It is still possible to approximate their shape with a trapezoidal waveform, but with a slightly different approach and larger error. Figure 3.9 displays three possible trapezoidal approximations of i_2. Similar approximations are possible for i_3. The effective current values resulted from these approximations were compared to effective value

of the original waveform for different sets of phase shifts. The results showed that the approximation illustrated in green dotted line has maximum -3% error, while the dark blue and light blue had +30% and ±8% maximum errors, respectively. The maximum value of the approximation in green dotted line in Figure 3.9 can be determined from inductor voltages. Knowing the maximums, their effective value can be determined using Equation (3.19).

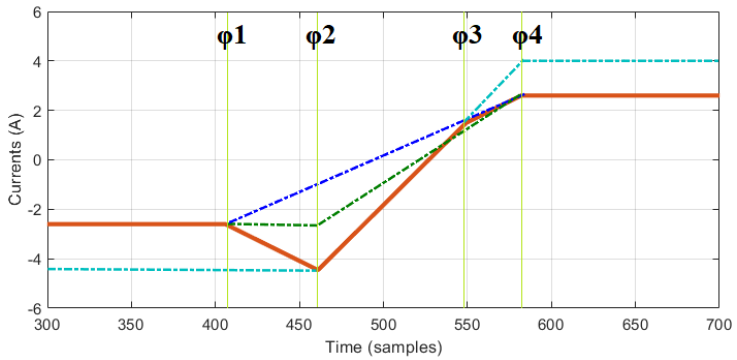

Figure 3.9: Trapezoidal approximations (dark blue, light blue and dark green) of the i_2 in Fig. 2 (red). Similar approximation applies to i_3.

The shape of inductor voltages, v_{Lk}, can be determined by subtracting the voltage across transformer windings, v_T, from output voltages of the active bridges. Figure 3.10 shows the general shape of transformer and inductor voltages. As shown in this figure, inductor voltages have steps with amplitudes of ±1.50, ±1 and ±0.5 times the DC link voltage, depending on their phase shift. Width of these steps is equivalent to phase shifts indicated in Figure 3.7. Integration of inductor voltages over half a cycle can be calculated from Equations (3.20) to (3.23).

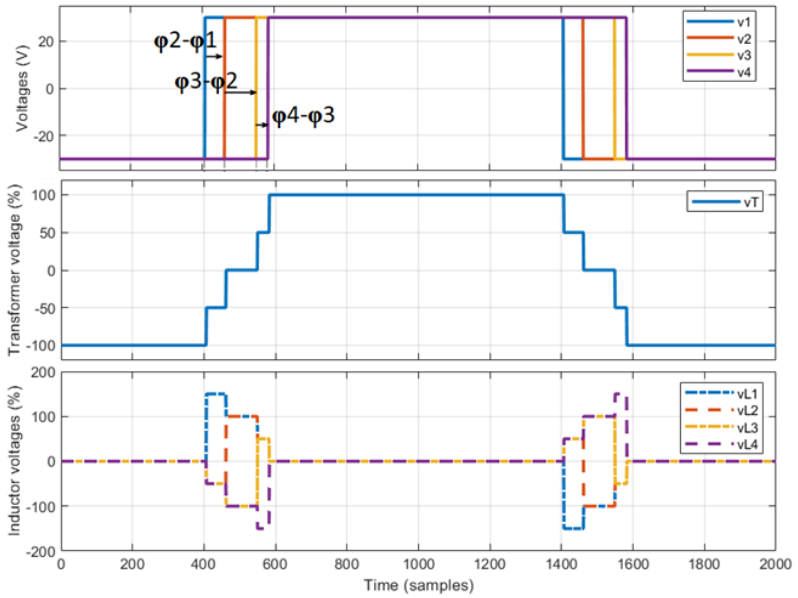

Figure 3.10: The voltages across the transformer and inductor windings, corresponding to the operating point illustrated in Figure 3.7. Voltage units are percentage of active bridge dc link voltages.

$$\int_0^{\frac{1}{2f}} v_{L1}(t)dt = (1.5(\varphi_2 - \varphi_1) + (\varphi_3 - \varphi_2) + 0.5(\varphi_4 - \varphi_3))V_{DC} \tag{3.20}$$

$$\int_0^{\frac{1}{2f}} v_{L2}(t)dt = (-0.5(\varphi_2 - \varphi_1) + (\varphi_3 - \varphi_2) + 0.5(\varphi_4 - \varphi_3))V_{DC} \tag{3.21}$$

$$\int_0^{\frac{1}{2f}} v_{L3}(t)dt = (0.5(\varphi_2 - \varphi_1) + (\varphi_3 - \varphi_2) - 0.5(\varphi_4 - \varphi_3))V_{DC} \tag{3.22}$$

$$\int_0^{\frac{1}{2f}} v_{L4}(t)dt = (0.5(\varphi_2 - \varphi_1) + (\varphi_3 - \varphi_2) + 1.5(\varphi_4 - \varphi_3))V_{DC} \tag{3.23}$$

Based on Equation (3.18), maximum value of currents can be predicted as

$$\frac{1}{2L}\int_0^{\frac{1}{2f}} V_L(t)dt \tag{3.24}$$

or expressed based on Equations (3.20) to (3.23) as the following matrix

$$I_M = \begin{bmatrix} I_{M1} \\ I_{M2} \\ I_{M3} \\ I_{M4} \end{bmatrix} = \frac{V_{dc}}{8L\pi f}\begin{bmatrix} -3 & 1 & 1 & 1 \\ 1 & -3 & 1 & 1 \\ -1 & -1 & 3 & -1 \\ -1 & -1 & -1 & 3 \end{bmatrix} \times \begin{bmatrix} \varphi_1 \\ \varphi_2 \\ \varphi_3 \\ \varphi_4 \end{bmatrix} \tag{3.25}$$

Effective currents can now be determined as a matrix, I_{RMS}, using Equations (3.19) and (3.25) as

$$I_{RMS} = I_M \sqrt{\frac{1}{\pi}(\pi - \frac{4}{3}\begin{bmatrix} -1 & 0 & 0 & 1 \\ 0 & -1 & 0 & 1 \\ -1 & 0 & 1 & 0 \\ -1 & 0 & 0 & 1 \end{bmatrix} \times \begin{bmatrix} \varphi_1 \\ \varphi_2 \\ \varphi_3 \\ \varphi_4 \end{bmatrix})} \tag{3.26}$$

where the matrix of coefficients is determined based on the fact that the approximation in Figure 3.9 sets the φ in Equation (3.19) equal to $\varphi_4 - \varphi_2$ and $\varphi_3 - \varphi_1$ for calculation of i_2 and i_3, respectively.

Knowing the effective currents, measured resistances of windings and datasheet values of drain source channel on-state resistance, total conduction losses in a MAB converter can be predicted. A more accurate and practical way of measuring the resistances will be explained in the next chapter.

3.2.2. Magnetic core losses

Prediction of magnetic core losses was already explained and iGSE (Equation (3.6)) was proposed as a suitable method for this purpose. The two important terms in Equation (3.6) that should be evaluated are B_m, maximum flux density, and $\int_0^{\frac{1}{f}} \left| {dB}/{dt} \right|^a dt$. The magnetic flux density itself can be calculated from Equation (3.7). The approach to approximation of the two terms in Equation (3.6) is similar to the approach that was taken in previous section on prediction of effective currents. Maximum value of magnetic flux densities in inductor cores can be determined from Equation (3.8), and a coefficient matrix similar to the one in Equation (3.25) as

$$B_{LM} = \begin{bmatrix} B_{LM1} \\ B_{LM2} \\ B_{LM3} \\ B_{LM4} \end{bmatrix} = \frac{V_{dc}}{8NS\pi f} \begin{bmatrix} -3 & 1 & 1 & 1 \\ -1 & -1 & 1 & 1 \\ -1 & -1 & 1 & 1 \\ -1 & -1 & -1 & 3 \end{bmatrix} \times \begin{bmatrix} \varphi_1 \\ \varphi_2 \\ \varphi_3 \\ \varphi_4 \end{bmatrix} \tag{3.27}$$

The second term, $\int_0^{\frac{1}{f}} \left| {dB}/{dt} \right|^a dt$, can also be calculated from Figure 3.10. The relationship between the voltage across the windings and the magnetic flux density in Equation (3.7) gives

$$\left| {dB}/{dt} \right| = \left| \frac{V(t)}{NS} \right| \tag{3.28}$$

and the second term can be calculated from

$$\left(\frac{V_{dc-k}}{N_{Lk} S_{Lk}} \right)^a \frac{1}{2\pi f} \begin{bmatrix} -3 & 1 & 1 & 1 \\ -1 & -1 & 1 & 1 \\ -1 & -1 & 1 & 1 \\ -1 & -1 & -1 & 3 \end{bmatrix} \times \begin{bmatrix} \varphi_1 \\ \varphi_2 \\ \varphi_3 \\ \varphi_4 \end{bmatrix}. \tag{3.29}$$

Although the shape of the voltage across the transformer winding is different from that of the inductor windings, the same concept can still be employed to determine losses in the magnetic core of the transformer. Based on Figure 3.10. This figure shows that the transformer voltage has steps of 0, ±50% and ±100% DC link voltage. Maximum flux density is calculated as

$$B_{maxT} = \frac{V_{dc}}{8NS\pi f} (2\pi + \varphi_1 + \varphi_2 - \varphi_3 - \varphi_4) \tag{3.30}$$

and the second term as

$$\int_0^{\frac{1}{f}} \left|\frac{dB_T}{dt}\right|^a dt = \left(\frac{V_{dc}}{N_{1T}S_T}\right)^a \frac{2\pi + \varphi_1 + \varphi_2 - \varphi_3 - \varphi_4}{2\pi f} \tag{3.31}$$

3.2.3. Comparison with the detailed model

The ROM or computational cost efficient model of losses that was proposed in this section, does the same job as the detailed model of losses that was presented in section 3.1. They are both based on the same principles and are expected to give almost the same result. In order to make sure that the calculations and approximations of the ROM were correct, the two models were compared for different operating points of a QAB converter. The DC link voltages are 60, 120, 240 and 480 V with inductances of 4, 16, 64 and 256 µH. Switching frequency is 20 kHz and the power flows from the first two ports to the third and the fourth port. Figure 3.11 shows the results of the comparison as the phase shifts increase linearly. The horizontal axis shows the phase difference between the first and the last port.

Figure 3.11-a to c compare predictions of different types of losses by the two models when DC link voltages are at their nominal values. The comparisons prove that the ROM gives almost the same output as the detailed model and the approximations are not far from the correct values. Figure 3.11-d compares predictions of total losses by the two models with 5% increase in DC link voltage of the second port. As explained in section 3.1.3, DC link voltage variations lead to hard switching losses when the power transfer is low. Unlike the detailed model, the ROM does not consider switching losses. This is the reason for big difference between the outcomes of the two models for phase shifts below four degrees. The Purpose of these comparisons was to verify that the calculations based on the shapes of the voltage and current waveforms are not far from the calculations based on accurate circuit analysis. Verifying correct predictions of the models, however, requires comparing against experimental measurements on a real converter, which will be presented in the next chapter.

(a)

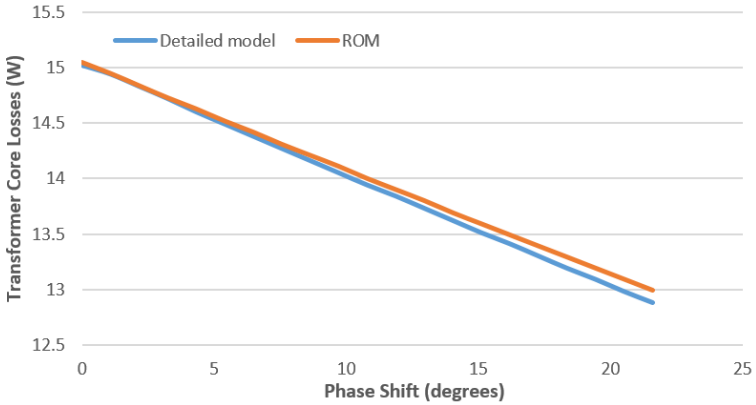

(b)

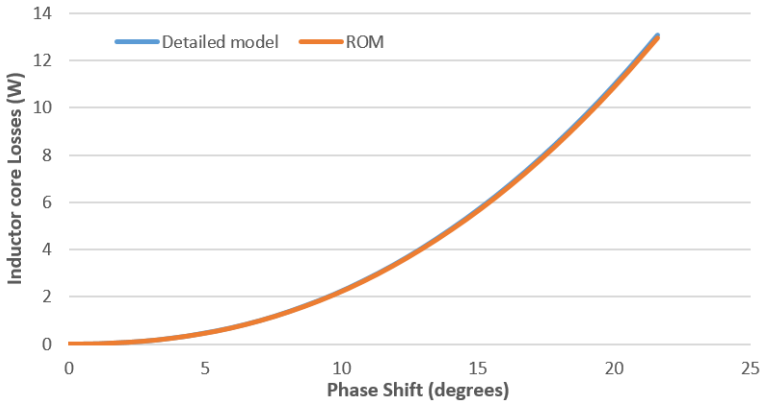

(c)

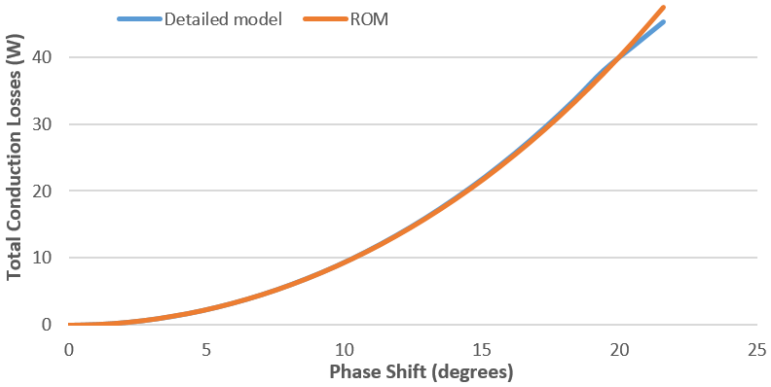

(d)

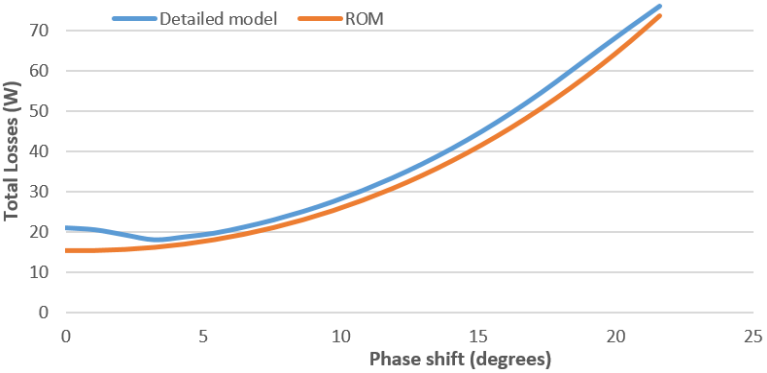

Figure 3.11: Comparing predictions of the ROM and the detailed model of losses in a QAB: (a) transformer core losses; (b) total inductor core losses; (c) total conduction losses; and (d) total losses when there is 5% voltage variation on one port.

The main goal of seeking a ROM was to be able to predict the losses quickly with simple calculations. In order to verify computational cost efficiency of the ROM, its runtime was compared with that of the detailed model. Both models were implemented in MATLAB environment of a PC. Each run of the detailed model took around 5.8 ms, while the ROM took around 85 μs to run. It shows that the ROM runs approximately 70 times faster than the detailed model. During the design procedure, computational cost is less important compared to accuracy of the optimal design, therefore, the detailed model is the proper candidate. For online control and optimization purposes, however, the time and processing power are limited and a ROM that can run fast without occupying the resources for a long time is the best option, although it might have low accuracy on certain operating points.

3.3. DC currents in windings and saturation of magnetic cores

A major challenge in operation of MAB converters is preventing saturation of magnetic cores. Saturation of the core occurs when the magnetic flux density exceeds a certain limit. In case of ferrite cores, this limit is commonly around 400 mT. This limit and the way to avoid it was explained in the design procedure in section 2.3 of previous chapter. If the design rules of section 2.3 is respected, the magnetic flux density should be limited to the value that is chosen as B_{max}. This design criterion limits amplitude of changes in the flux density. However, due to certain intrinsic behavior of MAB converters and non-ideal characteristics of some components, the balance between negative and positive duty cycles of voltages across the windings can be disturbed occasionally or continuously. The imbalance between positive and negative volt-seconds leads to a DC current in the windings and an offset in the magnetic flux density of the core. This offset is added to the changes of magnetic flux density and can lead to exceeding the saturation limit. This is displayed in Figure 3.12. Saturation of the core causes high currents and several types of failure in the converter. Therefore, avoiding core saturation is an important subject and many researches have tried to address this challenge. If the safety margin of B_{max} is wide, DC currents may not always result in core saturation but they increase the conduction losses in the windings and can lead to hard switching losses, too. This section studies the origins of DC currents in windings, how to measure them and how to avoid them.

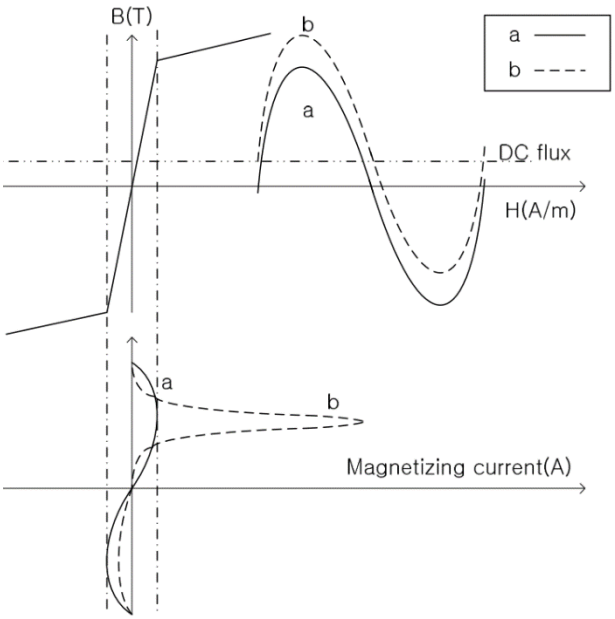

Figure 3.12: determining magnetizing current from B-H curve of a magnetic core when a sinusoidal voltage is applied to its winding (a) without any DC offset in the current, (b) with a DC offset in the current [85].

3.3.1. Origins

Duty cycle imbalance, or difference between duration of positive voltage and negative voltage, is the main reason for DC currents in transformer windings and saturation of its core. This imbalance is generally caused in two ways: changes in phase shifts and mismatch between turn-on or turn-off delays in switching. Figure 3.13 shows how a change in phase shift leads to a DC offset in the current of a TAB. In order to change phase shift of port 3 from φ to φ', duration of the period when its voltage (V3) is positive has been increase by Δt during one half cycle, where

$$\Delta t = \frac{2\pi(\varphi' - \varphi)}{f} \tag{3.32}$$

The increase in positive edge of V3 is to apply the change in phase shift and occurs only once, but results in a DC offset in the current equal to

$$\Delta I = \frac{\Delta t(V_{DC3} - V_{DC1})}{L_{13}} + \frac{\Delta t(V_{DC3} - V_{DC2})}{L_{23}} \tag{3.33}$$

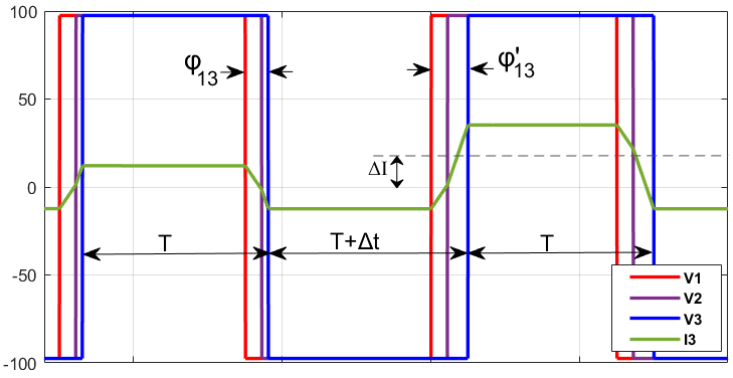

Figure 3.13: How a DC offset is generated in the current when phase shift changes. T is half of the switching period. The TAB has equal DC link voltages and inductances on every port.

Equation (3.33) is based on the MAB model with star-delta transform. It shows that the DC current offset is directly related to the magnitude of the change in the phase shift. There are different ways to apply changes in phase shifts and it depends on the algorithm that generates the switching signals. In case of the change displayed in Figure 3.13, one alternative is to increase duration of negative period of V3. This will lead to the same magnitude of DC current as expressed in Equation (3.33) but with opposite sign. Reducing duration of positive or negative edges of V1 and V2 are the other alternatives and all of them lead to generation of a DC offset in the current. It is worth noting that the change is phase shift of port 3 will lead to DC currents in windings of the other ports, too. The DC current offset of ports 1 and 2 are equal to the first and the second term of Equation (3.33). If these DC offsets of the currents are larger than their AC amplitude, the currents will constantly remain positive or negative, as illustrated in Figure 3.14. In this situation, soft switching conditions are lost and even if the core is not saturated, hard switching losses will have a significant impact on performance of the converter. The phase shift of port 3 is reduced from φ to φ', hence Δt has a negative value.

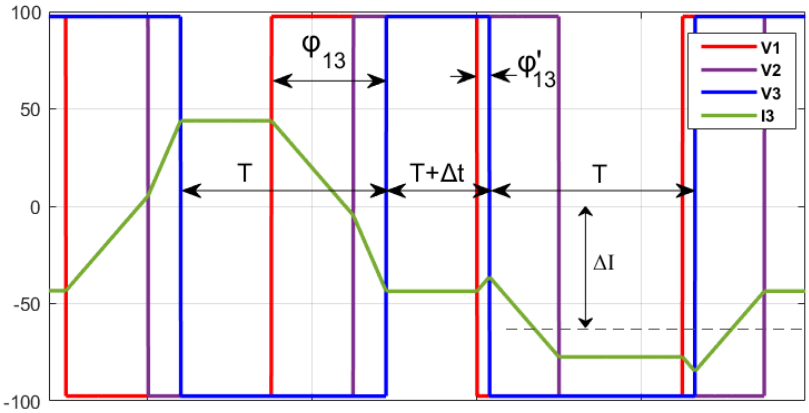

Figure 3.14: A large change in phase shift of port 3 leads to loosing ZVS on this port, as the current is always negative because of the large DC current offset. Since phase shift reduces in this example, Δt has a negative value.

The second source of DC current offset is mismatch between characteristics of certain components. Different delays in gate drive circuits, unmatched PCB design and different turn-on or turn-off delays in semiconductors can result in imbalance between positive and negative duty cycles of voltages of the active bridges [86]. A delay in turn-on of a switch does not have a significant impact on operation of the converter if soft switching conditions are true. The reason is that during turn-on, the current in the switches is negative and conducted by the body diodes. If one switch is turned on with a small delay, its body diode will conduct the current, probably with a slightly higher voltage drop. The turn-off process, on the other hand, will be significantly affected if one switch is turned-off with a delay. During turn-off of two diagonal switches, body diodes of the other two switches start conducting. Delayed turn-off of a switch will cause a short circuit on the output, in series with one of the body diodes. Oppositely, if soft switching conditions are not true, the turn-on process will be affected while the turn-off process will remain intact (assuming the delay is shorter than the dead time between switchings). An unsymmetrical short circuit in the output, even for a short time, means the integration of voltage across the windings will not be zero during a full cycle and a DC current offset will be generated in the windings.

Figure 3.15 shows an active bridge with the parasitic inductances around each switch, modeled as series inductors, Lp1 to Lp4. Each diagonal pair of these inductors conduct during half a cycle. Therefore, a mismatch between Lp1+Lp4 and Lp2+Lp3 will lead to unequal voltage drops in different half cycles, meaning that integration of the voltage on the windings will not be zero over a full cycle. Mismatch between resistance of channels or forward voltage drop of body diodes have the same consequences.

Discretization of the controller and PWM signal generator is another potential source of imbalance between positive and negative volt-seconds. The PWM signal generators generally use counters and comparators to synthesize the switching signals. Usually they have to round some values such as periods or arbitrary phase shifts. Sometimes this rounding can lead to imbalance. Unlike the imbalance cause by phase shift change, which happened occasionally, the imbalance caused by mismatch or discretization can exist for a long time. Therefore, the offset increases over time and even a very small imbalance can have a large cumulative impact on performance of the converter. The following sections study the possible ways to prevent DC currents in the windings.

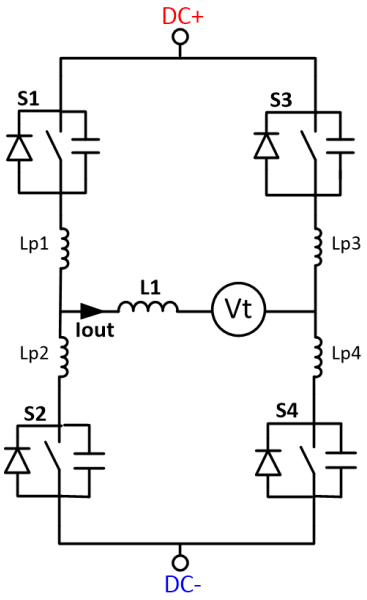

Figure 3.15: An active bridge with its parasitic inductances in series with each switch. Vt is the voltage across transformer windings.

3.3.2. Avoiding DC currents in windings

Several works have addressed the issue of DC currents in transformer windings [85], [87]–[90]. A passive solution that is sometimes used is to add a gap to the core. Application of gapped cores are common in flyback converters because the currents in the coupled inductors always include a DC offset [91]. Adding a small gap to magnetic cores does not increase the maximum safe swing of magnetic flux density because the relationship between magnetic flux density and integration of voltage (Equation (3.7)) does not change by adding an air gap. The relationship between magnetic flux density and a constant current flowing in the windings, on the other hand, will change as

$$B = \frac{\mu N I}{l} \tag{3.34}$$

because l, the magnetic length of the core, and μ, the magnetic permeability, change by adding an air gap. Therefore, a magnetic core that has a small air gap can tolerate a certain amount of DC current in its windings without saturation. Air gaps in transformer cores reduce magnetizing inductance, hence increasing magnetizing current and its resulting losses. It will increase the leakage inductance too, decreasing the coupling between the windings. The fringing effect of magnetic fields around the air gap can be a source of additional losses in the windings [92]. Altogether, these reasons are usually enough for avoiding application of gapped cores in transformers of MAB converters.

Series capacitors are another option for blocking flow of DC currents in the windings and preventing saturation in the cores. Application of series capacitors has its own limitations. Since the power current will be passing through the capacitors, their equivalent series resistance (ESR) add to the losses of the system and their AC impedance introduces a voltage drop. The major drawback of this solution is reliability issues of capacitors. Increasing footprint and cost of the converter are the other drawbacks.

Different solutions based on control signals have been proposed in the literature to avoid DC currents during phase shift changes. Some methods are based on instantaneous values of voltages and currents, therefore, require high-resolution PWM hardware [85]. A method is proposed in [93], which does not need any knowledge of voltages or currents, and is applicable to any PWM hardware. The method is based on applying phase shift change in two steps. In the two-step phase-shift change, 50% of the change is applied in positive half cycle of the voltage, and the other 50% is applied in the negative half cycle. Figure 3.16 shows the concept. Changing the phase shifts is done through prolongation of positive/negative voltage edges, similar to what has been explained in previous section. The prolongation (Δt) is determined from (3.32), as before, but it is divided by two equal parts. As shown in Figure 3.16, the two halves of Δt are applied in two consecutive half cycles. Therefore, a DC offset of $\frac{\Delta I}{2}$ (from Equation (3.33)) is generated in the first half cycle. This offset is immediately cancelled by the $-\frac{\Delta I}{2}$ DC offset, which will be generated in the next half cycle. Figure 3.17 shows that the two-step phase-shift change method works properly even in cases where DC link voltages and duty cycles have different values. Therefore, it can be concluded that applying phase-shift changes in two steps on two consecutive switching half cycles through prolongation/truncation of positive and negative voltage durations can effectively prevent generation of DC currents in the windings. Being an open-loop sensor-less method, which does not require additional hardware, makes this method an effective cost-efficient solution for avoiding DC current during power transients.

Although the two-step phase-shift change can effectively solve the problem with DC currents caused by change of phase shift, it cannot eliminate DC currents that are caused by mismatch between delays and parasitic components. To suppress those DC currents, an active cancelling approach has to be implemented. The first and main requirement of any active method that aims to suppress the DC currents due to mismatch, is instantaneous measurement of the DC current that is flowing in the windings. Since the mismatch and its resulting DC

currents are part of the non-ideal characteristics of the components, analytical prediction is not an option and closed-loop cancellation based on measurement is the effective approach to take. However, measuring the DC currents in the windings of MAB converters is a challenging task. The next sections will discuss measurement of the DC currents and active methods of cancelling them.

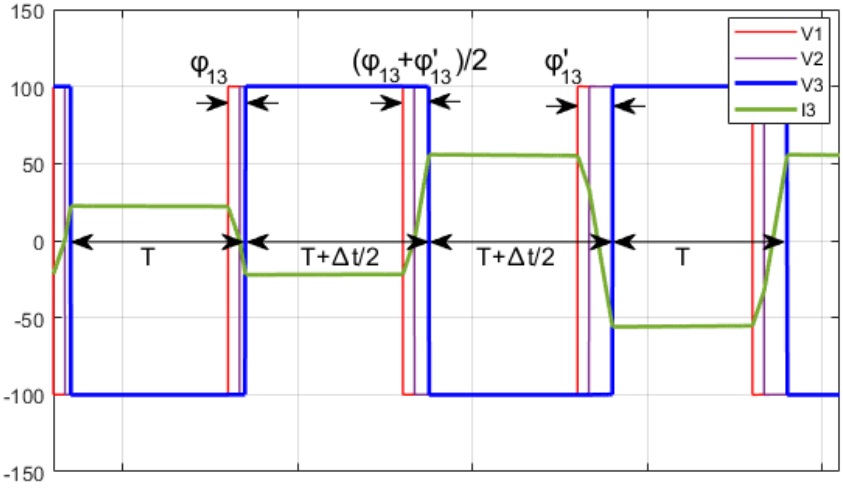

Figure 3.16: Applying phase-shift change in two steps causes no DC offset in the current. The phase shift change is applied to port 3 (V3).

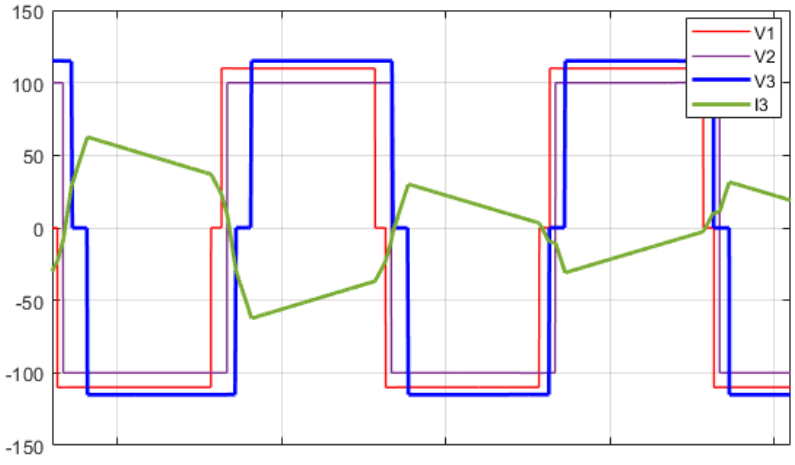

Figure 3.17: Performance of the two-step phase-shift change in a case with arbitrary DC link voltages and duty cycles.

3.3.3. Measurement challenges

The currents flowing through transformer windings of MAB converters have different triangular- and trapezoidal-like shapes, some of them illustrated in Figure 3.7. Measuring a small DC offset in a current waveform with these shapes that have high harmonic content is a challenging task. The first challenge involves measurement precision. The precision limit of commercial sensors is usually in the range of 0.2% to 0.5%. The current sensor must be chosen

based on the nominal AC current of each port, while magnitude of a DC offset that can cause saturation is much smaller. In other words, magnitude of the DC current is very small compared to the nominal measuring range and the accuracy of small DC current measurements will be poor.

The second challenge is filtering the large AC component to be able to measure the small DC component. Adding passive low-pass filter is a common solution, but it reduces the bandwidth and introduces latency, especially in this case where amplitude of the AC component can be significantly larger than that of the DC component. High bandwidth is an important requirement because delays in reacting to DC currents not only leads to saturation of the magnetic cores, large currents and additional losses, but can also affect operation of other control loops such as closed-loop control of power. Digital filters are the next candidate for cancelling the AC components. Using an analog-to-digital converter (ADC) hardware, consecutive measurements are stored and averaged over a period to determine the DC offset. Considering the switching frequency of MAB converters and number of samples per period that can effectively cancel the noise and the AC component, an ADC with sampling rate of several tens of mega Hertz is required. Most microcontrollers on the market have sampling rates of 1 or 2 Msamples/s, which means maximum 40 samples per period in case of a MAB with switching frequency of 50 kHz, which is not enough for cancelling the noise and the AC component through averaging.

There are methods in the literature that try to perform cancellation of the AC component or detect core saturation using magnetic circuits. Reference [94] proposes application of an additional magnetic core. As shown in Figure 3.18, the second core acts as a transformer in series with windings of the main transformer. A hall sensor is installed within a small air gap in this core. Since the AC components of magnetic flux of primary and secondary cancel each other, the sensor only measures the DC component in an ideal condition. Correct performance of the proposed method is validated in [94] for the resonant converter shown in Figure 3.18. The converter illustrated in Figure 3.18 has only two ports, the first one is the source and the second one is an uncontrolled half-bridge rectifier. Therefore, imbalance in switching of the primary can be considered as the source magnetizing current and the only origin of DC currents in the windings that can be corrected by applying proper control. In case of a bidirectional DAB, the additional transformer is able to detect any DC offsets in the current, but cannot specify whether it is caused by the primary or the secondary. Therefore, no correcting actions can be taken. In a MAB converter, similarly, this method requires series windings from every port and

has only one output, which can only detect existence of a DC current offset. Additional wiring and core size are the other challenges of this method.

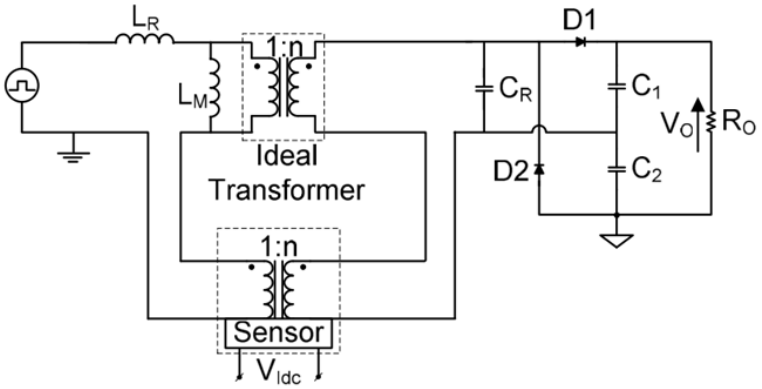

Figure 3.18: Application of an additional transformer in series with primary and secondary windings of a resonant converter to measure the DC current [94].

A “magnetic ear” is proposed in [95], which employs the saturation characteristics of magnetic cores. The setup is illustrated in Figure 3.19, with an auxiliary U magnetic core attached to the main core. Orthogonal placement of the auxiliary core is recommended to avoid disturbing the main magnetic flux inside the transformer core.

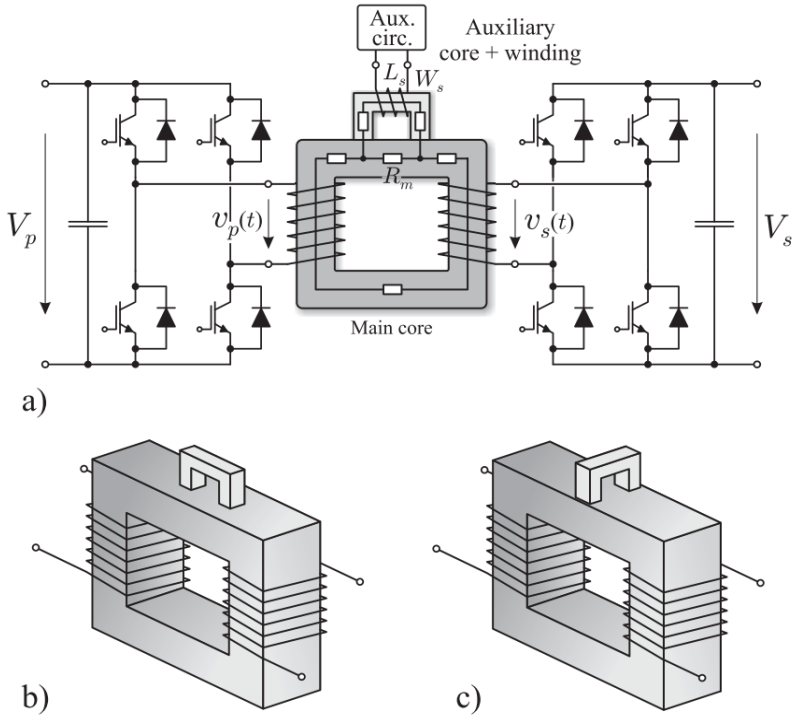

Figure 3.19: (a) the "magnetic ear" proposed in [95] to detect saturation of transformer magnetic cores. The axuilary core can be placed (b) in parallel or (c) orthogonal to the main magnetic flux.

If a DC current leads to saturation of the main core, its permeability will drop. Since the main core is part of the magnetic circuit of the auxiliary core, the reduction in its permeability leads to a decrease in inductance of Ls, the winding around the auxiliary core. This decrease is detected by the auxiliary circuit attached to the winding. There are other methods in the literature that use more or less the same concepts to detect saturation of the magnetic cores [96]–[99]. Similar to the previous method, it is not possible to detect the source of the DC current. Saturation of transformer magnetic core is still avoidable using these methods, through trying to generate a DC current offset in the opposite direction. This is possible through creating an intentional imbalance between duration of positive and negative voltage edges on one port. However, saturation of the core is not the only problem of having a DC current in the windings. Additional conduction losses and losing soft switching conditions are important issues that might occur, as well. In this regard, creating an intentional opposite DC offset to cancel the magnetic flux offset will solve the saturation issue but double the additional conduction losses and the probability of losing soft switching conditions. Knowing the active bridge that is the original source of imbalance, it becomes possible to cancel it and avoid saturation, additional losses and hard switching at the same time. The next section will propose a magnetic circuit that can effectively cancel AC component on current measurement point of each port.

3.3.4. A setup for fast and accurate sensing of DC current

An innovative setup was proposed and tested for fast and accurate measurement of a DC offset of a high-frequency AC current signal. The setup is based on creating a copy of the AC component, using a current transformer (CT) and pass it through the sensor in the opposite direction of the main current. The two opposite AC components will cancel each other and the sensor will only measure the DC component. As illustrated in Figure 3.20, this setup is based on a Hall effect sensor and a CT with ratio of 1:1. Due to Lenz's law, a copy of the AC component of the main current will flow in the secondary winding of the CT, which is short-circuited, but in the opposite direction.

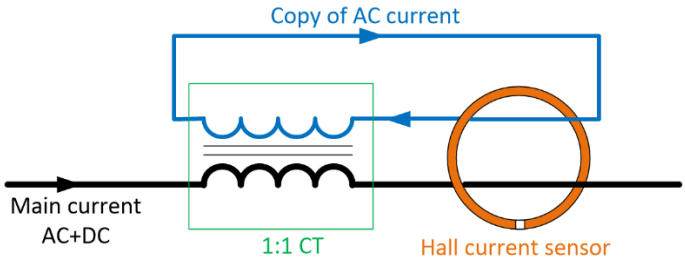

Figure 3.20: Measuring DC offset current using a current transformer and a Hall Effect current sensor.

Hall effect current sensors are able to measure both AC and DC currents. They measure the current based on Lorentz's force, acting on charges moving in a magnetic field [96]. This type of current sensors include a magnetic core, through which the conductor flowing the main current passes and generates a magnetic field. In the proposed setup, the secondary winding passes through the magnetic core of the Hall effect sensor as well as the main conductor. As the secondary winding and the main wire conduct equal AC currents but in reverse direction, their magnetic fields will cancel each other. Therefore, the Hall effect sensor will only sense the DC component of the current, flowing in the main conductor. It must be mentioned that the since the AC components are cancelled, the sensor can be chosen based on the amplitude of the DC component. For instance, the AC current amplitude can be 50 A, while measuring range of the sensor is 5 A because the DC current is expected to smaller than 5A. Therefore, it can be concluded that the proposed setup can solve the challenges of precision and AC filtering together.

Implementation and experimental measurements:

The proposed setup was built and tested to verify correct operation and assess its performance regarding cancellation and bandwidth of the output. Figure 3.21 shows the setup that was built with a flat EE core and a one-turn CT.

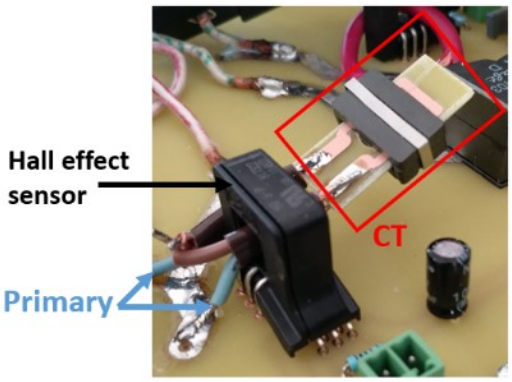

Figure 3.21: The proposed setup for measuring DC current, including a CT and a Hall effect sensor.

The sensor was tested using a DAB converter. Figure 3.22 shows the output of the Hall effect sensor (the green waveforms) in similar situation, with and without AC cancellation. It shows that peak-to-peak amplitude of the AC component in the output of the Hall effect sensor is reduced from 240 mV to around 45 mV.

(a)

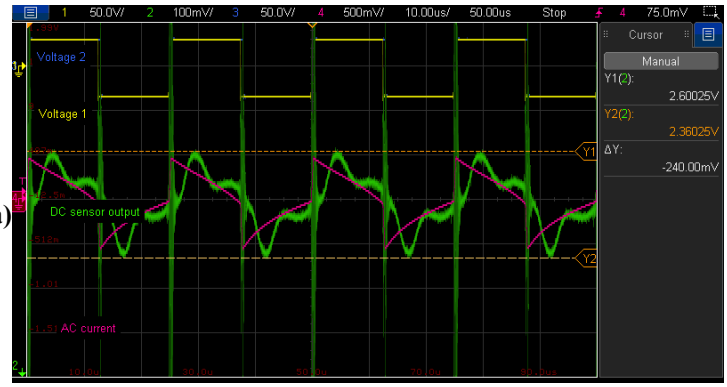

(b)

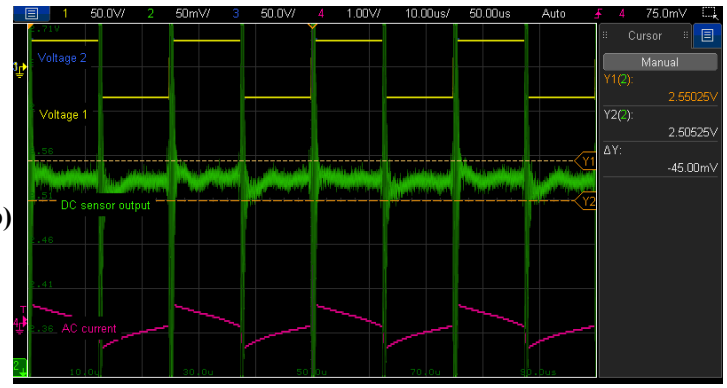

Figure 3.22: Evaluation cancellation of AC component of the current in steady state: (a) no AC cancellation; (b) with AC cancellation. Channels 1and 3 (yellow and blue) indicate the active bridge voltages of the DAB. Channel 2 (green) is the output of the Hall effect sensor. Channel 4 (pink) is the output of a clamp AC current sensor.

After validation the AC cancellation, a dynamic test was performed in order to assess dynamic performance of the proposed DC current measurement setup. To do this, a step change in phase shift was applied to the DAB, leading to a damping DC current. The result shows that the transient DC current is detected by the sensor. Figure 3.23 shows that amplitude of the transient DC current is comparable to amplitude of attenuated AC component, confirming acceptable performance of the proposed AC cancellation method.

(a)

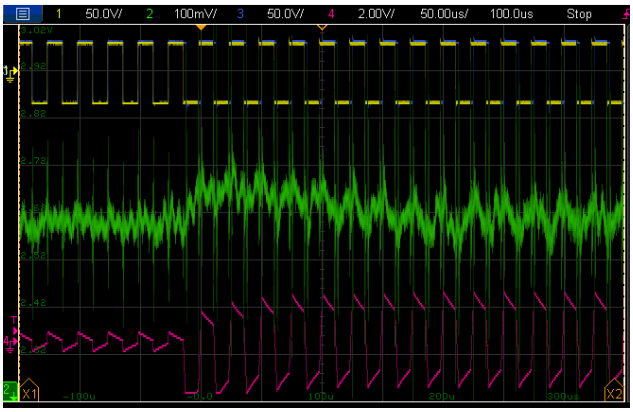

Figure 3.23: Evaluating performance of proposed DC current measurement setup during a power transient. Channels 1and 3 (yellow and blue) indicate the active bridge voltages of the DAB. Channel 2 (green) is the output of the Hall effect sensor. Channel 4 (pink) is the output of a clamp AC current sensor.

Further analysis:

Performance of the AC cancellation is significantly affected by the CT. More specifically, it depends on how well the CT transfers the AC component to its secondary while blocking the DC component. Transfer function of a CT can be considered similar to a first order high pass filter. Characteristics and transfer function of a CT was studied in different research works [100]–[103]. Figure 3.24 shows a sample spectrum of trapezoidal current waveform along with two different sample high-pass filter transfer functions.

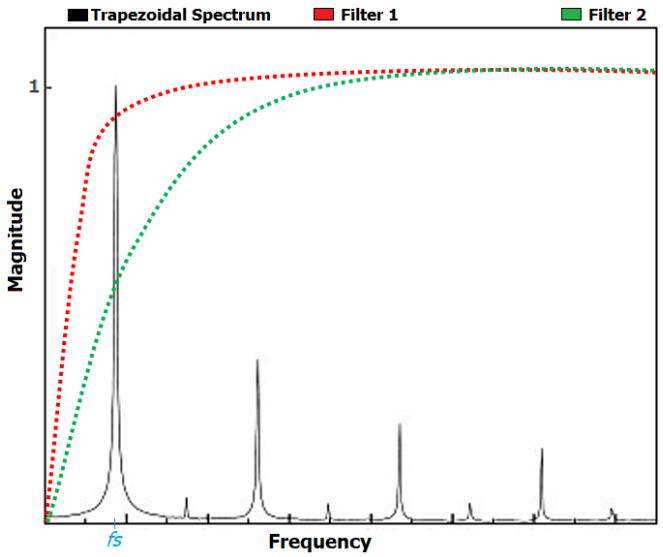

Figure 3.24: A sample spectrum analysis of MAB current waveforms and transfer functions of different filters.

The red transfer function in Figure 3.24 corresponds to a CT with good AC cancellation because the first harmonic component is transferred to the secondary with a very small attenuation. The negative point with this transfer function is that they eliminate a big part of dynamics in the current. In other words, they transfer the current dynamics that correspond to the ranges much smaller than the switching frequency, *fs*, to the secondary without effective attenuation. Therefore, these dynamics of the current will be cancelled when measured by the Hall effect sensor. Regarding the green transfer function shown in Figure 3.24, the dynamics are not be copied into the secondary and will not be cancelled. The problem with this transfer function is that in addition to attenuating dynamics of the current, it attenuates the switching frequency, too, undermining its AC cancellation capability.

Transfer function of a CT is given as

$$\frac{L_M s}{R_2 + (L_M + L_{lk})s} \tag{3.35}$$

where L_M is the magnetizing inductance, and R_2 and L_{lk} are the series resistance and leakage inductance, respectively. It implies that the leakage inductance affects the gain of the CT at high frequencies. Therefore, the leakage inductance can undermine quality of AC cancellation if it is not minimized. The second point concluded from this equation is that the cut-off frequency of the CT increases if the resistance is increased.

In order to assess the impact of characteristics of CT on AC cancellation and dynamic response of the measurement setup, two other CT designs were tested. Figure 3.25 shows two CTs with an EFD and a toroid core that were used for further analysis. In the following Characteristics of all the CTs were measured using an impedance analyzer at the switching frequency of the DAB. The results are listed in Table 3-1. Transfer function of the three CTs, based on Equation (3.35), is plotted in Figure 3.26. Based on the transfer functions and the values in Table 3-1, the EFD and toroid CTs are expected to have better AC cancellation compared to the EE core. On the other hand, the EE core is expected to have better capability of detecting slow dynamics of the current because those dynamics are attenuated through CT and therefore will not be cancelled in the Hall effect sensor.

Figure 3.25: Different types of CT that were tested in the proposed DC current measurement setup: EFD core on the left and toroid core on the right.

Table 3-1 Parameters of the designed QAB converter

CT Core type	Magnetizing inductance	Resistance	Leakage inductance	Gain at 20 kHz
EE	1.4 µH	40 mΩ	40 nH	0.8
EFD	5 µH	12 mΩ	70 nH	0.97
Toroid	106 µH	10 mΩ	150 nH	1

Steady state and dynamic tests were performed on CTs with EFD and toroid cores. Performance of these CTs in steady state AC cancelation is illustrated in Figure 3.27. Peak-to-

peak amplitude of the AC component is reduced to 34 and 28 mV in case of the CTs with EFD core and the toroid core, respectively. It can be concluded from comparing the results that AC cancellation is performed better by the CTs shown in Figure 3.27, as predicted from their transfer function.

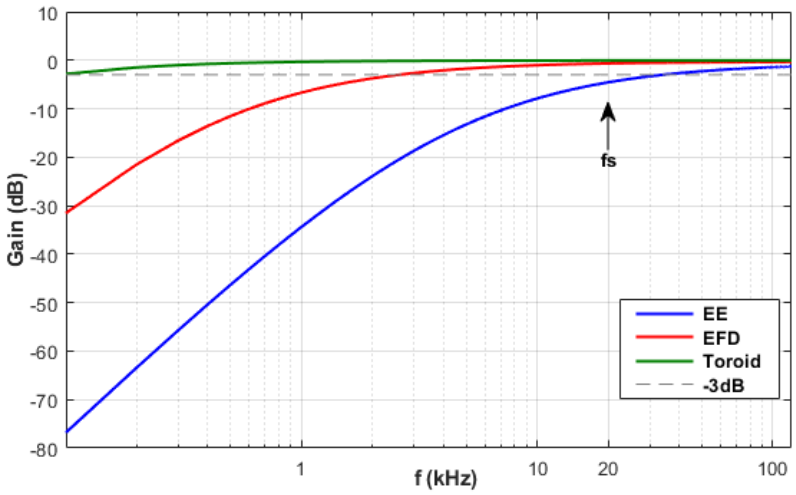

Figure 3.26: Transfer function of the CTs.

(a)

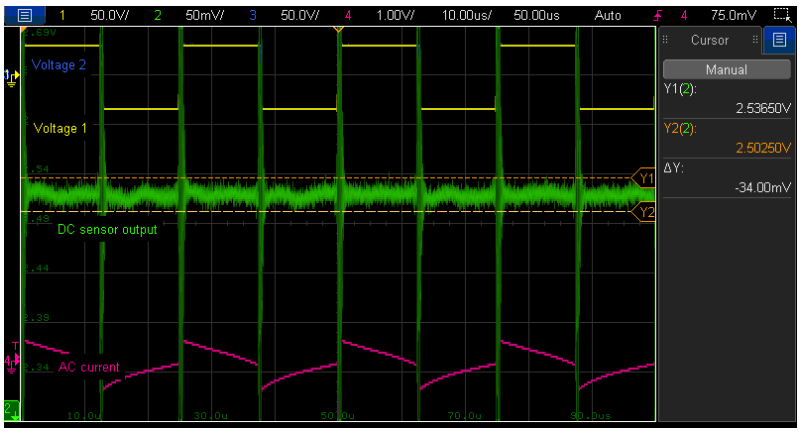

(b)

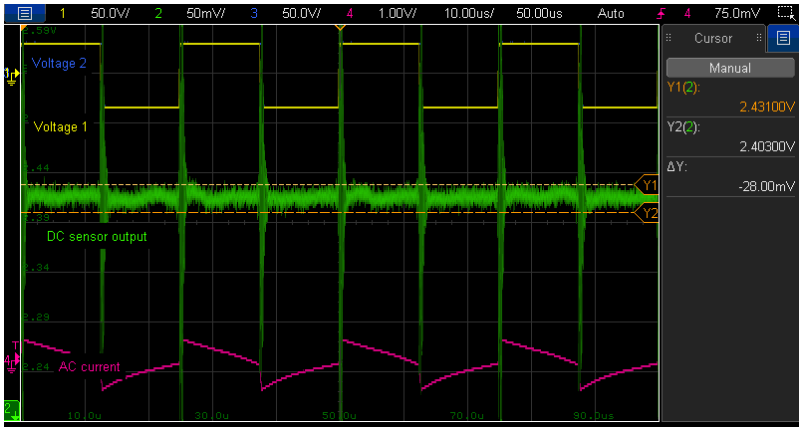

Figure 3.27: Comparing cancellation of AC component of the current in steady state with different CTs: (a) “EFD CT”; and (b) “Tore CT”. Channels 1and 3 (yellow and blue) indicate the active bridge voltages of the DAB. Channel 2 (green) is the output of the Hall effect sensor. Channel 4 (pink) is the output of a clamp AC current sensor.

The second test was repetition of the test in Figure 3.23 in order to assess dynamic characteristics of the CTs with EFD and toroid cores and compare it to Figure 3.23. The results of dynamic test on the CTs with EFD and toroid cores are illustrated in Figure 3.28. Transfer functions of these CTs showed that they transfer nearly all current dynamics to the secondary, so these dynamics will be cancelled in the Hall effect sensor. Therefore, they are not expected to detect transient DC currents. The results shown in Figure 3.28 confirm this prediction.

(a)

(b)

Figure 3.28: Comparing cancellation of AC component of the current during a power transient with different CTs: (a) "EFD CT"; and (b) "Tore CT". Channels 1and 3 (yellow and blue) indicate the active bridge voltages of the DAB. Channel 2 (green) is the output of the Hall effect sensor. Channel 4 (pink) is the output of a clamp AC current sensor.

Conclusion:

The proposed method was tested experimentally with different cores. The results showed that the AC cancellation setup has acceptable performance and the potential to be used for closed-loop DC current suppression in MAB converters. Experimental validation of this control will be presented in the next chapter. Analytical study of the CTs showed that their characteristics has an impact on the quality of AC cancellation. It is possible to adjust those characteristics by changing the core, number of turns, or adding passive components to the secondary of the CT. Therefore, the proposed DC current measurement has the potential to be

optimized regarding priorities of their application. They can be optimized for maximizing cancellation of AC components or increasing the bandwidth to detect transient DC currents.

3.4. DC link voltage variation

The MAB converter, chosen as the building block of a cluster of converters, is responsible for exchanging energy between different objects, i.e., batteries, photovoltaic panels, DC grid and AC grid. In this work, interface converters are assumed for connecting the MAB to photovoltaic panels and the AC grid. As explained in the introduction, a cluster of MAB converters has the potential to perform grid forming and supporting functions of the DC grid, or providing ancillary services such as voltage and frequency support. However, these functions are out of scope of this work. It is assumed in this work that the DC grid is formed and maintained by a separate converter and no ancillary services are provided to the AC grid. The photovoltaic panels are connected through a DC/DC converter that performs MPPT function and controls the corresponding DC link voltage. Therefore, it is safe to assume that DC link voltages of these ports will not experience significant changes.

Contrary to the ports connected to photovoltaic panels, the DC grid and the AC grid, the port that is connected to the batteries is subject to continuous changes of DC link voltage. The extent of the changes of battery voltage depends on its technology and maximum depth of discharge. Figure 3.29 shows how output voltage of different battery technologies vary as the battery is discharged from full state to empty state. Lead acid and lithium iron phosphate (LFP,) batteries are the two most common technologies in microgrid applications. While the former is usually discharged no further than 50% of its capacity, the latter one can be discharged as far as 80% without major impact on its capacity retention.

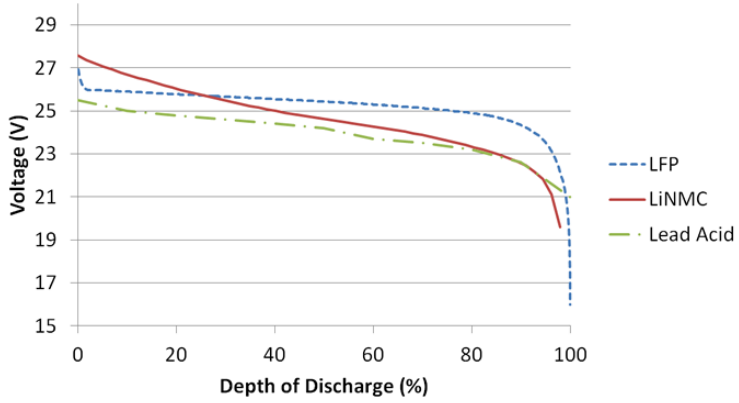

Figure 3.29: Variation of voltage with respect to depth of discharge for different battery technologies for a 24 V battery pack.

Figure 3.29 shows that considering the maximum depth of discharge, voltage variation will be around 5% and 10% for lead acid and LFP batteries, respectively. This variation in DC link voltage can have an impact on performance of the MAB converter. Different measures can be taken to minimize this impact and maintain high efficiency of the converters. These measures were discussed in section 2.4.2 of previous chapter. The following sections will have a closer look on these solutions and make a comparison between them in terms of efficiency.

3.4.1. Comparison between possible solutions

When DC link voltage of one port deviates from its nominal value, amplitudes of active bridge output voltages will become unequal (after applying the transformer turn ratios). As shown previously in section 2.4.2, this variation leads to an increase in reactive power transfer, larger currents and higher losses. It can result in hard switching in the MOSFETs, too. One approach to address this issue is to try to equalize volt-seconds on every port. This approach is based on square-wave analysis. This method prevents the current from becoming capacitive on the ports with smaller DC link voltages (or leading the voltage) by preventing the current from changing its sign before the switching of the output voltage. This will help avoiding reactive power exchange between the ports and hard switching. Trying to equalize the voltage phasors is an equivalent approach, which is based on first harmonic analysis. These two approaches were compared with full conduction in terms of RMS current magnitudes in section 2.4.2 of previous chapter. Since a model of losses is proposed in this chapter, it is now possible to compare these modulations in terms of global losses.

The ratios between conduction losses, core losses and switching losses depend on design parameters such as maximum current density in the windings, maximum magnetic flux in the magnetic cores, the chosen MOSFET devices and even the dead time in generation of switching signals. Since these parameters change from one converter design to another, the results of the comparison between global losses of different modulations depends on the converter design, too. The comparison in this section is based on a QAB with DC link voltages of 100 V, 200 V, 400 V and 800 V on the first, second, third and fourth ports, respectively, and nominal power of 2 kW on each port. Since this work is studying application of MAB converters in a green building, the four ports represent the batteries, the PV panels, the DC grid, and the AC grid, respectively. Maximum current density and magnetic flux were set to 5 A/mm² and 150 mT, respectively. Table 2-1 shows some of the converter design parameters based on the procedure presented in the previous chapter.

Table 3-2 Parameters of the designed QAB converter

Input Parameter	Value	Output Parameter	Value
DC link voltages	100, 200, 400, 800 V	Transformer core	PM74 ferrite core, 3C94 material
Nominal power	2 kW	Inductor core	Toroid 25/15/10 with 1 mm air gap
Switching frequency	40 kHz	Transformer turns	4, 8, 16, 32
Maximum flux density	150 mT	External inductors	5, 20, 80, 320 μH
Maximum current density	5 A/mm²	MOSFETs	SUP90220E, SiHP22N60EF, C2M0280120D, C2M0280120D

Results of the comparison will be presented as 3D surfaces as a function of DC link voltage of the first port and the power transfer. The DC link voltage changes in the range of 90% to 100% its nominal value, which is 100 V. DC link voltage of the rest of the ports are kept constant at their nominal value. The power increases linearly from 0 to 100% nominal power in every port. The first and the third port, representing batteries and DC grid, absorb power, while the second and the fourth port, representing PV and AC grid, provide power.

Conduction losses:

The conduction losses of different voltage modulations are compared in Figure 3.30. Similar to what has been observed previously in Figure 2.22, “full conduction” modulation leads to higher losses when power transfer is low and voltage variation is large. Compared to the comparison in Figure 2.22, the results in Figure 3.30 show larger differences between different modulations at high power. This can be due to the fact that when DC link voltage of the first port is smaller than its nominal values, the “equal Volt-seconds” and “equal phasors” employ three-level voltage modulations on the second, third and fourth ports. This will reduce the effective voltage in those ports, which requires larger effective current and results in larger conduction losses. In this regard, three out of four effective currents will increase in a QAB converter, compared to a DAB where “equal Volt-seconds” and “equal phasors” modulations lead to increase in only one out of two effective currents.

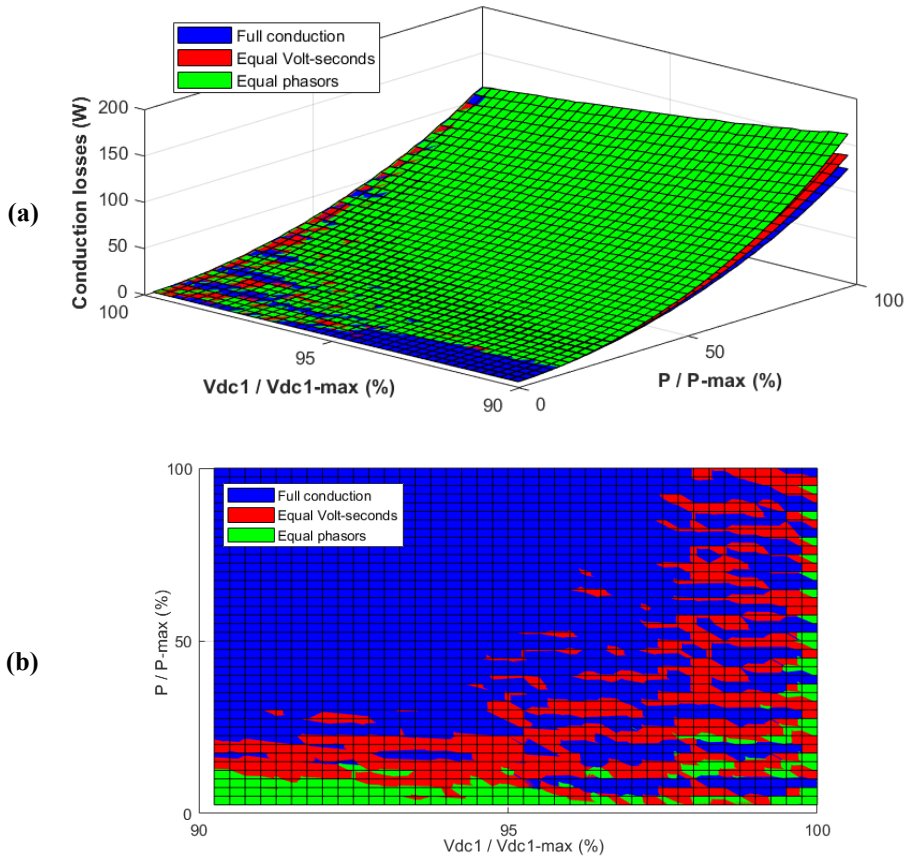

Figure 3.30: Comparing conduction losses when DC link voltage of the first port changes between 90% and 100% nominal voltage, and the power transfer of all ports increase from 0 to 100% nominal power. The rest of DC link voltage are constant at their nominal value. (a) shows the 3D view; (b) is the bottom view, indicating the modulation with smallest losses.

The difference between "equal Volt-seconds" and "equal phasors" modulations at high-power and large voltage variation region is significantly larger than what has been observed in Figure 2.22. The reason is that the results in Figure 3.30 are from a model of losses that is based on square-wave analysis, while Figure 2.22 was based on first harmonic analysis. Therefore, the impact of reactive power exchange between the sources through higher harmonics is better illustrated in Figure 3.30. "Equal phasors" modulation prevents reactive power exchange between the sources through the first harmonic only. "Equal Volt-seconds", on the other hand, is based on square-wave analysis and prevents reactive power exchange of all the harmonics at the same time, hence showing a better performance in terms of conduction losses compared to "equal Volt-seconds" modulation.

Magnetic core losses:

Sum of the losses in magnetic cores of the four inductors is shown in Figure 3.31 for the three voltage modulations. Since the magnetic flux in inductor cores are related to the current through the windings, their losses have a general shape similar to that of conduction losses. It

is noticeable that the magnetic core losses are significantly smaller than conductions losses, meaning that smaller magnetic cores could be used. The methods for measurement and suppression of dc currents that were proposed in section 3.3 have the potential to minimize the risk of saturation, allowing for further reduction in footprint of the system.

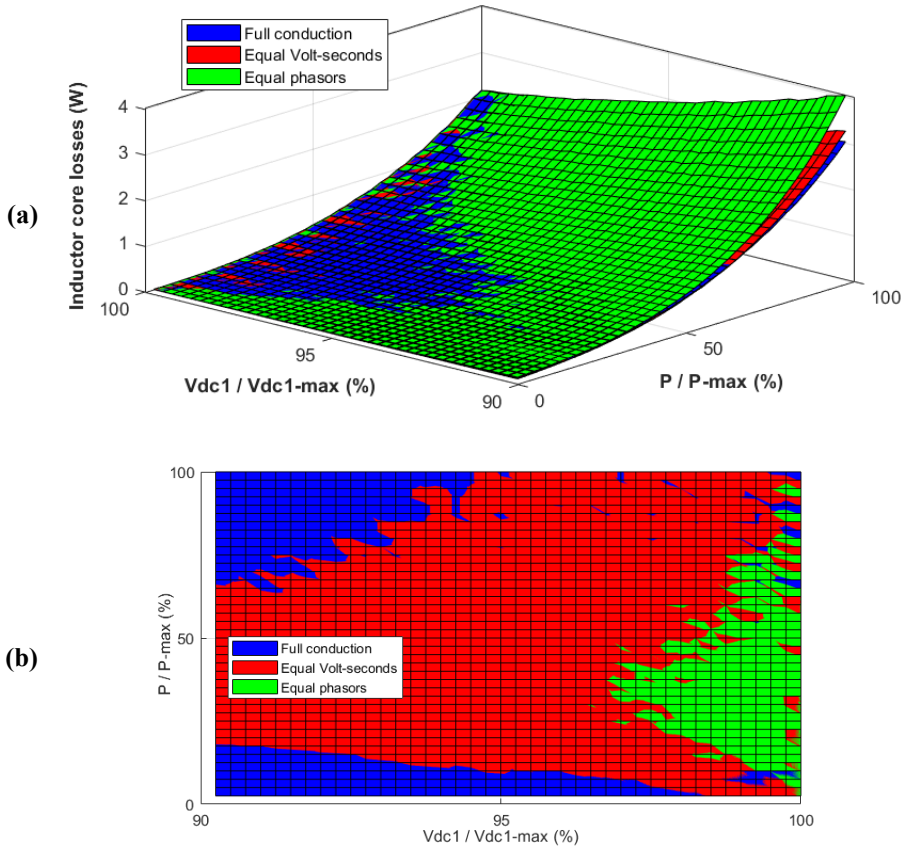

Figure 3.31: Comparing losses in magnetic cores of the inductors of a QAB with different voltage modulations. (a) shows the 3D view; (b) is the bottom view, indicating the modulation with smallest losses.

Unlike an inductor, the magnetic flux density in a transformer core is related to Volt-seconds of the voltages on its windings. This fact is clearly illustrated in Figure 3.32, comparing the transformer core losses in different voltage modulations.

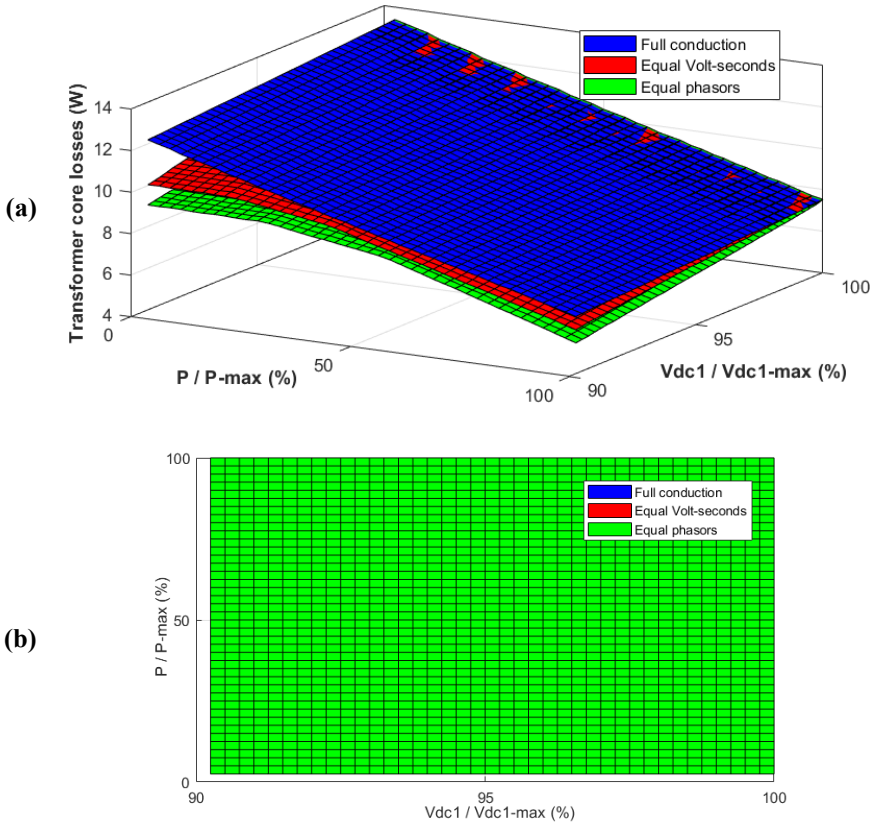

Figure 3.32: Comparing losses in magnetic core of the transformer of a QAB with different voltage modulations. (a) shows the 3D view; (b) is the bottom view, indicating the modulation with smallest losses.

Since "full conduction" modulation maximizes the Volt-seconds across the windings, it corresponds to the largest losses in the transformer core. The transformer core losses in this case increase slightly as the DC link voltage of the first port increases. The other two modulations reduce the Volt-seconds and lead to smaller transformer core losses. Another noticeable fact is that the transformer core losses reduce as the power transfer increases. This reduction is a result of the increase in currents, which means larger voltage drop on inductors and smaller voltage across transformer windings.

Switching losses:

Figure 3.33 displays the hard switching losses in the QAB converter. The soft switching losses and turn-off losses were negligible and ignored in this figure, therefore "equal Volt-seconds" and "equal phasors" have no switching losses because they assure soft switching over the whole range of power and voltage variation. This figure shows that "full conduction" modulation leads to hard switching at low power and large voltage deviation region. The size of the hard switching region and the magnitude of the hard switching losses depend on

characteristics of the MOSFETs. Large output capacitance extends the hard switching region and increases the magnitude of these losses. MOSFETs with smaller output capacitance generally have larger on-state resistance. The optimal point of this tradeoff between conduction and switching losses of the MOSFETs can be determined using the proposed model of losses and the mission profile of the converter.

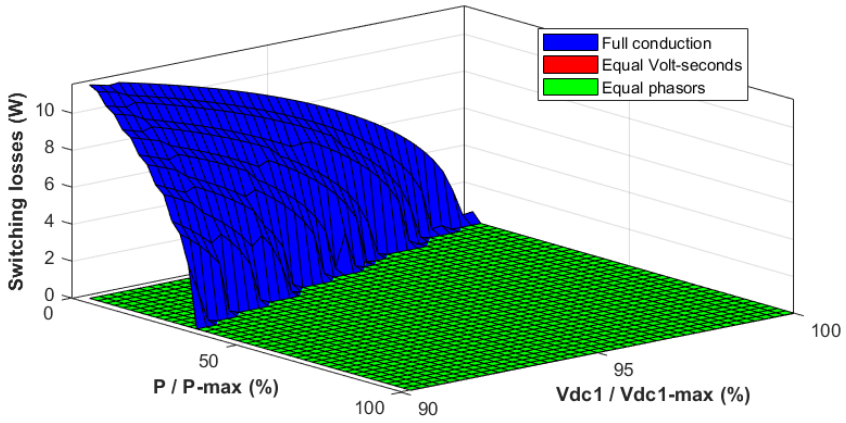

Figure 3.33: Comparing switching losses in a QAB with different voltage modulations. The turn-off losses and soft switching losses were negligible and not shown in this figure.

Overall comparison:

Sum of total converter losses is shown in Figure 3.34. It shows that the major difference between the three modulations occurs in the regions where variation of the DC link voltage is large. In these regions, if the power transfer is low, "full conduction" involves larger losses because of hard switching, and if the power transfer is high, "equal Volt-seconds" and "equal phasors" involve larger losses because of larger effective currents.

The comparisons presented so far were based on linear increase of power from 0 to 100% nominal power on every port. Mission profile of MAB converters usually include different power flows. Considering the application of this research, the power flow studied in Figure 3.30 to Figure 3.34 corresponds to a situation where the PV panels and the AC grid are providing the energy for the loads on the DC grid and charging the batteries. A different power flow was compared to see how the losses evolve as the power changes. Figure 3.35 shows the losses of different voltage modulations where the AC grid alone is providing the loads on the DC grid, i.e., the power transfer of the first and the second ports are constantly 0, while the third and the fourth port linearly increase from 0 zero 100% nominal power. The general comparison results are the same as Figure 3.34, but with a wider hard switching rage in "full conduction". The reason is that power transfer of two ports is zero; therefore, their current is small during switching moments for a wider range and cannot totally discharge their output capacitance.

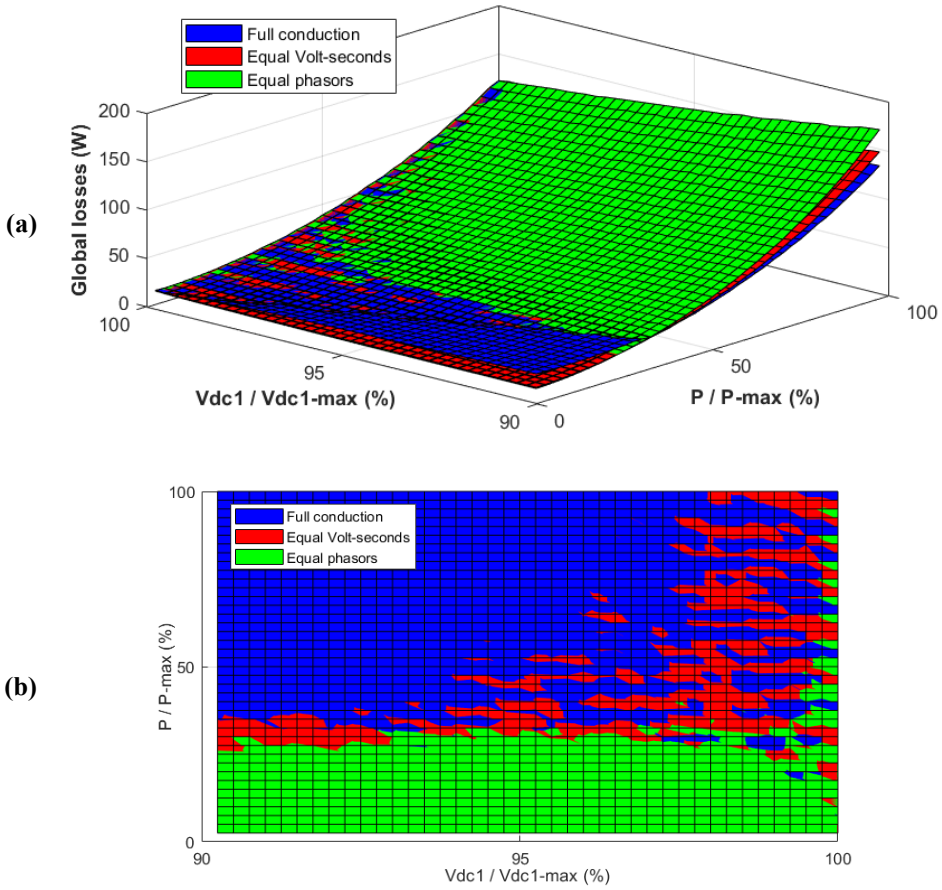

Figure 3.34: Comparison of total losses due to different voltage modulations in a QAB as the DC link voltage of the first port and the power transfer change. (a) shows the 3D view; (b) is the bottom view, indicating the modulation with smallest losses.

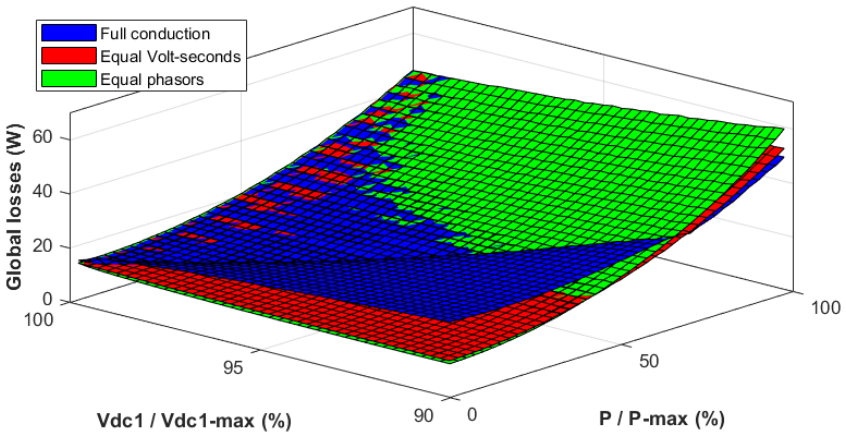

Figure 3.35: Comparison of total losses due to different voltage modulations in a QAB as the DC link voltage of the first port and the power transfer change. The axis representing P/Pmax shows the power transfer of the third and the fourth port, while the first and the second ports do not exchange any real power.

3.4.2. Conclusion

Three different voltage modulations were compared in terms of total converter losses as the DC link voltage of one port deviates from its nominal value. The comparison between "equal phasors" and "equal Volt-seconds" shows that the latter one has a better performance because it minimizes reactive powers of all harmonics. Although the comparison in Figure 3.34-b shows that "equal phasors" results in lower losses in low power region, it must be noted that the difference between the two is very small in that region. On the other hand, Figure 3.34-a shows a better comparison, indicating that "equal Volt-seconds" performs significantly better in higher power region. Therefore, the two main candidates for implementation in control system of a MAB are "full conduction" and "equal Volt-seconds". As expected, "full conduction" results in lower losses at high power, but can lead to hard switching when the power is low and the voltage variation is large. "Equal Volt-seconds" on the other hand, maintains soft switching in low power and large voltage variation conditions, but results in large conduction losses in high power and large voltage variation conditions. In case of small voltage variations, the difference between the two methods is not significant. Furthermore, comparing Figure 3.34-a and Figure 3.35 reveals that the limits between the regions where each modulation performs better dynamically change as the operating parameters vary.

Different approaches can be taken with regard to voltage modulation in the control scheme of MAB converters. The ideal control scheme would be able to analytically predict which modulation leads to least possible losses based on the operating conditions, i.e., DC link voltages and power flow inside the converter. Determining the modulation that leads to least losses analytically is difficult. Employing a lookup table of pre-calculated regions is another option, but considering the number of parameters (three powers and one voltage) it can be a large table. The third option is determining the optimal voltage modulation in real-time, based on the efficient loss model and control method that were presented earlier in this chapter and the previous one. In applications where the converter is going to operate in a certain voltage and power range for most of its lifetime, only one voltage modulation can be implemented, trying to simplify the control system and reduce the calculations.

The goal of this research work is application of a cluster of MAB converters and it was shown in the second chapter that clustering helps employ the converters close to their nominal power during a major portion of their lifetime. Regarding the results of the comparisons in this section, "full conduction" modulation is the proper choice for this application.

3.5. Conclusion

MAB converters were proposed as the building block of the cluster of converters in the first chapter. The previous chapter studied modeling and control of these converters. It showed that a model of losses not only helps better understanding of the internal phenomena of the MAB converters, but also is a useful tool in optimizing their design and control. This chapter was dedicated to studying the losses in MAB converters and the challenges of employing them in real conditions. Firstly, two different models of losses were proposed, one being more detailed and the other one being computational cost efficient. Formation of DC currents in transformer windings, leading to saturation of magnetic cores, were studied afterwards. The origins of DC currents, challenges of measuring and avoiding them were also discussed. Another challenge in operation of MAB converters is deviation of DC link voltages from their nominal value. This challenge and the potential ways to address it was the subject of the last part of this chapter. The next chapter will present a prototype that was built and tested in G2Elab to validate the models and controls proposed in this chapter and the previous one.

4. Results

MAB converters have been proposed as the building blocks of the cluster of converters that was introduced in the first chapter. The second and the third chapters studied modeling, control and operation of MAB converters. They put forward a design procedure, certain models of losses and power control schemes, along with methods of measuring and suppressing DC currents in the windings. This chapter is dedicated to the presentation of a QAB converter that was designed and built based on the proposed design procedure. This prototype was then used to evaluate accuracy of the proposed models, validate performance of the power control methods and assess correct measurement and suppression of DC currents in the windings.

4.1. Design of the converter

Nominal power:

The power level chosen for the prototype is 2 kW. Based on the definition that was discussed in section 2.3.1, this means that this converter will be able to transfer 2 kW to/from each port simultaneously without exceeding 37 degrees of phase shift between voltages of its active bridges. The final application of the MAB converter is exchanging energy in a microgrid that is equipped with renewable energy generation, energy storage devices, a DC network and a connection to the utility AC grid. A QAB converter is a suitable candidate for this application, with DC link voltages of 100 V, 200 V, 400 V and 800 V on the ports that connect to the batteries, PV panels, DC grid and AC grid, respectively. The switching frequency is 40 kHz, a value that is compatible with common smart buildings EMC standards. Table 4-1 summarizes the voltage and current rating. The current is calculated assuming 90% efficiency.

Table 4-1: Nominal voltage and current of the prototype

Parameter	**Port 1**	**Port 2**	**Port 3**	**Port 4**
Connection to	Batteries	PV panels	DC grid	AC grid
Voltage	100 V	200 V	400 V	800 V
DC link current	22 A	11 A	5.5 A	2.75 A
Power direction	Bidirectional	Unidirectional	Bidirectional	Bidirectional

The following design parameters are chosen based on the procedure proposed in chapter 2 and the model of losses introduced in chapter 3. For components such as magnetic cores and semiconductors, a list of material and components available in the market is used. A program was coded in MATLAB, checking every possible component and choosing the one that leads to the least losses at nominal power.

Inductors:

Table 4-2 shows a summary of the design parameters of the inductances, determined from the design program.

Table 4-2: Design parameters of the inductor determined from the design program.

Parameter	**Port 1**	**Port 2**	**Port 3**	**Port 4**
Design inductance	4.9 µH	19.6 µH	78.4 µH	313 µH
Core (material)	ETD34 (3C90)	ETD34 (3C90)	ETD34 (3C90)	ETD34 (3C90)
Air gap	1 mm	1 mm	1 mm	1 mm
Number of turns	6	12	25	51
Wire	5.3 mm² Litz	2.6 mm² Litz	1.3 mm² Litz	0.7 mm² Litz

Building the converter was stopped at early steps as the lockdown measures were established in France due to COVID-19 pandemic. Following the end of the lockdown, the future situation was not predictable. The ETD34 core was not available in the components' stock of G2Elab and had to be purchased which could take weeks because of the pandemic. Finally, it was decided to make the inductors using a gapped toroid core that was available, as shown in Figure 4.1. Design parameters and measured inductance of the inductors are presented in Table 4-3.

Figure 4.1: The inductors made in G2Elab using a gapped toroid core

Table 4-3: Design parameters of the inductors determined based on a toroid core.

Parameter	Port 1	Port 2	Port 3	Port 4
Core	Toroid 25/15/10	Toroid 25/15/10	Toroid 25/15/10	Toroid 25/15/10
Air gap length	1 mm	1 mm	1 mm	1 mm
Number of turns	5	10	20	40
Measured inductance (deviation from design)	3.72 µH (-24%)	15.4 µH (-21%)	65.6 µH (-16%)	251 µH (-20%)

Transformer:

Table 4-4 shows a summary of the design parameters of the transformer, determined from the design program. As shown in Figure 4.2, the windings were placed over each other because the topology of the core did not allow for any other type of placement. Considering the voltage level, no additional insulation were added between different layers of windings. The Litz wires for transformer windings were the same as the ones used for the inductors.

Table 4-4: Design parameters of the transformer determined from the design program.

Parameter	Port 1	Port 2	Port 3	Port 4
Core	PM74 N27			
Number of turns	4	8	16	32
Wire	5.3 mm² Litz	2.6 mm² Litz	1.3 mm² Litz	0.7 mm² Litz

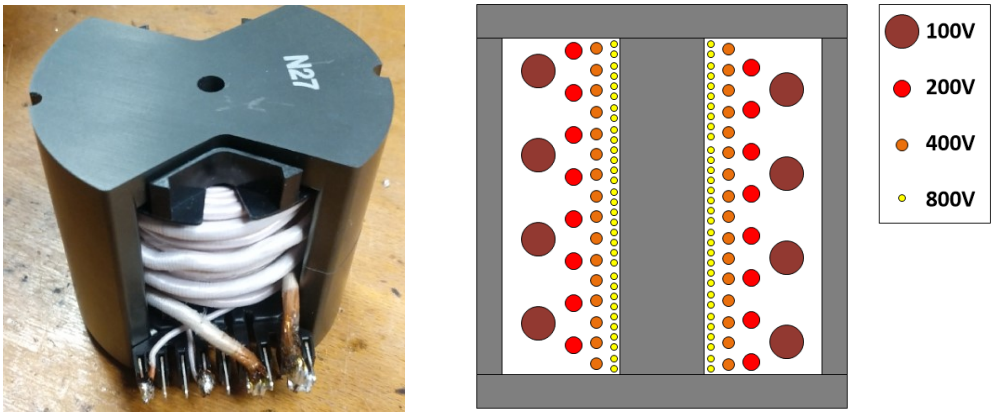

Figure 4.2: The transformer built for the 2kW QAB prototype and a schematic of winding placement.

Switches:

Table 4-5 shows a summary of the chosen MOSFETs. The design program, presented in chapter 2, was set to find the components that give the highest efficiency at nominal power, where conduction losses are the main losses in the semiconductors. Therefore, the MOSFETs with the lowest on-state channel resistances were chosen. The "IPP65R045C7 CoolMOS" has a relatively large output capacitance and using it for port 3 could lead to loss of soft switching conditions even at 50% nominal power. For this reason, and in order to maximize the safety margin of blocking voltage for prototyping purposes, the "C2M0280120D SiC MOSFET" was used for port 3 in the prototype. The experimental results proved this choice correct. As the "IPP65R045C7 CoolMOS" had a relatively wide hard switching range in port 2, its hard switching range would be even wider if it were used in port 3, because the current in port 3 is generally smaller compared to port 2. A thorough discussion will be presented later in this chapter.

Table 4-5: The MOSFETs chosen by the design program.

Parameter	Port 1	Port 2	Port 3	Port 4
MOSFET	SUP90220E	IPP65R045C7	IPP65R045C7*	C2M0280120D
Max. Blocking Voltage	200 V	650 V	650 V	1200 V
Max. Continuous Current	64 A	46 A	46 A	10 A
Technology	Si MOSFET	CoolMOS	CoolMOS	SiC MOSFET

Heat sinks:

In order to limit the rise in junction temperature of the MOSFETs, proper heat sinks were chosen. Maximum temperature rise was set to 50 °C and resulted in choosing RA-T2X-38E for the MOSFETs of the first two ports, and OMNI-UNI-18-50 heat sinks were chosen for port 3 and port 4, based on their datasheet values.

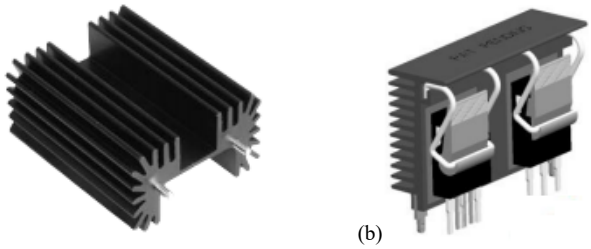

(a) (b)

Figure 4.3: Heat sinks: (a) RA-T2X-38E heat sink for each switch of port 1 and port 2; and (b) OMNI-UNI-18-50 heat sink for each arm of port 3 and port 4.

4.2. Measuring parameters

After preparing the components and building the prototype, some of the parameters could be measured. The prototype is shown in Figure 4.4. The parameters that were measured are listed in Table 4-6. The T model shown in Figure 4.5 was considered for the transformer, and the inductors were modeled as an ideal inductor in series with a resistance. DC and AC resistances, leakage inductances and magnetizing inductances were measured using a KEYSIGHT E4990A impedance analyzer. AC resistances were measured using the impedance analyzer at 40 kHz. The last of row of Table 4-6 indicates the DC resistance measured between the connection points of the QAB to its DC sources, using an Agilent 34405A digital multi-meter, while one switch in each arm was turned on. The total measured DC resistance includes DC resistances of the transformer winding, inductor windings, two MOSFET channels, wires, connections and PCB traces of the corresponding ports. The rest of modeling parameters such as MOSFET output capacitance and thermal resistances of MOSFETs and heat sinks, were extracted from datasheets.

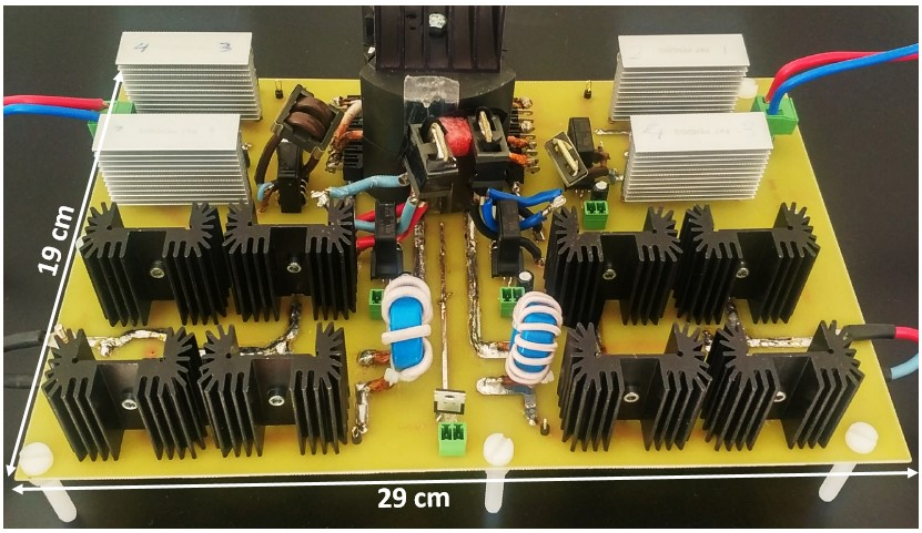

Figure 4.4: The 4x2kW prototype.

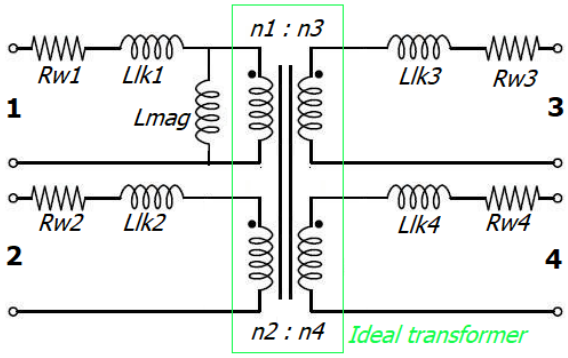

Figure 4.5: The T model of the transformer. Rw and Llk indicate winding resistances and leakage inductances of each port, respectively. The magnetizing inductance of the core is marked as Lmag.

Table 4-6: Summary of parameters of the prototype that were measured.

Parameter		Port 1	Port 2	Port 3	Port 4
Transformer	Leakage inductance (µH)	0.525	0.639	0.962	6.31
	Magnetizing inductance (mH)	0.182	0.729	2.91	11.6
	Winding AC resistance (mΩ)	14.4	27.5	52.3	247
	Winding DC resistance (mΩ)	11.8	19.3	47.5	169
Inductors	Inductance (µH)	3.72	15.4	65.6	251
	Winding AC resistance (mΩ)	3.4	9.6	46	135
	Winding DC resistance (mΩ)	1	3.7	19	56
Total measured DC resistance (mΩ)		100	160	670	830

4.3. Test setup

4.3.1. Global hardware setup

The test setup is illustrated in Figure 4.6. A NI myRIO 1900 system is used as the control system, running the control scheme programmed in NI LabVIEW environment. The system is based on a Zynq system including both an ARM processor and an FPGA. The calculations and control methods are computed in the processor part. The FPGA of myRIO 1900 includes the logical circuits for generating switching signals with the phase shifts that are received from the processor. Analog to digital conversion, digital filtering and scaling of the analog inputs, including voltage and current measurements, are also performed in FPGA to optimize speed and then delivered to the feedback loops, which are implemented in the processor.

(a)

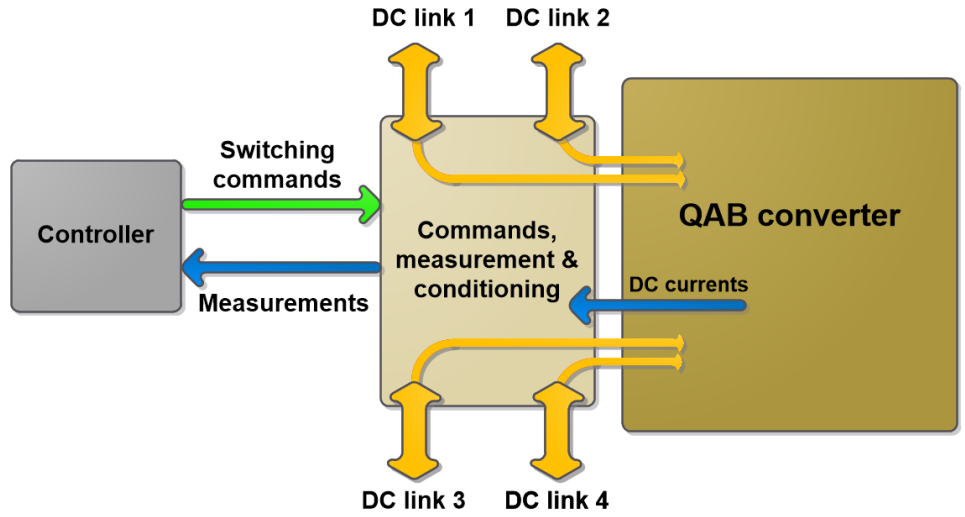

(b)

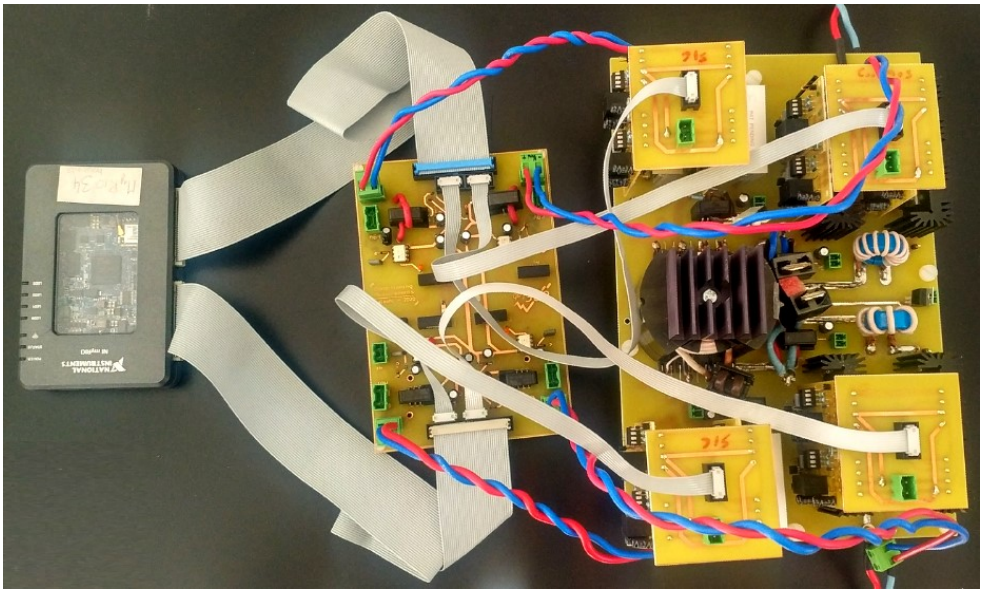

Figure 4.6: The test setup: (a) the schematics; and (b) the real test setup, including the QAB converter, the measurement and conditioning board and the controller. The yellow arrows in (a) indicate power connections, and the rest are command and measurement signals.

The switching signals, generated by the controller, are sent to an interface board, designated as "Commands, measurements & conditioning" in Figure 4.6-a, which is responsible for sending the commands to the corresponding gate drivers. The same board also acts as an interface between the DC links and the QAB converter, in order to be able to measure the DC link voltages and currents. Measurement of DC currents in the winding is made on the QAB converter board, sent to the interface board, and then delivered to the controller as a feedback signal along with the DC link voltage and current measurements. The DC links can be connected to electronic DC sources, electronic DC loads or a parallel connection of both, depending on the test.

Due to safety reasons and partial opening of G2Elab after the first lockdown in France during Covid-19 pandemic, DC link voltages were reduced to 60 V, 120 V, 240 V and 480 V in all of the experimental tests in the following sections. This 40% reduction in DC link voltages is equivalent to 64% reduction in power transfer. In order to increase the power transfer capacity of the converter, switching frequency was reduced to 20 kHz. Nominal power of the converter with these values will be around 1.4 kW on each port.

Three main types of tests were defined for experimental validation of this research. The first type is validating the power control methods that were proposed earlier in chapter 2. Comparing predictions of the loss model, proposed in chapter 3, with the measurement is the subject of the second tests. The third category involves evaluating performance of the sensor setup proposed for measurement of the DC currents in transformer windings, as well as effective suppression of these currents. The following sections will present the tests and their results.

4.3.2. Control scheme

The control scheme is based on the assumption that the converter is going to operate in a cluster of converters, receiving its power flow command from the higher-level control system, which controls the cluster. Therefore, the main inputs of the converter control system are the reference powers that each port must provide or absorb. While trying to realize the reference power flow specified by the higher-level controller, the converter control system is responsible for addressing its internal challenges such as DC currents in the windings, connecting/disconnecting ports, and managing voltage modulations due to DC link voltage variations.

The control system that was designed and implemented on the prototype includes different loops and functions, as illustrated in Figure 4.7. The first and major loop is the “power control loop”. This loop controls the phase shifts to realize the reference power flow. The designed “power control loop” gets the reference powers from a “user-input panel”, and uses the measurements of power as the feedback parameter to perform closed-loop control. This loop determines the phase shifts, which are sent to the “two-step phase shift change” control and then delivered to the “generation of switching signals” on FPGA.

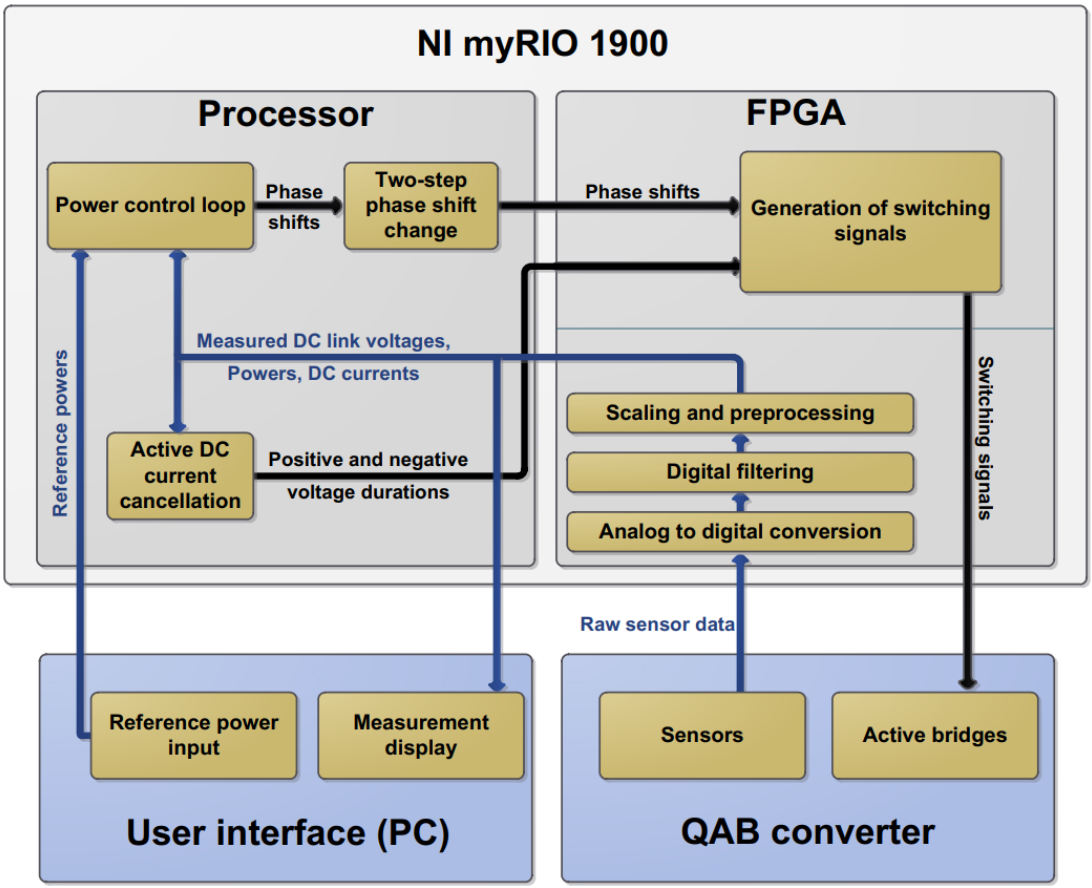

Figure 4.7: Schematics of the control system with its loops and connections to converter and user interface.

The second control loop is the "active DC current cancellation" loop, which gets the measured DC currents from FPGA and control the durations of positive and negative voltages. Some functionalities are not indicated in Figure 4.7 for simplicity. These additional functions include manual control of positive and negative voltage durations, in order to generate intentional DC currents in the windings (used in section 4.6.2); four user-controlled on/off controls that can turn each active bridge on and off, in order to switch to a TAB or DAB, if required (used in section 4.5.1).

4.3.3. Hardware-in-the-loop validation

Hardware-in-the-loop (HIL) testing is becoming more and more popular tool in design and testing of power electronic systems. Many power electronic systems involve medium to high frequency switchings, causing nonlinear and large dynamic behavior. These nonlinearities and dynamics can have a deteriorating impact on performance of the converters and/or their control systems. For this reason, software simulations are not considered as the final validation tool in power electronics. Novelties in power electronics are usually presented with experimental validation, in order to show that the proposed system is robust against nonlinearities and

dynamics that occur in real systems. A major challenge in experimental validation are the potential fault or abnormal conditions that can occur when implementing control systems on embedded control hardware. These conditions could cause severe damage to the prototypes and/or the control hardware itself. Using HIL real-time simulations for early validation of embedded control codes is a solution that makes significant improvements in the time-consuming and costly process of prototyping and experimental validation in power electronics.

An important factor in HIL simulations is that the HIL device has to perform all the state space calculations in a small time-step that is more than 100 times faster than the dynamics of the simulated system. Otherwise, the response of the HIL simulation cannot be considered real-time or even near real-time. Real-time simulation is a mature trend in power systems, as they usually work with parameters that vary as fast as 50 Hz. Average processors have been long capable of simulating power systems in real-time with time step of 100 to 200 micro seconds. Meanwhile, in case of power electronic converters, the switching frequency can be tens and hundreds of kilo Hertz and the dynamics are much faster than power systems. The HIL simulator must be able to solve all state equations in one microsecond or even less. This is not possible with the current processor speeds. FPGAs are the best candidates for this purpose; however, FPGAs with enough gates and ALUs were not commercially available until around a decade ago. With emergence of large FPGAs, their application in real-time simulation of power electronic systems has triggered. It must be mentioned that there are no clearly defined guidelines for implementing the power electronic systems on FPGAs or processors. Rather, the decision must be made for each case depending on several details such as complexity of the models, the amount of mathematical calculations, and the possibility of partitioning the system or parallel processing.

After implementing the control systems in myRIO 1900 using codes and available blocks in the LabVIEW environment, and before connecting it to the prototype, HIL simulation was used for a first validation of the embedded control. Early validations were done using a Typhoon HIL 402 real-time simulator, a low-end simulator, which was available in the laboratory. The setup is displayed in Figure 4.8. The Typhoon HIL 402 simulator did not have a FPGA big enough for simulating a QAB with 16 switches. Running the real-time simulation was only possible through partitioning the circuit, exponentially reducing the size of state space. On the other hand, partitioning led to inaccurate results with high switching frequencies. Therefore, it was decided to purchase a more powerful HIL simulator. Eventually, the OPAL RT 5700 was chosen due to communalities with other simulators that were already present in the laboratory

in the SYREL (Electrical Networks) team. The OPAL RT 5700, shown in Figure 4.9, was therefore used for further HIL validation of the embedded control.

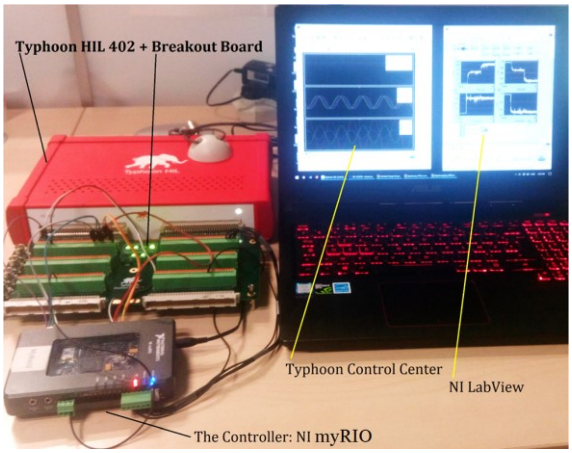

Figure 4.8: Real-time simulations using a Typhoon HIL 402 simulator.

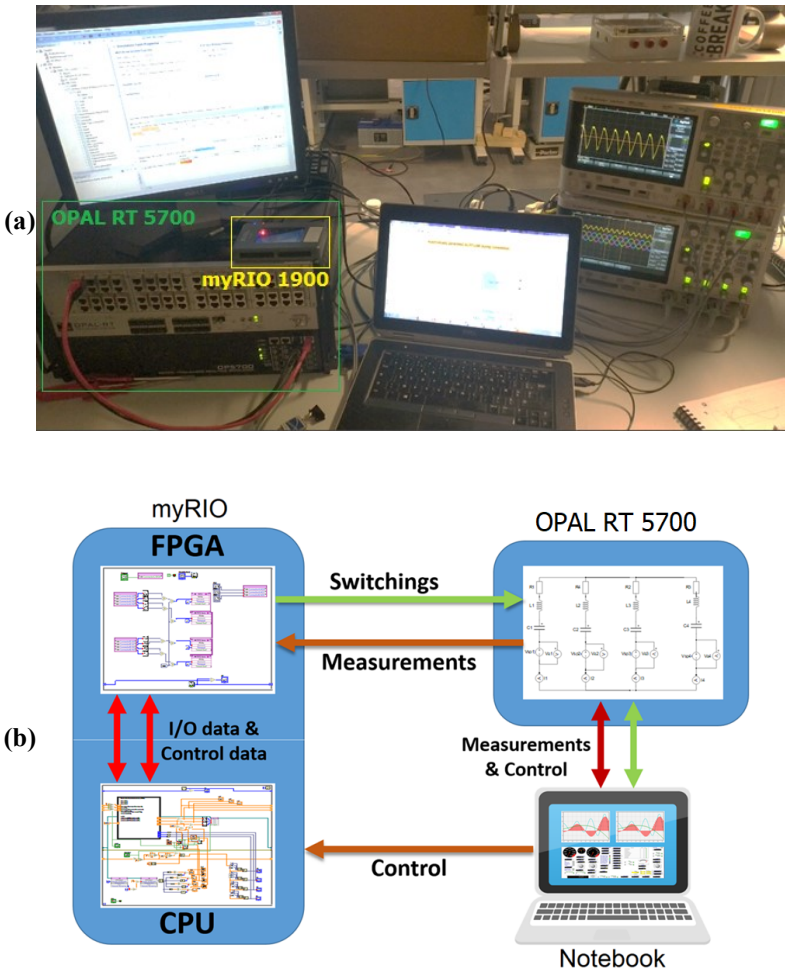

Figure 4.9: Real-time simulation setup with OPAL RT 5700 simulator.

HIL simulations helped in finding and rectifying the abnormal conditions and faults in coding the control system quickly and without any risk of damages. First validation of power control and DC current suppression methods was performed using OPAL RT 5700 target. After verifying correct operation of the embedded control system, it was connected to the converter prototype for the final goal, which was experimental validation of the proposed models and control methods. In this regard, HIL simulation was a handy tool that helped fast and safe debugging of the control hardware. The following sections will present the results of experimental tests.

4.4. Power flow control

Among the three power control methods that were proposed in chapter 2, the computational cost efficient method that was based on modular matrices was chosen for implementation. The proposed control scheme includes a feed forward, which is based on the modular matrices, and a feedback loop, which is a PI controller. Figure 4.10 shows this control system. Output of the feed forward loop, φ, is an estimation of the phase shift that will correspond to the reference power. The feedforward loop will quickly change the operating point of the converter to an operating point close to the reference power flow. The feedback loop is responsible for small modification of the phase shifts, hence the power flow, towards the desired power value. This scheme helps reducing dynamics of the system and enhances convergence speed when the reference powers change. Additionally, a "change detection" unit is employed to reset the output of the integrator in the PI controller whenever a new reference power arrives.

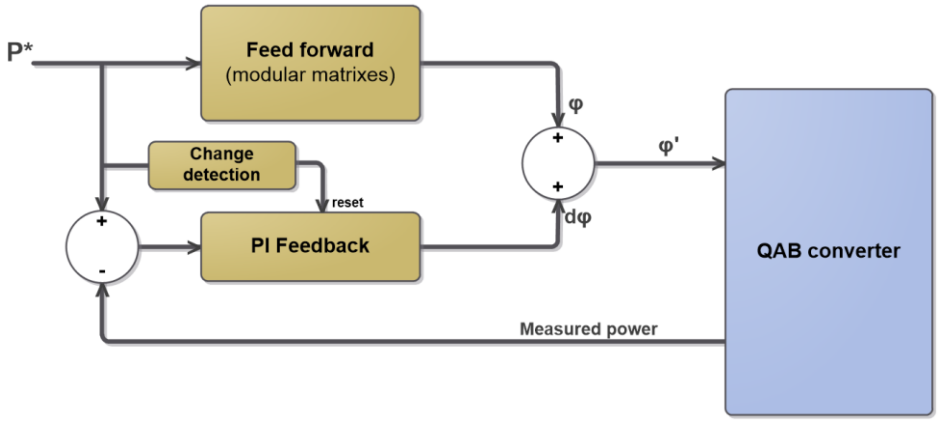

Figure 4.10: Closed-loop control scheme with a feed forward loop (modular matrices) and a feedback loop (PI).

In addition to the proposed control system, a closed-loop control based solely on a PI feedback loop ("FB") and an open-loop control based solely on the feed forward loop ("FF")

were also tested. Figure 4.11 and Figure 4.12 show the results of similar tests on “FB” and “FF” control systems, respectively.

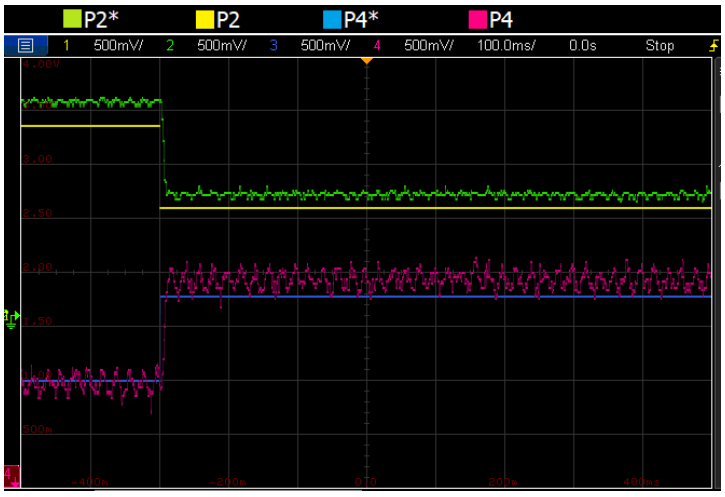

Figure 4.11: Open loop results of a step change in reference powers. The reference values (P2* and p4*) are shown along with their corresponding measured values (P2 and P4).

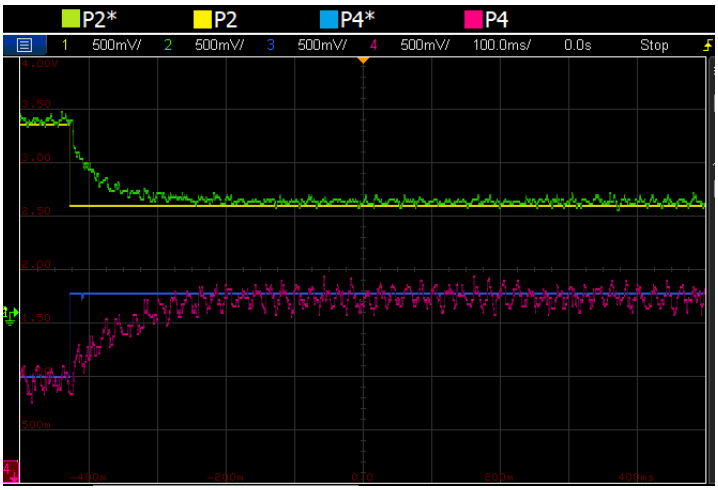

Figure 4.12: Closed loop results of the same test as Figure 4.11. The control system is composed of a PI feedback loop alone.

Due to the limited number of input signals on the oscilloscope, only two out of four measured powers of the QAB were captured along with their reference values. The results of the same test with the same values on the closed-loop control system with both feedback and feedforward loops (“FB+FF”), as illustrated in Figure 4.10, are shown in Figure 4.13.

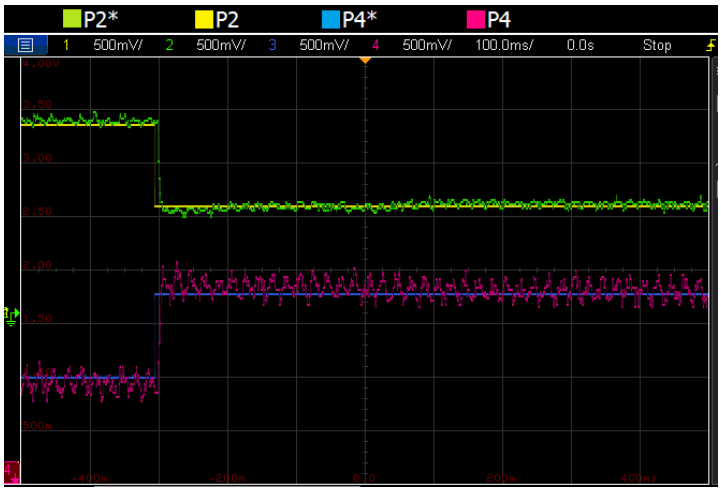

Figure 4.13: Closed loop results of the same test as Figure 4.11. The control system has both PI feedback and matrix feedforward loops activated.

Results of the open-loop control, "FF", show that the actual powers follow the reference values with a steady state error. The error, as explained in chapter 2, is a result of the approximation that was used in the power control method and mismatch between modeled values and real values of the components. It should be noted that sum of the reference powers is set to zero ($\sum P_i^* = 0$) and the losses of a real converter are not considered. Therefore, realizing the exact value of reference powers is not possible. Port 4 represents the active bridge that is connected to the AC network through and interface AC/DC converter. This port is considered as the port that provides all the losses. In this regard, Port 4 is always controlled with an open loop; while the rest of the ports have a closed-loop PI controller. This is the reason for the small steady state error in P4 in Figure 4.13 despite being a closed-loop control test. Results of the "FB" control system confirm its ability to follow the reference powers without steady state error, however its speed is much lower compared to "FF" control. The "FB+FF", combining convergence speed of "FF" and steady state error elimination of "FB", shows a good performance both in terms of speed and accuracy in following reference powers (Figure 4.13).

Another test of power control scheme is shown in Figure 4.14 and Figure 4.15. In this test, power of port 1 and port 3 are recorded.

The open-loop results shown in Figure 4.14 show that powers of port 1 and port 3 follow their reference values with a steady state error, similar to what has been already observed with port 2 and port 4. Since both ports are controlled in closed-loop, their steady state error is eliminated with "FB+FF" control, as shown in Figure 4.15. The power step changes in the tests shown in Figure 4.14 and Figure 4.15 are applied independently in port 1 and port 3. The goal was to see the coupling between the powers. Small variations is observed in P1 as a change

occurs in P3, and vice versa. Comparing the coupling in Figure 4.14 and Figure 4.15 reveals that the small variations are quickly damped by the closed loop control.

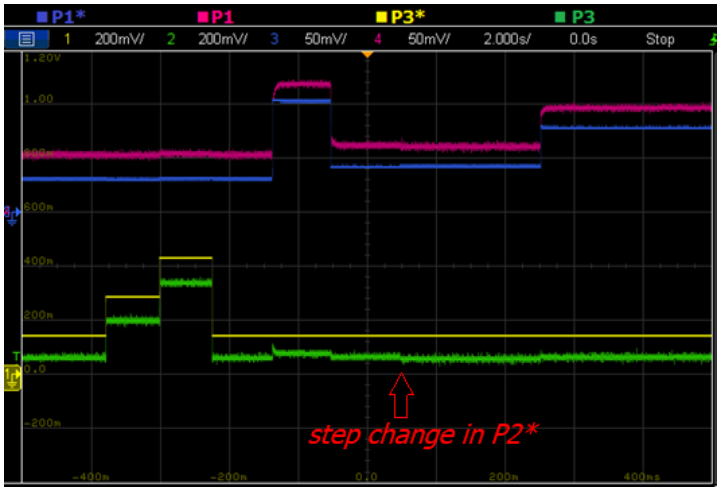

Figure 4.14: Open loop results of a step change in reference powers. The reference values (P1* and p3*) are shown along with their corresponding measured values (P1 and P3).

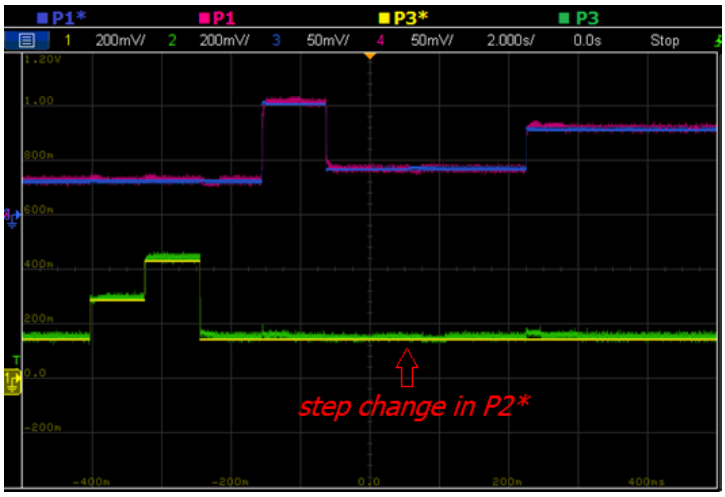

Figure 4.15: Closed loop results of the same test as Figure 4.14.

4.5. Model of losses

The loss models, proposed in chapter 3, were the subject of second category of tests. Different scenarios of power flow were defined and the measured losses were compared against the losses predicted by the models. Electronic DC sources/loads were connected to the active bridges and their output/input power was measured. In order to measure the input/output power of each port, DC link currents were measured using Agilent 34405A digital multi-meters. The losses were determined as the difference between sum of incoming powers and sum of outgoing powers of the QAB. The Efficiency was defined as sum of outgoing powers divided by sum of incoming powers. The loss model presented in section 3.1 is referred to as “model 1” and the computational cost efficient model, presented in section 3.2, will be designated as “model 2”.

Four scenarios were defined, based on application of the QAB in a green building. These scenarios will be studied in the following. An additional model, labeled "model 3", was defined based on the loss model in section 3.1, similar to "model 1". The difference between "model 1" and "model 3" is the way the soft switching conditions and switching losses are determined. "Model 3" uses the sign and magnitude of the current at the beginning of the dead time for this purpose (the calculations presented in the first part of section 3.1.3), while "model 1" considers the evolution of the current during the dead time (the enhanced model presented in the final part of section 3.1.3). Predictions of these models are almost identical, except in case of scenario 4. Therefore, "model 3" is not shown in the results of other scenarios to keep the figures as simple as possible.

Scenario 1:

In the first scenario, PV panels are the sole provider of the input energy, which is equally divided between the batteries and the loads on the DC grid. Figure 4.16 shows the results.

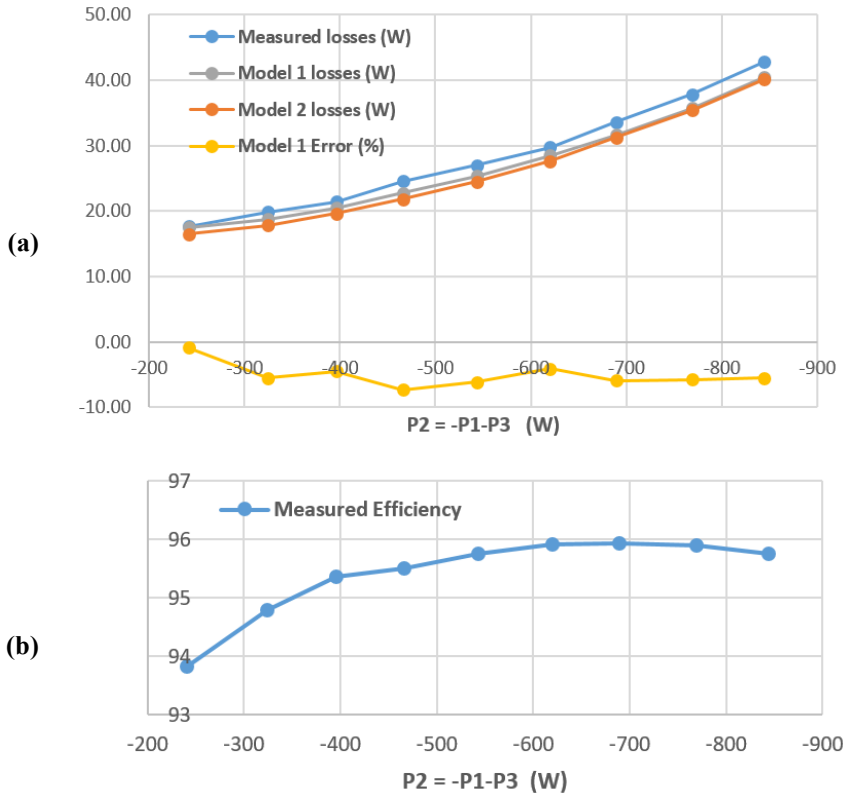

Figure 4.16: (a) Comparing measured losses with predictions of the loss models. (b) Evolution of efficiency as the powers increase. Port 2 is the source of energy and feeds port 1 and port 3 equally. Power transfer of port 4 is kept close to zero.

The results show that both models are able to predict the losses with a reasonable error. The converter operated up to around 60% nominal power with around 96% efficiency.

Scenario 2:

In this scenario, PV panels and AC grid are providers of the input energy, which is equally divided between the batteries and the loads on the DC grid. Figure 4.17 shows the results of this test.

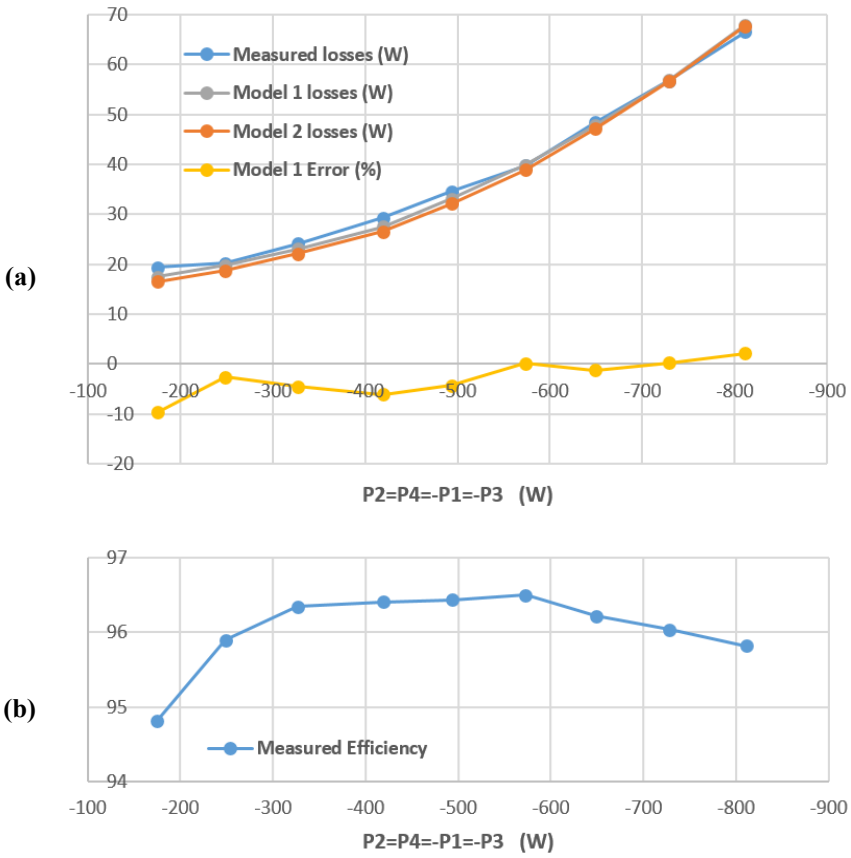

Figure 4.17: (a) Comparing measured losses with predictions of the loss models. (b) Evolution of efficiency as the powers increase. Port 2 is the source of energy and feed port 1 and port 3 equally. Power transfer of port 4 is kept close to zero.

The results show that the error of both models is within a reasonable range. Efficiency of the converter is higher at low powers compared to the previous scenario. It can be related to port 4, which does not transfer any power in scenario 1, leading to hard switching losses at low powers. In case of scenario 2, all the ports are transferring power leading to soft switching in every port and higher efficiency.

Scenario 3:

In scenario 3, PV panels provide energy for the loads on the DC grid. Power flow of port 2 and port 4 are around zero. Figure 4.18 shows the results of this test.

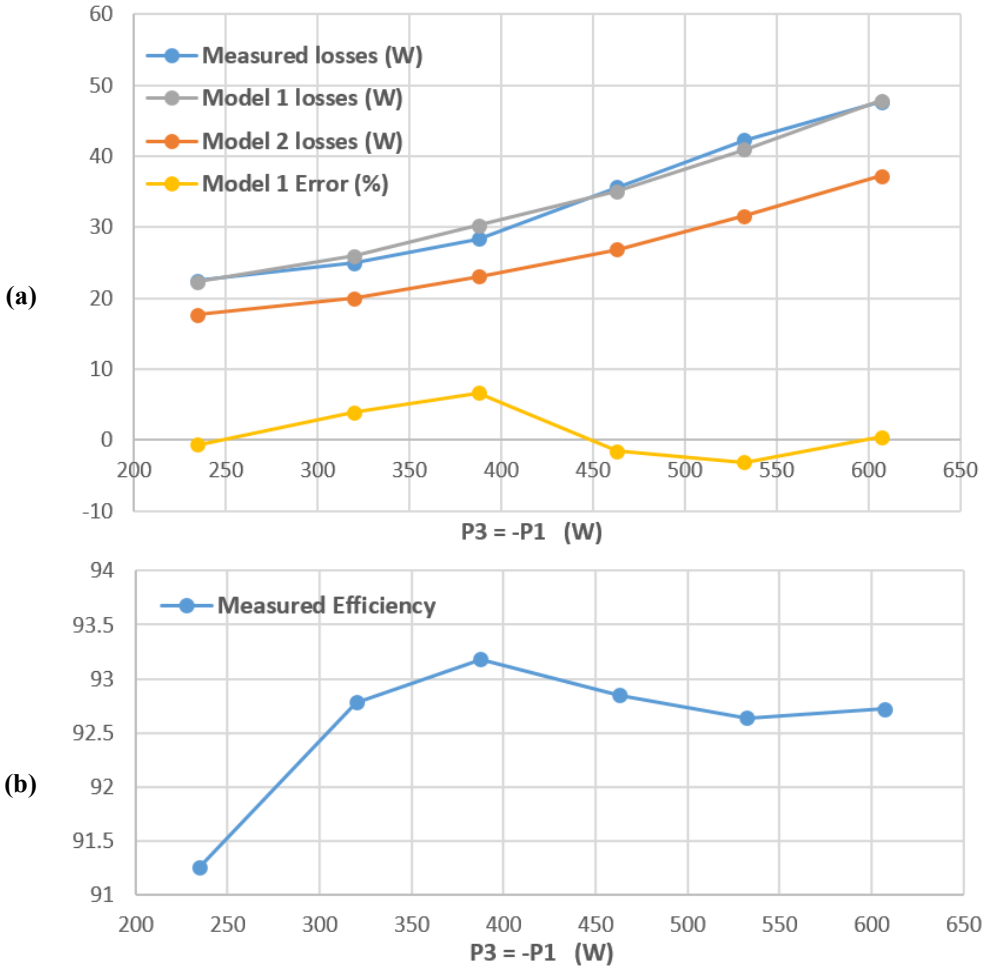

Figure 4.18: (a) Comparing measured losses with predictions of the loss models. (b) Evolution of efficiency as the powers increase. Port 1 is the source of energy and feed port 3. Power transfers of port 2 and port 4 are kept close to zero.

The results show that the error of "model 1" is within a reasonable range. The predictions of "model 2" however, are far from the measured losses. The reason for this big difference is the hard switching losses that occur in port 2 and port 4. Probably for the same reason, efficiency of the converter is lower compared to the previous scenarios. Another reason for lower efficiency can be the fact that two out of four ports do not contribute to real power exchange, while they involve certain amounts of reactive power, adding to the total conduction losses. It is worth noting that the CoolMOS devices used in port 2 have large output capacitance and body diode reverse recovery current. These characteristics result in wider hard switching range and higher hard switching losses, compared to the other switches in the converter.

Scenario 4:

In this scenario, PV panels and the AC network equally provide energy for the loads on the DC grid. Power flow of port 2 is around zero. Figure 4.19 shows the results of this test.

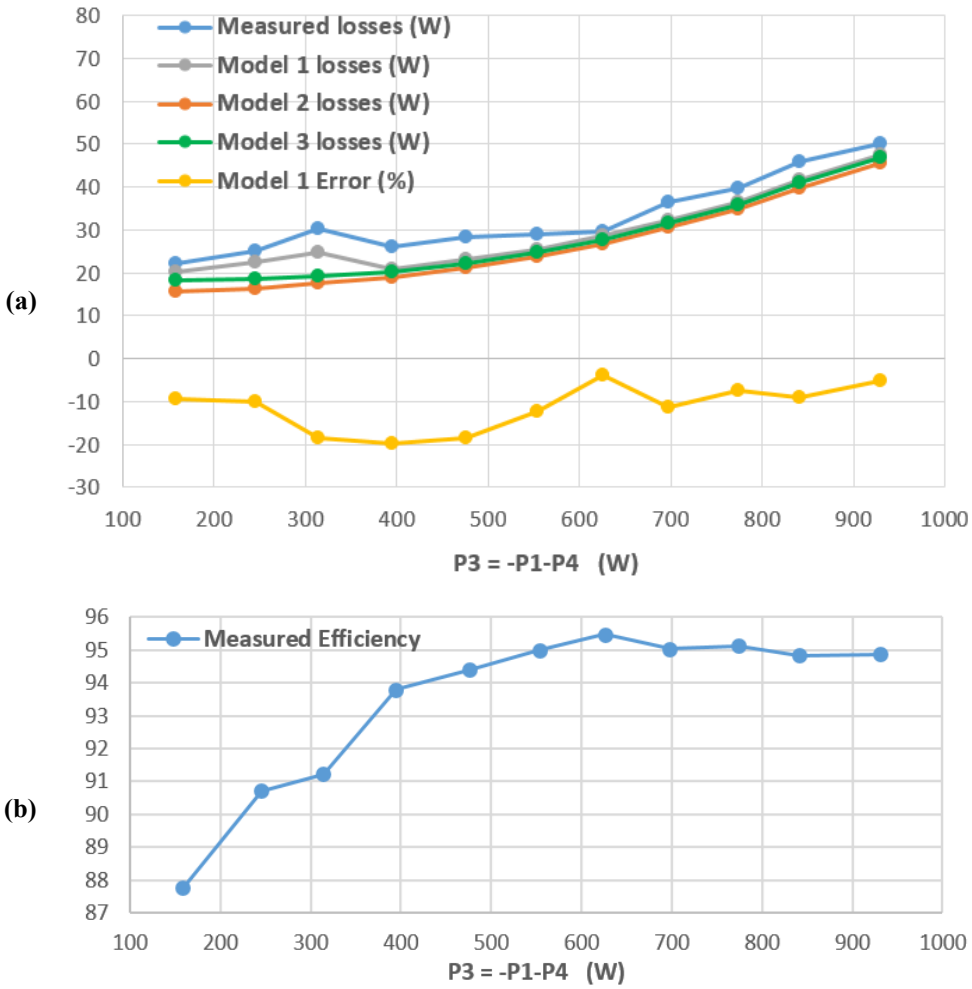

Figure 4.19: (a) Comparing measured losses with predictions of the loss models. (b) Evolution of efficiency as the powers increase. Port 1 and port 4 are the sources of energy and equally feed port 3. Power transfer of port 2 is kept close to zero.

As already explained, "model 3" in Figure 4.19-a is similar to "model 1", except that it determines switching conditions based on sign of the current at the beginning of the dead time. "Model 1", on the other hand, determines switching conditions and losses based on the enhanced switching model that was proposed in the end of section 3.1.3. Figure 4.19 clearly shows that the enhanced model has better performance in predicting switching modes. It implies the importance of considering evolution of the current during dead time.

It is noticeable that even the enhanced model involves large errors in predicting the losses, especially in low powers. As the power increases above 50% nominal power, the error falls inside the range of 10%. The error can be due to various factors affecting evolution of voltages and currents during dead time and nonlinear nature of reverse recovery losses in the MOSFETs. Similar to scenario 3, the CoolMOS switches involve hard switching losses. This subject will be studied more closely in the next section. The efficiency in this scenario is higher compared

to scenario 3 because three out of four ports are contributing to power transfer, reducing conduction losses.

4.5.1. Further assessment of the models

In order to better study the behavior observed in scenario 4, two additional tests were performed. The additional tests were done based on scenario 4 and with the exact phase shifts as the original test. In the first additional test, port 2 was disconnected from the converter, turning it to a TAB converter. Since this port was not exchanging any real power, but added to the switching losses and conduction losses in previous test, better efficiency is expected in this test, especially at low powers. The power flow is expected to change slightly. The efficiency of this test is labeled as "TAB mode" in Figure 4.20.

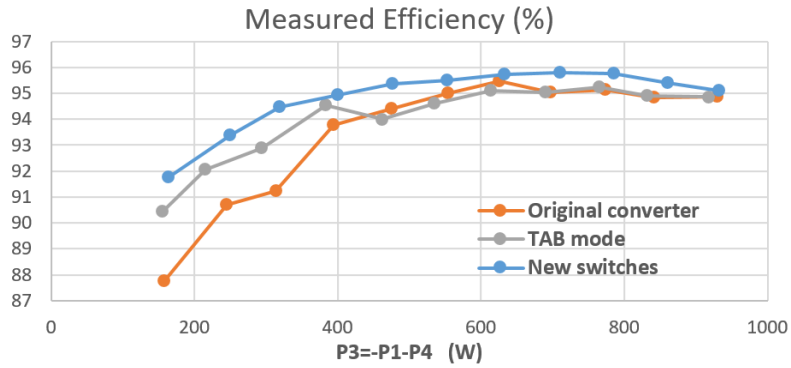

Figure 4.20: Comparing efficiency of different test in scenario 4.

The proposed solution was implemented on converter control as whenever the reference power of a port becomes zero, the control system turns off all the switches of that port. The results of a test scenario is displayed in Figure 4.21-a, where P2 and P4 are providing power for P1 and P3. During this test, P2 drops to zero and the control turns off its MOSFETs. The results show small dynamics in the system, as can be clearly seen in P3 (the red arrow in Figure 4.21-a). Small dynamics were already observed during power transients (Figure 4.14 and Figure 4.15), therefore, another test was performed in order to better recognize the origin of the dynamics in Figure 4.21-a. The results shown in Figure 4.21-b correspond to a manual disconnection of the second port with some delay after P2 is set to zero. The results have no indications of dynamic behavior. It can be concluded that this solution does not add significant dynamics to the system, but allows reducing the losses. Nonetheless, the close-loop control system is able to quickly damp any dynamics. Therefore, the QAB converter can continue to operate as a TAB without a need for modifying the feed-forward loop and its calculation of phase shifts.

It must be noted that this solution is possible thanks to the symmetric design of the converter, having an inductor on each port, as already explained in section 2.3.5. An asymmetric structure such as the structure proposed in [75] with a master port, would require modifications in the control system if the master port is disconnected.

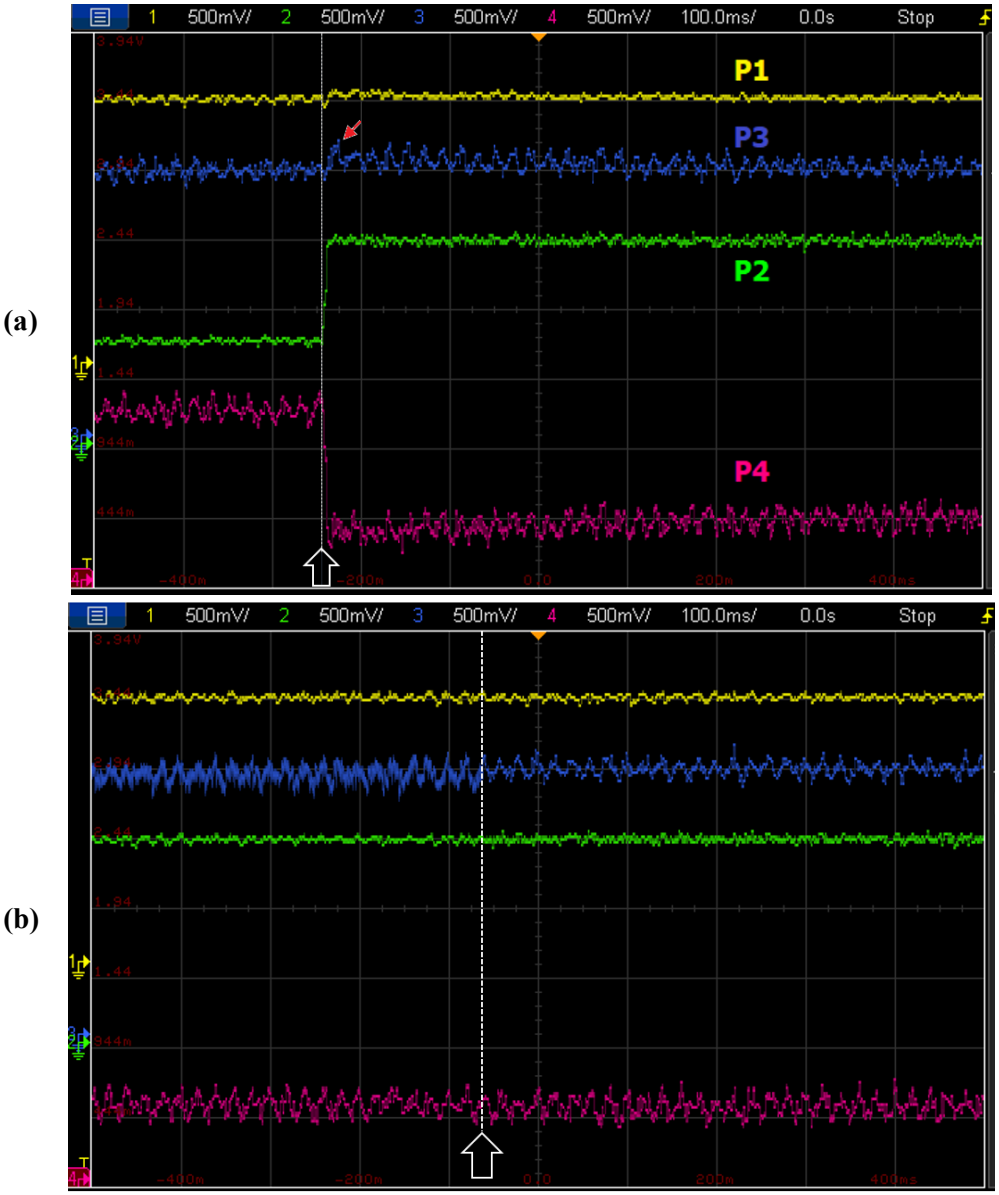

Figure 4.21: Performance of the converter if the ports with zero power transfer are disconnected: (a) automatically, by the control system; and (b) manually, after their power is set to zero. In this test P2 drops to zero and is disconnected at the moment indicated by the white dotted line.

The second additional test was to replace the CoolMOS switches by "SiHP22N60EF" silicon MOSFETs with fast body diodes. The new switches have smaller output capacitance and negligible reverse recovery losses. These characteristics result in better performance at low powers. This is illustrated in Figure 4.20, labeled as "New switches". However, on-state channel resistance is higher than that of the "IPP65R045C7" CoolMOS. Therefore, it will involve more

conduction losses at high powers, compared to the original converter. Due to the testing limits, the converter was tested up to around 66%, where the two switches show almost equal efficiency. The original converter is expected to have better efficiency at higher powers.

Due to the improvements observed in the additional tests, application of reverse parallel silicon carbide Schottky diodes can be another solution for reduction of losses. This solution is expected to improve efficiency of the original converter at low powers through reducing reverse recovery losses during hard switching. Compared to "TAB mode", which requires an additional control for connecting/disconnecting the ports, adding diodes does not involve any changes in the control; and unlike "New switches", employing diodes will not affect efficiency of the converter at higher powers. Therefore, it can be a suitable solution, which can be implemented independently or in combination with previous solutions, if the converter was to work at a wide range of power. This solution was not tested experimentally.

4.5.2. Conclusion

Comparison between the measured losses and the losses predicted by the models indicate that the proposed models can be counted upon under certain operating conditions, but can have significant errors in other operating points. Therefore, it is important to determine the range of validity of the models. Studying the proposed models revealed that their predictions have acceptable accuracy if the power transfer is high enough, which is the case in final application of this research. It can also be concluded that modeling the phenomena occurring inside all the components of the converter, such as evolution of voltages and currents during dead time and reverse recovery of body diodes, requires complex models.

The results of the original and additional experiments, proposed in this section, showed that performance of a MAB converter can be optimized by choosing proper components and control methods. This optimization can be performed globally or based on a specific application and for a specific mission profile. A model of losses is the main tool that is used for this optimization. Considering the fact that a cluster converter will usually work at high power operating points, the priority is to use MOSFETs with lowest conduction losses. Application of silicon carbide Schottky diodes can enhance the efficiency if certain MOSFETs have non-optimal switching characteristics. Disconnecting the ports that do not exchange power can be a complimentary solution to avoid large losses during the periods certain ports are not exchanging any real power.

4.6. DC currents in transformer windings

Formation of DC currents in transformer windings was studied in the previous chapter. Performance of the proposed DC current measurement setup was verified, too. The measurement setup will be used in the following experiments to assess correct operation of the method proposed for cancelation of DC currents during power transients. Finally, an active cancellation method of DC currents, based on the proposed measurement setup will be tested.

4.6.1. Sensor-less cancellation

The experiments that were presented in section 3.3.4 showed how power transients and the resulting changes in phase shifts lead to DC currents in transformer windings. These DC currents are usually damped very quickly, without major consequences. In applications where the transformer size is optimized, such as embedded applications, the margins can be limited and these transient currents can saturate the core, leading to distorted current waveforms. The distortion in the currents can cause malfunction in operation of other parts of the converter, hence, it is important to avoid them. The two-step phase shift control proposed in section 3.3.2 proved good performance in simulation results. Experimental validation of this method is shown in Figure 4.22.

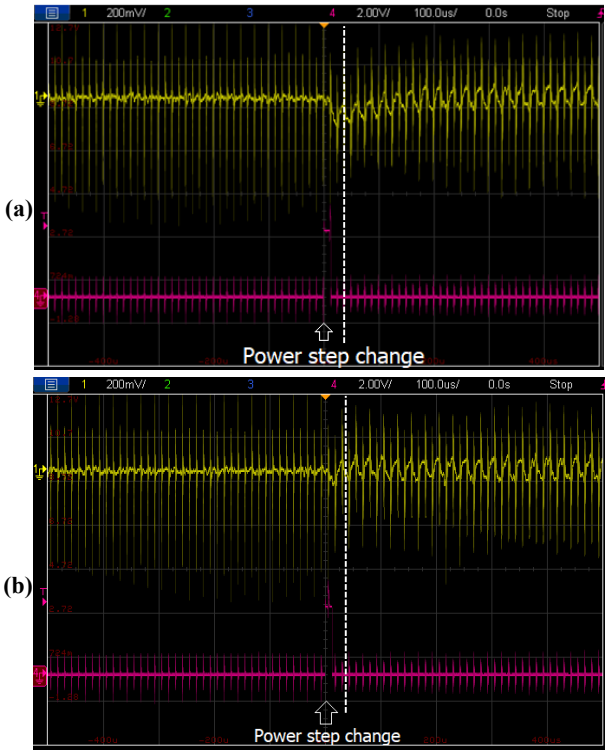

Figure 4.22: Performance of DC current cancellation during power transients. (a) Formation of DC current during power transient when cancellation is off; and (b) Preventing formation of DC current when the cancellation control is on. The yellow curve shows output of the DC current sensor setup. The white dotted line indicates the change in power flow and hence the phase shift, activating the two-step phase shift control to avoid formation of a DC current.

Whenever the control system detects a change in power flow, and consequently in the phase shift, it activates the two-step phase shift control. This control sends the mean value of the old and the new phase shift to the PWM unit for half a period. After this period, it send the new phase shift value to the PWM unit. The experiments shown in Figure 4.22 indicate correct operation of this control.

4.6.2. Active cancellation

As discussed in section 3.3.1, mismatch between characteristics of components, such as switches, gate drivers, or parasitic elements, can lead to a steady state imbalance between positive and negative voltages across transformer windings. These mismatches can result in a very small DC current offset, which can accumulate to a large DC current over time, saturating the core. Using a feedback from measuring these DC currents, it is possible to suppress them through trying to re-equalize length of positive and negative voltages across the windings. The DC current measurement setup, proposed in section 3.3.4, was used for this purpose.

The results of the experiments are illustrated in Figure 4.23. A DC current is generated in the windings by an intentional mismatch between length of positive and negative voltages. During the first series of tests, the active cancellation was disabled, allowing DC currents to flow as the ratio between duration of positive voltage and negative voltage changed. Variation of "No Control" curve in Figure 4.23 shows how quickly the current can have nonlinear increase when there is a mismatch. It also reveals a small mismatch that already exists in the converter, as the DC current is not zero at the center of the curve. In the next step, the active cancellation including a feedback loop was activated. A proportional (P) controller was first used in the feedback loop. The P controller is simple to implement and does not have a risk of instability, but the results show that is not able of effective DC currents cancellation. Therefore, the next test involved using a proportional-integral (PI) controller in the feedback loop. The results show that the active cancellation with a PI feedback loop is able to effectively suppress the DC currents in the windings.

Figure 4.23 shows that although the active cancellation loop significantly reduces the DC currents, it might not always be able to totally suppress them. This is due to the discretization of the signal generator hardware that defines a limit for the smallest possible modification to duration of positive or negative voltages. This limit in myRIO system that was used as the control hardware was 25 ns. Usually this limit is small enough to be sure of effective cancellation of the DC currents. In any case, if time step of the control hardware is large, small modifications can be performed directly through gate drivers. Changing the gate resistance or

gate-to-source voltage can generate small delays in turn-on and turn-off of the MOSFETs. A gate driver with adjustable gate voltages has been studied in [104].

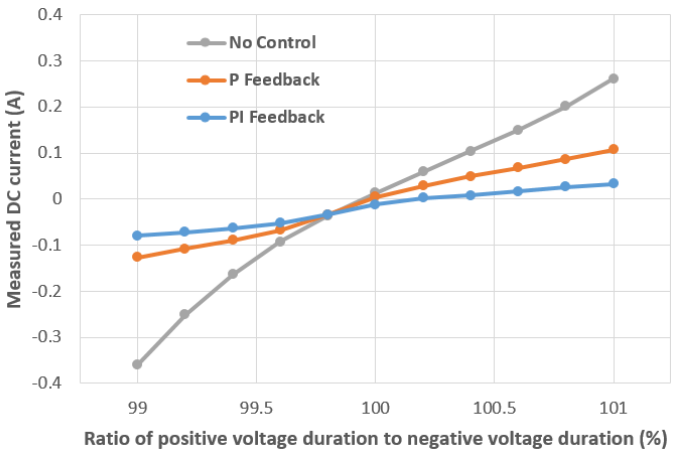

Figure 4.23: Active suppression of DC currents in the windings. The ratio of positive to negative voltage duration across the transformer windings is intentionally changing around 1 in order to generate a DC current.

4.7. Conclusion

This chapter presented a prototype of a QAB converter that was built for the purpose of experimental validation of the theoretical research works that were proposed in previous chapters. The first step was using the proposed design procedure to design a 4×2 kW QAB converter. Implementation of the models and control loops on a control hardware was explained. The control system was then debugged and verified via real-time HIL simulations. Only after this step, the experimental tests began. Performance of the proposed power control loops were studied in the first step. Predictions of loss models were compared against measurements in different scenarios. The proposed solutions for passive and active mitigation of DC currents in the windings were tested in the end and their correct operation was verified. The next chapter will present a thorough conclusion of all the subjects proposed in this thesis so far and an outlook to future works.

Conclusions

Wide application of renewable energy sources (RES) is pursued all over the world as one the most promising solutions that can address the climate change. Along with its advantages, implementations of RES have brought about several challenges. Many traditional strategies, architectures, and components are subject to reassessment and update regarding characteristics of RES, which significantly differ from those of classical resources of electricity. Increased application of energy storage devices in large and small scale is one of the changes that occurred in order to address the intermittent nature of RES. The DC nature of many RES, storage devices and loads push towards introduction of LVDC in micro- and nanogrids. One of the challenges that is a result of these changes, is the energy conversion architecture used for exchanging energy between the renewable resources, the storage devices, the existing AC network and the new DC network.

Chapter 1 was dedicated to introducing the goal of this research work, i.e., to address the challenge of energy exchange in microgrids with energy storage devices and DC networks. A cluster of multiport active-bridge (MAB) converters was proposed as a solution that involves several advantages. It was shown that the proposed solution benefits from intrinsic modularity both on cluster level and on converter level. This modularity helps simplify design, control and optimization even on a large scale. Furthermore, the architecture is compatible with emerging concepts such as internet of energy. With the help of simulations based on data from a smart building, it was illustrated that employing a cluster of multiple small converters reduces energy conversion losses and increases efficiency of the system, even when the power transfer is low. Clustering improves reliability due to the fact that the system can continue to provide services even if a fault occurs in one converter. An optimization strategy based on a simple model of losses was proposed and verified through simulations, to show how the additional flexibility introduced by clustering can be used for optimization purposes.

Chapter 2 introduced MAB converters as a candidate for building blocks of the cluster. The topology was introduced along with examples of its applications in more-electric aircraft, electric vehicles, microgrids, and battery managements systems. A brief comparison was presented between MAB topology and other possible candidates. Due to their symmetric and modular structure, application of MAB converters increases the potential to benefits from advantages of clustering. Furthermore, MAB converters provide galvanic isolation between their ports, which helps easier coordination of protection systems in a smart grid. They are able

to perform bidirectional power exchange between sources of different voltage levels. The transformer turn ratio provides the degree of freedom to connect DC sources whose voltage level are largely different. Different modeling methods, based on square-wave analysis and first harmonic analysis were proposed in this chapter. It was shown that accuracy of the first harmonic approximation is acceptable for most of the applications, such as power control. The converter models were used for putting forward a design procedure and different power control methods. The design procedure showed that a model of losses is required for optimizing the designed converter. Employing a model of losses makes it possible to design a converter that is optimized for a specific mission profile and certain operation conditions. This approach was used to design and build a converter, which was presented later in chapter 4.

Chapter 3 studied non-ideal characteristics of MAB converter and challenges of operation of a real converter. Two models of losses were proposed in this chapter, one being a detailed model that can be used for design purposes. The second model was a computational cost efficient model that can be used for real-time optimization purposes. The two models were compared in terms of accuracy and their runtime. The results showed that the efficient model has the same results as the detailed model if soft switching is guaranteed. It was concluded that the detailed model is suitable for offline applications, where accuracy is a priority rather than speed. The efficient model, on the other hand, is a better choice for real-time control and optimization purposes of cluster converters. As the cluster converters usually operate in soft switching conditions, the efficient model is expected to have enough accuracy in predicting the losses. Furthermore, Sources of DC currents in transformer windings were studied. Studying the methods of eliminating these DC currents, showed that measuring them is a challenge. An innovative sensor setup was proposed and tested. Test results confirmed correct operation of the method and its potential to be optimized for different purposes. The last part of chapter 3 was dedicated to variations of DC link voltages, how they affect performance of the converter, and the possible solutions to counter them. The comparisons based on the losses of different solutions showed that if the converter is going to operate close to its nominal power, full conduction voltage modulation is the optimal modulation.

Chapter 4 presented a 4×2 kW quadruple active-bridge converter that was designed and built in G2Elab for the aim of validating the models and controls that were proposed in previous chapters. Several tests and scenarios were designed and implemented for verification purposes. The power flow control was tested under different conditions. The results showed that the proposed control system is capable of controlling the flow of power in the converter, benefiting

from quick response of the feed-forward loop and steady state error correction capability of PI feedback loop at the same time. Predictions of proposed models of losses were compared against experimental measurements. The comparisons showed that each model has good accuracy under certain operating conditions and power level; therefore, it is vital to determine the domain of validity of the models before using them. Performance of passive and active DC current cancellation was verified in the end of chapter 4. The experiments showed that the proposed passive and active methods are able to effectively suppress steady state and transient DC currents.

This research has been done as a part of Eco SESA program. Eco SESA is a multidisciplinary project, aiming to produce knowledge, concepts, tools and methods to re-think the planning, management and governance of urban energy systems, as well as the design of their components. To reach safe, efficient, sustainable and accessible energy, these contributions were shared between the scientific communities and the city and energy stakeholders. The idea behind this specific research work was to propose a new hardware and architecture that can be used as a tool by other groups of Eco SESA, namely researchers involved in electrical networks. In this regard, the focus of the work was mainly on, but not limited to, power electronics. The goal was to be application-oriented and keep in mind how the final solution is going to be used in the electrical network. Proposing computational-cost-efficient power control method and model of losses was an attempt in this direction.

Outlook

Trying to address different aspects of the proposed solution and its application opened the door to a wide range of questions and possibilities. During the course of this PhD project, some of these possibilities were studied deeply and some of these questions were answered, while many of them were probed only briefly or not at all. This is where the future works can start. Some of these subjects are

- Studying application of different topologies, such as resonant topology, that have the potential to be used as building blocks of a cluster of multi-port converters. A thorough comparison between those topologies and the proposed MAB topology.
- A closer study on different solutions of interfacing MAB converters to AC network. It is possible to make the connection using common three- or four-leg inverters, multi-level converters or even direct connection thanks to a matrix converter. These

solutions can be studied in detail and compared in terms of parameters such as efficiency, ancillary service capabilities, complexity of control, or cost.

- It was assumed in this work that the converters are operated in a non-islanded operating mode. DC network is formed and supported by a separate high power converter. The proposed cluster of converter provided active and reactive powers to optimize the power flow and the use of the batteries/production units connected to the network. However, it is possible to employ the cluster for grid-forming function in islanded operating mode. This function will probably require coordinated control between the converters in the cluster. A distributed control scheme can also be a potential candidate for this purpose.
- The proposed cluster of converters is able to provide ancillary services to the network. This work did not investigate these possibilities, concentrating the efforts on the power sharing. A multidisciplinary research work can determine to what extent a cluster of converters can be used for providing ancillary service to the electrical network and the impact on the converter, the energy transfer and internal storages.
- Some ancillary services, such as unbalanced operations, which happen often in LV networks, induce some power fluctuations in the converter on the AC input. These fluctuations can be overcome through oversizing the capacitances, but it leads to an increase of the cost and volume of the system. The main issues of these fluctuations is that they can interact with the MAB control and be transmitted to sources or loads who are not able to mitigate it. A solution should be investigated to either confine the perturbations or redirect them to a specific output thanks to adapted MAB control.
- Certain models and controls were proposed for real-time optimization of power flow in a cluster, but they were never used in this work for that purpose. Application of the models and control for online control and optimization of a cluster of converters is an important step to show that the findings of this work can contribute to improvements in energy systems of microgrids.
- The proposed efficient model of losses can be improved to have better predictions. It might even be possible to predict switching conditions and losses without major increase in the amount of calculations. In addition, the proposed model of switching

in the detailed model can be enhanced if evolution of the current during dead time is predicted more accurately.

- The proposed DC current measurement setup with AC cancellation CT was studied briefly and it was shown that it has the potential to be optimized for different applications. However, in order to increase its performances, enhancements such as the addition of passive components to the secondary of the CT for adjusting its transfer function or optimizing the design to increase the performances can be subject of a complementary research.

Résumé de la these:

Clustering

Dans ce travail, nous allons parler de clusters de convertisseurs. Aussi afin de bien préciser ce que l'on entend par ce terme, il est important de préciser ce qu'est un cluster de convertisseurs et les fonctions qu'il est susceptible de remplir. Dans un système énergétique doté d'un cluster de convertisseurs, chaque fonction est assurée par plusieurs convertisseurs, contrairement aux solutions classiques à convertisseur unique. La figure 1.1 illustre le cluster de convertisseurs proposé. La figure 1.1 présente plusieurs fonctions, par exemple la connexion des éoliennes au stockage et aux réseaux permettant l'échange d'énergie entre le réseau CA et le réseau CC. Comme on peut le remarquer, il y a plusieurs convertisseurs en parallèle pour chaque fonction. Les convertisseurs de la figure 1.1 sont des convertisseurs quad-active-bridge (QAB), qui seront présentés et étudiés en détail dans le chapitre suivant. Les convertisseurs QAB du cluster peuvent connecter en un seul endroit un réseau alternatif, un réseau continu, un dispositif de stockage et une ressource renouvelable, et échanger simultanément de l'énergie entre tous ces éléments. Chaque convertisseur QAB est conçu sur la base d'une fraction de la puissance nominale globale de la fonction correspondante.

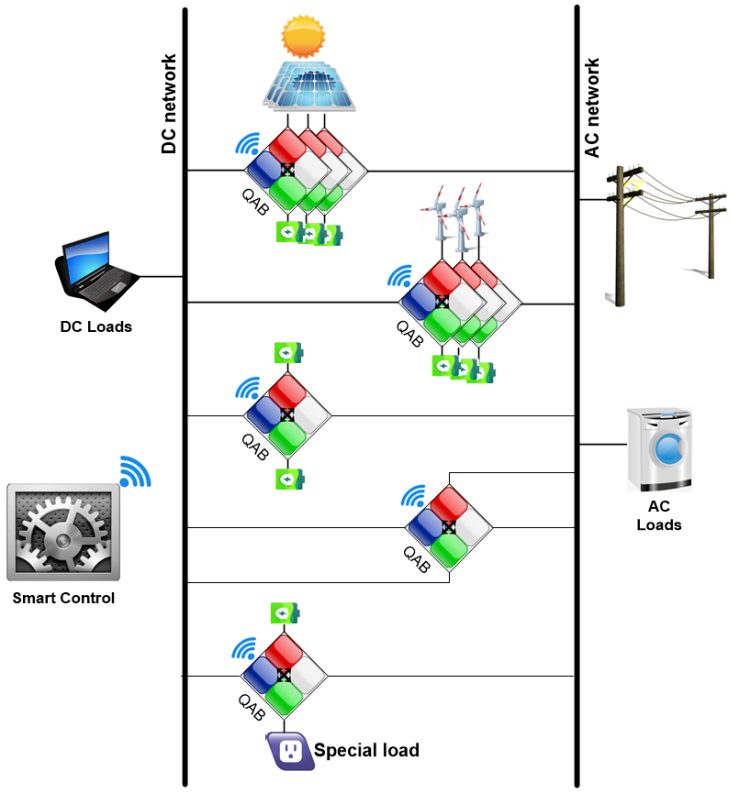

Figure 24: Un cluster de convertisseurs QAB, gérée par un contrôleur central.

Cette solution vise à résoudre les problèmes et les lacunes des solutions classiques actuelles qui utilisent un convertisseur par fonction, conçu pour pouvoir répondre à la demande maximale. Par conséquent, les convertisseurs fonctionnent généralement loin de leur puissance nominale avec un rendement bas pendant une partie considérable de leur cycle de vie. De plus, la perte d'un convertisseur peut entraîner la perte de tout le système ou d'une grande partie de celui-ci. Afin de relever ces défis, ce chapitre propose d'utiliser un cluster de convertisseurs. Chaque convertisseur est conçu pour une fraction de la puissance nominale. Dans ce cas, si un défaut survient dans un convertisseur, seule une petite partie de l'ensemble du système est perdue. La flexibilité et les fonctionnalités supplémentaires sont les autres avantages de l'utilisation d'un groupe de convertisseurs. Il est possible de réduire le coût global du système grâce à la standardisation des convertisseurs en tant qu'éléments constitutifs du cluster. Un contrôleur de haut niveau surveille les différents paramètres du micro-réseau et décide de la manière de répartir le flux d'énergie entre les convertisseurs du cluster. Lorsque le transfert de puissance est faible, certains convertisseurs sont déconnectés et les autres fonctionnent plus près de leur puissance nominale avec un meilleur rendement. Les résultats d'une simulation sur un cas d'étude ont montré que le rendement pouvait passer de 69 % avec un seul convertisseur à 82 % avec un groupe de plusieurs convertisseurs [40]. Il a été démontré qu'une amélioration

supplémentaire de l'efficacité est possible en appliquant des stratégies d'optimisation sur le groupe. Deux stratégies simples ont été testées et les résultats ont montré qu'elles étaient capables de réduire les pertes de 5% par rapport à un contrôle de cluster sans stratégie d'optimisation (accepté dans [41]).

Convertisseurs multiport active-bridge : introduction, conception et contrôle

Ce chapitre propose d'utiliser des convertisseurs multiports à active-bridges (MAB) comme éléments constitutifs du cluster de convertisseurs afin d'exploiter tout le potentiel du clustering. L'ensemble du système ressemble alors au schéma de la figure 1.1, où le même convertisseur MAB est utilisé pour différentes fonctions en tant qu'éléments constitutifs du cluster. Outre les améliorations en termes d'efficacité, de fiabilité et de flexibilité, certains avantages sont spécifiques à cette topologie, notamment :

6. L’échange bidirectionnel de puissance entre plusieurs ports en même temps, ce qui réduit les étapes de conversion et donc les pertes ;
7. La compatibilité des niveaux de tension, ou la possibilité de connecter des objets ayant des niveaux de tension différents en ajustant le rapport de transformation ;
8. La topologie symétrique, qui permet une conception, un contrôle et une optimisation plus faciles ;
9. La réduction des coûts grâce à la normalisation des blocs de construction et à la mutualisation des coûts de conception ;
10. La Fourniture d’une infrastructure matérielle pour la réalisation de réseaux intelligents et de l'internet de l'énergie.

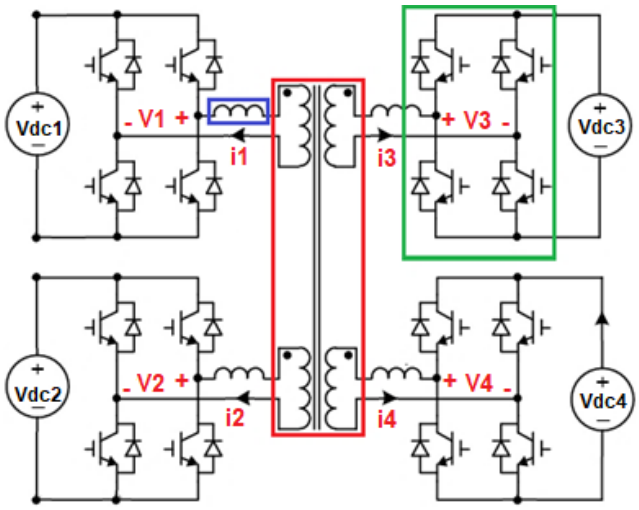

Figure 25: Un convertisseur QAB : la boîte verte montre un active-bridge ; la boîte rouge est un transformateur à enroulements multiples ; la boîte bleue est une inductance, qui peut être soit une inductance externe, soit l'inductance de fuite du transformateur.

Les MOSFETs dans les active-bridges commutent généralement dans des conditions de commutation douce. Par conséquent, les pertes de commutation sont négligeables et il est possible d'augmenter la fréquence de commutation. Une fréquence de commutation plus élevée signifie que les composants magnétiques du transformateur et des inductances peuvent être très petits, donc une réduction de la taille et du poids du convertisseur. Les inductances agissent comme un stockage d'énergie à haute fréquence et sont donc de petite taille. En outre, elles constituent un moyen de contrôler le flux de courant. La valeur de l'inductance est inversement proportionnelle à la puissance nominale du convertisseur. Par conséquent, les noyaux des inductances peuvent être très petits, même dans les convertisseurs de haute puissance.

Les déphasages sont les principaux paramètres de contrôle dans un MAB. Deux types de déphasages peuvent être définis : les déphasages internes et les déphasages externes, comme le montre la figure 2.2 pour un DAB. Le déphasage interne est le déphasage (ou le délai) entre la commutation de deux branches d'un seul pont actif. Le déphasage interne contrôle le rapport cyclique de la tension de sortie du pont actif et conduit à des périodes où la tension de sortie est nulle. Par conséquent, il sera appelé "rapport cyclique" à partir de maintenant, par souci de simplification. Le déphasage externe est le déphasage entre les premières harmoniques des tensions de sortie de deux ponts actifs. Le déphasage externe sera appelé "déphasage" à partir de maintenant. Un modèle peut déterminer les formes des courants, leurs valeurs crête et efficace, les pertes correspondantes et l'échange de puissance entre les ports. En outre, un modèle peut être utilisé pour déterminer les cycles d'utilisation et les déphasages à appliquer à chaque port afin d'obtenir le flux de puissance souhaité entre les ports.

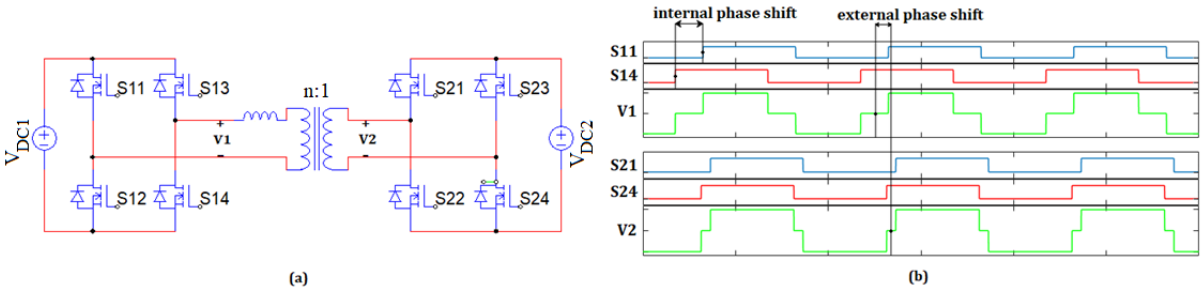

Figure 26: déphasages interne et externe dans la commutation d'un DAB. Les interrupteurs d'un même bras sont commutés de manière complémentaire.

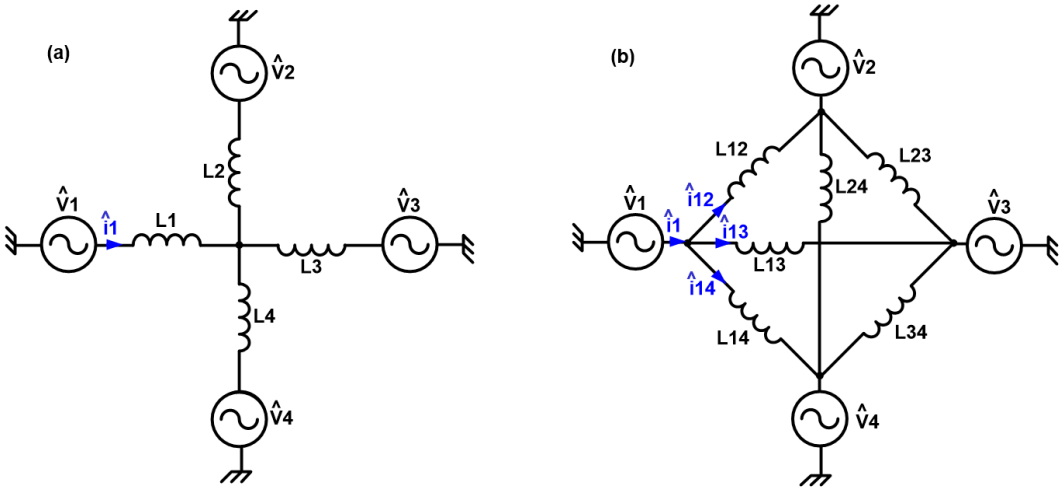

Figure 27: Différentes modélisation des convertisseurs MAB : (a) Modèle de première harmonique d'un convertisseur MAB ; (b) Modèle de première harmonique d'un MAB après application de la transformation étoile-triangle sur le réseau d'inductances.

Les convertisseurs MAB, en tant que candidat proposé pour une application dans un groupe de convertisseurs, sont étudiés dans ce chapitre. Leurs avantages sont présentés au départ puis plusieurs façons de les modéliser sont proposées. Les règles et considérations de conception sont discutées pour les principaux composants du convertisseur. Les modèles proposés sont utilisés pour trouver un moyen de contrôler le flux de puissance dans les convertisseurs MAB. Comme aucune solution analytique précise n'a été trouvée pour déterminer les flux de puissance, des méthodes approximatives et itératives sont proposées. Les méthodes proposées sont comparées en termes de précision, de vitesse de convergence et de quantité de calculs nécessaires. Une étude approfondie des compromis dans les optimisations de conception et de contrôle a montré qu'un modèle des pertes est nécessaire.

Convertisseurs multiport active-bridge : fonctionnement et pertes

Le chapitre précédent a présenté les convertisseurs MAB, étudié leur conception et proposé des méthodes pour leur modélisation et leur commande. Le convertisseur étudié dans le chapitre précédent était un convertisseur idéal, fonctionnant généralement dans des conditions idéales ou proches de l'idéal. Les différences entre un convertisseur réel et un convertisseur idéal peuvent entraîner une incohérence importante entre les performances attendues du convertisseur et celles qui seront observées dans le monde réel. De plus, les caractéristiques non idéales peuvent provoquer des conditions qui conduisent à une défaillance. À cet égard, il est important d'étudier un convertisseur avec des caractéristiques non idéales afin d'obtenir une compréhension plus précise du convertisseur et d'être capable de relever les défis de l'utilisation d'un convertisseur réel.

Une grande partie de la différence entre un convertisseur idéal et un convertisseur réel sont les inductances et les résistances dans les enroulements, les canaux MOSFET, les pistes du PCB et dans les dispositifs de mesure. Les décalages entre la valeur prédite et la valeur réelle de certains paramètres, telles que les inductances ou la résistance thermique entre les boîtiers MOSFET et les dissipateurs thermiques, constituent un autre type de caractéristiques non idéales. En outre, les variations des tensions de liaison CC sur certains ports et les retards inégaux dans les circuits de commande de grille sont des conditions qui peuvent se produire fréquemment pendant le fonctionnement d'un convertisseur MAB.

Les convertisseurs MAB ont été proposés comme bloc de construction du groupe de convertisseurs dans le premier chapitre. Le chapitre précédent a étudié la modélisation et le contrôle de ces convertisseurs. Il a montré qu'un modèle de pertes permet non seulement de mieux comprendre les phénomènes internes des convertisseurs MAB, mais constitue également un bon outil pour optimiser leur conception et leur contrôle. Ce chapitre est consacré à l'étude des pertes dans les convertisseurs MAB et aux défis de leur utilisation en conditions réelles. Tout d'abord, deux modèles différents de pertes sont proposés, l'un étant plus détaillé et l'autre plus efficace en termes de coûts de calcul. La présence de courants continus dans les enroulements des transformateurs, menant à la saturation des noyaux magnétiques, est ensuite étudiée. Les origines des courants continus, les défis pour les mesurer et les éviter sont également discutés. Un autre défi dans le fonctionnement des convertisseurs MAB est la

déviation des tensions de liaison CC de leur valeur nominale. Ce défi et les moyens potentiels de le relever font l'objet de la dernière partie de ce chapitre.

Résultats

Les chapitres précédents ont présenté une procédure de conception, certains modèles de pertes et des schémas de commande de puissance, ainsi que des méthodes de mesure et de suppression des courants continus dans les enroulements. Ce chapitre est consacré à la présentation d'un convertisseur QAB qui a été conçu et construit sur la base de la procédure de conception proposée. Ce prototype a ensuite été utilisé pour évaluer la précision des modèles proposés, valider les performances des méthodes de contrôle de la puissance et évaluer la mesure et la suppression correcte des courants continus dans les enroulements.

Table 7: Tensions et courants nominaux du prototype

Paramètre	**Port 1**	**Port 2**	**Port 3**	**Port 4**
Connexion	Batteries	PV panels	Réseau CC	Réseau CA
Voltage	100 V	200 V	400 V	800 V
Courant CC	22 A	11 A	5.5 A	2.75 A
Direction de puissance	Bidirectionnel	Unidirectionnel	Bidirectionnel	Bidirectionnel

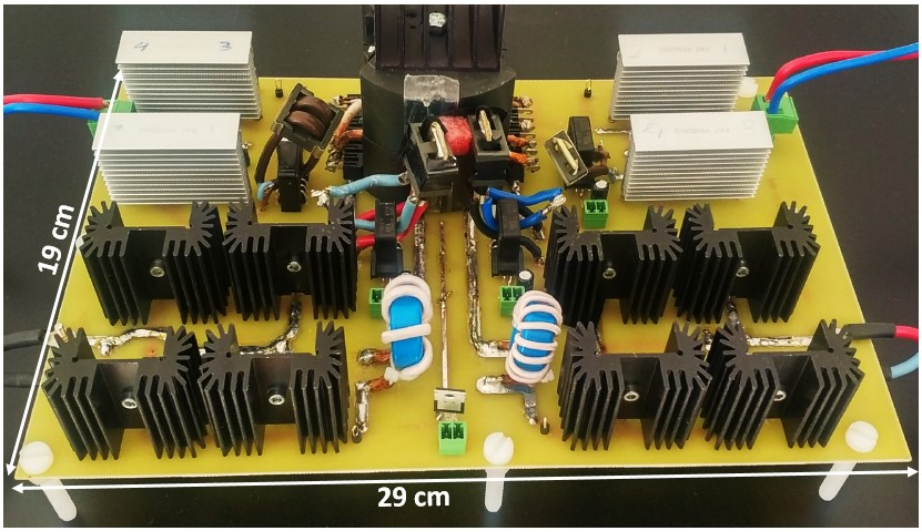

Figure 28: prototype QAB 4x2kW.

Le montage de l'essai est illustré à la figure 4.1. Un système NI myRIO 1900 est utilisé comme système de contrôle, exécutant le schéma de contrôle programmé dans l'environnement NI LabVIEW. Le système est basé sur un système Zynq comprenant un processeur ARM et un FPGA. Les calculs et les méthodes de contrôle sont calculés dans la partie processeur. Le FPGA

du myRIO 1900 comprend les circuits logiques pour générer les signaux de commande des MOSFETs avec les déphasages qui sont reçus du processeur. La conversion analogique-numérique, le filtrage numérique et la mise à l'échelle des entrées analogiques, y compris les mesures de tension et de courant, sont également effectués dans le FPGA pour optimiser la vitesse, puis transmis aux boucles de rétroaction, qui sont dans le processeur.

(a)

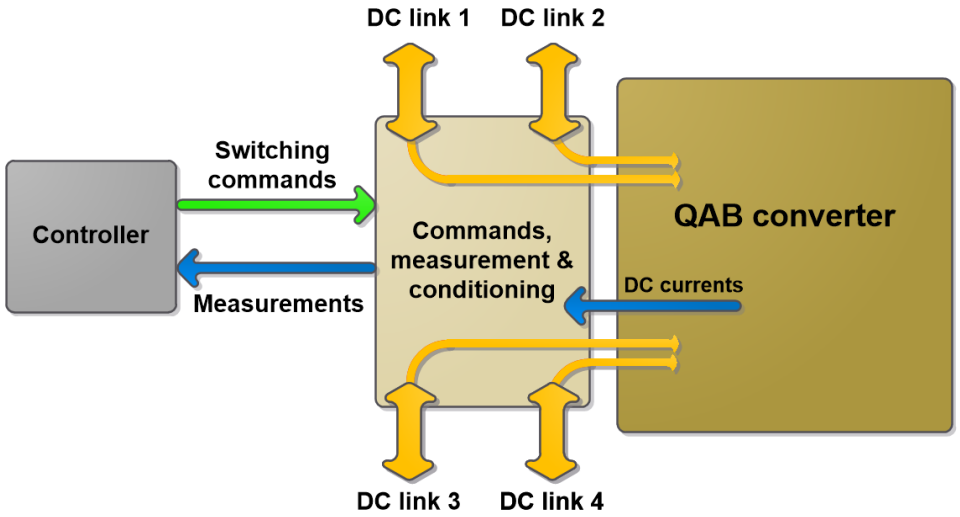

(b)

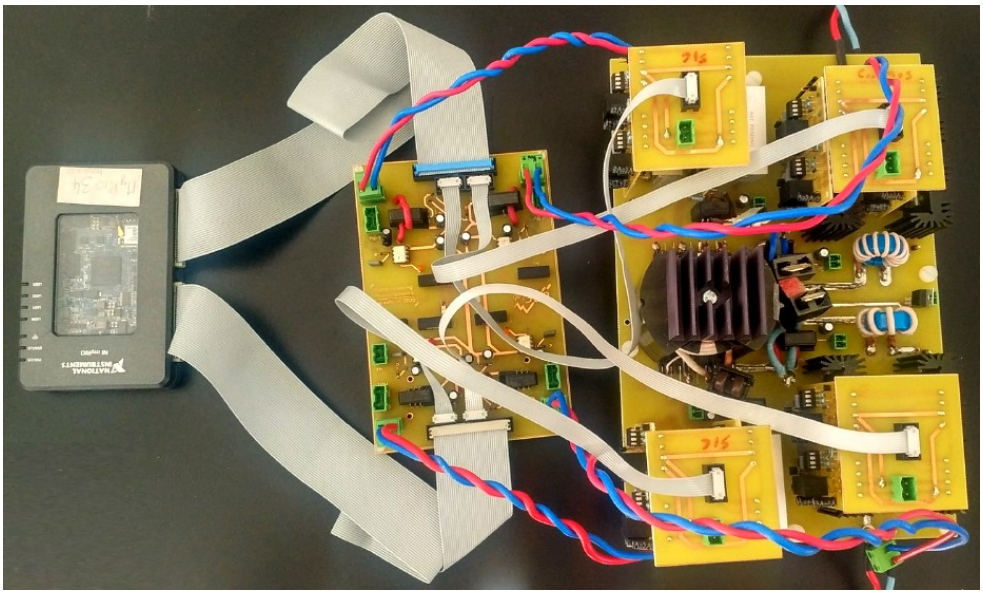

Figure 29: Le banc de test : (a) les schémas et (b) le montage d'essai réel, y compris le convertisseur QAB, la carte de mesure et de conditionnement et le contrôleur. Les flèches jaunes dans (a) indiquent les connexions d'alimentation, et les autres sont des signaux de commande et de mesure.

Validation hardware-in-the-loop (HIL)

Après avoir implémenté les systèmes de contrôle dans le myRIO 1900 à l'aide de codes et de blocs disponibles dans l'environnement LabVIEW et avant de le connecter au prototype, une simulation HIL a été utilisée pour une première validation du contrôle embarqué. Les simulations HIL ont permis de trouver et de rectifier les conditions anormales et les défauts de

codage du système de contrôle rapidement et sans risque de dommages. La première validation des méthodes de contrôle de la puissance et de suppression du courant continu a été effectuée en utilisant la cible OPAL RT 5700. Après avoir vérifié le bon fonctionnement du système de contrôle embarqué celui-ci a été connecté au prototype de convertisseur pour la validation expérimentale des modèles et des méthodes de contrôle proposés. À cet égard, la simulation HIL a été un outil pratique qui a permis un débogage rapide et sûr du contrôle commande. Les sections suivantes présentent les résultats des tests expérimentaux.

(a)

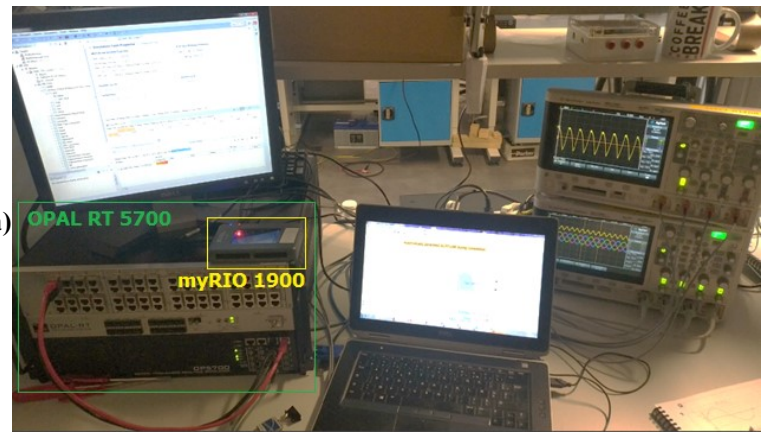

(b)

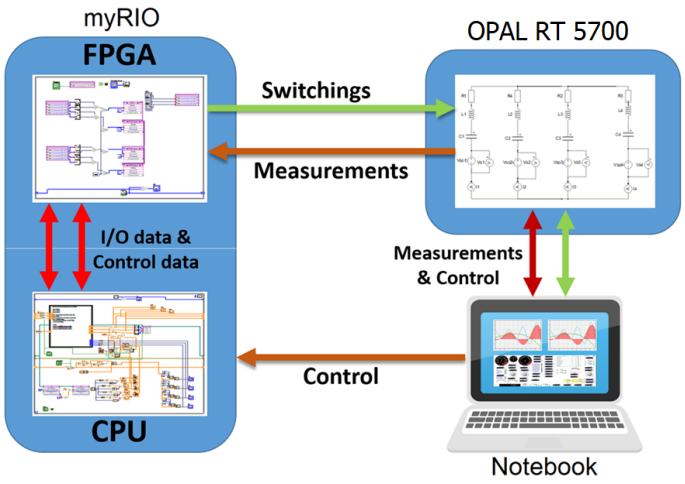

Figure 30: Configuration de la simulation en temps réel avec le simulateur OPAL RT 5700.

Contrôle de puissance

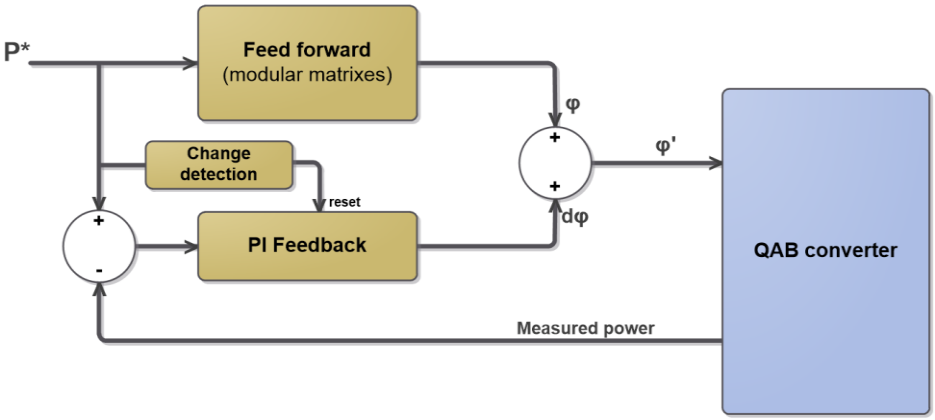

Figure 31: Schéma de commande en boucle fermée avec une boucle feed-forward et une boucle feed-back.

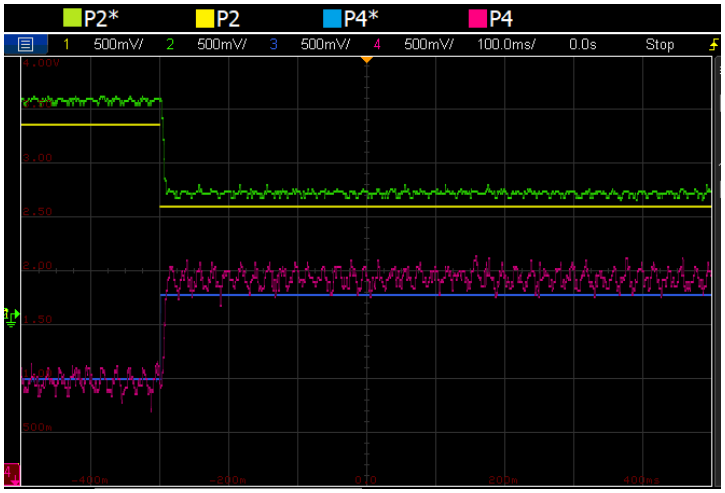

Figure 32: Résultats en boucle ouverte d'une variation en échelon des puissances de référence. Les valeurs de référence (P2* et p4*) sont indiquées avec les valeurs mesurées correspondantes (P2 et P4).

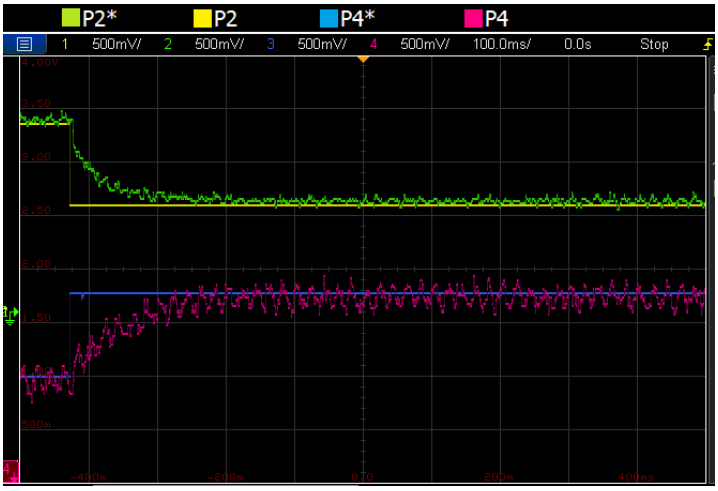

Figure 33: Résultats en boucle fermée du même test que la Figure 0.5. Le système de contrôle est composé d'une boucle de rétroaction PI seule.

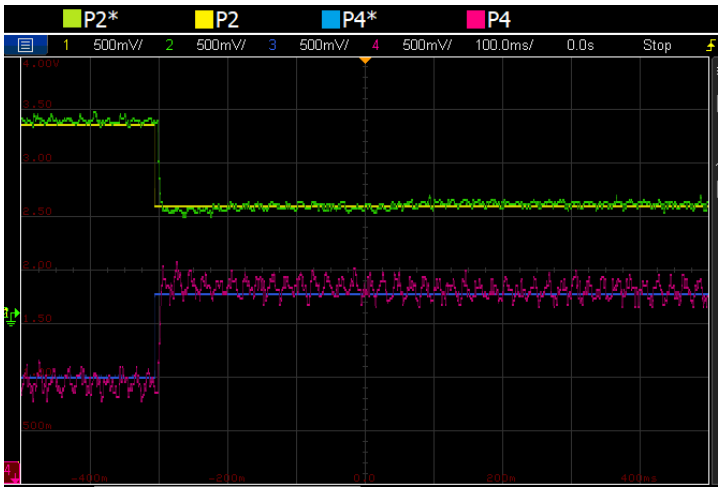

Figure 34: Résultats de la boucle fermée du même test que la Figure 0.5. Le système de contrôle comporte des boucles de rétroaction PI et de rétroaction matricielle activées.

Modèle de pertes

Scenario 1 :

Dans le premier scénario, les panneaux PV sont les seuls à fournir l'énergie qui est répartie équitablement entre les batteries et les charges du réseau CC. La figure 4.10 montre les résultats.

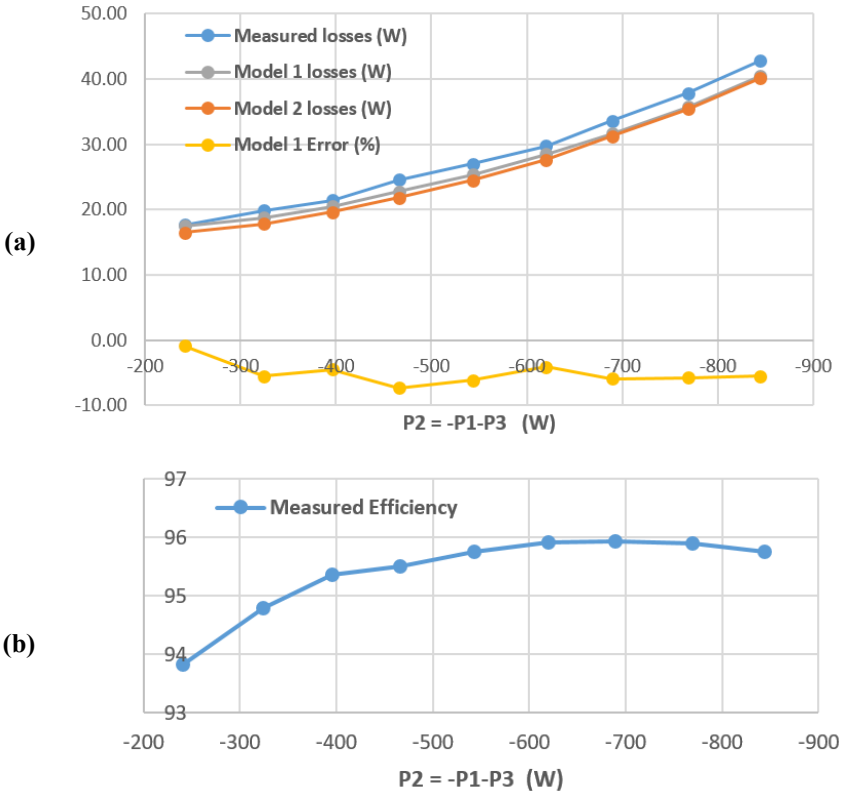

Figure 35: (a) Comparaison des pertes mesurées avec les prédictions des modèles de pertes. (b) Evolution du rendement au fur et à mesure que les puissances augmentent. Le port 2 est la source d'énergie et alimente les ports 1 et 3 de manière égale. Le transfert de puissance du port 4 est maintenu proche de zéro.

Scenario 2 :

Dans ce scénario, les panneaux PV et le réseau CA sont les fournisseurs d'énergie qui est répartie de manière égale entre les batteries et les charges du réseau CC. La figure 4.11 montre les résultats de ce test.

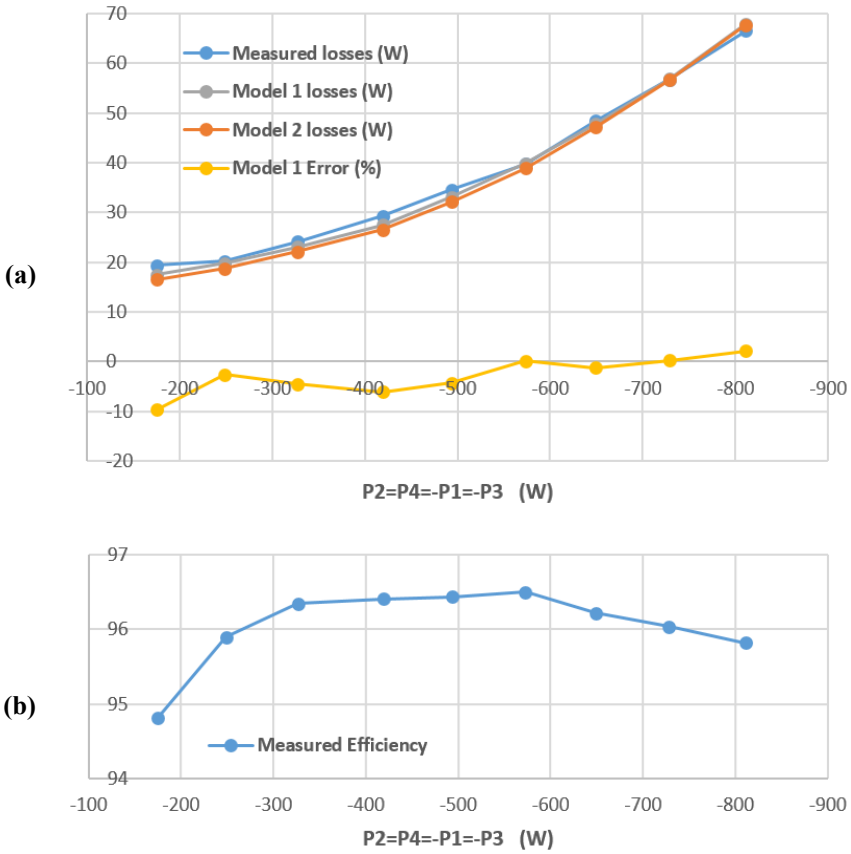

Figure 36: (a) Comparaison des pertes mesurées avec les prédictions des modèles de pertes. (b) Evolution du rendement au fur et à mesure que les puissances augmentent. Le port 2 est la source d'énergie et alimente le port 1 et le port 3 de manière égale. Le transfert de puissance du port 4 est maintenu proche de zéro.

Scenario 3 :

Dans le scénario 3, les panneaux PV fournissent de l'énergie pour les charges sur le réseau CC. Les flux de puissance des ports 2 et 4 sont proches de zéro. La figure 4.18 montre les résultats de ce test.

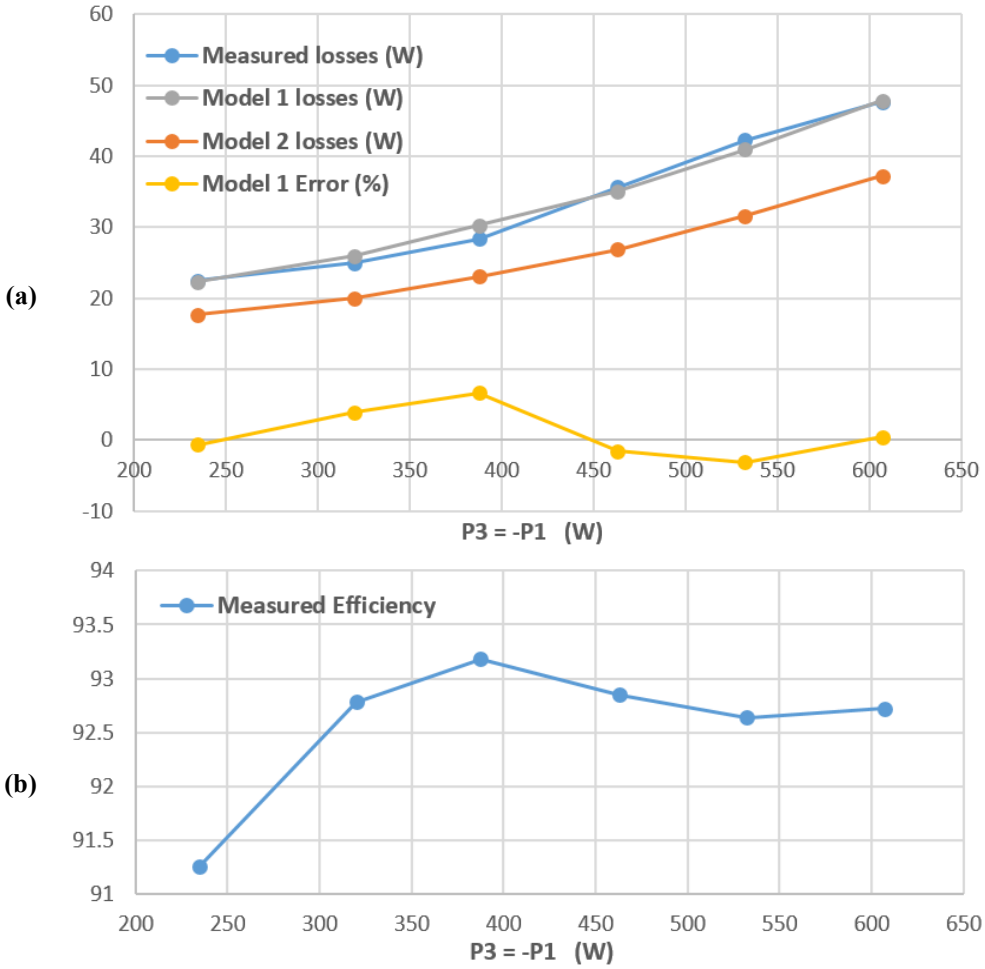

Figure 37: (a) Comparaison des pertes mesurées avec les prédictions des modèles de pertes. (b) Evolution du rendement au fur et à mesure que les puissances augmentent. Le port 1 est la source d'énergie et alimente le port 3. Les transferts de puissance des ports 2 et 4 sont maintenus proches de zéro.

Scenario 4 :

Dans ce scénario, les panneaux PV et le réseau CA fournissent également de l'énergie pour les charges du réseau CC. Le flux de puissance du port 2 est proche de zéro. La figure 4.19 montre les résultats de ce test.

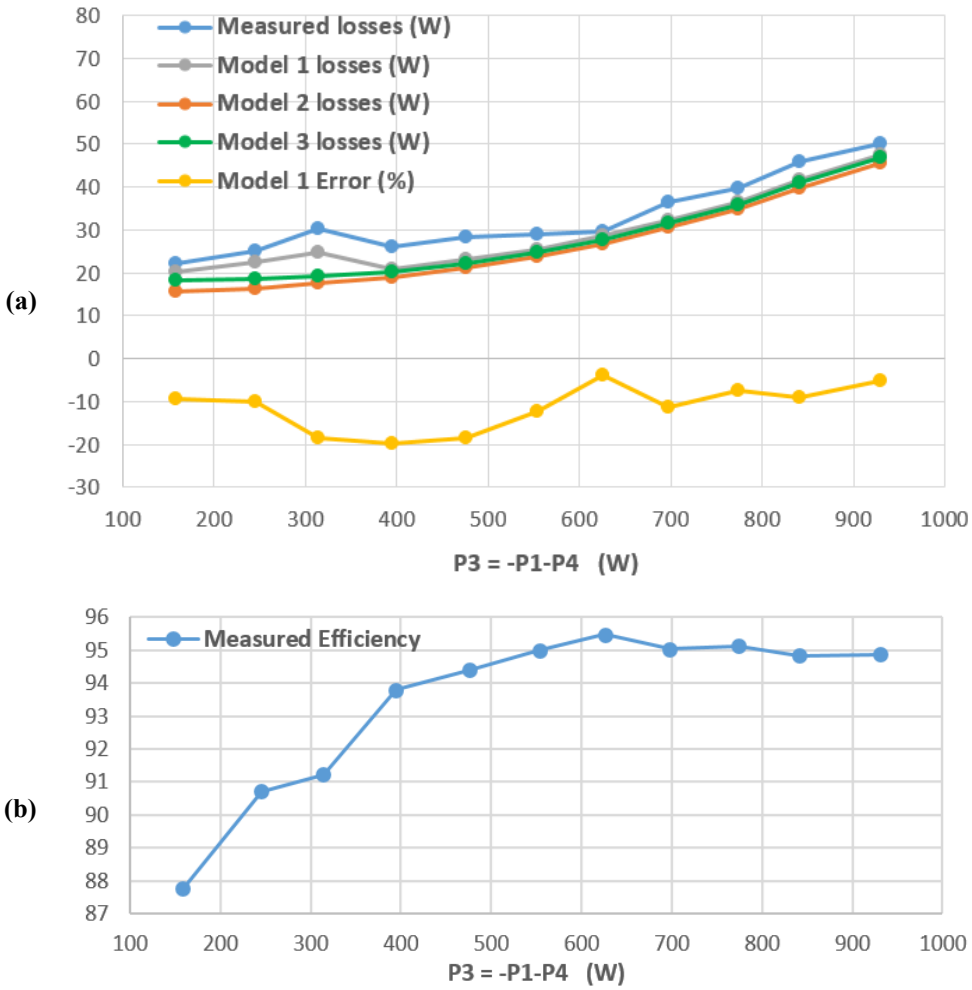

Figure 38: (a) Comparaison des pertes mesurées avec les prédictions des modèles de pertes. (b) Evolution du rendement au fur et à mesure que les puissances augmentent. Les ports 1 et 4 sont les sources d'énergie et alimentent également le port 3. Le transfert de puissance du port 2 est maintenu proche de zéro.

Courants continus dans les enroulements du transformateur

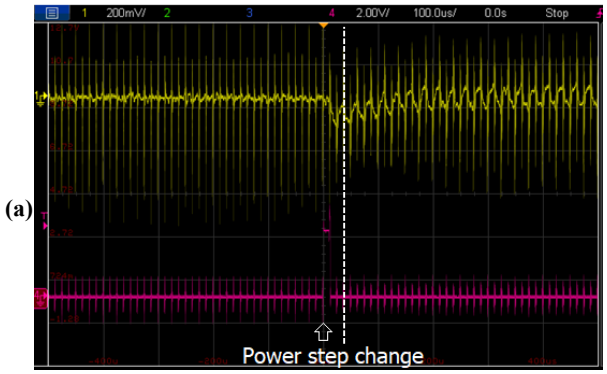

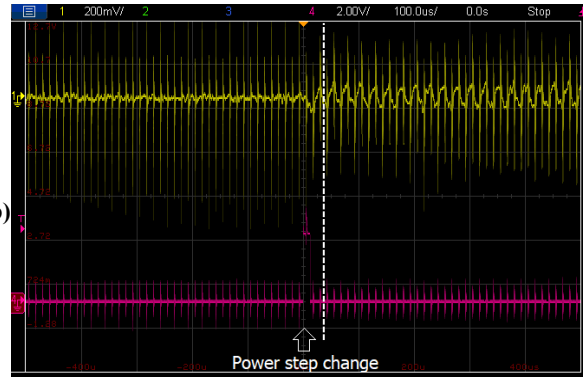

Figure 39: Performance de l'annulation du courant continu pendant les transitoires de puissance. (a) Formation de courant continu pendant les transitoires de puissance lorsque l'annulation est désactivée ; et (b) Prévention de la formation de courant continu lorsque la commande d'annulation est activée. La courbe jaune montre la sortie de la configuration du capteur de courant continu. La ligne pointillée blanche indique le changement du flux de puissance et donc le déphasage, activant la commande de déphasage en deux étapes pour éviter la formation d'un courant continu.

Annulation active

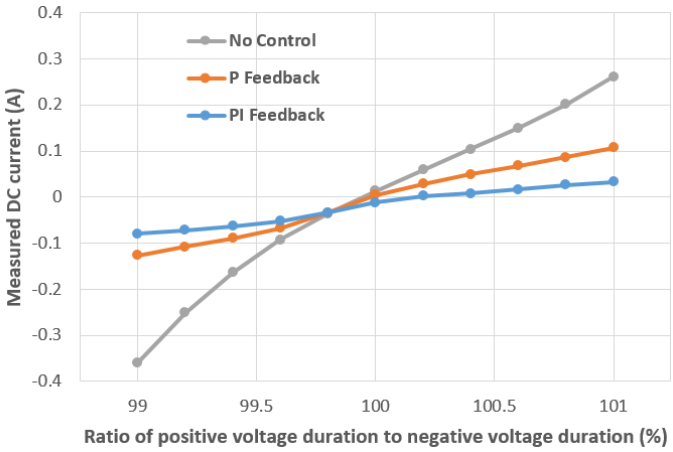

Figure 40: Suppression active des courants continus dans les enroulements. Le rapport entre la durée de la tension positive et négative aux bornes des enroulements du transformateur varie intentionnellement autour de 1 afin de générer un courant continu.

Conclusions

L'application à grande échelle des sources d'énergie renouvelables (SER) est considérée dans le monde entier comme l'une des solutions les plus prometteuses pour lutter contre le changement climatique. Parallèlement à ses avantages, la mise en œuvre des SER a entraîné plusieurs défis. De nombreuses stratégies, architectures et composants traditionnels font l'objet d'une réévaluation et d'une mise à jour en fonction des caractéristiques des SER, qui diffèrent sensiblement de celles des ressources classiques en électricité. L'application accrue de dispositifs de stockage d'énergie à petite et grande échelle est l'un des changements intervenus pour faire face à la nature intermittente des SER. La nature en courant continu de nombreuses sources d'énergie, de dispositifs de stockage et de charges pousse à l'introduction des réseaux courant continus à basse tension dans les micro- et nanoréseaux. L'un des défis résultant de ces changements est l'architecture de conversion d'énergie utilisée pour échanger de l'énergie entre les ressources renouvelables, les dispositifs de stockage, le réseau CA existant et le nouveau réseau CC.

Le chapitre 1 a été consacré à la présentation de l'objectif de ce travail de recherche, à savoir relever le défi de l'échange d'énergie dans les micro-réseaux avec des dispositifs de stockage d'énergie et des réseaux à courant continu. Un cluster de convertisseurs MAB (multiport active-bridge) a été proposé comme solution présentant plusieurs avantages. **Le chapitre 2** présente les convertisseurs MAB en tant que candidats pour les blocs de construction du cluster. **Le chapitre 3** a étudié les caractéristiques non idéales du convertisseur MAB et les défis du fonctionnement d'un convertisseur réel. **Le chapitre 4** a présenté un convertisseur quadruple active-bridge de 4×2 kW qui a été conçu et construit au G2Elab dans le but de valider les modèles et les contrôles qui ont été proposés dans les chapitres précédents.

Cette recherche a été effectuée dans le cadre du programme Eco-SESA. Eco-SESA est un projet multidisciplinaire, visant à produire des connaissances, des concepts, des outils et des méthodes pour repenser la planification, la gestion et la gouvernance des systèmes énergétiques urbains, ainsi que la conception de leurs composants. Pour parvenir à une énergie sûre, efficace, durable et accessible, ces contributions ont été partagées entre les communautés scientifiques et les acteurs de la ville et de l'énergie. L'idée derrière ce travail de recherche spécifique était de proposer un nouveau matériel et une nouvelle architecture qui peuvent être utilisés comme outil par d'autres groupes d'Eco-SESA, à savoir les chercheurs impliqués dans les réseaux électriques.

Aborder différents aspects de la solution proposée et de son application a ouvert la porte à un large éventail de questions et de possibilités. Au cours de ce projet de doctorat, certaines de ces possibilités ont été étudiées en profondeur et certaines de ces questions ont reçu une réponse, tandis que beaucoup d'entre elles n'ont été sondées que brièvement ou pas du tout. C'est là que les travaux futurs peuvent commencer. Certains de ces sujets sont :

- L’étude d'autres topologies comme éléments constitutifs du cluster.
- L’étudier de différentes solutions pour l'interface des convertisseurs MAB avec le réseau CA.
- L’utilisation du cluster pour construction d’un réseau en fonctionnement en îloté.
- La fournir des services auxiliaires au réseau.
- L’application des modèles et du contrôle pour le contrôle en ligne et l'optimisation d'un cluster de convertisseurs.
- L’amélioration du modèle de pertes proposé.
- L’amélioration du capteur de courant continu avec TC d'annulation du courant alternatif.

References

[1] BP, “Statistical Review of World Energy,” 2020. [Online]. Available: https://www.bp.com/content/dam/bp/business-sites/en/global/corporate/pdfs/energy-economics/statistical-review/bp-stats-review-2020-full-report.pdf.

[2] Hannah Ritchie, “Energy mix,” 2020. www.ourworldindata.org/energy-mix.

[3] Hannah Ritchie, “Access to Energy,” *Our World in Data*, 2019. www.ourworldindata.org/energy-access.

[4] N. Jones, “How to stop data centres from gobbling up the world’s electricity,” *NEWS FEATURE*, 2018. www.nature.com/articles/d41586-018-06610-y.

[5] IEA, “Global Energy Review 2020,” *Global Energy Review*, 2020. www.iea.org/reports/global-energy-review-2020.

[6] B. K. Bose, F. (Fred) Wang, A. Q. Huang, and H. Akagi, *Power Electronics in Renewable Energy Systems and Smart Grid: Technology and Applications*. Wiley-IEEE Press, 2019.

[7] S. Tripathi, Z. H. Ansari, S. Kumar, S. Majumder, and S. Ghosh, “Smart charger for low power electronic gadgets,” *Proc. Ind. Interact. Innov. Sci. Eng. Technol.*, pp. 19–21, 2020.

[8] A. K. Bhattacharjee, N. Kutkut, and I. Batarseh, “Review of Multiport Converters for Solar and Energy Storage Integration,” *IEEE Trans. Power Electron.*, vol. 34, no. 2, pp. 1431–1445, 2019, doi: 10.1109/TPEL.2018.2830788.

[9] I. Batarseh and K. Alluhaybi, “Emerging Opportunities in Distributed Power Electronics and Battery Integration,” *IEEE POWER Electron. Mag.*, no. June, 2020.

[10] I. Iskender and N. Genc, *Microgrid Architectures, Control and Protection Methods : Chapter 6, Power Electronic Converters in DC Microgrid*. Springer, Cham, 2020.

[11] J. He, D. Zhang, and D. Torrey, “Recent Advances of Power Electronics Applications in More Electric Aircrafts,” *AIAA Propuls. Energy Forum*, 2018, doi: 10.2514/6.2018-5008.

[12] Z. Chen, S. Member, J. M. Guerrero, S. Member, and F. Blaabjerg, “A Review of the State of the Art of Power Electronics for Wind Turbines,” vol. 24, no. 8, pp. 1859–1875, 2009.

[13] R. Ryndzionek and Ł. Sienkiewicz, “Evolution of the HVDC Link Connecting Offshore Wind Farms to Onshore Power Systems,” doi: 10.3390/en13081914.

[14] V. S. Prashun Gorai, Robert W. McKinney, Nancy M. Haegel, Andriy Zakutayev and V. Stevanovic, “A computational survey of semiconductors for power electronics,” *Energy Environ. Sci.*, vol. 12, pp. 3338--3347, 2019, doi: 10.1039/c9ee01529a.

[15] H. Umezawa, “Recent advances in diamond power semiconductor devices,” *Mater. Sci. Semicond. Process.*, vol. 78, no. February, pp. 147–156, 2018, doi:

10.1016/j.mssp.2018.01.007.

[16] S. Peyghami, P. Palensky, and F. Blaabjerg, “An Overview on the Reliability of Modern Power Electronic Based Power Systems,” *IEEE Open J. Power Electron.*, vol. 1, no. February, pp. 34–50, 2020, doi: 10.1109/ojpel.2020.2973926.

[17] Y. Yang, A. Sangwongwanich, and F. Blaabjerg, “Design for Reliability of Power Electronics for,” *CPSS Trans. Power Electron. Appl.*, vol. 1, no. 1, 2016.

[18] T. Dragicevic, P. Wheeler, and F. Blaabjerg, “Artificial Intelligence Aided Automated Design for Reliability of Power Electronic Systems,” *IEEE Trans. Power Electron.*, vol. 34, no. 8, pp. 7161–7171, 2019, doi: 10.1109/TPEL.2018.2883947.

[19] L. Kerachev, A. Andreta, Y. Lembeye, and J. C. Crébier, “A new step towards the Power Electronics Design Automation,” *PCIM Eur. 2017 - Int. Exhib. Conf. Power Electron. Intell. Motion, Renew. Energy Energy Manag.*, no. May, pp. 16–18, 2017, doi: 10.1109/SBMicro.2017.7990843.

[20] IEEE, “IEEE Vision for Smart Grid Controls: 2030 and Beyond,” 2013.

[21] J. Xiao, T. Zhao, K. L. Hai, and P. Wang, “Smart energy hub - Modularized hybrid AC/DC microgrid: System design and deployment,” *2017 IEEE Conf. Energy Internet Energy Syst. Integr. EI2 2017 - Proc.*, vol. 2018-Janua, pp. 1–6, 2017, doi: 10.1109/EI2.2017.8245453.

[22] M. Zulianello, V. Angelucci, and D. Moneta, “Energy Community and Collective Self Consumption in Italy,” *UPEC 2020 - 2020 55th Int. Univ. Power Eng. Conf. Proc.*, 2020, doi: 10.1109/UPEC49904.2020.9209893.

[23] D. Frieden, J. Roberts, and A. F. Gubina, “Overview of emerging regulatory frameworks on collective self-consumption and energy communities in Europe,” *Int. Conf. Eur. Energy Mark. EEM*, vol. 2019-Septe, 2019, doi: 10.1109/EEM.2019.8916222.

[24] Z. Ning, S. Qiuye, and M. Dazhong, “Storage control strategy for energy hub of We-Energy in the energy internet,” *Proc. 29th Chinese Control Decis. Conf. CCDC 2017*, pp. 7029–7033, 2017, doi: 10.1109/CCDC.2017.7978449.

[25] Y. R. Kafle, K. Mahmud, S. Morsalin, and G. E. Town, “Towards an internet of energy,” *2016 IEEE Int. Conf. Power Syst. Technol. POWERCON 2016*, 2016, doi: 10.1109/POWERCON.2016.7754036.

[26] M. A. F. Ghazvini, D. Steen, and L. A. Tuan, “A Centralized Building Energy Management System for Residential Energy Hubs,” *SEST 2019 - 2nd Int. Conf. Smart Energy Syst. Technol.*, pp. 1–6, 2019, doi: 10.1109/SEST.2019.8849066.

[27] L. Zhou, N. Liu, and Y. Zhang, “Energy Management for Smart Energy Hub Considering Gas Dispatch Factor and Demand Response,” *2nd IEEE Conf. Energy Internet Energy Syst. Integr. EI2 2018 - Proc.*, pp. 1–6, 2018, doi: 10.1109/EI2.2018.8582162.

[28] O. Dzobo and X. Xia, “Optimal operation of smart multi-energy hub systems incorporating energy hub coordination and demand response strategy,” *J. Renew. Sustain. Energy*, vol. 9, no. 4, 2017, doi: 10.1063/1.4993046.

[29] Y. Zhong, D. Xie, M. Zhou, Y. Wang, Y. Hou, and Y. Sun, “Hierarchical Optimal Operation for Integrated Energy System Based on Energy Hub,” *2nd IEEE Conf. Energy Internet Energy Syst. Integr. EI2 2018 - Proc.*, no. 61673161, pp. 1–6, 2018, doi: 10.1109/EI2.2018.8582362.

[30] M. Daneshvar, B. Mohammadi-Ivatloo, S. Asadi, K. Zare, and A. Anvari-Moghaddam, “Optimal Day-Ahead Scheduling of the Renewable Based Energy Hubs Considering Demand Side Energy Management,” *SEST 2019 - 2nd Int. Conf. Smart Energy Syst. Technol.*, pp. 1–6, 2019, doi: 10.1109/SEST.2019.8849131.

[31] M. Geidl, G. Koeppel, and P. Favre-Perrod, “The Energy Hub–A powerful concept for future energy systems,” *... Conf. ...*, no. March, pp. 13–14, 2007, [Online]. Available: https://www.ece.cmu.edu/~tanddconf_2004/2007/2007 Conf Papers/Andersson Paper final.pdf.

[32] L. Kerachev, A. Andreta, Y. Lembeye, and J. C. Crébier, “Generic approach for design, configuration and control of modular converters,” *PCIM Eur. 2017 - Int. Exhib. Conf. Power Electron. Intell. Motion, Renew. Energy Energy Manag.*, no. May, pp. 16–18, 2017, doi: 10.1109/SBMicro.2017.7990692.

[33] Z. Zhao, K. Li, Y. Jiang, S. Lu, and L. Yuan, “Overview on Reliability of Modular Multilevel Cascade Converters,” vol. 1, no. 1, 2015.

[34] V. Samavatian, “A Systematic Approach to Reliability Assessment of DC-DC Power Electronic Converters,” Universite Grenoble Alpes - University of Tehran, 2020.

[35] T. Wang Cai, S. Wang, L. Cozzi, B. Motherway, and D. Turk, *Towards a zero-emission, efficient, and resilient buildings and construction sector*. 2017.

[36] IRENA, *REthinking Energy 2017: Accelerating the global energy transformation*, vol. 55, no. July. Abu Dhabi: International Renewable Energy Agency, 2017.

[37] IEA, “Energy efficiency Market Report 2015: Market Trends and Medium-Term Prospects,” 2015.

[38] International Energy Agency, “World Energy Outlook 2019: Executive Summary,” 2019.

[39] C. R. Sullivan, “Winding loss calculation with multiple windings, arbitrary waveforms, and two-dimensional field geometry,” *Conf. Rec. - IAS Annu. Meet. (IEEE Ind. Appl. Soc.*, vol. 3, pp. 2093–2099, 1999, doi: 10.1109/ias.1999.806024.

[40] S. Galeshi, D. Frey, Y. Lembeye, and D. Motte-michellon, “Application of Clustered Multi-port Active-bridge Converters in Micro- grids Keywords Classical energy system of a micro-grid,” in *2019 21st European Conference on Power Electronics and Applications (EPE ’19 ECCE Europe)*, p. P.1-P.9.

[41] S. GALESHI *et al.*, “Optimal Energy Management of A Cluster of Converters in Micro-grids,” in *SYMPOSIUM DE GENIE ELECTRIQUE (SGE 2020)*, 2020.

[42] J. Bohler, F. Krismer, T. Sen, and J. W. Kolar, “Optimized modulation of a four-port isolated DC-DC converter formed by integration of three dual active bridge converter stages,” *INTELEC, Int. Telecommun. Energy Conf.*, vol. 2018-Octob, no. 3, 2019, doi: 10.1109/INTLEC.2018.8612312.

[43] M. Blanc and G. Inp, “Optimization of a DCDC Dual Active Bridge Converter for Aircraft Application,” no. May, pp. 16–18, 2017.

[44] D. Sal Y Rosas, D. Frey, J. L. Schanen, and J. P. Ferrieux, “Close loop control to bidirectional isolated single stage DAB with resonant circuit DC/AC converter to connection of batteries to the single phase grid,” *Conf. Proc. - IEEE Appl. Power Electron. Conf. Expo. - APEC*, pp. 1333–1340, 2017, doi: 10.1109/APEC.2017.7930869.

[45] J. Yang, G. Buticchi, C. Gu, S. Gunter, H. Yan, and P. Wheeler, “Transfer Function Based Input Impedance Determination of Triple Active Bridge Converter,” *IECON Proc. (Industrial Electron. Conf.*, vol. 2019-Octob, pp. 4917–4923, 2019, doi: 10.1109/IECON.2019.8926943.

[46] S. Nakagawa, J. Arai, R. Kasashima, K. Nishimoto, Y. Kado, and K. Wada, “Dynamic performance of triple-active bridge converter rated at 400 V, 10 kW, and 20 kHz,” *2017 IEEE 3rd Int. Futur. Energy Electron. Conf. ECCE Asia, IFEEC - ECCE Asia 2017*, pp. 1090–1094, 2017, doi: 10.1109/IFEEC.2017.7992193.

[47] V. N. S. R. Jakka and A. Shukla, “A triple port active bridge converter based multi-fed power electronic transformer,” *ECCE 2016 - IEEE Energy Convers. Congr. Expo. Proc.*, vol. 1, 2016, doi: 10.1109/ECCE.2016.7854797.

[48] M. A. Hernandez and D. S. y Rosas, “Single-Stage Bidirectional Triple Active Bridge AC-DC converter for Single Phase Grid Applications,” pp. 1–6, 2020, doi: 10.1109/kpec47870.2020.9167522.

[49] V. L. Pham and K. Wada, “Design of Series Inductances in Triple Active Bridge Converter Using Normalization Procedure for Integrated EV and PV System,” *ICPE 2019 - ECCE Asia - 10th Int. Conf. Power Electron. - ECCE Asia*, vol. 3, pp. 3027–3032, 2019.

[50] M. Neubert, A. Gorodnichev, J. Gottschlich, and R. W. De Doncker, “Performance analysis of a triple-active bridge converter for interconnection of future dc-grids,” *ECCE 2016 - IEEE Energy Convers. Congr. Expo. Proc.*, 2016, doi: 10.1109/ECCE.2016.7855337.

[51] and G. D. D. Venkat Nag Someswar Rao Jakka, Anshuman Shukla, “Dual-Transformer-Based Asymmetrical Triple-Port Active Bridge (DT-ATAB) Isolated,” vol. 64, no. 6, pp. 4549–4560, 2017.

[52] M. A. Hernandez and D. S. y Rosas, “Single-Stage Bidirectional Triple Active Bridge AC-DC converter for Single Phase Grid Applications,” pp. 1–6, 2020, doi: 10.1109/kpec47870.2020.9167522.

[53] J. Andrade, D. Sal Rosas, D. Frey, and J. P. Ferrieux, “Modified triple active bridge DC/AC three-phase converter with a series-resonant LC circuit on the AC-side,” *Proc. - 2017 IEEE South. Power Electron. Conf. SPEC 2017*, vol. 2018-Janua, pp. 1–6, 2018, doi: 10.1109/SPEC.2017.8333612.

[54] C. Gu *et al.*, “A Multi-port Power Conversion System for the More Electric Aircraft,” *IEEE Trans. Transp. Electrif.*, vol. 7782, no. c, 2020, doi: 10.1109/TTE.2020.3019446.

[55] C. Gu *et al.*, “Multi-port power conversion systems for the more electric aircraft,”

Proc. IECON 2018 - 44th Annu. Conf. IEEE Ind. Electron. Soc., pp. 5553–5558, 2018, doi: 10.1109/IECON.2018.8592915.

[56] G. Buticchi, L. F. Costa, D. Barater, M. Liserre, and E. D. Amarillo, "A Quadruple Active Bridge Converter for the Storage Integration on the More Electric Aircraft," *IEEE Trans. Power Electron.*, vol. 33, no. 9, pp. 8174–8186, 2018, doi: 10.1109/TPEL.2017.2781258.

[57] M. Phattanasak, R. Gavagsaz-Ghoachani, J. P. Martin, B. Nahid-Mobarakeh, S. Pierfederici, and B. Davat, "Control of a hybrid energy source comprising a fuel cell and two storage devices using isolated three-port bidirectional DC-DC converters," *IEEE Trans. Ind. Appl.*, vol. 51, no. 1, pp. 491–497, 2015, doi: 10.1109/TIA.2014.2336975.

[58] M. La Mendola, M. Di Benedetto, A. Lidozzi, L. Solero, and S. Bifaretti, "Four-Port Bidirectional Dual Active Bridge Converter for EVs Fast Charging," *2019 IEEE Energy Convers. Congr. Expo. ECCE 2019*, pp. 1341–1347, 2019, doi: 10.1109/ECCE.2019.8912252.

[59] C. Keles, A. Karabiber, M. Akcin, A. Kaygusuz, B. B. Alagoz, and O. Gul, "A smart building power management concept: Smart socket applications with DC distribution," *Int. J. Electr. Power Energy Syst.*, vol. 64, pp. 679–688, 2015, doi: 10.1016/j.ijepes.2014.07.075.

[60] K. Venugopal and P. Kanakasabapathy, "Multiport interleaved converter for DC microgrid applications," *2017 Innov. Power Adv. Comput. Technol. i-PACT 2017*, vol. 2017-Janua, pp. 1–6, 2017, doi: 10.1109/IPACT.2017.8244968.

[61] Y. Chen, P. Wang, Y. Elasser, and M. Chen, "Multicell Reconfigurable Multi-Input Multi-Output Energy Router Architecture," *IEEE Trans. Power Electron.*, vol. 35, no. 12, pp. 13210–13224, 2020, doi: 10.1109/tpel.2020.2996199.

[62] U. Abronzini, M. Di Monaco, F. Porpora, G. Tomasso, M. D'Arpino, and C. Attaianese, "High performance active battery management system with multi-winding transformer," *2019 IEEE Energy Convers. Congr. Expo. ECCE 2019*, pp. 1231–1236, 2019, doi: 10.1109/ECCE.2019.8912966.

[63] T. H. Phung *et al.*, "Integrated converter network for active balancing structure of battery," *CIPS 2016 - 9th Int. Conf. Integr. Power Electron. Syst.*, pp. 5–10, 2019.

[64] R. Gallay, "Metallized film capacitor lifetime evaluation and failure mode analysis," *Cern Accel. Sch. Power Convert. CAS 2014 - Proc.*, vol. 003, no. May 2014, pp. 45–56, 2018, doi: 10.5170/CERN-2015-003.45.

[65] F. Krismer, "Modeling and optimization of bidirectional dual active bridge DC- DC converter topologies," 2010.

[66] L. F. Costa, G. Buticchi, and M. Liserre, "Comparison of basic power cells for quad-active-bridge DC-DC converter in smart transformer," *2015 17th Eur. Conf. Power Electron. Appl. EPE-ECCE Eur. 2015*, vol. 1, pp. 1–10, 2015, doi: 10.1109/EPE.2015.7311703.

[67] D. Sal Rosas, J. Andrade, D. Frey, and J. P. Ferrieux, "Single stage isolated bidirectional DC/AC three-phase converter with a series-resonant circuit for V2G,"

2017 IEEE Veh. Power Propuls. Conf. VPPC 2017 - Proc., vol. 2018-Janua, pp. 1–5, 2018, doi: 10.1109/VPPC.2017.8330898.

[68] B. J. D. Vermulst, J. L. Duarte, C. G. E. Wijnands, and E. A. Lomonova, "Quad-active-bridge single-stage bidirectional three-phase AC-DC converter with isolation: introduction and optimized modulation," *IEEE Trans. Power Electron.*, vol. 32, no. 4, pp. 2546–2557, 2017, doi: 10.1109/TPEL.2016.2579682.

[69] M. Aguirre and A. Yazdani, "A single-phase dc-ac dual-active-bridge based resonant converter for grid-connected Photovoltaic (PV) applications," *2019 21st Eur. Conf. Power Electron. Appl. EPE 2019 ECCE Eur.*, pp. 1–10, 2019, doi: 10.23919/EPE.2019.8915475.

[70] S. Marti and H. Krishnaswami, "Novel MPPT Algorithm for Active Power Control of Multi-Level Dual-Active Bridge PV Converter Implemented in NI myRIO," pp. 2936–2940, 2018, doi: 10.1109/pvsc.2017.8366300.

[71] S. Galeshi, D. Frey, and Y. Lembeye, "Design procedure of dc-dc multi-port active-bridge converters," in *PCIM Europe Conference Proceedings*, 2020, vol. 1.

[72] D. Honorio, L. H. S. C. Barreto, A. Foote, B. Ozipineci, and J. O. P. Pinto, "Modular transformer in isolated multiport power converters," *Proc. - 2017 IEEE South. Power Electron. Conf. SPEC 2017*, vol. 2018-Janua, pp. 1–5, 2018, doi: 10.1109/SPEC.2017.8333585.

[73] M. Rashidi, A. Bani-Ahmed, R. Nasiri, A. Mazaheri, and A. Nasiri, "Design and implementation of a multi winding high frequency transformer for MPSST application," in *International Conference on Renewable Energy Research and Applications (ICRERA)*, 2017, vol. 5, pp. 13–16.

[74] X. She, R. Burgos, G. Wang, F. Wang, and A. Q. Huang, "Review of solid state transformer in the distribution system: From components to field application," *2012 IEEE Energy Convers. Congr. Expo. ECCE 2012*, pp. 4077–4084, 2012, doi: 10.1109/ECCE.2012.6342269.

[75] S. BANDYOPADHYAY, P. Purgat, Z. Qin, and P. Bauer, "A Multi-Active Bridge Converter with Inherently Decoupled Power Flows," *IEEE Trans. Power Electron.*, vol. 8993, no. c, pp. 1–15, 2020, doi: 10.1109/tpel.2020.3006266.

[76] S. Galeshi, D. Frey, and Y. Lembeye, "Modular Modeling and Control of Power Flow in A Multi-Port Active-Bridge Converter," in *SGE 2018*, 2018, no. Sge, pp. 3–5.

[77] S. Galeshi, D. Frey, and Y. Lembeye, *Efficient and scalable power control in multi-port active-bridge converters*. 2020.

[78] B. J. D. Vermulst, J. L. Duarte, E. A. Lomonova, and K. G. E. Wijnands, "Scalable multi-port active-bridge converters: Modelling and optimised control," *IET Power Electron.*, vol. 10, no. 1, pp. 80–91, 2017, doi: 10.1049/iet-pel.2016.0191.

[79] G. Oggier, G. O. Garc, S. Member, and A. R. Oliva, "Switching Control Strategy to Minimize Dual Active Bridge Converter Losses," vol. 24, no. 7, pp. 1826–1838, 2009.

[80] M. Blanc, Y. Lembeye, J. Ferrieux, C. Rizet, and T. Bensalah, "Optimization of a DC / DC dual active bridge converter for aircraft application," *Eur. Power Electron. Drives*,

vol. 28, no. 4, pp. 182–199, 2018, doi: 10.1080/09398368.2018.1489482.

[81] A. Rolán, F. C. López, S. Bogarra, L. Monjo, and J. Pedra, “Reduced-Order Models of Squirrel-Cage Induction Generators for Fixed-Speed Wind Turbines under Unbalanced Grid Conditions,” *IEEE Trans. Energy Convers.*, vol. 31, no. 2, pp. 566–577, 2016, doi: 10.1109/TEC.2015.2504793.

[82] M. Converter *et al.*, “Reduced-Order Small-Signal Models of Modular,” vol. 66, no. 3, pp. 2257–2268, 2019.

[83] V. Purba, B. B. Johnson, M. Rodriguez, S. Jafarpour, F. Bullo, and S. V. Dhople, “Reduced-order Aggregate Model for Parallel-connected Single-phase Inverters,” *IEEE Trans. Energy Convers.*, vol. 34, no. 2, pp. 824–837, 2019, doi: 10.1109/TEC.2018.2881710.

[84] S. Galeshi, D. Frey, and Y. Lembeye, “Computational Cost Efficient Model of Losses for Multi-port Active-bridge Converters,” in *IEEE Energy Conversion Congress and Exposition (ECCE)*, 2020, pp. 2928–2933, doi: 10.1109/ecce44975.2020.9236119.

[85] S. Han, I. Munuswamy, and D. Divan, “Preventing transformer saturation in bi-directional Dual Active Bridge Buck-Boost DC/DC converters,” *2010 IEEE Energy Convers. Congr. Expo. ECCE 2010 - Proc.*, pp. 1450–1457, 2010, doi: 10.1109/ECCE.2010.5618254.

[86] M. Wattenberg, U. Schwalbe, and M. Pfost, “Impact of DC-bias on dual active bridge control and how to avoid it,” *2019 21st Eur. Conf. Power Electron. Appl. EPE 2019 ECCE Eur.*, pp. 1–8, 2019, doi: 10.23919/EPE.2019.8915516.

[87] Z. Zhao *et al.*, “Measurements and calculation of core-based B-H curve and magnetizing current in DC-biased transformers,” *IEEE Trans. Appl. Supercond.*, vol. 20, no. 3, pp. 1131–1134, 2010, doi: 10.1109/TASC.2010.2041211.

[88] R. Chattopadhyay, U. Raheja, G. Gohil, V. Nair, and S. Bhattacharya, “Sensorless Phase Shift Control for Phase Shifted DC- DC converters for Eliminating DC Transients from Transformer Winding Currents,” pp. 1882–1889, 2018.

[89] A. Gertsman and S. Ben-Yaakov, “Zeroing transformer’s DC current in resonant converters with no series capacitors,” *2010 IEEE Energy Convers. Congr. Expo. ECCE 2010 - Proc.*, no. 2, pp. 4028–4034, 2010, doi: 10.1109/ECCE.2010.5618289.

[90] B. Zhao, Q. Song, W. Liu, and Y. Zhao, “Transient DC bias and current impact effects of high-frequency-isolated bidirectional DC-DC converter in practice,” *IEEE Trans. Power Electron.*, vol. 31, no. 4, pp. 3203–3216, 2016, doi: 10.1109/TPEL.2015.2445831.

[91] P. Mantzanas and T. Dürbaum, “A novel detailed analysis of the flyback converter utilizing a transformer with nonlinear magnetizing inductance,” *PCIM Eur. 2017 - Int. Exhib. Conf. Power Electron. Intell. Motion, Renew. Energy Energy Manag.*, no. May, pp. 16–18, 2017, doi: 10.1109/SBMicro.2017.7990940.

[92] A. J. Hanson, “Enabling Miniaturized Grid-Interface Power Conversion,” MIT - Massachusetts Institute of Technology, 2019.

[93] R. Chattopadhyay, U. Raheja, G. Gohil, V. Nair, and S. Bhattacharya, “Sensorless

phase shift control for phase shifted DC-DC converters for eliminating DC transients from transformer winding currents," *Conf. Proc. - IEEE Appl. Power Electron. Conf. Expo. - APEC*, vol. 2018-March, pp. 1882–1889, 2018, doi: 10.1109/APEC.2018.8341274.

[94] L. Shu, W. Chen, and Z. Song, "Prediction Method of DC Bias in DC-DC Dual-Active-Bridge Converter," *CPSS Trans. Power Electron. Appl.*, vol. 4, no. 2, pp. 152–162, 2019, doi: 10.24295/cpsstpea.2019.00015.

[95] G. Ortiz, J. Mühlethaler, and J. W. Kolar, "'Magnetic ear'-based balancing of magnetic flux in high power medium frequency dual active bridge converter transformer cores," *8th Int. Conf. Power Electron. - ECCE Asia "Green World with Power Electron. ICPE 2011-ECCE Asia*, no. 2, pp. 1307–1314, 2011, doi: 10.1109/ICPE.2011.5944377.

[96] A. Patel and M. Ferdowsi, "Current sensing for automotive electronics - A survey," *IEEE Trans. Veh. Technol.*, vol. 58, no. 8, pp. 4108–4119, 2009, doi: 10.1109/TVT.2009.2022081.

[97] S. Klopper and J. A. Ferreira, "A sensor for balancing flux in converters with a high-frequency transformer link," *IEEE Trans. Ind. Appl.*, vol. 33, no. 3, pp. 774–779, 1997, doi: 10.1109/28.585868.

[98] D. Wilson, "A new pulsewidth modulation method inherently maintains output transformer flux balance," in *Proc. of the 8th National Solid-State Power Conversion Conference (POWERCON)*, 1981.

[99] W. M. Polivka, A. Cocconi, and S. Cuk, "Detection of Magnetic Saturation in Switching Converters," in *Proc. PCI*, 1982, p. 583.

[100] D. Frey, J. Schanen, and I. Dia, "Harmonics propagation in industrial networks in the range of 2 to 150kHz," *Conf. Proc. - IEEE Appl. Power Electron. Conf. Expo. - APEC*, pp. 2649–2654, 2013, doi: 10.1109/APEC.2013.6520670.

[101] A. Rodrigo-Mor, F. A. Muñoz, and L. C. Castro-Heredia, "Principles of charge estimation methods using high-frequency current transformer sensors in partial discharge measurements," *Sensors (Switzerland)*, vol. 20, no. 9, 2020, doi: 10.3390/s20092520.

[102] Y. Xu, X. Gu, B. Liu, B. Hui, Z. Ren, and S. Meng, "Special requirements of high frequency current transformers in the on-line detection of partial discharges in power cables," *IEEE Electr. Insul. Mag.*, vol. 32, no. 6, pp. 8–19, 2016, doi: 10.1109/MEI.2016.7656806.

[103] D. B. Solovev and M. A. Gorkavyy, "Current transformers: Transfer functions, frequency response, and static measurement error," *2019 Int. Sci. Technol. Conf. "EastConf", EastConf 2019*, 2019, doi: 10.1109/Eastonf.2019.8725351.

[104] G. Kevin, "Stage de fin d'etude en IUP GEII," 2006.